Principles of pattern formation in multicellular systems with diffusible signals and feedback networks

Doctoral thesis for obtaining the

academic degree Doctor of

Natural Sciences

(Dr. rer. nat.)

submitted by

Narendra Landge, Amit

at the

Faculty of Sciences

Department of Biology

Konstanz, 2023

Date of oral examination: 12.01.2024

Examination board:
Prof. Lutz Becks (Chairperson)
Prof. Patrick Müller
Prof. Iain Couzin

Table of Contents

Acknowledgements

Science is a highly collaborative adventure. For this adventure, the companions matter as much as the journey. I have been blessed with the company and support of amazing scientists, colleagues, friends, and family members throughout this fascinating journey. I would like to thank them all from the bottom of my heart!

To Patrick, who is not only an excellent scientist, but also a great mentor, I am extremely grateful! He offered me a challenging PhD project, but along with that provided all the guidance and support needed to tackle the challenges. When the lab moved from Tübingen to Konstanz, he offered that I also move to Konstanz allowing me to get enough time and required support to complete the thesis. He helped me to attend an international scientific conference and present my work at the Flatiron Institute in New York. I also thank him for our regular meetings and scientific discussions. I learned from him the importance of calm and rational questioning, rigorous and systematic experimentation, attention to detail, dedication, and professionalism. Working in his lab has truly helped me to uncover my potential as a scientist. Thank you, Patrick!

I am grateful to my thesis committee members for lending me their valuable time and scientific expertise. I thank Prof. Detlef Weigel and Prof. Marja Timmermans from my thesis committee in Tübingen. Their feedback was really helpful to ensure that my PhD research stays on the right track. I am grateful to Prof. Iain Couzin for agreeing to be my second thesis advisor when I enrolled in the University of Konstanz. I thank him for his feedback during the thesis committee meeting and for suggesting that I should structure my thesis as a cumulative thesis.

Daniel, you have given me unconditional support as a professional and as a friend. I know that you are an amazing scientist and I can't thank you enough! Your timely help was crucial to complete the revisions for the single-molecule morphogens paper. I thank you for helping me with the German translation for the summary of this thesis. Furthermore, I thank you for being a friend with whom I can share my success and my troubles. Manu, I think of you as a really close friend. I thank you a gazillion times for all your help and advice! It is a pleasure to work with you, because you are very professional and a considerate person at the same time. I thank you both for the sweet rumtopf and for helping me when I had covid. PhD life is tough, but it was easier because of you; I am forever grateful to both of you!

I would like to express my gratitude to the amazing postdocs in our lab who helped me in the lab and offered great professional and personal advice on many occasions. I am grateful to Katherine, Anna, Hernan, Anica, Murat, Moritz, and Luciano. Katherine has the most admirable work-ethic and I hope that I'll be able to even half as good as her! I thank Anna for her valuable feedback on my presentations and for her professional advice. Also, whenever she asked me for my scientific opinion, she did it with such a professional ease and impressed upon me the importance of asking and giving feedback with professionalism and mutual respect. Whenever, I need advice on image

analysis problems, I go to Hernan, because he knows image analysis like the back of his hand! He has the ability to explain complex scientific topics using simple concepts and a step-by-step process making them easy to grasp. Hernan, I thank you very much for all your help and I am taking a very good care of the Madagascar jewel that you gifted me! I thank Anica for making it so easy to keep proper documentation of the fish lines that I had to manage. I learned the importance of good organization and work-life balance from you. Thank you, Anica! I thank Murat for his valuable insights into biological pattern formation and mathematical modeling. His expertise was crucial when we set up the new file-server in Konstanz and he is a walking encyclopedia of developmental biology! I am thankful to Moritz for his out-of-the-box perspectives on my project and for all his help while communicating with the Uni-Konstanz workshop. Even though I did not have a lot of personal contact with Luciano, his professional help and advice during the early phase of my PhD project was crucial and I am very thankful to him!

It is already hard to make a PhD and even more so in a foreign country. However, the support system created by other PhD students, who are in the same boat as you, helps you to go through some of the most difficult times. My friends Anasuya, Minakshi, Joe, Anupam, and Xixi are the definition of that support system! I shared some of the happiest moments of my PhD life with them and they are a source of motivation to me. Especially, I am thankful to Ana and Anupam, because they just get me and talking to them gives me strength to keep going ahead, even when the path is difficult. Also, other PhD students in the lab, at the MPI, and at the University of Konstanz have helped me countless times. I am thankful to all of them. Particularly, I want to say thank you to Gary, Autumn, David, and Hannes.

The role of technical and administrative support staff to is indispensable to provide a productive and seamless scientific work environment. I am grateful for the support of our technical assistants Maria and Christine, fish caretaker Dieter, and secretary Herta and other people who have helped me during my time at the FML in Tübingen! When the lab moved from Tübingen to Konstanz, Marianne provided indispensable support to each of us to get started in the new workplace and she still continues to be indispensable. Thank you very much, Marianne! I also thank our current secretary Karin for her support! I thank our fish caretakes at the university!

The last part of the PhD journey was especially difficult and stressful for me. I was blessed to have Alina by my side in the difficult times, when I was low on motivation. She not only motivated me, but also challenged my views and opinions about science. She helped me realize that being fascinated by science is as important, if not more, as rational thinking to perform good research. I am extremely grateful to Alina for believing in me and for supporting me!

I am grateful to my parents for teaching me the importance of hard work and honesty and giving me the freedom to pursue my academic ambitions. I owe all my success to them! Without them, I am nothing!

I would like to acknowledge that my work was made possible by the excellent, state-of-the-art research infrastructure of the Friedrich Miescher Laboratory of the Max Planck Society and the University of Konstanz. I acknowledge the research funding from the European Research Council that supports our work. I thank the International Max Planck Research School, of which I was a part for my time in Tübingen, and the Graduate School of Biological Sciences at the University of Konstanz.

There are countless others who have helped and encouraged me during my PhD journey one way or another. I would like to thank Laura, Michael, Hadeer, Vinod ji, Nicola, Lea, Lola, Sabrina, Benedict, Nikki, Cedric, Lisa, Konstantin, Cornelius, and Pia.

Summary

Biological systems display a spectacular array of spatial and temporal patterns at multiple levels of organization- subcellular to multicellular and beyond. Emergence of these patterns in complex biological systems can result from interactions of system components. The general principles governing these interactions can be similar, even if the pattern-forming units are different. These principles of pattern formation can be formulated using the framework of reaction-diffusion systems. Reaction-diffusion systems can give rise to self-organized patterns driven by interactions of diffusible system components. Using mathematical methods, precise reaction-diffusion conditions for the emergence of self-organized patterns can be derived. For example, activator-inhibitor systems can give rise to self-organized periodic spatial patterns known as 'Turing patterns', if the inhibitor diffusivity is higher than activator diffusivity. The requirement of different diffusivities of activator and inhibitor is called 'diffusivity constraint'. However, the 'diffusivity constraint' is not a general feature of pattern-forming reaction-diffusion networks, because mathematical analyses of multicomponent reaction-diffusion networks incorporating non-diffusible components have revealed networks that do not require diffusivity constraint for pattern formation. How do activator-inhibitor patterning systems achieve large differences in effective diffusivities during embryonic development? What are the molecular mechanisms that result in short-range activator and long-range inhibitor? What are the implications of the novel multicomponent reaction-diffusion networks for natural and synthetic multicellular pattern formation? Can we create synthetic multicellular systems capable of pattern formation based on the multicomponent reaction-diffusion networks? My thesis addresses these important questions using molecular biology, microscopy, synthetic biology, and mathematical modeling approaches.

My theoretical synthesis based on multicomponent reaction-diffusion systems suggested that pattern-forming reaction-diffusion systems are more common than previously thought. Using concepts of graph theory and linear stability analysis I explained how self-organized Turing patterns can emerge in reaction-diffusion systems without strict constraints on the biophysical parameters. In addition, I investigated a well-known activator-inhibitor system involved in germ layer patterning during embryonic development – the Nodal-Lefty system. We used advanced single-molecule imaging

and tracking methods to show that in developing zebrafish embryos, Nodals and Leftys disperse by hindered diffusion in the extracellular space. Moreover, Nodals (activators) have lower effective diffusivity and shorter range than Leftys (inhibitors), because they bind strongly to extracellular receptors. Surprisingly, we observed unexpected patterns of extracellular localization for Nodal and Lefty in our experimental data. To explain these seemingly contradictory observations, I developed an agent-based model of Nodal and Lefty dispersal. By systematically varying the parameters of the agent-based model, we revealed the role of extracellular geometry in differential localization of the Nodals and Leftys in the distinct extracellular regions.

To translate our knowledge of reaction-diffusion systems and multicellular pattern formation into a synthetic multicellular patterning system, I designed and implemented a synthetic reaction-diffusion network in *Escherichia coli* using genetic circuits and diffusible signaling molecules. Using these engineered bacteria, I created a synthetic multicellular system. This system displayed spontaneous traveling-wave patterns of gene expression driven by genetic feedbacks and boundary conditions. These traveling waves exhibited an intriguing ability to sense domain boundaries. Our perturbation analyses revealed the role of feedback networks, diffusible signals, and boundary conditions in the emergence and directionality of multicellular traveling-wave patterns. Overall, this thesis offers insights into mechanisms of biological pattern formation and elucidates the implementation and analysis of a synthetic multicellular pattern-forming system.

Zusammenfassung

Biologische Systeme zeigen eine beeindruckende Vielfalt räumlicher und zeitlicher Muster auf verschiedenen Organisationsebenen - von subzellulär bis zu mehrzellig und darüber hinaus. Das Auftreten dieser Muster in komplexen biologischen Systemen kann durch Interaktionen der Systemkomponenten entstehen. Die allgemeinen Prinzipien, die diese Interaktionen regulieren, können ähnlich sein, auch wenn die Muster-bildenden Einheiten unterschiedlich sind. Diese Prinzipien der Musterbildung können im Rahmen von Reaktions-Diffusions-Systemen formuliert werden. Reaktions-Diffusions-Systeme können selbstorganisierte Muster erzeugen, die durch die Wechselwirkungen diffundierender Systemkomponenten gesteuert werden. Mit mathematischen Methoden können präzise Reaktions-Diffusions-Bedingungen für das Auftreten selbstorganisierter Muster abgeleitet werden. Zum Beispiel können Aktivator-Inhibitor-Systeme selbstorganisierte, periodische, räumliche Muster, bekannt als 'Turingmuster', erzeugen, wenn die Diffusivität des Inhibitors höher ist als die des Aktivators. Die Voraussetzung unterschiedlicher Diffusivitäten von Aktivator und Inhibitor wird als „diffusivity constraint“, etwa „Diffusivitätseinschränkung" bezeichnet. Diese Einschränkung ist jedoch keine allgemeine Eigenschaft von Musterbildungs-Reaktions-Diffusionsnetzwerken, da mathematische Analysen von mehrkom-ponentigen Reaktions-Diffusionsnetzwerken unter Einbeziehung nichtdiffundierender Komponenten Netzwerke aufzeigen, die keine Diffusivitätseinschränkung für die Musterbildung erfordern. Wie erreichen Aktivator-Inhibitor-Musterbildungssysteme während der embryonalen Entwicklung große Unterschiede in der effektiven Diffusivität? Was sind die molekularen Mechanismen, die zu einem Aktivator mit kurzer Reichweite und einem Inhibitor mit großer Reichweite führen? Welche Implikationen haben diese neuartigen mehrkomponentigen Musterbildungs-Reaktions-Diffusionsnetzwerke für die natürliche und synthetische Musterbildung in mehrzelligen Systemen? Können wir synthetische, mehrzellige Systeme zur Musterbildung auf der Grundlage von mehrkomponentigen Reaktions-Diffusionsnetzwerken erschaffen? Meine Dissertation behandelt diese wichtigen Fragen unter Verwendung von Methoden der Molekularbiologie, Mikroskopie, synthetischen Biologie und mathematischen Modellierungsansätzen.

Meine theoretische Analyse auf Basis von Mehrkomponenten-Reaktions-Diffusions-Systemen legt nahe, dass Muster-bildende Reaktions-Diffusions-Systeme häufiger vorkommen könnten als bisher angenommen. Unter Verwendung von Konzepten der

Graphentheorie und der linearen Stabilitätsanalyse erkläre ich wie selbstorganisierte Turing-Muster in Reaktions-Diffusions-Systemen ohne strikte Einschränkungen bei biophysikalischen Parametern entstehen können. Darüber hinaus untersuchte ich ein bekanntes Aktivator-Inhibitor-System, das an der Musterbildung der Keimblätter während der embryonalen Entwicklung beteiligt ist - das Nodal-Lefty-System. Mithilfe von fortschrittlicher Einzelmolekülmikroskopie und Trackingmethoden zeigen wir, dass sich in Zebrafischembryonen Nodals und Leftys durch gehemmte Diffusion im extrazellulären Raum verbreiten. Nodals (Aktivatoren) haben eine niedrigere effektive Diffusivität und eine kürzere Reichweite als Leftys (Inhibitoren), weil sie stark an extrazelluläre Rezeptoren binden. Überraschenderweise beobachteten wir unerwartete Muster extrazellulärer Lokalisierung für Nodal und Lefty in unseren experimentellen Daten. Um diese scheinbar widersprüchlichen Beobachtungen zu erklären, habe ich ein agentenbasiertes Modell der Nodal- und Leftyverteilung entwickelt. Durch systematische Variation der Parameter des agentenbasierten Modells konnten wir feststellen, welche Rolle die extrazelluläre Geometrie für die differentielle Lokalisierung der Nodal- und Leftymoleküle in verschiedenen Regionen des extrazellulären Raumes spielt.

Um unser Wissen über Reaktions-Diffusions-Systeme und Musterbildung in mehrzelligen Systemen in ein synthetisches, mehrzelliges Musterbildungssystem zu übersetzen, habe ich ein synthetisches Reaktions-Diffusions-Netzwerk mit genetischen Schaltkreisen und diffundierenden Signalmolekülen in *Escherichia coli* entworfen und implementiert. Unter Verwendung dieser gentechnisch veränderten Bakterien habe ich ein synthetisches, mehrzelliges System geschaffen. Dieses System zeigte spontane, Wanderwellen der Genexpression, die durch genetische Rückkopplung und spezifische Rahmenbedingungen ermöglicht werden. Diese Wanderwellen zeigten die faszinierende Fähigkeit, Domänengrenzen wahrzunehmen. Unsere Störungsanalysen enthüllten die Rolle von Rückkopplungsnetzwerken, diffundierenden Signalen und Rahmenbedingungen für das Entstehen und die Richtung von mehrzelligen, Wanderwellen. Zusammen genommen liefert diese Dissertation Einblicke in Mechanismen der biologischen Musterbildung und erläutert die biologische Umsetzung und Analyse eines synthetischen, mehrzelligen Musterbildungssystems.

1. Introduction

Laws of nature shape the living and non-living matter in a fascinating array of patterns which has inspired the curious human mind to decipher these laws and understand the principles of pattern formation. From the regular arrangement of water molecules inside a miniscule snowflake to the astronomical galactic spirals, the non-living matter is arranged into forms of mathematical precision. Personally, I am even more fascinated by the spectacular forms and patterns displayed by living matter - may it be the multicellular spirals of the slime mold *Dictyostelium discoidium*, the phylotactic arrangements of leaves or the periodic patterns of spots and strips of animal pelage. Periodic, spiral, and fractal patterns can emerge in living systems at a vast range of spatial and temporal scales. The observations of these patterns have inspired investigations of mathematical principles that govern them. The works of D'Arcy Wentworth Thompson - On Growth and Form (Thompson, 1942) - and Alan Turing - The chemical basis of morphogenesis (Turing, 1952) – are prominent examples of the application of mathematical methods to unravel the overarching rules that govern emergence of biological forms and patterns. Many scientific works inspired by these seminal publications have advanced our understanding of biological patterns and forms.

In this doctoral thesis, I present our current understanding of biological pattern formation and efforts to advance it. The aim of my research was to understand the mechanisms governing emergence of spatiotemporal patterns in multicellular systems. During my research, I developed methods to not only understand the principles of pattern formation, but also to engineer multicellular pattern-forming systems based on these principles. I investigated the mechanisms of pattern formation in the context of embryonic development and in a synthetic bacterial multicellular system that I developed using complex multicomponent genetic circuits. I also had the good fortune to collaborate with brilliant scientists and address questions pertaining different aspects of multicellular patterning. We asked questions regarding the involvement of the reaction-diffusion mechanism in the emergence of self-organized multicellular patterns. We analyzed in detail – at the single-molecule level – the mechanisms of diffusible signal dispersal in developing zebrafish embryos.

Before presenting the results of this scientific undertaking, I would like to provide a brief scientific account of the field and scope of my research. Then, I will present the

results in the form of two peer-reviewed publications and one unpublished research article. In the end, I will discuss the outcomes of my research and their implications to arrive at insightful conclusions. I hope that this thesis advances the scientific understanding of multicellular pattern formation mechanisms, captivates the reader, and inspires scientific curiosity.

1.1. Biological pattern formation

The variety of biological pattern-forming systems is vast. But, they can be classified by the level of biological organization at which they operate (Figure 1). At each level, the pattern-forming unit and the exact nature of interactions may vary, but the general principles of pattern formation may be similar. For example, subcellular-level pattern formation can have protein molecules as a pattern-forming unit with interactions mediated through binding-unbinding and protein conformational changes; on the other hand, multicellular-level patterns can be formed with cells as a pattern-forming unit and interactions driven by cell-cell signaling and gene expression. In both cases, the rules of interactions (activation, inhibition, interaction network, etc.) that lead to pattern formation can be very similar.

Let's consider a few examples of biological patterns to get insights into the pattern-forming units, their interactions, and the processes that lead to pattern formation (Figure 1). At the subcellular level, the MinD-MinE system generates patterns of intracellular protein localization (Lutkenhaus, 2007). In *Escherichia coli*, the pole-to-pole oscillations of MinD-MinE are required to position the cell division machinery at the middle of the bacterial cell (Raskin & de Boer, 1999). These oscillations are driven by interactions of MinD (an adenosine triphosphatase, i.e., an ATPase) and MinE (an ATPase activating enzyme) – MinD dimerizes upon binding to adenosine-triphosphate (ATP) and binds to cell membrane with increased affinity. The membrane bound MinD-ATP can recruit more MinD-ATP generating a positive-feedback. MinE has an inactive cytosolic conformation, but it is activated upon binding to membrane bound MinD-ATP and stimulates ATPase activity of MinD, leading to membrane detachment. These activator-inhibitor interactions of MinD-MinE can produce self-organized spatial and temporal patterns of protein distribution. This system was engineered to produce intracellular spiral wave patterns in mammalian cells (Rohith et al., 2022) (Figure 1A top). Furthermore, upon reconstitution on a supported lipid-bilayer, MinD-MinE can produce

diverse patterns - spiral waves, spots, labyrinth, mesh (Glock et al., 2019; Loose et al., 2008) (Figure 1A bottom). The patterns are able to exhibit geometry sensing as shown by geometric confinement in the reconstituted system (Schweizer et al., 2012). Further, the system can be used to achieve pattern-driven molecular transport by diffusiophoresis *in vitro* and *in vivo* (Ramm et al., 2021). Thus, a simple two-protein system can produce complex subcellular patterns driven by activator-inhibitor type interactions mediated through protein conformation changes.

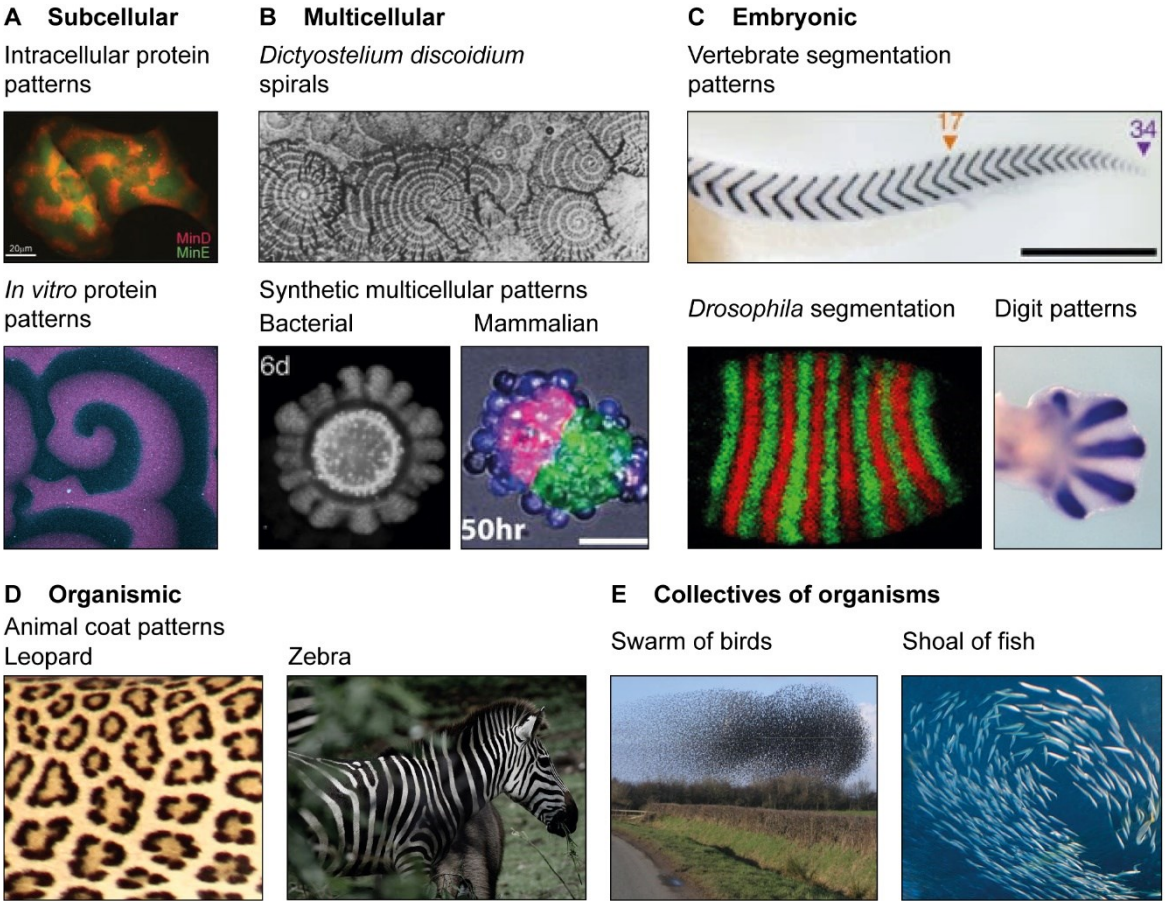

Figure 1: Examples of biological pattern formation
A) Subcellular spiral patterns generated by localization of proteins. Top image shows fluorescently labelled MinD-MinE proteins generating spiral patterns inside a mammalian cell. MinD and MinE are bacterial proteins required for the proper positioning of the cell division machinery. The image is adapted from (Rohith et al., 2022). Bottom image shows patterns of MinD proteins labelled with a fluorescent dye reconstituted *in vitro* on a supported lipid bilayer. The image is adapted from (Glock et al., 2019). **B)** Patterns of spatial multicellular organization in natural and artificial systems. Top image shows spiral patterns formed by the slime mold *Dictyostelium discoidium*, adapted from (Newell, 1983). Bottom images show, left - patterns of bacterial colony growth formed using lateral inhibition mechanism (Duran-Nebreda et al., 2021), right – patterns of 3D cellular assembly driven by differential adhesion in mammalian cells engineered with synthetic Notch receptors (Toda et al., 2018). **C)** Examples of embryonic

patterns of gene expression driving morphogenesis. On top – zebrafish segmentation patterns visualized by staining the segment boundary marker *cb1045 (xirp2a)*; image from (Liao et al., 2016). On bottom left – *Drosophila* embryonic segmentation patterns visualized by staining the pair rule genes *even-skipped (eve)* and *odd-skipped (odd)*. Image adapted from (Clark & Akam, 2016). On bottom right – mouse limb at E12.5 embryonic stage showing *Sox9* staining for determining the formation of digit pattern (Sheth et al., 2012). **D)** Animal coats showing the spotted patterns of leopard (left) and the stripe patterns of zebra (right). **E)** Patterns generated by collective behavior of organisms – swarm of birds (left), shoal of fish (right). Images for D) and E) - adapted from Wikimedia Commons.

At the multicellular level, similar spiral patterns can be observed in colonies of the slime mold *Dictyostelium discoidium* (Figure 1B top). These patterns are produced by collective cell migration and aggregation of the amoebae driven by cyclic adenosine 3', 5'-monophosphate (cAMP) waves (Tyson & Murray, 1989). Upon nutrient depletion, the cells signal to their neighbors via extracellular cAMP leading to production of more cAMP by adenylate cyclase (positive feedback) and cAMP secretion. The extracellular cAMP can diffuse through the medium to stimulate the neighboring cells. The cAMP receptors become desensitized upon prolonged exposure and cAMP production is halted. Intracellular cAMP is hydrolyzed by phosphodiesterase. This system behaves like an excitable medium producing waves of cAMP propagating outward from the signaling center. These waves direct chemotactic movements and cell migration to generate intriguing multicellular patterns (Figure 1B top). One key principle common to the subcellular MinD-MinE system and this multicellular system is the amplification of initial perturbations by positive feedback. The inhibitory interactions driven by MinE in the MinD-MinE system are akin to the receptor desensitization and cAMP hydrolysis in this multicellular system. These observations provide insights into similar principles of pattern formation at the subcellular and multicellular levels, even though the pattern-forming units and the exact nature of interactions are different.

One may ask if synthetic biological patterning systems can be designed based on the principles of pattern formation observed in natural systems. To this end, synthetic multicellular patterning systems have been designed and characterized (Duran-Nebreda et al., 2021; Karig et al., 2018; Sekine et al., 2018; Toda et al., 2018). Duran-Nebreda et al. (Duran-Nebreda et al., 2021) designed a synthetic bacterial multicellular system based on the local activation and long-range inhibition principle (Gierer & Meinhardt, 1972). The synthetic system produced periodic patterns of cell density along the edge of a growing *Escherichia coli* lawn (Figure 1B bottom-left) by inhibiting cell division and

promoting cell-cell adhesion via the cellular production of a diffusible signal. The diffusible signal was produced by all cells and served as a long-range inhibitor. The cells themselves were considered as a local activator with the ability to replicate and spread locally. The diffusible signal (inhibitor) induced the expression of a cell adhesion protein and an inhibitor of cell division, thereby inhibiting cell movement and replication. A similar activator-inhibitor system design has been implemented to produce stochastic spatial patterns of gene expression in synthetic bacterial and mammalian multicellular systems (Karig et al., 2018; Sekine et al., 2018). However, synthetic multicellular patterning is not limited to activator-inhibitor system designs, as evident from the differential-cell-adhesion-based patterns generated by the synNotch system (Toda et al., 2018) (Figure 1B bottom-right). Here, the authors were able to achieve two-layer and three-layer spatial organization of cells by using an engineered delta-notch cell signaling system (Morsut et al., 2016) to drive the expression of different cell adhesion receptors (E-cadherins). The cells expressing the same cadherins adhere strongly to each other to form the core of the structure and the outer layers are formed by cells that adhere loosely. Using a repertoire of different cadherins, a rule-based logic of differential cell adhesion was implemented to create spherically asymmetric three-layered multicellular structures starting from random initial cell distributions (Figure 1B bottom-right). This rule-based mechanism doesn't require activator-inhibitor type interactions; however, one can imagine how multicellular organisms may combine different mechanisms in the context of embryonic patterning and morphogenesis.

During embryonic development, an initial mass of cells with unspecified fates orchestrates a coordinated program of cell division, growth, migration, adhesion, cell-cell signaling, and gene expression to specify cell fates, undergo morphogenetic changes, and eventually become a fully-patterned embryo encoding the complete body plan of the organism. Various spatially periodic patterns are observed during different stages of embryonic development. Figure 1C shows zebrafish segmentation patterns (top), *Drosophila* segmentation patterns (bottom-left), and mouse digit patterns (bottom-right). All the three periodic patterns are established by gene-regulatory networks, but using different interaction logic – zebrafish segmentation involves traveling waves of gene expression that are generated by genetic-oscillator circuits driven by delayed negative-feedbacks and these traveling waves sequentially specify the segments (Dequéant & Pourquié, 2008); *Drosophila* segments are an outcome of sequential and

combinatorial control of gene expression driven by initial asymmetric distribution of maternal factors (Levine, 2008; Nüsslein-Volhard & Wieschaus, 1980); mouse digit-patterning involves a reaction-diffusion network of genes and diffusible signaling molecules leading to emergence of self-organized periodic patterns with a wavelength determined by the reaction-diffusion parameters of the system (Raspopovic et al., 2014; Sheth et al., 2012). These examples demonstrate that similar periodic patterns of gene expression and cell fates can be driven using similar genetic regulators and diffusible signals, but with different interaction logic.

At higher levels of biological organization, even more complex patterns can emerge (Figure 1D-E) on larger spatial and temporal scales than considered above. The pattern-forming units can be cells, tissues, organisms, or even populations. The frameworks established to understand pattern formation at the lower levels of biological organization could be adapted or extended to explain pattern formation at the higher levels in order to generate valuable insights into general principles of biological pattern formation.

1.2. Pattern formation mechanisms

In this section, I focus on two well-known mechanisms for multicellular pattern formation mainly evoked in the context of morphogenesis. The first mechanism known as ‘positional information’ refers to a mechanism by which genetic information is converted into spatial patterns of cellular differentiation (Wolpert, 1969). The original framework of positional information proposed by Lewis Wolpert was mainly focused on establishing a coordinate system that cells can use to determine their fates in an embryo. The idea of positional information has been combined with the concepts of induction, morphogen gradients, morphogen thresholds, and the molecular basis of gradient formation and interpretation to arrive at the current understanding of spatial patterning and morphogenesis in embryonic development (Rogers & Schier, 2011). In brief, the concept of induction refers to ability of a cell or tissue to induce neighboring cells to adopt a particular fate, while a morphogen (‘form producer’) is a diffusible substance that can instruct cells to acquire different fates based on its concentration. When cells are exposed to morphogen concentration above a certain threshold, they turn on a developmental program and acquire fates specific to that threshold (Figure

2A). The morphogen produced by the source cells (green) diffuses to form a concentration gradient, allowing target-cells (blue, white, red) to sense different concentrations depending on their position. Cells that sense concentrations above threshold T1 acquire ‘blue’ fate, cells that sense intermediate concentrations acquire ‘red’ fate, and cells that sense concentrations lower than T2 acquire ‘white’ fate. This framework provides a mechanism for generating spatial patterns of cellular differentiation during embryonic development. But, how could periodic patterns of alternating cell fates be established, and how to account for interactions of two or more morphogens? The answer lies in the reaction-diffusion mechanism.

The concept of reaction-diffusion as a basis for embryonic pattern formation was developed by Alan Turing (Turing, 1952) and the duo of Alfred Gierer and Hans Meinhardt (Gierer & Meinhardt, 1972). The general idea is that morphogens could interact by activating or inhibiting each other to shape their spatial distribution in an embryo. These interactions can lead to periodic patterns of morphogen concentrations that can be sensed by cells to acquire different fates. To get a deeper understanding of the reaction-diffusion mechanism, I will provide mathematical analysis of a simple two-component reaction-diffusion system – the activator-inhibitor system (Figure 2B).

The activator-inhibitor system consists of two morphogens. The activator can self-activate and activate its inhibitor. The inhibitor can inhibit both the activator and itself. This system can be described by the following coupled partial differential equations:

$$\frac{\partial}{\partial t} Act = k_{act} * Act - k_d * Inh + D_A * \nabla^2 Act$$

$$\frac{\partial}{\partial t} Inh = k_{inh} * Act - k_d * Inh + D_I * \nabla^2 Inh$$

$Act(x,t)$ and $Inh(x,t)$ denote activator and inhibitor concentrations as functions of space and time (x,t). The reaction rates for activator and inhibitor production are k_{act} and k_{inh}, and the decay rate is k_d. The diffusion coefficients for the activator and inhibitor are D_A and D_I, respectively. Here, I deliberately use simple reaction-diffusion equations with linear kinetics to explain the basic concepts without high mathematical complexity.

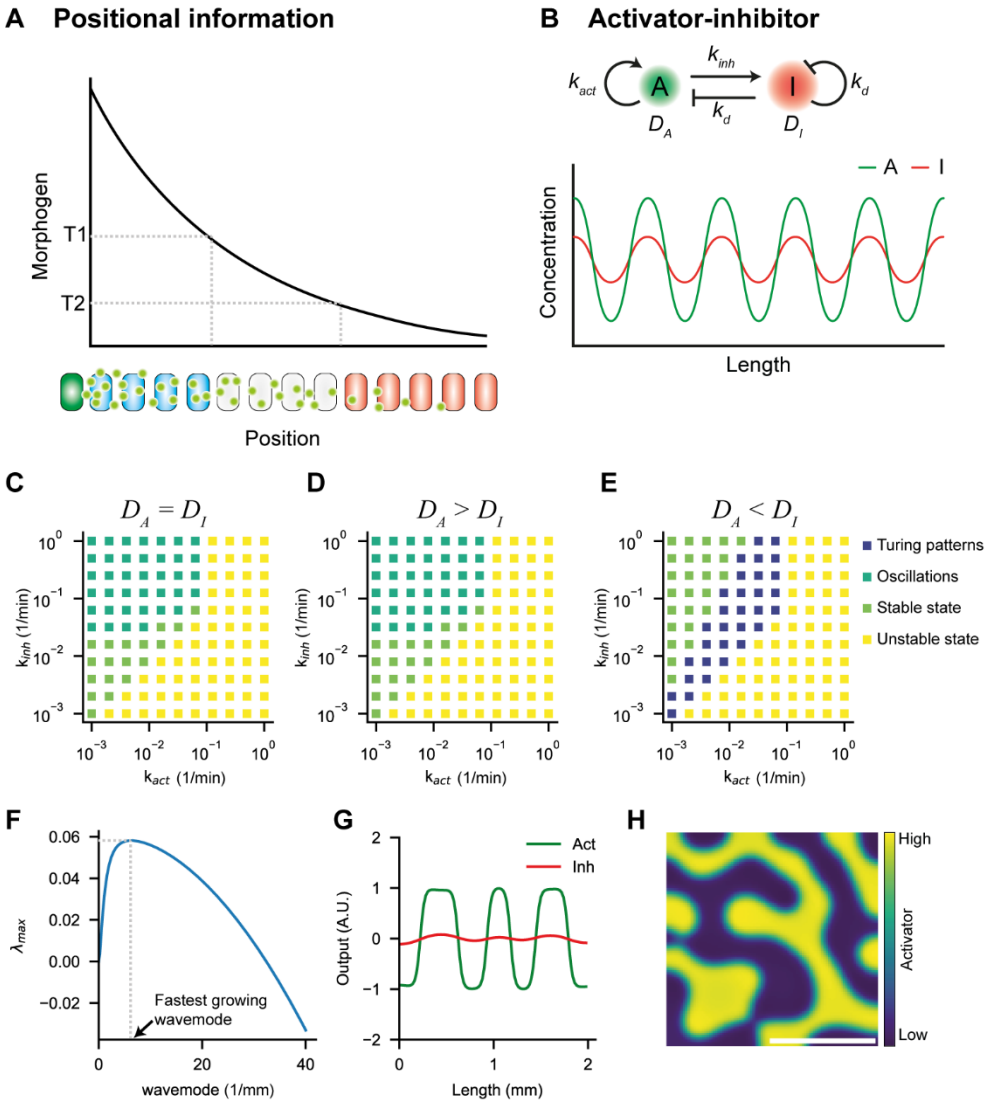

Figure 2: Mechanisms of pattern formation
A) Schematic illustrating the concept of positional information model (famously known as the French flag model). The green cell (source) produces and secretes morphogen molecules (light green circles). As the morphogen diffuses, generating a gradient of morphogen concentration, cells receive different amounts based on their position. The model postulates the existence of thresholds of morphogen concentrations, above which specific genes are activated conferring different cells-fates (blue, white, red) based on the cell positions. The schematic was recreated based on (Rogers & Schier, 2011). **B)** The activator-inhibitor network (Gierer & Meinhardt, 1972; Turing, 1952). The activator (A - green circle) activates itself and the inhibitor (I – red circle) inhibits both activator and itself. Both these substances are diffusible. The activation and inhibition rates (k_{act}, k_{inh}, k_d) and diffusion coefficients (D_A, D_I) are indicated in the network. Spatially periodic self-organized patterns of activator and inhibitor (also called as Turing patterns) can emerge under the right reaction and diffusion parameters. **C-E)** Linear stability analyses for the activator-inhibitor system showing different patterning regimes over the parameter space of k_{act} and k_{inh} and indicated conditions for D_A and D_I. In C) $D_A = D_I = 1\ \mu m^2 s^{-1}$, in D) $D_A = 1000\ \mu m^2 s^{-1}$, $D_I = 1\ \mu m^2 s^{-1}$, and in E) $D_A = 1\ \mu m^2 s^{-1}, D_I = 1000\ \mu m^2 s^{-1}$. In C-E) $k_d = 0.1\ min^{-1}$. **F)** Dispersion relation plot

showing eigenvalues or growth rates (λ_{max}) of different wavemodes (q) for the parameter combination $k_{act} = 0.063$, $k_{inh} = 0.063$. The fastest growing wavemode gives the unique wavelength of the Turing pattern. **G-H)** Simulation results for the activator-inhibitor equations on 1-dimensional (G) and 2-dimensional (H) domains, with $D_A = 1\ \mu m^2 s^{-1}$, $D_I = 1000\ \mu m^2 s^{-1}, k_{act} = 0.06\ min^{-1}, k_{inh} = 0.25\ min^{-1}, k_d = 0.1\ min^{-1}$, and no-flux boundary conditions. Scale bar in H) is 1 mm. To avoid infinities in the numerical solutions, appropriate saturation terms (cubic saturation) were used, similar to (Marcon et al., 2016).

How can this system give rise to spatially periodic patterns (also known as 'Turing patterns') and under what conditions of reaction and diffusion rates? To answer this question, one can perform linear stability analysis and determine the stability of the steady state. The steady state is linearly stable if the eigenvalues of the linear system are negative. If at least one of the eigenvalues is positive, then the steady state becomes unstable. The steady state of the system is calculated by equating the time-derivatives to zero.

$$\frac{\partial}{\partial t} Act = 0, \qquad \frac{\partial}{\partial t} Inh = 0$$

This gives the steady state $Act = 0$ and $Inh = 0$.

Now, to perform linear stability analysis, we calculate the eigenvalues of the system by solving the eigenvalue problem:

$(\boldsymbol{J} - q^2\boldsymbol{D} - \lambda\boldsymbol{I})\boldsymbol{X} = 0$, wherein λ is the eigenvalue for the wavemode $q = \frac{n\pi}{L}$, for $n = 0, 1, 2, \ldots, L$ is the domain length, $\boldsymbol{J} = \begin{bmatrix} k_{act} & -k_d \\ k_{inh} & -k_d \end{bmatrix}$ is the Jacobian matrix, $\boldsymbol{D} = \begin{bmatrix} D_A & 0 \\ 0 & D_I \end{bmatrix}$ is the diffusivity matrix, $\boldsymbol{X} = \begin{bmatrix} Act \\ Inh \end{bmatrix}$, and $\boldsymbol{I} = \begin{bmatrix} 1 & 0 \\ 0 & 1 \end{bmatrix}$.

For the system to have a non-trivial solution:

$$Determinant(\boldsymbol{J} - q^2\boldsymbol{D} - \lambda\boldsymbol{I}) = 0$$

Hence,

$$\begin{vmatrix} k_{act} - q^2 D_A - \lambda & -k_d \\ k_{inh} & -k_d - q^2 D_I - \lambda \end{vmatrix} = 0$$

By solving this equation, we can calculate the eigenvalues for all possible wavemodes and for the given values of reaction-diffusion parameters $k_{act}, k_{inh}, k_d, D_A$, and D_I. Note

that eigenvalues are complex numbers $(a + ib; i = \sqrt{-1})$ with real part a and imaginary part b. Based on the eigenvalue's real and imaginary part, one can deduce the stability of the steady state. The first wavemode $(q = 0)$ refers to the homogeneous state of the system, where the role of diffusion can be ignored. For the emergence of Turing patterns, the homogeneous state of the system should be stable, i.e., all the eigenvalues of the first wavemode should be negative. For the subsequent wavemodes, a diffusion-driven instability can arise, if one of the eigenvalues becomes positive i.e., for some $q = \frac{n\pi}{L}, n > 0$; real part of λ should become positive. When the diffusion-driven instability occurs for a unique wavemode, the system can give rise to Turing patterns (Diego et al., 2018; Marcon et al., 2016; Scholes et al., 2019; Smith & Dalchau, 2018; Zheng et al., 2016).

To elaborate, the eigenvalues provide the growth rates of different wavemodes in the Fourier series expansion of Act and Inh around the steady state:

$$\boldsymbol{X}(x,t) \approx \sum_{n=0}^{\infty} a_n e^{\lambda_n t} \cos(q_n x),$$

where, $a_n e^{\lambda_n t}$ is the Fourier coefficient, λ_n denotes the real part of the largest eigenvalue for the nth wavemode, $q_n = \frac{n\pi}{L}$ denotes the nth wavemode, and L denotes the domain length (Smith & Dalchau, 2018). Note that only the wavemodes with positive eigenvalues can grow over time, as the Fourier coefficient term $e^{\lambda_n t}$ increases over time for positive eigenvalues $(\lambda_n > 0)$. Also, it is expected that the term with the largest eigenvalue (λ_{max}) will dominate, and the corresponding wavemode (q_{max}) will determine the wavelength of the pattern (wavelength = $\frac{2\pi}{q_{max}}$) (Figure 2F). For example, if eigenvalue with the largest positive real part occurs for the 6th wavemode $(q_{max} = \frac{6\pi}{L})$, then the wavelength of the pattern will be $\frac{L}{3}$. Additionally, the imaginary part of the eigenvalue determines if the system can show temporal oscillations (if $\lambda_n = a + ib$, and $b > 0$).

Based on the mathematical theory described above, one can compute the eigenvalues of the system and infer the patterning outcomes at different reaction-diffusion rates as shown in Figure 2C-E. We can observe that, when the inhibitor diffusion coefficient is higher than that of the activator $(D_I > D_A)$, a part of the parameter space can fulfill the

conditions for emergence of Turing patterns (Figure 2E). This requirement of higher inhibitor diffusivity for Turing pattern formation is known as the 'diffusivity constraint' (Diego et al., 2018; Klika et al., 2012; Landge et al., 2020; Maini et al., 2012; Marcon et al., 2016; White & Gilligan, 1998; Zheng et al., 2016). A detailed synthesis of the concepts of the 'diffusivity constraint' requirements and how multicomponent reaction-diffusion systems can relax this constraint is provided in *section 2*. Figure 2G and 2H show numerical simulation results that confirm the emergence of Turing patterns at the reaction-diffusion parameters derived from the linear stability analysis.

Thus, reaction-diffusion systems offer a framework to account for interactions of morphogens to generate self-organized spatial patterns for mathematically predictable biochemical and biophysical parameters. But, how do morphogens spread in the complex multicellular tissues to generate positional information and determine cell fates? What are the biological mechanisms of morphogen dispersal? The next section provides a brief introduction.

1.3. Mechanisms of morphogen dispersal

A developing embryo offers a complex, dynamic, multicellular environment wherein morphogens spread away from their source and generate concentration gradients to provide positional information and ensure proper spatial patterning of the embryo. How does reliable production of morphogen gradients take place in this complex multicellular environment? Different models of morphogen dispersal have been proposed. They can be classified into diffusion-based models (free diffusion, hindered diffusion, facilitated diffusion) and cell-based models (transport via cytonemes, or transcytosis) (Müller et al., 2013; Müller & Schier, 2011; Rogers & Schier, 2011).

The free diffusion model (Figure 3A) proposes that morphogens diffuse in the extracellular space with negligible effects of tissue geometry and binding to extracellular receptors. Here, the diffusion coefficient (D) of the morphogen can be easily determined based on the Stokes-Einstein equation: $\mathrm{D} = \frac{\mathrm{k_B T}}{6\pi\eta\mathrm{R}}$, where $\mathrm{k_B}$ is the Boltzmann's constant, T is the absolute temperature, η is the medium viscosity, and R is the morphogen radius. However, experimental estimates of morphogen diffusion coefficients are much lower than the theoretical predictions offered by the free diffusion model (Müller et al., 2013). This discrepancy could be explained by the hindered-diffusion

model (Figure 3B), which considers the effects of tortuosity and morphogen immobilization by binding to extracellular receptors and matrix proteins. Tortuosity refers to the increase in the path-length due to obstacles between the start and end points, which can decrease the effective diffusion coefficient of the morphogen by up to 2.5-fold. The combined effect of tortuosity and binding-mediated hindrance can lower the effective diffusion coefficient even further (> 10-fold).

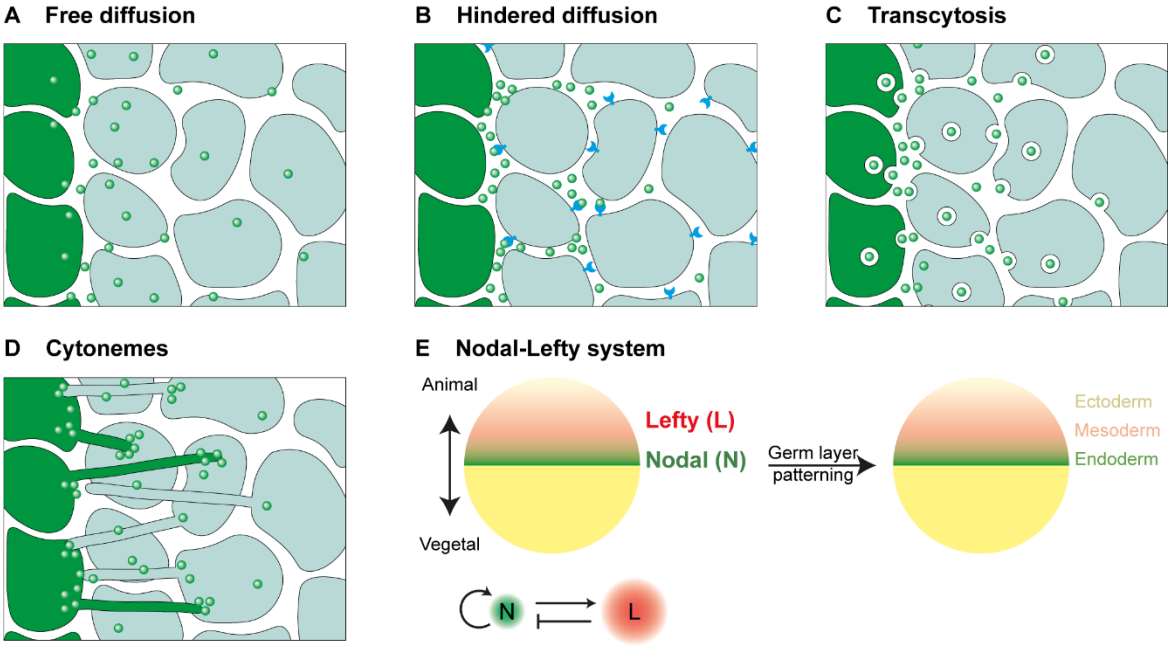

Figure 3: Mechanisms of signal dispersal
A-D) Schematics showing different models of signal transport. The source cells depicted in green on the left side of the panel produce the signaling molecules (small green circles). Receiver cells are depicted in light green. Free diffusion model assumes that the molecules disperse by Brownian motion. The hindered diffusion model proposes extracellular diffusion of molecules is hindered by the tortuous path and binding to receptors (receptors: depicted in blue). In the transcytosis model, molecules are repeatedly endocytosed and exocytosed to enable their dispersal. The cytoneme model proposes that long filopodial extensions called cytonemes can transport signaling molecules. **E)** A zebrafish embryo showing gradients of TGF-β superfamily proteins - Nodal and Lefty - required for proper germ layer patterning. Nodal and Lefty form an activator-inhibitor pair where Nodal is a short-range activator and Lefty is a long-range inhibitor.

The cell-based models propose that morphogen molecules move intracellularly or via filopodial cell extensions. According to the transcytosis model, multiple rounds of endocytosis and exocytosis of morphogens ensure uptake of morphogens from the source cells and their dispersal in the field of target cells (Figure 3C) (Müller et al., 2013; Romanova-Michaelides et al., 2022). This model predicts that the extracellular

fraction of the morphogens is small and the effective diffusion coefficients are low due to the slow process of repeated endocytosis and exocytosis. Recent analysis of the bone morphogenetic protein decapentaplegic (Dpp) transport in *Drosophila* wing imaginal disc using a photoconversion assay revealed that endocytosed Dpp molecules can get recycled and secreted back in the extracellular space (Romanova-Michaelides et al., 2022). However, in addition to the transcytosis, extracellular diffusion of Dpp was also important for the gradient formation.

The cytoneme model states that dynamic actin-based filopodial cell extensions called cytonemes (Casas-Tintó & Portela, 2019; Ramírez-Weber & Kornberg, 1999) can transport morphogen molecules from the source cells to the target cells (Figure 3D). These extensions should be able to detect the source cells and enable the exchange of morphogen molecules and carry them towards the target cells. In the *Drosophila* wing imaginal disc, apical cytonemes have been shown to orient towards the source of Dpp (Hsiung et al., 2005; Stanganello & Scholpp, 2016). Cytonemes also play an important role in Wnt signaling in the flight muscle progenitors (myoblasts) of *Drosophila*. The myoblasts project cytonemes, containing the Wnt receptor Frizzled (Frz), towards the Wnt-producing cells in the wing imaginal disc. The Wnt-Frz complexes formed at the Wnt-producing cells are transported towards the myoblasts along the dynamic cytonemes (Huang & Kornberg, 2015; Stanganello & Scholpp, 2016). In contrast, cytonemes can also arise from the source cells and extend towards the target cells, as shown in the case of Wnt8a transport in the zebrafish neural plate (Stanganello et al., 2015). Accumulation of Wnt8a at the plasma membrane initiates formation of a new cytoneme, which extends towards the target cells carrying the Wnt8a molecules on its tip. Upon contact with the target cells, Wnt8a molecules are endocytosed by the target cells activating the Wnt signal transduction cascade (Stanganello et al., 2015; Stanganello & Scholpp, 2016).

The diffusion-based and cell-based models have been experimentally tested during embryonic development in different species (reviewed in (Akiyama & Gibson, 2015; Müller et al., 2013; Stanganello & Scholpp, 2016)). The Nodal-Lefty morphogen system in zebrafish embryo is crucial to understand how the morphogens (Nodal and Lefty) produce strikingly different concentration gradients despite similar molecular sizes (Müller et al., 2012; Müller et al., 2013) (Figure 3E). Nodals and Leftys are TGF-

β superfamily ligands involved in germ layer patterning (Rogers & Müller, 2019). The Nodal-Lefty system also behaves as an activator-inhibitor system wherein Nodal acts as short-range activator and Lefty acts as a long-range inhibitor (Müller et al., 2012). In our recent work, we performed single-molecule imaging and tracking of these morphogens in live zebrafish embryos (Kuhn et al., 2022). In this work, I developed a data-driven agent-based model of morphogen dispersal to gain insights into how the geometry of the extracellular space regulates morphogen distribution (Kuhn et al., 2022) (Please see, *section 3*).

Using the knowledge of reaction-diffusion mechanisms and morphogens, can we build synthetic multicellular systems to generate spontaneous spatial and temporal patterns? This question is central to my main PhD project. In the next section, I provide a brief introduction to the concepts used for designing and implementing synthetic multicellular patterning systems.

1.4. Emergence of synthetic multicellular patterns

In the last two decades, synthetic multicellular systems have been developed to generate synchronized biological clocks (Danino et al., 2010; Potvin-Trottier et al., 2016), activator-inhibitor spatial patterns (Karig et al., 2018; Sekine et al., 2018), layered multicellular structures (Toda et al., 2018), spatial patterns in bacterial colony growth (Duran-Nebreda et al., 2021), sender-receiver systems (Basu et al., 2005), micropatterns of human embryonic stem cells (Warmflash et al., 2014). Our understanding of natural cell signaling systems has enabled these advances in the development of synthetic multicellular systems. In addition, theoretical advances in identification of reaction-diffusion networks capable of pattern formation has provided guidelines for designing synthetic multicellular patterning networks (Diego et al., 2018; Marcon et al., 2016; Scholes et al., 2019; Zheng et al., 2016). In this section, I present basic concepts of synthetic genetic circuits and networks.

A synthetic genetic circuit, in its most basic form, consists of an input (for example, a signaling molecule (S)) and an output (for example, a protein (P)) (Figure 4A). The signaling molecule may directly (by binding to a transcriptional regulator) or indirectly (via a signal-transduction pathway) induce transcription of a specific target gene, followed by the protein production. The input-output relationship (or the dose-response

function) of this circuit can be determined by quantifying the protein production at different doses of the signaling molecules. If the protein (P) production increases linearly with increasing signal (S) dosage, the dose-response function can be written as $P = k * S$, where k gives the protein output per unit of the signal. However, most biological circuits show a sigmoid dose-response function (Figure 4B) of the form $P = l + (\frac{S^n}{K_T^n + S^n})$, where l or leakiness is the basal protein expression level in absence of the signal, K_T or activation threshold is the signal concentration that induces half of the maximum protein expression above the basal level, and n is the Hill coefficient indicating cooperativity involved in signal binding and transcriptional activation. The ratio of maximum protein output to the leakiness gives the dynamic range of the circuit. Mostly, circuits with low leakiness and high dynamic range are desirable to allow tunability and coupling of output of one circuit to the input of another for generating synthetic biological networks with modular design (Meyer et al., 2019). By coupling two or more circuits, one can produce complex feedback networks. For example, if the protein produced in response to the input signal is coupled to another circuit responsible for the biosynthesis of more signal molecules, then a positive feedback network can be generated.

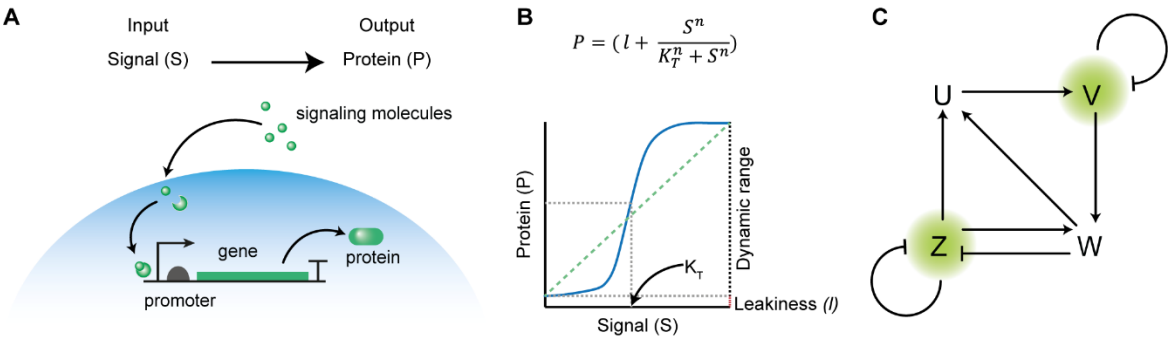

Figure 4: Synthetic biological pattern formation
A) A simple genetic circuit takes signaling molecules (S) as an input and produces protein (P) as an output. For synthetic biological circuits, one can use signaling molecules that activate expression of a target gene downstream a known promoter sequence upon binding to a transcriptional activator. **B)** The input-output or the dose-response function gives the amount of protein produced at different doses of the signal. This function is governed by the promoter leakiness (l), dynamic range, signal threshold concentration (K_T), and cooperativity given by the Hill coefficient (n). The blue line on the plot shows a sigmoid dose-response function, which is usually observed for biological circuits. The dotted green line shows a linear dose-response. **C)** A four-component reaction-diffusion network obtained using RDNets (Marcon et al., 2016).

Complex multicomponent reaction-diffusion networks can be designed using RDNets – a software developed by Luciano Marcon (Marcon et al., 2016). RDNets was used to perform a high-throughput mathematical analysis to generate an atlas of pattern-forming reaction-diffusion networks. The analysis of over 1.4 million network topologies resulted in many three-component (84) and four-component (512) network topologies capable of Turing pattern formation. Some of the networks were capable of generating Turing patterns without the diffusivity constraint. One such network is shown in Figure 4C. This network has features that favor its implementation using synthetic biological circuits. For example, the diffusible components have no direct interactions, but they interact via the non-diffusible components. Hence, the diffusible components can serve as biological signaling molecules that activate non-diffusible components such as genetic regulators in a synthetic biological network. This network has a positive feedback module consisting of (U, V, W) and a negative feedback module consisting of (Z, W). The modular network design is advantageous, because the feedback modules can be separately implemented using synthetic biological circuits. Due to these unique features and advantages, I used this network as a starting point for the design of a synthetic multicellular patterning system (Section 4).

2. Paper 1 – Pattern formation mechanisms of self-organizing reaction-diffusion systems

2.1. Synopsis

Reaction-diffusion systems have been widely used to study pattern formation. However, their mathematical complexity has made some of the concepts inaccessible for general developmental biology community. Furthermore, some of the old paradigms based on the analysis of simple two-component reaction-diffusion system need to be updated in light of recent findings based on the analysis of multicomponent reaction-diffusion networks. Hence, a comprehensive synthesis of the complex theoretical concepts was necessary to make these concepts more accessible and applicable in the future research. To this end, we synthesized the complex concepts of multicomponent reaction-diffusion, graph-theoretical methods, and model reduction methods and presented them in a more accessible manner in this manuscript. This work was published on 30 January, 2020 and has been widely cited.

2.2. Author contributions

Patrick Müller conceived the topic and I wrote the first draft under his guidance. We revised the draft with input from the co-authors Benjamin M. Jordan and Xavier Diego.

Developmental Biology 460 (2020) 2–11

Contents lists available at ScienceDirect

Developmental Biology

journal homepage: www.elsevier.com/locate/developmentalbiology

Pattern formation mechanisms of self-organizing reaction-diffusion systems

Amit N. Landge [a], Benjamin M. Jordan [b], Xavier Diego [c], Patrick Müller [a,d,*]

[a] Systems Biology of Development Group, Friedrich Miescher Laboratory of the Max Planck Society, 72076, Tübingen, Germany
[b] Department of Organismic and Evolutionary Biology, Harvard University, Cambridge, MA, 02143, USA
[c] European Molecular Biology Laboratory, Barcelona Outstation, 08003 Barcelona, Spain
[d] Modeling Tumorigenesis Group, Translational Oncology Division, Eberhard Karls University Tübingen, 72076, Tübingen, Germany

A B S T R A C T

Embryonic development is a largely self-organizing process, in which the adult body plan arises from a ball of cells with initially nearly equal potency. The reaction-diffusion theory first proposed by Alan Turing states that the initial symmetry in embryos can be broken by the interplay between two diffusible molecules, whose interactions lead to the formation of patterns. The reaction-diffusion theory provides a valuable framework for self-organized pattern formation, but it has been difficult to relate simple two-component models to real biological systems with multiple interacting molecular species. Recent studies have addressed this shortcoming and extended the reaction-diffusion theory to realistic multi-component networks. These efforts have challenged the generality of previous central tenets derived from the analysis of simplified systems and guide the way to a new understanding of self-organizing processes. Here, we discuss the challenges in modeling multi-component reaction-diffusion systems and how these have recently been addressed. We present a synthesis of new pattern formation mechanisms derived from these analyses, and we highlight the significance of reaction-diffusion principles for developmental and synthetic pattern formation.

1. Introduction

Patterns are ubiquitous in nature – from the molecular arrangements in crystals and snowflakes to the dynamics of societies and the formation of galaxies. Many of these spatial patterns are strikingly similar across orders of magnitude in length scales, but it is currently largely unclear whether equivalent patterns are formed by similar self-organizing mechanisms. Numerous theories have been put forward with the goal to unravel the principles of pattern formation (reviewed in Roth, 2011), but few of them are as universal as the theory of reaction-diffusion (RD) systems first proposed by Alan Turing (1952). Turing's theory explains the complex self-organizing mechanisms underlying embryonic patterning using simple reactions of just two diffusible components. These systems have fascinating properties: First, they can form truly self-organized patterns in the absence of initial asymmetries, thereby generating *de novo* positional information (Meinhardt and Gierer, 2000). Second, a large variety of pattern forms (e.g. spots and stripes, Fig. 1a) can be generated by simply varying the reaction and diffusion parameters (Kondo and Miura, 2010; Marcon and Sharpe, 2012), which could in principle account for the structural and morphogenetic diversity of life forms. Third, RD patterns are responsive to external perturbations and possess the remarkable ability to regenerate after perturbations (Gierer and Meinhardt, 1972; Kondo, 2017; Müller and Nüsslein-Volhard, 2016).

The dynamics of a number of biological systems that are compatible with the principles underlying the RD mechanism have recently been quantitatively studied (Diego et al., 2018; Marcon et al., 2016; Nakamasu et al., 2009; Raspopovic et al., 2014; Scholes et al., 2019; Zheng et al., 2016), but it remains unclear how commonly the principles of RD systems are actually realized in living systems. Qualitative similarities between *in silico* RD patterns and *in vivo* patterns are generally not sufficient to conclude the involvement of an RD mechanism (Hiscock and Megason, 2015). In addition, owing to its simplicity, Turing's theory has been questioned by developmental biologists: How could a simple two-component RD system explain the complex morphogenetic program orchestrated by multiple genetic and molecular regulators? Due to mathematical and computational limitations it has been difficult to address this long-standing criticism and to extend simple RD models to realistic multi-component biological processes. Here, we discuss how these challenges have been tackled in recent studies, yielding new insights into the mechanisms and conditions that lead to pattern formation in realistic RD systems.

2. The local self-activation and lateral inhibition proposal

The simplest and most well-known example of an RD system is the *activator-inhibitor system*. The activator-inhibitor system, coined by Hans Meinhardt and Alfred Gierer (Gierer and Meinhardt, 1972), consists of two diffusible components that interact through specific reactions.

* Corresponding author. Systems Biology of Development Group, Friedrich Miescher Laboratory of the Max Planck Society, 72076, Tübingen, Germany.
E-mail address: patrick.mueller@tuebingen.mpg.de (P. Müller).

https://doi.org/10.1016/j.ydbio.2019.10.031
Received 26 June 2019; Received in revised form 29 October 2019; Accepted 29 October 2019
Available online 30 January 2020

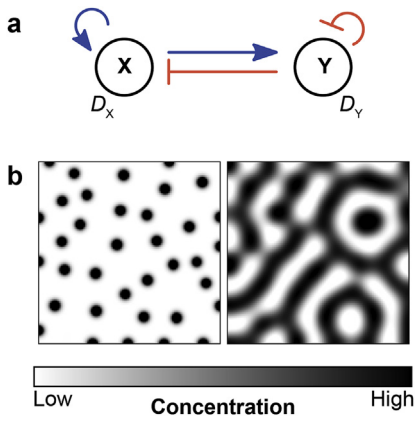

Fig. 1. The basic concept of reaction-diffusion (RD)-mediated pattern formation. (a) Network representation of a self-organizing activator-inhibitor system. The activator X promotes production of itself and of the inhibitor Y, while the inhibitor restricts activator production (arrow: activation, bar-headed line: inhibition). **(b)** Examples of two-dimensional Turing patterns generated using the activator-inhibitor network shown in (a) with the equations $\frac{\partial X}{\partial t} = D_X\nabla^2 X + \left(\frac{X^2}{1+K_X X^2} + X_0\right) \Big/ Y - \mu_X X$ and $\frac{\partial Y}{\partial t} = D_Y\nabla^2 Y + X^2 - \mu_Y Y$ (based on Meinhardt, 2012), where $D_X = 0.2$ and $D_Y = 10$ are the diffusivities of X and Y, $X_0 = 0.1$ is the basal production rate of X, and $\mu_X = \mu_Y = 5$ are the decay rate constants. The saturation constants are $K_X = 0$ for the spot pattern on the left and $K_X = 0.25$ for the stripe pattern on the right.

Turing had already laid the foundation for such a two-component system with linear reaction terms (Turing, 1952), but Meinhardt and Gierer proposed a model with biochemically more realistic nonlinear reaction terms (Gierer and Meinhardt, 1972; Meinhardt, 2012; Turing, 1952). As shown in Fig. 1a, in this model the activator X with diffusivity D_X promotes its own synthesis and that of the inhibitor Y with diffusivity D_Y, which in turn inhibits the activator and itself. Interestingly, this system can self-organize from an initially uniform distribution to give rise to stationary periodic patterns of activator and inhibitor concentrations (Murray, 2013; Turing, 1952). Such patterns with a characteristic periodicity or wave-length are termed *Turing patterns* (Fig. 1b, Box 1).

For the network in Fig. 1a, the well-established condition for Turing pattern formation is that the inhibitor must have a much larger diffusivity than the activator ($D_Y \gg D_X$) (Murray, 2013; Turing, 1952). This differential diffusivity requirement led to the proposal of the famous *local self-activation and lateral inhibition* model by Meinhardt and Gierer (Gierer and Meinhardt, 1972; Meinhardt and Gierer, 2000). According to this model, the local auto-activation by the activator and the lateral inhibition of its activity by the antagonist is crucial for self-organized pattern formation. The model postulates that the activator amplifies small random fluctuations to form a local concentration maximum, which subsequently leads to the activation of the inhibitor. Next, the inhibitor dampens the concentration increase in the vicinity of the activator peak. The higher diffusivity of the inhibitor also allows the incipient activator peaks to grow by 'siphoning out' inhibitor molecules from the peak region. Outside the range of lateral inhibition, another activator peak can then arise leading to the sequential emergence of a stationary periodic pattern. Intuitively, it appears that this simple principle could also be extended to more complex multi-component RD systems by considering two groups of interacting substances: the slow diffusers and the fast diffusers. The slow diffusers would have a shorter range and taken together should form an auto-activating module, whereas the latter with a larger range should form an inhibitory module (Meinhardt and Gierer, 2000). However, in reality this intuitive approach is not applicable to more complex systems (Marcon et al., 2016). In the following, we describe recent studies of multi-component RD systems that have provided evidence against the generality of the local self-activation and lateral inhibition proposal by showing that the differential diffusivity condition can be partially or even completely relaxed. These recent studies place the emphasis on feedback loops rather than individual activator and inhibitor molecules and provide a new way to understand RD systems.

3. Insights into RD systems beyond two-component Turing systems

Owing to advances in technology, recent computational analyses of multi-component RD systems have revealed novel insights into pattern formation mechanisms. The apparently simple local self-activation and lateral inhibition concept and the conditions underlying two-component systems get increasingly complex with the number of network components. A graph-theoretical approach can help to dissect these complex networks into functional modules (Diego et al., 2018; Marcon et al., 2016), and we introduce the relevant terminology in Box 2 to illustrate the key concepts of this approach.

3.1. Relaxation of diffusivity constraints

To describe the rules to relax the differential diffusivity constraints, we consider three-component systems with two diffusible nodes and one non-diffusible node (Fig. 2), where a node represents an interacting molecular species within the network. In contrast to classical two-component models with exclusively diffusible molecules (Fig. 1a), such an extended network more realistically reflects biological systems, in which signal transduction components such as membrane-bound receptors and nuclearly localized transcription factors are cell-autonomous and therefore non-diffusible with respect to all other cells within the tissue. Consistent with the central tenets derived from the analysis of two-component systems, the network topology shown in Fig. 2a requires differential diffusivity for Turing pattern formation (Marcon et al., 2016). This means that the two molecules must diffuse at very different rates, a condition that is difficult to implement in biological systems (Müller et al., 2013; Rogers and Müller, 2019). The need for differential diffusivity stems from the trade-off between the stability and the instability conditions (Box 1), i.e. the system must be stable without diffusion but become destabilized in the presence of diffusion. Using linear stability analysis and graph theory (Box 1 and Box 2), it was shown that if all nodes complementary to the stabilizing linear subgraphs (*l*-subgraphs) of the same size as the destabilizing module are diffusible, then differential diffusivity is required to produce a diffusion-driven instability (Diego et al., 2018). For the network in Fig. 2a, the subgraph containing nodes 2 and 3 is *destabilizing* and has a size of 2. The only *stabilizing* subgraph with a size of 2 is the cycle containing nodes 1 and 2. The complementary node to this stabilizing subgraph is node 3, which is diffusible. Thus, this network requires differential diffusivity ($D_1 > D_3$) for Turing pattern formation. It naturally follows that systems with only diffusible nodes always require components with different diffusivities. Systems that require differential diffusivity for self-organized pattern formation are termed Type I networks (Marcon et al., 2016).

Recent studies of multi-component RD systems have shown the presence of additional network types. Already more than two decades ago, it had been speculated that the differential diffusivity requirement might be relaxed in multi-component RD systems (White and Gilligan, 1998), and it was subsequently demonstrated that the addition of a non-diffusible node in a three-node RD system can indeed allow self-organized pattern formation with equal diffusivities (Klika et al., 2012). More recently, a systematic analysis of realistic multi-component systems revealed numerous three- and four-node RD networks, in which differential diffusivity is no longer required for pattern formation (Marcon et al., 2016). For example, the network topology shown in Fig. 2b can generate Turing patterns even with *equal* diffusion coefficients of the diffusible nodes ($D_1 \geq D_3$). This network type is called a Type II system. Furthermore, Type III networks (e.g. Fig. 2c) can lead to pattern formation without any diffusivity constraints ($D_1 \geq D_3$ or $D_1 < D_3$) (Marcon et al., 2016).

Box 1
| Conceptual basis for pattern formation in self-organizing RD systems.

The RD mechanism amplifies local fluctuations in the concentration of initially nearly homogenously distributed molecules by a diffusion-driven instability. For the formation of Turing patterns, two key conditions must be satisfied: First, the *stability condition* requires that the system reaches a stable and spatially homogeneous steady state in the absence of diffusion. In other words, when the diffusivities of activator and inhibitor are set to zero, the activator and inhibitor should maintain uniform and constant concentrations. Second, the *instability condition* dictates that in the presence of diffusion, the steady state must become destabilized by a so-called diffusion-driven instability, leading to the amplification of small random concentration fluctuations to yield a unique and time-invariant Turing pattern (Murray, 2013; Turing, 1952).

The figure below (Box 1) depicts this mechanism in a one-dimensional spatial domain. Initially, the concentration of a diffusible component exhibits minor fluctuations around a homogeneous steady state over this one-dimensional domain. The fluctuations can be interpreted as being composed of waves of different wavelengths (q). For instance, the spatial wave in panel **(a)** below is composed of six distinct waves. Under the stability and instability conditions given by reaction and diffusion parameters, the system can undergo a diffusion-driven instability, which amplifies these fluctuations. Importantly, different fluctuations are amplified at different growth rates. Over time, the fluctuation with the highest growth rate dominates and gets fixed, such as the wave with wavelength q_5 shown in panel **(b)** below.

Based on a mathematical technique termed *linear stability analysis*, the stability and instability conditions for Turing pattern formation are expressed in terms of eigenvalues of the linearized equations, which provide the growth rates of intrinsic spatial fluctuations. Mathematically, the eigenvalues can be plotted as a function of each wave mode (fluctuation) to obtain the *dispersion relation*, whose shape determines the nature of the diffusion-driven instability (Cross and Hohenberg, 1993). According to the stability condition, all eigenvalues should be negative in the absence of diffusion, i.e. when all species are assumed to be non-diffusible; therefore, no fluctuation can grow without diffusion. Furthermore, the instability condition requires that in the presence of diffusion at least one eigenvalue is positive. Typically, the spatial mode with the maximum real part of the eigenvalue will be the one that grows fastest – leading to the growth of a fluctuation and a diffusion-driven instability.

In the classical activator-inhibitor RD network (Fig. 1), if the inhibitor has a sufficiently higher diffusivity than the activator, the system can cause a diffusion-driven instability leading to spatial pattern formation. Note that the same fluctuation is amplified simultaneously for both the activator and the inhibitor, and the resulting pattern has a single wavelength. In two-dimensional spatial domains, complex patterns with periodic stripes, spots, etc. can emerge (panel **(c)** below), and the periodicity is determined by the underlying wavelength of the pattern. In three dimensional geometries, RD systems can create tubules and laminar sheets (Bansagi et al., 2011).

Schematic depiction of the self-organizing RD mechanism. (a) Initial random perturbations in the concentration of a molecular species consist of numerous different waves, where q_i indicates the wavelength. **(b)** A Turing pattern is established by selective amplification of a specific wave form. Here, the wave with wavelength q_5 is amplified. **(c)** Periodic Turing patterns in one dimension (a wave) and in two dimensions (stripes and spots).

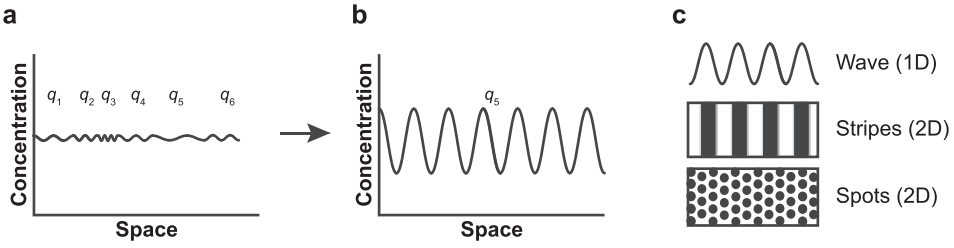

A comprehensive graph-theoretical analysis (Box 2) has provided an explanation for these surprising findings (Diego et al., 2018). The position of non-diffusible nodes in a network transforms the instability condition (Box 1) and thus determines whether a system requires differential diffusivity for pattern formation. Specifically, to implement a Type II system – which allows for equal diffusivities of the diffusible network components (Fig. 2b) – at least one stabilizing *l*-subgraph of the same size as the destabilizing module needs to have a complementary non-diffusible node (Box 2). In Fig. 2b, the stabilizing *l*-subgraph is the cycle between nodes 1 and 3, and its complementary node (node 2) is non-diffusible. To implement a Type III system – which has no restrictions on the diffusivities of the diffusible network components (Fig. 2c) – the destabilizing module needs to be the *l*-subgraph of the smallest size that has only diffusible complementary nodes (Diego et al., 2018). In Fig. 2c, the cycle between nodes 2 and 3 is the destabilizing *l*-subgraph of the smallest size (size 2) with a diffusible complementary node (node 1). Here, the Type III system (Fig. 2c) can be distinguished from the Type II system (Fig. 2b) by noting that the non-diffusible node (node 2) in the Type III system lacks the auto-regulatory feedback that is present in the Type II system. In short, placing non-diffusible nodes complementary to stabilizing modules and forming part of the destabilizing modules yields network topologies with relaxed diffusivity constraints. Thus, the Type I, Type II and Type III networks, which may superficially appear to be very similar (Fig. 2a–c), can require diverse biophysical properties based on variations in network topology.

It has been postulated that the interactions between diffusible and non-diffusible nodes lower the *effective* diffusion coefficient of the diffusible activator, thus indirectly relaxing the diffusivity constraint (Zheng et al., 2016). However, this proposed mechanism fails to explain pattern formation at equal diffusivities. It rather seems that non-diffusible nodes act as *capacitors* that integrate the input from diffusible nodes (Marcon et al., 2016). In classical two-component networks, differential diffusivity drives the system away from a homogeneous and stable equilibrium to generate patterns. In multi-component Type II and Type III networks, this is achieved by the non-diffusible nodes that can quickly amplify small perturbations since they are not subject to the equilibrating effect of diffusion (Marcon et al., 2016). The existence of these newly discovered network topologies strongly argues against the previous local self-activation and lateral inhibition hypothesis, which stated that differential diffusivity is a *conditio sine qua non* for

Box 2

| Graph-theoretical framework for the analysis of multi-component RD systems.

Mincheva and Roussel pioneered a graph-theoretical approach to analyze Turing instabilities in multi-component RD systems (Mincheva and Roussel, 2006), which inspired a new framework to identify self-organizing systems and to group the network components into functional modules (Diego et al., 2018; Marcon et al., 2016). Here, we only introduce the most basic concepts needed for our discussion, and further details can be found in Marcon et al. (2016) and Diego et al. (2018).

The figure below (Box 2) shows a four-node interaction graph. The nodes represent diffusible or non-diffusible molecules, and their interactions are depicted by the edges connecting these nodes (arrow: activation, bar-headed line: inhibition). An activating edge has a positive weight, whereas an inhibitory edge has a negative weight (denoted by the constants k_{ij}, which give the activation (+) or inhibition (−) rates of the node j by the node i). For the graph-theoretical analysis, the interaction graph is simplified by defining linear subgraphs (*l*-subgraph). An *l*-subgraph is a set of one or more disjoint cycles of the interaction graph, where a cycle is a closed path spanning one or more nodes. The nodes that are excluded from a subgraph are *complementary* nodes with respect to the subgraph. The size of an *l*-subgraph is the total number of nodes it comprises. In the figure, *l*-subgraphs 1, 2, and 3 are composed of one cycle each and have sizes 1, 2, and 3, respectively. The *l*-subgraph 4 is composed of two cycles and has a size of 4. The weight of a cycle is the product of the weights of all of its edges. The weight of an *l*-subgraph is the product of the weights of its cycles multiplied by -1 if the number of cycles in the subgraph is an odd number. The *l*-subgraphs with positive weights are stabilizing, and those with negative weights are destabilizing. In brief, subgraphs with overall inhibitory effect are stabilizing, whereas subgraphs with overall activating effect are destabilizing.

Interestingly, the stabilizing and destabilizing subgraphs directly determine the stability and instability conditions (Box 1). The pattern formation conditions are satisfied when i) the stabilizing interactions dominate in the absence of diffusion, and ii) destabilizing interactions dominate when certain nodes are diffusible. Importantly, it is not the whole graph structure that matters, but only linear subgraphs – which drastically simplifies the analysis of complex networks. Thus, the graph-theoretical framework provides a basis for deriving the pattern formation conditions of RD systems.

Graph-theoretical framework for RD networks. An interaction graph is a graph-theoretical representation of the network topology and consists of nodes and the interactions among them. A four-node interaction graph and its linear subgraphs are shown. Notations are the same as in Fig. 2.

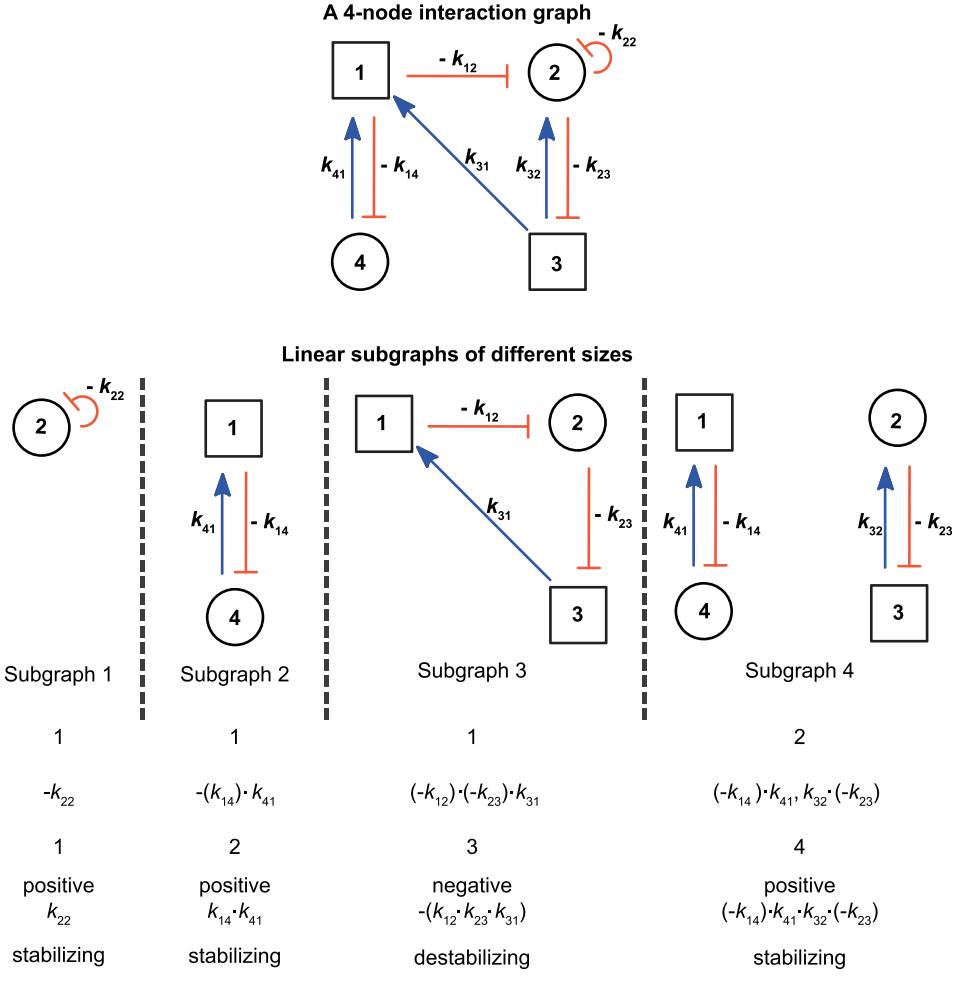

	Subgraph 1	Subgraph 2	Subgraph 3	Subgraph 4
Number of cycles	1	1	1	2
Cycle weight	$-k_{22}$	$-(k_{14})\cdot k_{41}$	$(-k_{12})\cdot(-k_{23})\cdot k_{31}$	$(-k_{14})\cdot k_{41}$, $k_{32}\cdot(-k_{23})$
Subgraph size	1	2	3	4
Subgraph weight	positive k_{22}	positive $k_{14}\cdot k_{41}$	negative $-(k_{12}\cdot k_{23}\cdot k_{31})$	positive $(-k_{14})\cdot k_{41}\cdot k_{32}\cdot(-k_{23})$
Subgraph effect	stabilizing	stabilizing	destabilizing	stabilizing

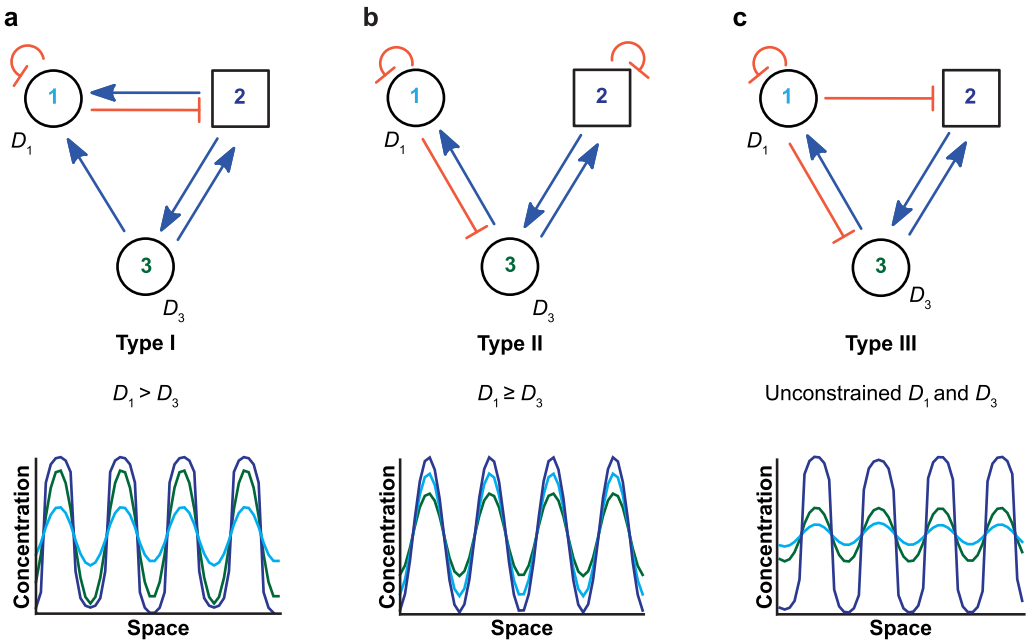

Fig. 2. Relaxation of diffusivity constraints. (a–c) Examples of Turing network types based on diffusivity constraints along with representative 1D patterns for each network generated using RDNets (Marcon et al., 2016). Circle: diffusible node, square: non-diffusible node, D_i: diffusion coefficient, arrow: activation, bar-headed line: inhibition.

self-organized biological pattern formation.

Surprisingly, Type II and Type III networks constitute the majority – about two thirds – of minimal three-node and four-node RD networks (Marcon et al., 2016). These discoveries therefore open new possibilities for RD networks to be considered as working hypotheses in experimental and computational modeling studies of biological patterning systems. Moreover, the multi-component network topologies also offer enticing models for synthetic biological patterning systems (see below).

3.2. Discovery and design of robust Turing networks

It has been thought that Turing networks require intricate fine-tuning of the reaction and diffusion parameters to yield stable patterns (Butler and Goldenfeld, 2011; Diego et al., 2018). This idea, known as the *robustness problem*, was mainly based on the analysis of a limited number of RD systems such as the activator-inhibitor system, which necessitated large differences in diffusivities of the involved components (Gierer and Meinhardt, 1972; Turing, 1952). However, as discussed above, recent insights obtained from the analysis of realistic multi-component RD systems enable the design and discovery of robust Turing networks with smaller differences or even equal diffusivities of the involved signaling molecules. Here, we discuss general principles that can aid in the discovery and the design of robust RD networks. For the sake of clarity and simplicity, we define robust systems as networks that give rise to self-organizing Turing patterns for a wide range of reaction-diffusion parameters. According to this definition, robust RD networks have a large Turing space (Fig. 3).

Recent studies have shown that robust network topologies tend to possess common elements (Diego et al., 2018; Marcon et al., 2016; Scholes et al., 2019; Zheng et al., 2016). Although these studies used different mathematical formulations, they suggest very similar rules for the design of robust Turing networks. While some studies used Hill-type reaction terms (Scholes et al., 2019; Zheng et al., 2016), others incorporated linear reaction terms with cubic saturation kinetics (Diego et al., 2018; Marcon et al., 2016). It has been suggested that in order to build robust multi-component Turing networks, one should 1) use as many classical two-component activator-inhibitor modules (Fig. 1a) as possible in the network, and 2) add additional regulations that complement the existing core topology (Zheng et al., 2016). Consistent with this view, it was demonstrated by numerical screening that the presence of core network topologies similar to the activator-inhibitor module could confer robustness to the RD system (Scholes et al., 2019). Moreover, networks with competitive Hill-type reaction kinetics are on average more robust, albeit less common, than networks with non-competitive Hill-type kinetics (Scholes et al., 2019). However, the generality of these insights may be limited by the numerical screening approach with specific choices of kinetic functions (Scholes et al., 2019; Zheng et al., 2016), where only partial parameter spaces of small networks can be explored

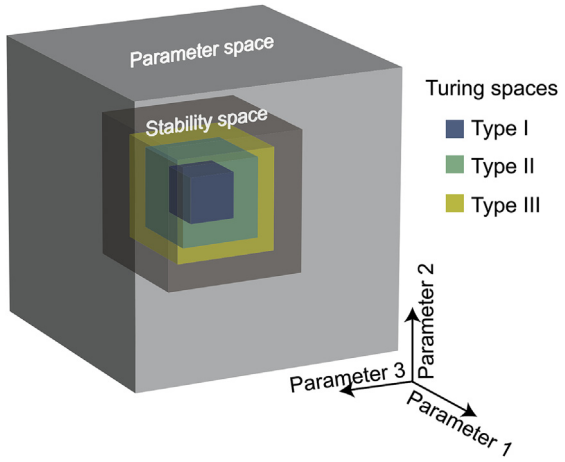

Fig. 3. Simplified schematic of the relationship between network robustness and network types. The parameter space comprises all possible parameter combinations. The stability space comprises only those parameter combinations that fulfill the stability condition. All networks within the same topological family have the same stability space, but their Turing space varies according to their network type. In this simplified schematic, the multi-dimensional parameter space only encompasses three parameters for ease of visualization, but the exact sizes and shapes of the spaces are more intricate for most systems.

due to computational constraints. In contrast, any network regardless of the choice of kinetic functions or number of links can be studied with a graph-theoretical approach (Diego et al., 2018; Marcon et al., 2016). This has shown that the network type based on diffusivity constraints (Type I, II or III) is a key determinant of the Turing space (Fig. 3) (Diego et al., 2018). Minimal Turing networks can be grouped into topological families, where a topological family refers to a group of networks with the same distribution of edges among the nodes (e.g. 7 topological families for three-node networks with 6 positive or negative interactions) (Diego et al., 2018; Marcon et al., 2016). All networks within a topological family have the same stability space, i.e. the steady state of all of these networks is stable for the same parameter space (Fig. 3). The Turing space occupies a portion of the stability space, and this portion increases from Type I to Type II networks and from Type II to Type III networks. Thus, topological family and network type govern the robustness of a given Turing network. Type II and Type III networks are more robust than Type I networks because the diffusivity constraint largely constricts the Turing space in Type I systems. This implies that Type II and III networks are more suitable for the design of robust synthetic RD systems. Furthermore, the large degree of robustness of Type II and Type III networks also suggests that that they are more likely to be adapted for pattern formation processes during evolution (Marcon et al., 2016). Importantly, even larger systems that have more than the minimal number of links can be analyzed within the framework of measuring the stability and instability volume. However, since this approach is based on linear reaction terms, the accuracy of the robustness prediction for a particular system will depend on how well the linear approximation holds far from equilibrium.

3.3. Rules to determine the phase relationships in spatial patterns

Another important aspect of RD networks is their ability to generate spatially overlapping (in-phase) or mutually exclusive (out-of-phase) patterns (Fig. 4a and b), similar to the observed patterns of biological regulators (Marcon et al., 2016). These spatial expression patterns can act as critical cues to relay positional information for the determination of cell fates during development as well as for the maintenance of differentiated cell populations (Green and Sharpe, 2015).

Interestingly, the pattern phases are governed solely by the nature of regulatory interactions among the components, and it is possible to predict the overlap between species from the network topology without the need for numerical simulations (Diego et al., 2018). Fig. 4a and b depict the classical activator-inhibitor and substrate-depletion RD models, respectively (Murray, 2013). In the activator-inhibitor model the activator induces itself and the inhibitor, whereas in the substrate-depletion model the activator (node 1 in Fig. 4b) consumes the substrate (node 2 in Fig. 4b) for its own activation, leading to the depletion of the substrate by fueling the activator. The in-phase pattern produced by the activator-inhibitor network (Fig. 4a) can be altered to an out-of-phase pattern (Fig. 4b) by simply changing the signs of all edges emerging from and coming to any chosen node. For example, in Fig. 4a inverting the edges emerging from node 1 (a to $-a$, and c to $-c$) followed by an inversion of the edges coming to the same node ($-b$ to b, and $-c$ to c), converts the initial activator-inhibitor network to the substrate-depletion network, thereby altering the pattern phasing. Note that the self-regulatory loops (auto-activation or auto-inhibition) remain unchanged as they undergo a double inversion (c to $-c$, and $-c$ to c). This principle can be extended to multi-component RD systems. For an N-node RD network, there are 2^{N-1} possible phase relationships, which can be comprehensively analyzed by systematically altering the network topologies (Diego et al., 2018). For three-node networks, for example, there are $2^{3-1} = 4$ possible phase relationships (Fig. 4c). Thus, the network topology is the key determinant of pattern phases. In the future, these insights could be used to design synthetic self-organizing tissues with any combination of spatially overlapping or separated gene expression patterns (see below).

4. Novel theoretical frameworks for RD systems

4.1. Moving local equilibria

The classical approach of analyzing Turing instabilities solely based on the shape of dispersion relations (Cross and Hohenberg, 1993), which describe the growth rates of different spatial perturbations around a homogeneous steady state (Box 1), has major limitations: The dispersion relation approach is applicable only in special cases where the growth of small spatial perturbations around a steady state is driven by nearly linear interactions (Halatek and Frey, 2018; Smith and Dalchau, 2018a). However, in real biological scenarios, patterning information can be generated before reaching a stable steady state (Bergmann et al., 2007), and it has been proposed that the stability of the homogeneous steady state is not a necessary condition for Turing pattern emergence (Smith and Dalchau, 2018a). To address these limitations associated with the analysis of linearized RD systems, Halatek and Frey proposed a mathematical framework, which can predict the behavior of nonlinear dynamical systems that are far from the steady state (Halatek and Frey, 2018). It is based on the idea that the dynamics of a mass-conserving system – a system where the molecules do not exit the system but are interconverted – can be studied by partitioning it into local spatial compartments and analyzing the stability of the local equilibrium or steady state of each compartment. In the absence of diffusion-driven mass redistribution, the compartments are not coupled leading to stable local equilibria. However, in the presence of diffusion the diffusive coupling of the compartments leads to lateral mass redistribution, thereby causing the displacement of local equilibria. These *moving local equilibria* have been postulated to guide the emergence of self-organized patterns and to scaffold their final shape (Halatek and Frey, 2018). This framework has been successfully applied to the MinD-MinE patterning system, which controls the positioning of the division plane in bacteria, and in the future it will be interesting to explore the generality of the key role of lateral mass redistribution in the emergence of spatial order for multi-component RD networks.

4.2. Wave-pinning for self-organizing scale-invariant patterns

Another prime example of a mass conserving system is the network that controls eukaryotic cell polarization in response to external stimuli (Mori et al., 2008). A simplified two-component model of this system considers two forms of a cell-polarity regulator: i) a highly diffusible cytosolic inactive form, and ii) a membrane-localized active form with 100-fold lower diffusivity. Mass conservation in this system arises from the interconversion of active and inactive forms, which are restricted within a cell. At a given concentration of the inactive form, the active form concentration has the bistable steady states S- and S_+ (Fig. 5). A transient polarizing signal of sufficient amplitude can bias the initially homogeneous distribution of the active form to drive the emergence and propagation of a wave due to the bistable reaction kinetics (Fig. 5). The propagation of the wave is halted, i.e. the wave is *pinned*, when the interconversion rates of the two forms are balanced and the final polar pattern is established (Fig. 5) (Mori et al., 2008). The wave-pinning framework for single cells has recently been extended to models for the patterning of whole tissues, e.g. for the Nodal/Lefty system that regulates early *Xenopus* embryogenesis (Middleton et al., 2013), and the theory might also be relevant for pattern formation in organoids (Ishihara and Tanaka, 2018).

It is currently unclear whether wave-pinning and classical diffusion-driven instabilities represent different mechanisms (Brena-Medina and Champneys, 2014; Halatek and Frey, 2018; Trong et al., 2014; Verschueren and Champneys, 2017). Given the common ingredients of reaction and diffusion, the mechanisms are certainly related, but most importantly they can be clearly distinguished based on their different patterning behaviors: While classical Turing patterns have a fixed wavelength leading to different numbers of peaks in differently sized

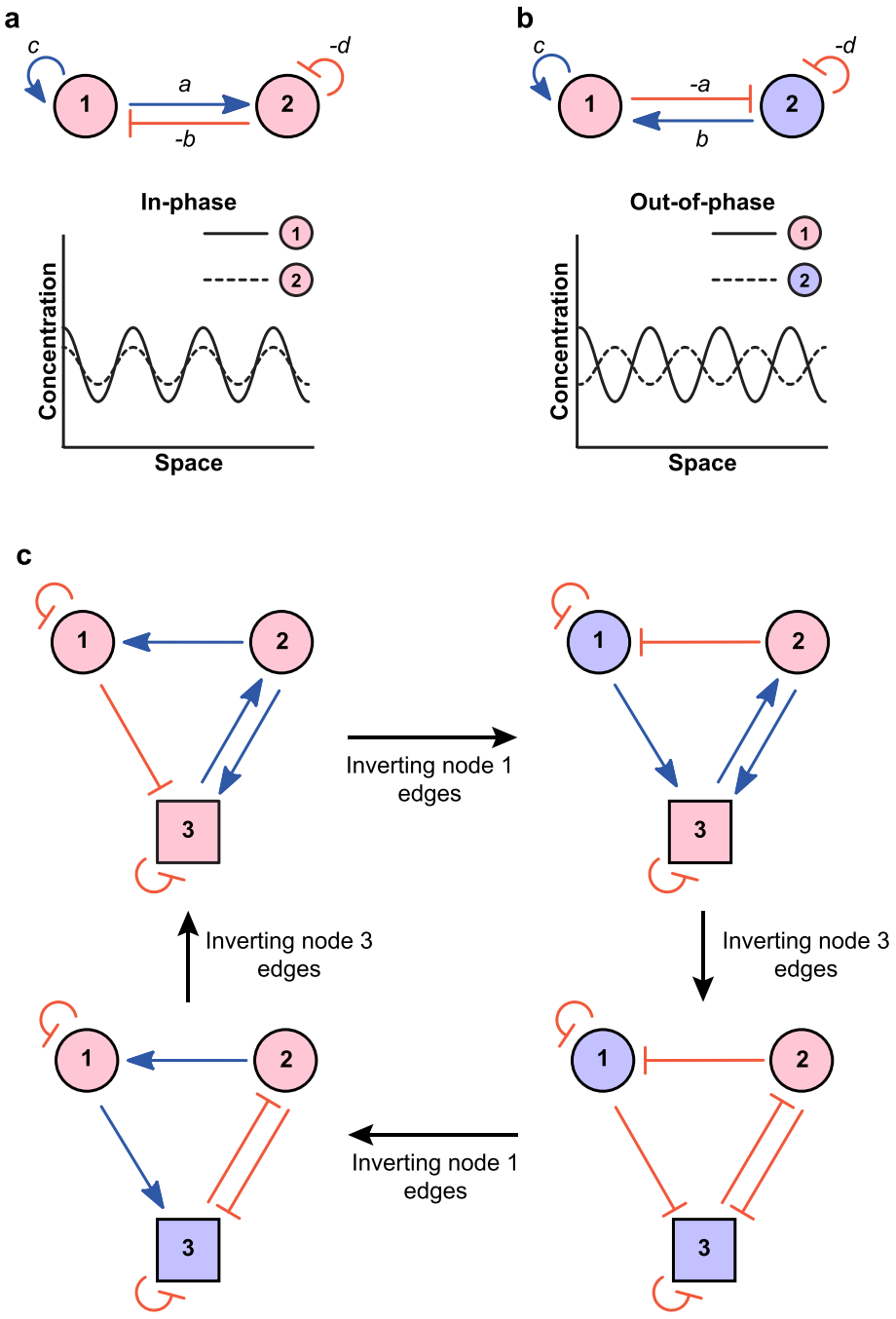

Fig. 4. Rules to determine pattern phases. (a) The activator-inhibitor network topology produces in-phase Turing patterns. **(b)** The substrate-depletion network topology produces out-of-phase Turing patterns. **(c)** An example showing the generation of all possible phase relationships for three-node networks. Nodes with the same color indicate that they are in-phase. Notations are the same as in Fig. 2.

domains, the dimensions of wave-pinning-induced patterns proportionately scale with the domain size (Diego, 2013; Ishihara and Tanaka, 2018; Mori et al., 2008) as experimentally observed in many biological patterning systems (reviewed in Čapek and Müller, 2019; Ishihara and Tanaka, 2018; Umulis and Othmer, 2013). Importantly, it has also been shown that is possible to systematically design an RD system that can only exhibit the behavior characteristic of wave-pinning – but not of Turing patterns – by analyzing the graph structure of the underlying network (Diego, 2013).

4.3. *Incorporating tissue mechanics and fluid flows*

A long-standing limitation of RD models is that they typically do not account for potential effects of tissue mechanics and extracellular fluid flows on pattern formation. A new model has recently addressed this limitation and provides a glimpse into a general framework of pattern formation based on the theory of biological mixtures (Ateshian, 2007). The new model incorporates the effects of two distinct phases within multicellular tissues: the poroelastic network of cells, and the extracellular fluid phase (Recho et al., 2018). In this biphasic model, the tissue architecture was assumed to be dependent on the concentration of signaling molecules: Activating signals would increase the local cell volume fraction relative to the extracellular phase, whereas inhibitory signals would decrease it (Recho et al., 2018). Thus, extracellular fluid movements could be guided by tissue mechanics depending on local changes in the cell volume fraction. The biphasic model predicted several

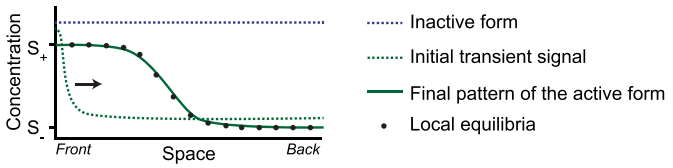

Fig. 5. Emergence of a wave-pinning pattern in a bistable reaction-diffusion system. A schematic wave-pinning pattern across the length of a cell or a tissue is shown. The active form distribution is polarized by a transient stimulus at the front of the domain. Consequently, the wave front of active form concentration propagates across the domain before it eventually arrests and 'pins'. The maxima and minima of the wave correspond to the top and bottom steady states (S_+ and S-), respectively, of the bistable system (Mori et al., 2008), and it was recently shown that wave propagation is driven by shifts in local equilibria (Halatek and Frey, 2018).

new types of instabilities that can lead to pattern formation, including self-organizing patterns driven by the active transport of signaling molecules along the extracellular fluid as well as the large-scale flow of cells themselves. Interestingly, patterning could even be achieved with a single signaling molecule, and the resulting patterns exhibited robust scaling properties to regulate tissue proportions in differently sized fields (Recho et al., 2018), similar to the properties of the wave-pinning model discussed above. The ability to achieve Turing instabilities with virtually any two-component reaction scheme (e.g. inhibitor-inhibitor interactions) is another fascinating property of this model, which could explain pattern formation in the absence of classical activator-inhibitor dynamics (Madzvamuse et al., 2015; Recho et al., 2018). Although many assumptions and predictions of this mathematical framework await experimental validation, the emerging ideas will likely inspire new advances in the field.

4.4. Model reduction approaches for RD systems

One of the major problems with the application of RD systems to model patterning is the complexity of biological networks. Biological networks usually possess a large number of interacting components. However, beyond four-node RD networks the computational power required for numerical analysis is enormous, and analytical solutions can be practically impossible for many research groups. In the following, we discuss how model reduction strategies have been employed to tackle these challenges.

Smith and Dalchau recently formulated a model reduction approach resembling a quasi-steady-state approximation (QSSA) (Smith and Dalchau, 2018a). QSSA assumes that in a system of chemical reactions the concentrations of chosen intermediate species remain constant. This can enable reduction of complex differential equations to much simpler algebraic equations. Using this approach, it is possible to eliminate all non-diffusible nodes from an N-node RD system with M diffusible nodes ($2 < M < N$). In simple terms, this is achieved by assuming that the non-diffusible species have equilibrium concentrations at all times, thus enabling their elimination from the system. Consequently, this approach preserves the characteristics of the parameter space to a large extent, i.e. the reduced system has the same stability space and Turing space as the original system. Furthermore, the pattern wavelength is unaffected by model reduction (Smith and Dalchau, 2018a). However, there are caveats to this approach. First, a reduced system that contains only diffusible nodes cannot form Turing patterns with equal diffusivities even if the original system can do so. Second, the system dynamics are not preserved upon model reduction, and the reduced model exhibits faster patterning dynamics due to the underlying mathematical assumptions. Third, this approach cannot be applied to RD systems in which all species are diffusible. Even with these limitations, the model reduction approach can be very useful when the main objective is to find pattern-forming parameters. Generally, very few species are cell non-autonomous and diffusible even in large biological networks, and this model reduction approach can allow the extraction of the Turing space with considerably less computational power in a short amount of time.

Another important concept that simplifies the application of Turing-like systems to biological patterning is the kernel-based Turing (KT) model (Kondo, 2017), which depends on the shape of an activation-inhibition kernel rather than on partial differential equations such as those shown in the legend for Fig. 1a. The KT model assumes that the local concentration of a patterning molecule in a tissue depends on net activating and inhibitory signals received from nearby cells. This approach reduces model complexity since it does not assume any molecular mechanism of activation or inhibition. In this model, the kernel function is a sum of two Gaussian functions, which defines the extent of activating and inhibitory signals received from a cell at a distance (Fig. 6a). The total signal received from the surrounding cells is obtained by mathematical integration of the kernel, which determines the synthesis rate of a patterning molecule that is degraded at a constant rate. Interestingly, these basic assumptions can lead to the spatial patterning of this molecule (Fig. 6b and c), thereby giving rise to spatial information and influencing the cellular state. The nature of the signal, its means of propagation, and the cellular state governed by the signal are not explicitly defined in the kernel function and must be determined based on the biological system of interest. For example, in the case of the striped patterns on adult zebrafish, the projections of the pigment cells (yellow xanthophores and black melanophores) might constitute the signal carriers that determine the cellular state of pigmentation (Kondo, 2017; Nakamasu et al., 2009), but the KT model can also incorporate potential contributions of diffusion since it is agnostic to molecular details. The activation-inhibition kernel can be informed experimentally by analyzing the dynamics in wildtype and activation (Aramaki and Kondo, 2018) or inhibition (Nakamasu et al., 2009) conditions, and the KT model is particularly useful as a guiding framework when the detailed molecular mechanisms underlying pattern formation are unknown.

5. Significance for developmental and synthetic biology

As described above, the network topology is crucial to understand the pattern formation conditions of RD systems. While the complete set of interactions and thus the network topology of real biological patterning systems under investigation is rarely known, frameworks like the KT model may provide a useful starting point. Additional factors that can influence pattern formation include intrinsic noise, delays in signal transduction, transcription and translation as well as the geometry of the system (Gaffney and Monk, 2006; Umulis and Othmer, 2012). Furthermore, developmental patterning systems are often strongly influenced by pre-patterns resulting from a biased distribution of maternal factors (reviewed in Rogers and Müller, 2019); as opposed to purely self-organizing systems with homogeneous initial conditions, *self-regulating* systems with interacting diffusible and non-diffusible factors and initial pre-patterns therefore often better describe developmental patterning (Rogers and Müller, 2019). In spite of these challenges, experiment-guided computational modeling of RD systems can not only provide crucial insights into mechanisms of biological patterning but also aid in building synthetic patterning systems as outlined below (for an excellent review with more biological examples, see Schweisguth and Corson, 2019).

Vertebrate digit patterning depends on the signaling molecules BMP and Wnt as well as the cell-autonomous transcription factor Sox9 (Badugu et al., 2012; Raspopovic et al., 2014). In the mouse limb bud, the expression of *Sox9* and the distribution of the BMP signal transducer pSmad overlap, whereas both Wnt signaling and *BMP* expression are out-of-phase with respect to *Sox9* expression (Fig. 7a). Based on these observations and the known interactions between BMP, Wnt and Sox9, a three-node Turing network was proposed to underlie digit patterning, in which BMP and Wnt are diffusible nodes and Sox9 is a non-diffusible node (Raspopovic et al., 2014) (Fig. 7b). Computer simulations of this three-node model recapitulated the observed expression patterns, except

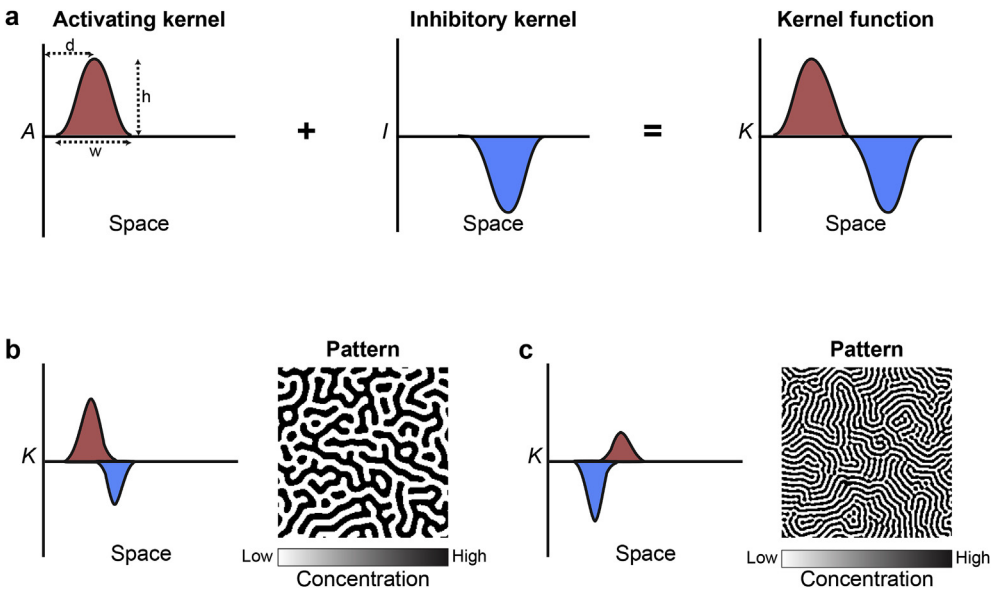

Fig. 6. Schematic depiction of pattern formation using kernel functions. (a) Summation of an activating spatial kernel *A* and an inhibitory spatial kernel *I* gives the spatial kernel function *K*. The amplitude (h), width (w), and distance (d) of the activating and inhibitory kernels are the defining characteristics of the kernel function. **(b,c)** Examples of kernel functions with their corresponding patterns simulated using the web-based KT model simulator (Kondo, 2017). Simulation parameters used in (b): activating kernel h = 15.5, w = 1.0, d = 4.13; inhibitory kernel h = -11.0, w = 0.81, d = 7.00. Simulation parameters used in (c): activating kernel h = 7.50, w = 1.0, d = 7.00; inhibitory kernel h = -15.0, w = 0.81, d = 4.13.

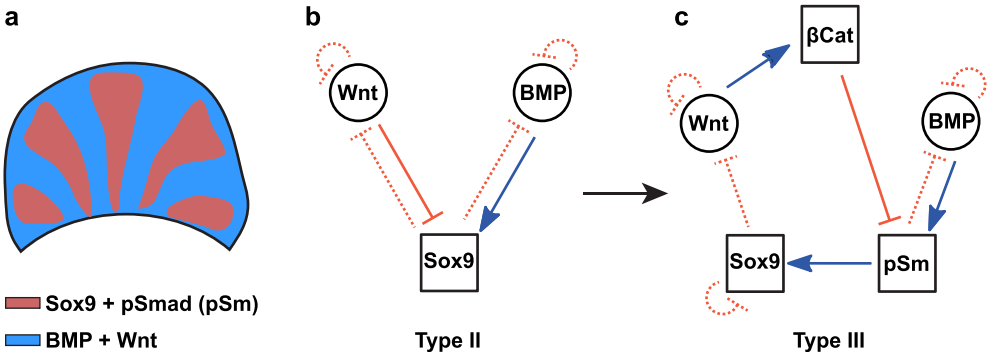

Fig. 7. Turing networks for vertebrate digit patterning. (a) A schematic representation of the in-phase and out-of-phase gene expression patterns in a developing vertebrate limb (pSmad and pSm indicate pSmad1/5/8). **(b)** Turing network employed in Raspopovic et al. (2014) to explain digit pattern formation. **(c)** Extension of the Turing network used in Marcon et al. (2016).

for the out-of-phase relationship between *BMP* expression and BMP signaling as measured by the distribution of the signal transducer pSmad. The three-node Turing network was subsequently extended to a five-node network (Fig. 5c) using the software RDNets (Marcon et al., 2016). The five-node network incorporated the BMP signal transducer pSmad and the Wnt signal transducer β-catenin as two additional non-diffusible nodes. In this updated model, indirect repression of Sox9 by β-catenin was able to explain all of the experimentally observed phase relationships, including the out-of-phase relation between *BMP* expression and BMP signaling. Additional negative feedbacks between Sox9, BMP and Wnt signaling were postulated (Marcon et al., 2016), but these interactions remain to be tested experimentally.

Attempts to construct synthetic RD systems capable of biological pattern formation have also been recently made in bacteria and mammalian cells (Davies, 2017; Karig et al., 2018; Luo et al., 2019; Santos-Moreno and Schaerli, 2018; Sekine et al., 2018). A synthetic activator-inhibitor genetic circuit was employed in bacteria to create stochastic patterns of fluorescent protein expression (Karig et al., 2018). These patterns were driven by a stochastic RD system and do not require classical Turing instabilities, thereby opening new opportunities for synthetic biological pattern formation. In another study, a synthetic mammalian pattern formation system was constructed (Sekine et al., 2018), based on the known differential diffusivity of the signaling molecules Nodal and Lefty (Müller et al., 2012; Rogers and Müller, 2019). However, this synthetic activator-inhibitor system could only generate irregular patterns of Nodal-positive cells surrounded by Nodal-negative cells (Sekine et al., 2018). Many mechanistic details of pattern formation in the bacterial and mammalian systems remain unknown, and Santos-Moreno and Schaerli therefore recently stated that *"[…] the engineering of a genuine Turing system remains yet to be achieved*" (Santos-Moreno and Schaerli, 2018). Previous studies were conceptually limited to two-component synthetic networks and differential diffusivity, but it will also be interesting to explore synthetic biological pattern formation using multi-component RD systems with relaxed diffusivity constraints (Diego et al., 2018; Marcon et al., 2016; Smith and Dalchau, 2018b).

6. Summary

In the past decade, the theory of RD-mediated pattern formation has witnessed exciting new developments and novel theoretical insights. The discovery of multi-component Turing networks that do not require differential diffusivity has challenged the classical view of local self-activation and lateral inhibition. A new understanding of the differential diffusivity criterion and patterning robustness from the analysis of multi-component RD systems has opened unprecedented opportunities for the discovery of biological patterning systems and the design of robust synthetic self-organizing systems (Marcon et al., 2016; Smith and Dalchau, 2018b; Zheng et al., 2016). It is therefore possible that these recent insights may enable novel therapeutic advances for future tissue engineering approaches. However, many challenges in mathematically

modeling complex biological signaling networks remain: More realistic models will require the incorporation of important effects such as tissue mechanics and compartmentalization as well as the integration of large signal transduction cascades and their interactions. At the same time, our understanding of the mechanisms underlying pattern formation is dependent on simplified abstract models. Striking the proper balance between realistic physical models and mathematical abstraction will likely inspire new studies of self-organization to derive meaningful biological insights in the future.

Definitions

Parameter space - The multi-dimensional space comprising all possible parameter combinations (Fig. 3).

Stability space - The fraction of the parameter space that satisfies the stability condition, i.e. the system is stable at the homogeneous steady state under these parameters in the absence of diffusion (Box 1, Fig. 3).

Turing space - The fraction of the stability space that results in time-invariant Turing patterns (Fig. 3).

Robustness - The probability of randomly picking pattern-forming parameter combinations from the parameter space. The pattern-forming parameter combinations essentially constitute the Turing space. Hence, a larger Turing space yields a more robust RD network.

Acknowledgments

We thank Hans Othmer, Daniel Čapek and Mohammad ElGamacy for valuable discussions. This work was supported by the Max Planck Society and the ERC Starting Grant *QUANTPATTERN* (637840).

References

Aramaki, T., Kondo, S., 2018. Method for disarranging the pigment pattern of zebrafish by optogenetics. Dev. Biol. pii: S0012-1606(18) 30467–6.
Ateshian, G.A., 2007. On the theory of reactive mixtures for modeling biological growth. Biomechanics Model. Mechanobiol. 6, 423–445.
Badugu, A., Kraemer, C., Germann, P., Menshykau, D., Iber, D., 2012. Digit patterning during limb development as a result of the BMP-receptor interaction. Sci. Rep. 2, 991.
Bansagi Jr., T., Vanag, V.K., Epstein, I.R., 2011. Tomography of reaction-diffusion microemulsions reveals three-dimensional Turing patterns. Science 331, 1309–1312.
Bergmann, S., Sandler, O., Sberro, H., Shnider, S., Schejter, E., Shilo, B.-Z., Barkai, N., 2007. Pre-steady-state decoding of the Bicoid morphogen gradient. PLoS Biol. 5 e46–e46.
Brena-Medina, V., Champneys, A., 2014. Subcritical Turing bifurcation and the morphogenesis of localized patterns. Phys. Rev. E - Stat. Nonlinear Soft Matter Phys. 90, 032923.
Butler, T., Goldenfeld, N., 2011. Fluctuation-driven Turing patterns. Physical Review E 84, 11112.
Čapek, D., Müller, P., 2019. Positional information and tissue scaling during development and regeneration. Development. In press.
Cross, M.C., Hohenberg, P.C., 1993. Pattern formation outside of equilibrium. Rev. Mod. Phys. 65, 851–1112.
Davies, J., 2017. Using synthetic biology to explore principles of development. Development 144, 1146–1158.
Diego, X., 2013. On the theory of cell migration: durotaxis and chemotaxis, Departament de Resistència de Materials i Estructures a l'Enginyeria. Universitat Politècnica de Catalunya.
Diego, X., Marcon, L., Müller, P., Sharpe, J., 2018. Key features of Turing systems are determined purely by network topology. Phys. Rev. X 8, 021071.
Gaffney, E.A., Monk, N.A., 2006. Gene expression time delays and Turing pattern formation systems. Bull. Math. Biol. 68, 99–130.
Gierer, A., Meinhardt, H., 1972. A theory of biological pattern formation. Kybernetik 12, 30–39.
Green, J.B.A., Sharpe, J., 2015. Positional information and reaction-diffusion: two big ideas in developmental biology combine. Development 142, 1203–1211.
Halatek, J., Frey, E., 2018. Rethinking pattern formation in reaction-diffusion systems. Nat. Phys. 14, 507–514.
Hiscock, T.W., Megason, S.G., 2015. Mathematically guided approaches to distinguish models of periodic patterning. Development 142, 409–419.
Ishihara, K., Tanaka, E.M., 2018. Spontaneous symmetry breaking and pattern formation of organoids. Curr. Opin. Struct. Biol. 11, 123–128.
Karig, D., Martini, K.M., Lu, T., DeLateur, N.A., Goldenfeld, N., Weiss, R., 2018. Stochastic Turing patterns in a synthetic bacterial population. Proc. Natl. Acad. Sci. 115, 6572.
Klika, V., Baker, R.E., Headon, D., Gaffney, E.A., 2012. The influence of receptor-mediated interactions on reaction-diffusion mechanisms of cellular self-organisation. Bull. Math. Biol. 74, 935–957.
Kondo, S., 2017. An updated kernel-based Turing model for studying the mechanisms of biological pattern formation. J. Theor. Biol. 414, 120–127.
Kondo, S., Miura, T., 2010. Reaction-diffusion model as a framework for understanding biological pattern formation. Science 329, 1616–1620.
Luo, N., Wang, S., You, L., 2019. Synthetic pattern formation. Biochemistry 58, 1478–1483.
Madzvamuse, A., Ndakwo, H.S., Barreira, R., 2015. Cross-diffusion-driven instability for reaction-diffusion systems: analysis and simulations. J. Math. Biol. 70, 709–743.
Marcon, L., Diego, X., Sharpe, J., Müller, P., 2016. High-throughput mathematical analysis identifies Turing networks for patterning with equally diffusing signals. eLife 5, e14022.
Marcon, L., Sharpe, J., 2012. Turing patterns in development: what about the horse part? Curr. Opin. Genet. Dev. 22, 578–584.
Meinhardt, H., 2012. Turing's theory of morphogenesis of 1952 and the subsequent discovery of the crucial role of local self enhancement and long-range inhibition. Interface Focus 2, 407–416.
Meinhardt, H., Gierer, A., 2000. Pattern formation by local self-activation and lateral inhibition. Bioessays 22, 753–760.
Middleton, A.M., King, J.R., Loose, M., 2013. Wave pinning and spatial patterning in a mathematical model of Antivin/Lefty-Nodal signalling. J. Math. Biol. 67, 1393–1424.
Mincheva, M., Roussel, M.R., 2006. A graph-theoretic method for detecting potential Turing bifurcations. J. Chem. Phys. 125, 204102–204102.
Mori, Y., Jilkine, A., Edelstein-Keshet, L., 2008. Wave-pinning and cell polarity from a bistable reaction-diffusion system. Biophys. J. 94, 3684–3697.
Müller, P., Nüsslein-Volhard, C., 2016. Obituary: Hans Meinhardt (1938-2016). Development 143, 1231–1233.
Müller, P., Rogers, K.W., Jordan, B.M., Lee, J.S., Robson, D., Ramanathan, S., Schier, A.F., 2012. Differential diffusivity of Nodal and Lefty underlies a reaction-diffusion patterning system. Science 336, 721–724.
Müller, P., Rogers, K.W., Yu, S.R., Brand, M., Schier, A.F., 2013. Morphogen transport. Development 140 (8), 1621–1638.
Murray, J.D., 2013. Mathematical biology II: Spatial models and biomedical applications. Springer, New York.
Nakamasu, A., Takahashi, G., Kanbe, A., Kondo, S., 2009. Interactions between zebrafish pigment cells responsible for the generation of Turing patterns. Proc. Natl. Acad. Sci. 106, 8429–8434.
Raspopovic, J., Marcon, L., Russo, L., Sharpe, J., 2014. Digit patterning is controlled by a Bmp-Sox9-Wnt Turing network modulated by morphogen gradients. Science 345, 566–570.
Recho, P., Hallou, A., Hannezo, E., 2018. Theory of mechano-chemical patterning in biphasic biological tissues. Proc. Natl. Acad. Sci. 116, 5344–5349.
Rogers, K.W., Müller, P., 2019. Nodal and BMP dispersal during early zebrafish development. Dev. Biol. 447, 14–23.
Roth, S., 2011. Mathematics and biology: a Kantian view on the history of pattern formation theory. Dev. Gene. Evol. 221, 255–279.
Santos-Moreno, J., Schaerli, Y., 2018. Using synthetic biology to engineer spatial patterns. Advanced Biosystems 3, 1800280.
Scholes, N.S., Schnoerr, D., Isalan, M., Stumpf, M.P.H., 2019. A comprehensive network atlas reveals that Turing patterns are common but not robust. Cell Systems 9, 243–257 e244.
Schweisguth, F., Corson, F., 2019. Self-organization in pattern formation. Dev. Cell 49, 659–677.
Sekine, R., Shibata, T., Ebisuya, M., 2018. Synthetic mammalian pattern formation driven by differential diffusivity of Nodal and Lefty. Nat. Commun. 9, 5456.
Smith, S., Dalchau, N., 2018a. Beyond activator-inhibitor networks: the generalised Turing mechanism arXiv 1803.07886.
Smith, S., Dalchau, N., 2018b. Model reduction enables Turing instability analysis of large reaction–diffusion models. J. R. Soc. Interface 15, 20170805.
Trong, P.K., Nicola, E.M., Goehring, N.W., Kumar, K.V., Grill, S.W., 2014. Parameter-space topology of models for cell polarity. New J. Phys. 16, 065009–065019.
Turing, A.M., 1952. The chemical basis of morphogenesis. Philosophical Transactions of the Royal Society (part B) 237, 37–72.
Umulis, D.M., Othmer, H.G., 2012. The importance of geometry in mathematical models of developing systems. Curr. Opin. Genet. Dev. 22, 547–552.
Umulis, D.M., Othmer, H.G., 2013. Mechanisms of scaling in pattern formation. Development 140, 4830–4843.
Verschueren, N., Champneys, A., 2017. A model for cell polarization without mass conservation. SIAM J. Appl. Dyn. Syst. 16, 1797–1830.
White, K.A.J., Gilligan, C.A., 1998. Spatial heterogeneity in three-species, plant-parasite-hyperparasite, systems. Philos. Trans. R. Soc. Biol. Sci. 353, 543–557.
Zheng, M.M., Shao, B., Ouyang, Q., 2016. Identifying network topologies that can generate Turing pattern. J. Theor. Biol. 408, 88–96.

3. Paper 2 – Single-molecule tracking of Nodal and Lefty in live zebrafish embryos supports hindered diffusion model

3.1. Synopsis

In this collaborative study, we used single-molecule imaging and tracking approaches to understand the mechanisms of Nodal and Lefty dispersal in live zebrafish embryos. The Nodal-Lefty system forms an activator-inhibitor network with Nodal being the short-range activator and Lefty being the long-range inhibitor. Even though, Nodals and Leftys have similar molecular sizes, they show order of magnitude differences in their effective diffusivities. The hindered-diffusion model can explain these differences, if Nodal diffusion is strongly hindered by binding to extracellular receptors and Lefty diffusion is only weakly hindered. Our findings supported the hindered-diffusion model. Furthermore, analysis of Nodal and Lefty localization in distinct extracellular regions (cell-cell interfaces and cavities) provided counterintuitive results. To explain these seemingly paradoxical data, I developed an agent-based model of signal movement and dispersal. Systematic simulations of the model provided crucial insights into key factors regulating Nodal and Lefty distribution in the distinct extracellular compartments.

3.2. Author contributions

The detailed author contributions are provided in the paper. Here, I highlight my contributions to this study – I developed an agent-based model of signal dispersal in realistic geometries based on the experimental datasets, with suggestions from the co-authors. I wrote the code, performed model simulations and data analysis. I wrote the section of the manuscript pertaining to the agent-based modeling and provided comments on other parts of the manuscript. I performed experiments along with Daniel Čapek to validate the fusion proteins used in the study.

nature communications

Article

https://doi.org/10.1038/s41467-022-33704-z

Single-molecule tracking of Nodal and Lefty in live zebrafish embryos supports hindered diffusion model

Received: 15 April 2022

Accepted: 28 September 2022

Published online: 15 October 2022

Check for updates

Timo Kuhn[1], Amit N. Landge[2,5], David Mörsdorf[3,4,5], Jonas Coßmann[1], Johanna Gerstenecker[1], Daniel Čapek[2], Patrick Müller[2,3] ✉ & J. Christof M. Gebhardt[1] ✉

The hindered diffusion model postulates that the movement of a signaling molecule through an embryo is affected by tissue geometry and binding-mediated hindrance, but these effects have not been directly demonstrated in vivo. Here, we visualize extracellular movement and binding of individual molecules of the activator-inhibitor signaling pair Nodal and Lefty in live developing zebrafish embryos using reflected light-sheet microscopy. We observe that diffusion coefficients of molecules are high in extracellular cavities, whereas mobility is reduced and bound fractions are high within cell-cell interfaces. Counterintuitively, molecules nevertheless accumulate in cavities, which we attribute to the geometry of the extracellular space by agent-based simulations. We further find that Nodal has a larger bound fraction than Lefty and shows a binding time of tens of seconds. Together, our measurements and simulations provide direct support for the hindered diffusion model and yield insights into the nanometer-to-micrometer-scale mechanisms that lead to macroscopic signal dispersal.

The development of an embryo from a single cell to a complex organism is coordinated by cellular communication via signaling molecules called morphogens. Morphogens are produced in localized sources, from which they spread to form concentration gradients. Target cells along a morphogen gradient perceive different amounts and durations of morphogen signaling and respond by switching on different cell fate programs. By coupling molecular concentrations to distributions in space, morphogens can therefore provide positional information to orchestrate tissue patterning[1].

The range of a morphogen gradient needs to span multiple cell diameters from the source in order to provide positional information. While special transport mechanisms – for instance along cell extensions – are important in certain developmental contexts[2–6], the most prominent theory to explain the establishment of a morphogen gradient is the synthesis-diffusion-clearance model[7–13]. In this model, morphogens are produced in a localized source, from which they spread into neighboring tissues by diffusion. The length-scale of the gradient is determined by morphogen clearance – degradation or cellular uptake – as well as the morphogen's diffusivity. While the free diffusivity of a morphogen is a biophysical property that can be influenced by factors in the tissue environment such as temperature and viscosity, the hindered diffusion model postulates that the effective diffusivity of a molecule can be further influenced by transient binding interactions[2,7]. Indeed, there are numerous reports demonstrating direct binding of morphogens to intra- and extracellular molecules such as receptors[14,15], collagen[16] and heparin sulfate proteoglycans[7,13,17–22] that can modulate the shape of a morphogen gradient, but it remains unclear whether binding truly affects

[1]Institute of Biophysics, Ulm University, Albert-Einstein-Allee 11, 89081 Ulm, Germany. [2]University of Konstanz, Universitätsstraße 10, 78464 Konstanz, Germany. [3]Friedrich Miescher Laboratory of the Max Planck Society, Max-Planck-Ring 9, 72076 Tübingen, Germany. [4]University of Vienna, Department of Neurosciences and Developmental Biology, Djerassiplatz 1, 1030 Vienna, Austria. [5]These authors contributed equally: Amit N. Landge, David Mörsdorf. ✉e-mail: patrick.mueller@uni-konstanz.de; christof.gebhardt@uni-ulm.de

morphogen diffusivity or rather retention, uptake and stability. Beyond flat tissue culture systems[23], the tenets of the hindered diffusion model – i) free diffusion far away from cell surfaces, ii) hindered diffusion due to the tissue architecture, iii) further reduction due to binding[2,7]– have not been directly demonstrated for any morphogen in an in vivo tissue context.

The secreted TGF-β superfamily ligands Nodal and Lefty are prime examples of an activator-inhibitor morphogen pair whose different signaling ranges have been postulated to arise from differential hindrance[2,24,25]. This system has been best characterized in zebrafish embryos, where the Nodal signaling proteins Squint and Cyclops are produced in the marginal zone and induce the formation of mesoderm and endoderm during early development, beginning around 4 h post-fertilization (hpf)[9,26–30]. Nodal signaling is antagonized by secreted Leftys[27,31–34], which inhibit Nodals from binding to their receptors[35,36].

Hindered diffusion has been proposed to result in the formation of Nodal and Lefty concentration gradients[2,25] where Cyclops has an ultra-short range of only a few micrometers, Squint has a short-to-mid range, Lefty1 acts at a long range, and Lefty2 has an ultra-long range leading to a nearly uniform distribution throughout the embryo[25]. Previous observations of the Nodal/Lefty system are consistent with the hindered diffusion model. First, free diffusion coefficients measured by fluorescence correlation spectroscopy (FCS) in a diffraction-limited spot far away from cell surfaces yielded similar local diffusion coefficients on a sub-micrometer scale for zebrafish Nodals and Leftys[2,14,25]. Second, effective diffusion coefficients on a tissue level across a cube of approximately 8 × 8 × 8 cells measured by fluorescence recovery after photobleaching (FRAP) were found to be much lower for Nodals than for Leftys (Cyclops < Squint < Lefty1 < Lefty2)[25,37–39]. Third, it has been shown that Nodals bind their receptors with nanomolar affinity[14], and manipulating the levels of the co-receptor Oep modulated the Nodal signaling range and distribution[40,41]. However, it remains unclear whether and how such treatments affect Nodal and Lefty movement, how effective diffusivity through a tissue emerges from interactions at the molecular scale, how binding on the cell surface contributes to Nodal and Lefty movement, and how tissue geometry affects morphogen spreading.

Here, we present single-molecule imaging and tracking of HaloTag-tagged fluorescent Cyclops, Squint, Lefty1 and Lefty2 in the extracellular environment of live developing zebrafish embryos. We monitored the movement of these morphogens on the nanoscale and observed a major influence of the local extracellular architecture on the diffusion properties. We found that molecules moving in extracellular cavities between cells were predominantly diffusing freely. In contrast, we observed hindered diffusion within cell-cell interfaces with larger bound fractions of Nodal molecules compared to Lefty. Time-lapse microscopy enabled us to observe individual binding events of tens of seconds for Cyclops and Squint. We developed an agent-based model of single-molecule movements and found a major contribution of tissue architecture, receptor levels and affinity on morphogen distributions. Overall, our single-molecule fluorescence measurements directly support a model of hindered diffusion for Nodal and Lefty, where Nodals – but not Leftys – are transiently trapped on the cell surface, explaining their short action range.

Results

Single-molecule imaging of HaloTag-labeled morphogens in live zebrafish embryos

To observe the movement of individual morphogens, we used a reflected light-sheet microscope (RLSM), which is ideally suited to image single molecules in live embryos[42,43]. In order to visualize Nodals and Leftys we fused them to HaloTags. We inserted the HaloTag between the pro- and mature domains of Cyclops and Squint and added them to the C-termini of Lefty1 and Lefty2, generating active and properly localized proteins analogous to previous approaches[25] (Fig. 1a, Supplementary Fig. 1, Materials and Methods). The HaloTag allows precise titration of the amount of fluorescence label, ensuring low densities of labeled molecules in every frame over the entire measurement period (Supplementary Fig. 2). To visualize single molecules, we injected embryos at the one-cell stage with only 1-2 pg of each mRNA (Fig. 1b, Material and Methods), 30 times less than what has been used for the assessment of effective diffusivities in FRAP experiments[25] and 60 times less than what is required to induce a full body axis in zebrafish[37]. In addition, we co-injected mRNA encoding membrane-targeted green fluorescent protein[44] (memGFP) to visualize cell outlines. After injection, embryos were incubated in JF549[45] dye solution to covalently label the HaloTag fusion protein. Subsequently, we extensively washed the embryos to remove unbound dye (Fig. 1b, Material and Methods).

We started to image the embryos with our RLSM setup at the end of the 128-cell stage (Fig. 1c) and continued the measurements up to sphere stage, shortly before gastrulation[46]. All fluorophores detected in each frame were used to track molecules in time using the software TrackIt[47] (Material and Methods). Given the compartmentalization of the embryonic tissue into intra- and extracellular regions, we performed our tracking analysis in separate sub-regions. To automatically identify extracellular regions, we analyzed memGFP images by training a convolutional neural network (CNN)[48] with a manually annotated data set (Fig. 1d, Material and Methods). The intra- and extracellular masks classified in this manner were visually inspected and manually corrected. On average 33% of a prediction mask was truncated and subsequently 8% manually corrected. The early blastoderm comprises loosely packed cells[49], subdividing the extracellular space into regions of close cell-cell contacts and large intercellular cavities where cell contacts are missing. We therefore further manually classified the extracellular space into interface and cavity regions and performed our single-molecule analysis separately in those regions (Fig. 1d, Material and Methods).

Nodals have similar diffusion coefficients but higher immobile fractions compared to Leftys

We first characterized the mobility of Nodals and Leftys in interfaces and cavities of the extracellular space by acquiring continuous movies of each morphogen at a rate of 85 frames per second (Supplementary Movie 1). When the single-molecule positions were integrated over all frames, the distributions of Nodals and Leftys well resembled the known localizations[25]: Cyclops was largely found in puncta, Squint in both puncta and diffusely, whereas Lefty1 and Lefty2 nearly uniformly occupied the extracellular space (Fig. 2a, Supplementary Fig. 1, Supplementary Movies 2–5). Interestingly, all secreted molecules were more likely to be found in cavities than in interfaces based on the ratio of localization densities as a measure of the probability to encounter a morphogen in one of the two extracellular compartments (Fig. 2b), and we found an increase in the localization density ratio commensurate with the morphogens' effective global diffusivities[25] (Cyclops: 1.53-fold, Squint: 2.66-fold, Lefty1: 3.83-fold, Lefty2: 4.03-fold, sec-Halo: 4.20-fold).

We then sorted the distances between consecutive fluorophore localizations within a track (jump distances) into histograms (Fig. 3a). These distances constitute two-dimensional projections of the three-dimensional tracks detected within the depth of focus of the objective. In both interfaces and cavities, Cyclops, and to a lesser degree Squint, showed a larger probability of short jump distances (<0.3 μm) than Lefty1 and Lefty2, indicating reduced mobility of Nodals. In contrast, in cavities, both Nodals and Leftys exhibited a higher probability of long jump distances – and hence higher mobility – compared to interfaces. We quantified the mobility of morphogens by analyzing the corresponding cumulative distribution of jump distances[50] (Fig. 3b). In our analysis, we did not correct for bias from the projection of tracks or

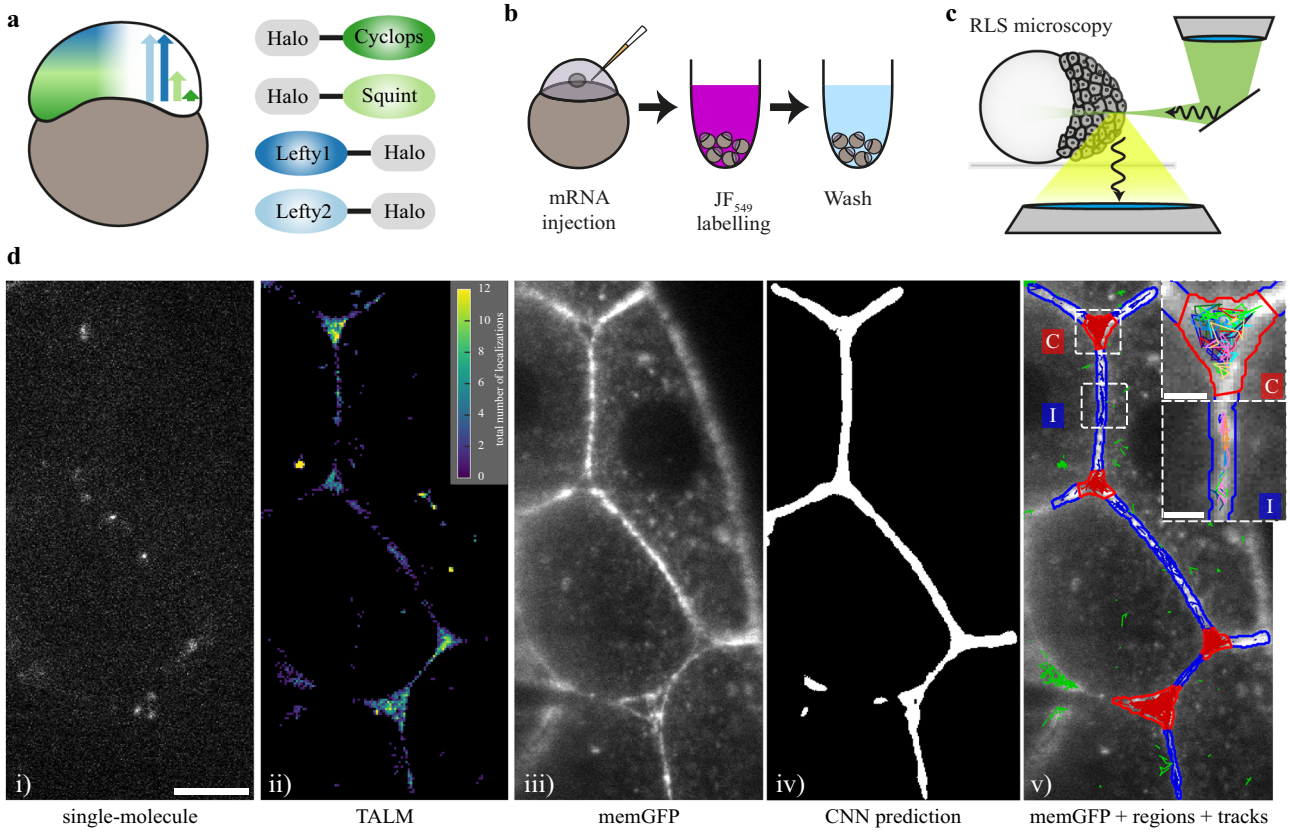

Fig. 1 | Single-molecule imaging of HaloTag-labeled Nodal and Lefty in live zebrafish embryos using RLSM. a Schematic of the presumed concentration gradients of Nodal (dark and light green) and Lefty (dark and light blue) in early zebrafish embryos (left) and sketch of HaloTag fusion proteins of mature Cyclops, mature Squint, Lefty1 and Lefty2 (right). **b** Schematic of the labeling workflow: mRNA encoding the fusion proteins was injected at the one-cell stage. Embryos were incubated in medium containing the HaloTag JF-549 ligand to covalently label the HaloTag. Excess dye was removed in washing steps. **c** Sketch of a zebrafish embryo imaged with a reflected light-sheet microscope. **d** Workflow of single-molecule imaging and image segmentation: i) signal of single Lefty2-HaloTag molecules at 561 nm laser illumination for 10 ms; ii) tracking-and-localization-microscopy (TALM) image showing the total number of localizations over 1000 frames or 11.7 s in each 2 × 2 pixel bin; iii) memGFP signal at 488 nm laser illumination averaged over 10 × 10 ms frames, outlining cellular membranes; iv) region of interest (ROI) mask of the extracellular space predicted by a convolutional neural net (CNN) based on the memGFP signal; v) overlay of the memGFP signal, the manually curated ROI separating cell-cell-interfaces (blue, I) and extracellular cavities (red, C); tracks assigned to interfaces (blue), cavities (red) and not assigned (green) are also shown. Scale bar: 10 μm. Insets in v): zoom of the indicated interface and cavity including an example set of tracks. Scale bar: 2 μm.

out-of-focus movement, which similarly applies to all morphogens and therefore does not alter their relative behavior. A three-component Brownian diffusion model best described the data (Supplementary Fig. 3), yielding the diffusion coefficients $D_{1,2,3}$ of slow, intermediate and fast diffusion and their relative amplitudes $A_{1,2,3}$[43,51–53]. The slow diffusion component likely originates from immobile or slowly moving morphogens, although the uncertainty of localizing single molecules may also be a contributor. The intermediate and fast diffusion components together approximate anomalous diffusion, which has been observed in many systems[50,52,54–58]. For the morphogens, anomalous diffusion likely arises from diffusion in the spatially restricted, highly complex and heterogeneous environment of the extracellular space.

We found that in both interfaces and cavities, the diffusion coefficients of intermediate ($D_{2,i}$ in interfaces ≈ 1.2–3.0 μm²s⁻¹, $D_{2,c}$ in cavities ≈ 4.8–6.7 μm²s⁻¹) and fast ($D_{3,i}$ ≈ 16–17 μm²s⁻¹, $D_{3,c}$ ≈ 26–30 μm²s⁻¹) diffusion were largely comparable between all four morphogens, yet overall higher in cavities (Fig. 3c, Supplementary Table 1 and Supplementary Table 2). The fast diffusion coefficients in cavities were comparable to those measured previously with FCS, which were reported in a range between ~30 μm²s⁻¹ and ~60 μm²s⁻¹ for Nodal and Lefty[2,14,25]. Interestingly, Cyclops showed lower diffusion coefficients in the immobile and intermediate diffusion classes, in agreement with its punctate localization pattern (Supplementary Fig. 1) and potentially indicating higher confinement of this morphogen. Diffusion of the HaloTag alone (sec-Halo) was faster than any morphogen in both interfaces and cavities in accord with its smaller size, whereas the HaloTag fused to GFP showed diffusion coefficients similar to those of the morphogens (Supplementary Fig. 4, Supplementary Table 1 and Supplementary Table 2).

The fraction of immobile molecules in interfaces and cavities was considerably larger for Cyclops ($A_{1,i}$ in interfaces 44%, $A_{1,c}$ in cavities 22%) and Squint ($A_{1,i}$ ≈ 35%, $A_{1,c}$ ≈ 9%) than for Lefty1 ($A_{1,i}$ ≈ 21%, $A_{1,c}$ ≈ 5%) and Lefty2 ($A_{1,i}$ ≈ 24%, $A_{1,c}$ ≈ 6%) (Fig. 3d), reflecting the higher probability of short jump distances for Nodals (Fig. 3a). Correspondingly, while the fraction of molecules with intermediate diffusivity was similar for Nodals and Leftys, the fraction of fast-diffusing molecules in interfaces and cavities was larger for Lefty1 ($A_{3,i}$ ≈ 40%, $A_{3,c}$ ≈ 64%) and Lefty2 ($A_{3,i}$ ≈ 37%, $A_{3,c}$ ≈ 61%) than for Cyclops ($A_{3,i}$ ≈ 17%, $A_{3,c}$ ≈ 48%). The fraction of fast-diffusing Squint molecules was lower than that of Leftys in interfaces, but comparable to the fraction of fast-diffusing Leftys in cavities ($A_{3,i}$ ≈ 31%, $A_{3,c}$ ≈ 63%) (Fig. 3d, Supplementary Table 1 and Supplementary Table 2). Taken together, our analysis of the diffusion data confirms that the fast diffusion coefficients of Nodals and Leftys are comparable[2,14,25] and suggests that the differential mobility of Nodal and Lefty reported previously[2,25,37,39] originates from a higher retention of Nodal in an immobile state. This retention is more efficient in interfaces, where the fractions of immobile molecules are larger and diffusion is slower than in cavities.

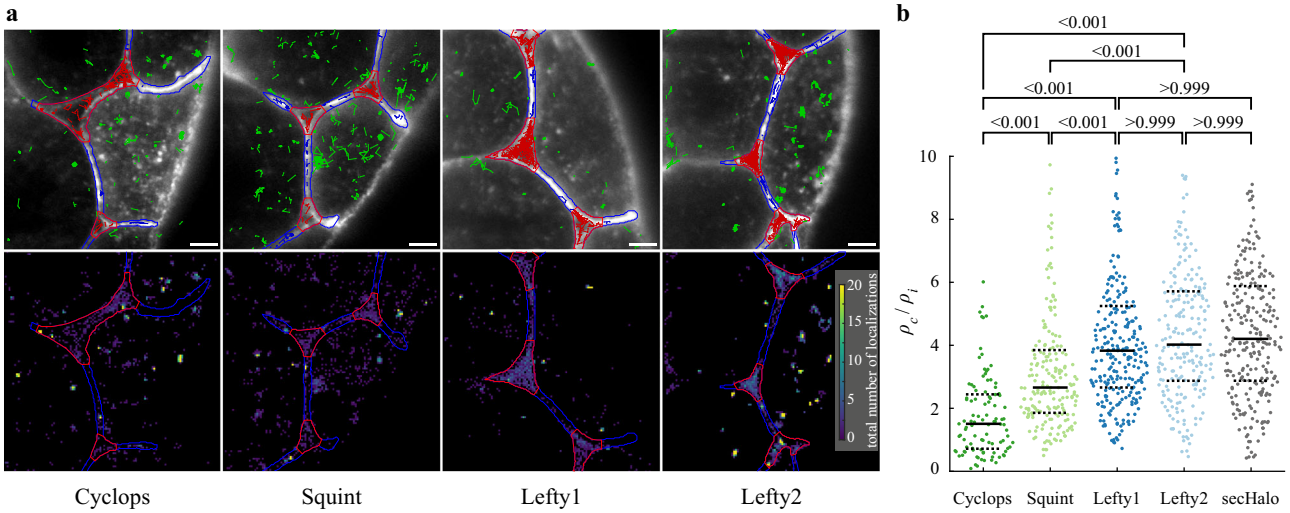

Fig. 2 | Localization of morphogens in cell-cell interfaces and extracellular cavities. a Top: Overlay of the memGFP signal, the manually curated ROI separating cell-cell-interfaces (blue, I) and extracellular cavities (red, C); tracks assigned to interfaces (blue), cavities (red) and not assigned (green) are also shown. Bottom: Tracking-and-localization-microscopy (TALM) image showing the total number of localizations over 1000 frames or 11.7 s in each 2 × 2 pixel bin; scale bar: 5 μm. **b** Ratios of localization densities in cavities and interfaces calculated for each movie (for statistics see Supplementary Table 5). Values above 10 are not displayed (3.4% of all movies). *p*-values (Cyclops - Squint, Cyclops - Lefty1, Cyclops - Lefty2, Squint - Lefty1, Squint - Lefty2: <0.001; Lefty1 - Lefty2, Lefty1 - secHalo, Lefty2 -secHalo: >0.999) were calculated using the Kruskal-Wallis-Test. Solid black lines indicate the median values, dashed black lines the 0.25 and 0.75 quantiles. Source data are provided as a Source Data file for Fig. 2b.

To explore the differential diffusion properties in interfaces and cavities, we calculated the angles within a track spanned by three consecutive localizations[59,60]. We only considered angles where the two jumps making up the angle covered a minimum distance of 1 px (166 nm), much larger than the localization error. In interfaces, both Nodal and Lefty showed an anisotropic angle distribution with a high probability to continue or reverse the previous direction (Fig. 3e). In contrast, the angle distribution was more isotropic in cavities. The angle distributions of both interfaces and cavities exhibited a prominent contribution of reverse motion (Supplementary Fig. 5a). In interfaces, jumps were mostly oriented along the direction of interface borders and the probability for a subsequent jump to go into the reverse direction strongly increased with the angle of the preceding jump to the interface border (Supplementary Fig. 5b, c, top). These effects were less prominent for cavities (Supplementary Fig. 5b, c, bottom). Overall, these observations reflect hindered diffusion in limited space, which is more restrictive in interfaces than in cavities.

Nodals bind in the extracellular space with retention times of ten to twenty seconds

To test the idea that Nodals are trapped in cell-cell interfaces, we next characterized the residence times of Cyclops and Squint in the bound state. We used time-lapse imaging, where two images are separated by dark times of different duration (Fig. 4a, Material and Methods). With this illumination scheme, it is possible to increase the measurable range of binding times and to resolve several photobleaching-corrected dissociation rate constants[47,61–63]. We chose frame cycle times of 11.7 ms, 58 ms, 199 ms and 1006 ms and were thus able to observe binding events of tens of seconds along the membrane for both Cyclops and Squint (Fig. 4).

We identified bound molecules in interfaces and cavities using a small tracking radius in combination with a minimum number of survived frames in the nearest neighbor algorithm[47] (Material and Methods). We then collected the durations of binding events for each time-lapse condition in survival-time distributions (Fig. 4c, Material and Methods). The distributions extended to longer durations for Cyclops than for Squint, indicating longer binding times for Cyclops. For the longest time-lapse condition, where photobleaching is not limiting, few binding events survived throughout the whole acquisition time (5% for Cyclops, 1.4% for Squint). Thus, our analysis will slightly underestimate the binding times. Lefty1 and Lefty2 exhibited much-reduced occurrences and durations of binding events in movies of 11.7 ms frame cycle time, comparable to those of the HaloTag alone (Supplementary Fig. 6a). Together with the low bound fractions obtained from the diffusion analysis, this indicates that binding in the extracellular space has a minor influence to the overall diffusion properties of Leftys, and we therefore refrained from quantifying their binding times. For Cyclops and Squint, we analyzed the survival-time distributions with our genuine rate identification (GRID) tool, which can reveal spectra of dissociation rates from fluorescence survival-time distributions by solving the inverse Laplace transformation[61] (Material and Methods). We obtained four dissociation rate clusters for both Cyclops and Squint (Fig. 4d), from which the inversely correlated binding times can be calculated. The longest binding time, corresponding to the slowest dissociation rate cluster, was 16.2 ± 2.6 s (mean ± s.d. of resampled spectrum), comprising 50.0 ± 4.1% (mean ± s.d. of resampled spectrum) of bound molecules for Cyclops. For Squint, we found shorter binding times of 11.0 ± 2.2 s comprising 28.9 ± 4.8% of bound molecules (Fig. 4e), consistent with the larger effective diffusion coefficient, the less punctate distribution compared to Cyclops[25] (Supplementary Fig. 1), and in good agreement with the previous dissociation rate predictions of 18 s for Cyclops and 4 s for Squint[25].

Some of the Cyclops and Squint molecules that we identified as bound showed slow diffusive motion along the membrane (Fig. 4b, Supplementary Movies 6, 7). This observation is in agreement with a fraction of slowly diffusing morphogens obtained in the analysis of molecular jump distances (Fig. 3c, d). Such motion might correspond to the diffusion of morphogen-receptor complexes within the membrane. To test this idea, we quantified the diffusion coefficients of bound morphogens by analyzing the mean-squared displacement (MSD) of bound tracks for different time intervals (Supplementary Fig. 7, Supplementary Movies 6, 7, Material and Methods). The majority of diffusion coefficients of both Cyclops and Squint was below 0.5 $\mu m^2 s^{-1}$ (Fig. 4f), indeed similar to previous quantifications of receptor diffusion in membranes[64,65]. Bound Squint molecules exhibited a higher tendency to diffuse along the membrane than bound

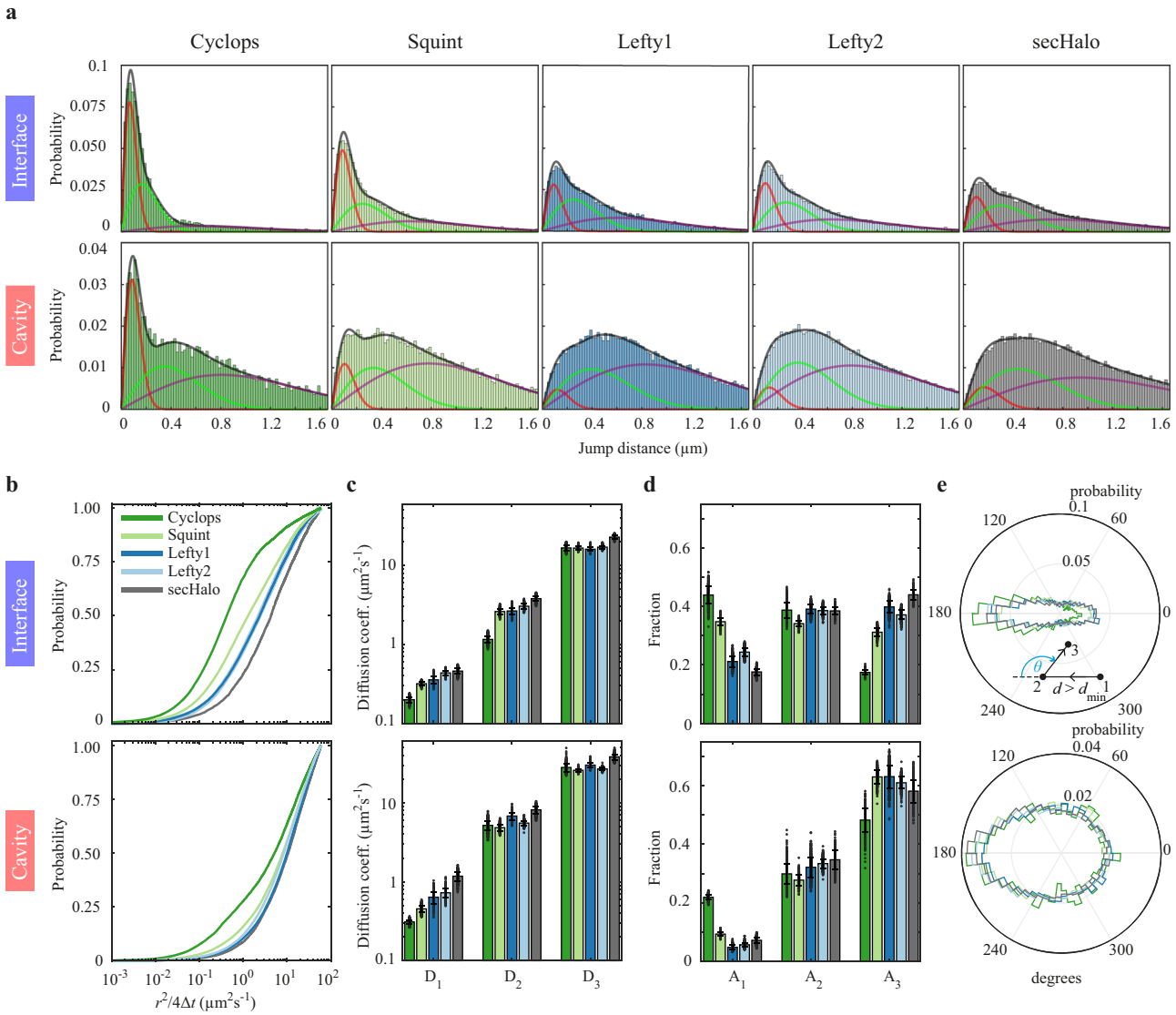

Fig. 3 | Mobility of morphogens in cell-cell interfaces and extracellular cavities. **a** Distribution of jump distances within single-molecule tracks in interfaces and cavities for the indicated morphogen and sec-Halo. Lines represent a three-component diffusion model (black) and the individual components (red, green, purple). **b** Cumulative distributions of jump distances. **c)** Diffusion coefficients and (**d**) fractions of the three-component diffusion model (Supplementary Table 1, 2). Data are presented as mean values ± s.d. from 500 resamplings with randomly selected 50% of the data. **e** Distribution of angles between two consecutive track segments. For full experimental statistics see Supplementary Table 5. Source data are provided as a Source Data file.

Cyclops molecules, which were more often confined to a small area, again consistent with the larger effective diffusion coefficient and less punctate distribution compared to Cyclops[25] (Supplementary Fig. 1).

Overexpression of oep increases the fraction of immobile Squint molecules

While our single-molecule imaging approach enables us to classify bound molecules by their time they spend within a certain area, the origin of binding of individual tracks remains obscure. Binding might reflect both specific interactions with receptors or unspecific retention by the tortuous environment. Nodals are well known to bind to the EGF-CFC co-receptor Oep[36,66], which is essential for Nodal signaling[67]. Furthermore, the signaling range and distribution of Squint was shown to be extended in the absence of *oep*[40,41], but a direct effect of Oep on Nodal dispersal at the nanometer-to-micrometer scale has not yet been directly demonstrated. To test whether immobile Squint in our experiments was due to binding to Oep, we co-injected 0.3 pg, 3 pg and 30 pg of Oep-encoding mRNA together with the Squint-HaloTag construct and compared the diffusion properties of Squint in conditions of *oep* overexpression with those of endogenous Oep levels. We found that the immobile fraction of Squint increased in interfaces and cavities, from 35% to 50% and from 9% to 25% respectively (Fig. 5b and Supplementary Fig. 8a), while the diffusion coefficients remained unaffected (Fig. 5a). Thus, our data show on a single-molecule level that Squint at least to some extent binds to Oep, which can directly hinder the diffusion of Nodal by transiently trapping the morphogen on the membrane.

Clarifying origins of differential morphogen localization using agent-based modeling

Interestingly, we found a higher fraction of immobile molecules combined with slower diffusion in cell-cell interfaces compared to extracellular cavities. These findings would intuitively suggest that morphogens should accumulate in interfaces, not cavities. However – surprisingly, and in contrast to intuition – we found that all secreted molecules were more likely to be found in extracellular cavities rather than in cell-cell interfaces. Mathematical modeling can help reveal the

https://doi.org/10.1038/s41467-022-33704-z

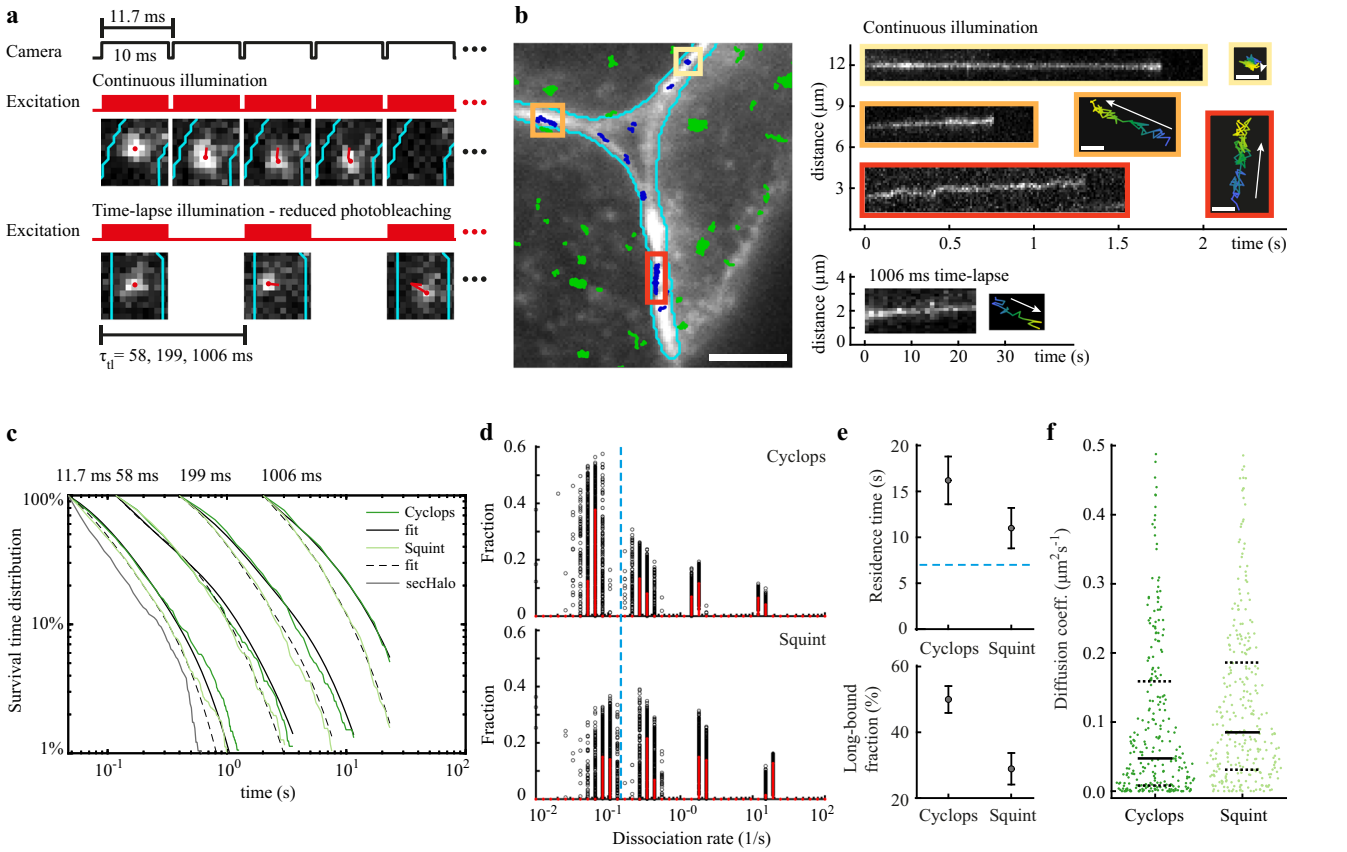

Fig. 4 | Residence times of Cyclops and Squint in the extracellular space. **a** Overview of camera exposure and laser excitation patterns in time-lapse illumination experiments and representative images of single molecules overlaid with tracks (red) and the boundary of the extracellular region (cyan). **b** Left panel: Overlay of the memGFP signal (white) with the boundary of the extracellular region (cyan) and tracked Cyclops molecules from a movie with continuous illumination. Bound Cyclops molecules in the extracellular space shown in blue, intracellular molecules shown in green. Scale bar: 5 µm. Right panels: continuous illumination kymographs of the yellow, orange and red regions indicated in the left image and below a kymograph from a 1006 ms time-lapse movie as well as position plots of the tracks color-coded according to start (blue) and end (yellow) times. Scale bar: 0.3 µm. **c** Survival-time distributions of bound morphogens and sec-Halo in the time-lapse conditions indicated on top (dark and light green lines) and survival time functions obtained by GRID for Cyclops (solid black lines) and Squint (dashed black lines). **d** State spectra of dissociation rates of Cyclops and Squint obtained by GRID using all data (red bars) and 500 resampling runs with randomly selected 80% of data (black data points) as an error estimation of the spectra. The dashed blue line indicates the boundary for long-bound molecules of 0.15 s^{-1}. **e** Residence times of Cyclops and Squint (top panel) and the corresponding fraction (bottom panel) obtained from the slowest dissociation rate cluster of the state spectra. Error bars denote s.d. of the resampled spectra in **d**). The dashed blue line indicates the boundary for long-bound molecules of 7 s. **f** Diffusion coefficients obtained from fitting the first 10 points of a mean-squared displacement plot of bound Cyclops and Squint molecules recorded for at least 20 frames ($n_{tracks,cyc}$ = 283, $n_{tracks,squ}$ = 337). Values above 0.5 µm²s^{-1} were discarded (11%). Solid black lines indicate the median values, dashed black lines are the 0.25 and 0.75 quantiles. For full experimental statistics see Supplementary Table 6. Source data are provided as a Source Data file for Fig. 4**c**, **d**, **f**.

origins of non-intuitive behaviors in biological systems[37,39,68]. We therefore devised a minimal model of single-molecule dispersal in order to test whether geometric constraints and binding might suffice to explain the cavity enrichment, or whether more complicated molecular mechanisms such as restricted entry control into interfaces have to be invoked.

To simulate single-molecule dispersal, we chose an agent-based model in a realistic zebrafish blastoderm geometry that directly relates to our experimental observations. We used an experimentally determined binary mask of extracellular space as two-dimensional simulation geometry (Fig. 6a). Single morphogens were simulated as "drunken sailors"[2] performing a random walk in the extracellular space. To simulate immobile and freely diffusing single molecules, we used jump sizes at each simulation step based on the measured diffusion coefficients for bound (0.5 µm²s^{-1}) and free (30 µm²s^{-1}) states (see Material and Methods). A single molecule became bound when it detected a receptor in proximity (≤ 20 nm). The simulated tracks for Nodals (Fig. 6a, blue track) and Leftys (Fig. 6a, red track) closely resembled the experimental observations. In particular, our simulation was able to recapitulate higher bound fractions in interfaces compared to cavities, differential angle distributions in both compartments as well as higher localization density in cavities compared to interfaces (Fig. 6b, c, Supplementary Fig. 9a–f).

Next, we systematically varied key parameters that might modulate morphogen localization in the extracellular space. A parameter screen revealed that receptor density (σ), residence time (τ), and width of the extracellular space in terms of extracellular fraction (η) are important determinants of extracellular molecule localization (Fig. 6b). As expected, strong binding ($\sigma > 0.5$ µm^{-1} and $\tau > 6$ s) yielded localization in cell-cell interfaces (Fig. 6b, c and Supplementary Fig. 9a). Surprisingly, for low binding ($\sigma < 0.5$ µm^{-1} and $\tau < 6$ s) extracellular molecules tended to localize in cavities. This tendency was augmented by decreasing the width of the extracellular space, suggesting an important role of tissue geometry for morphogen localization (Fig. 6b and Supplementary Fig. 9b). We verified the accumulation in cavities for multiple additional experimentally derived simulation geometries (Supplementary Fig. 9c). The narrow width of interfaces concentrated extracellular molecules to cell surfaces, thereby increasing the probability of interactions with receptors. This behavior resulted in a higher bound fraction in interfaces

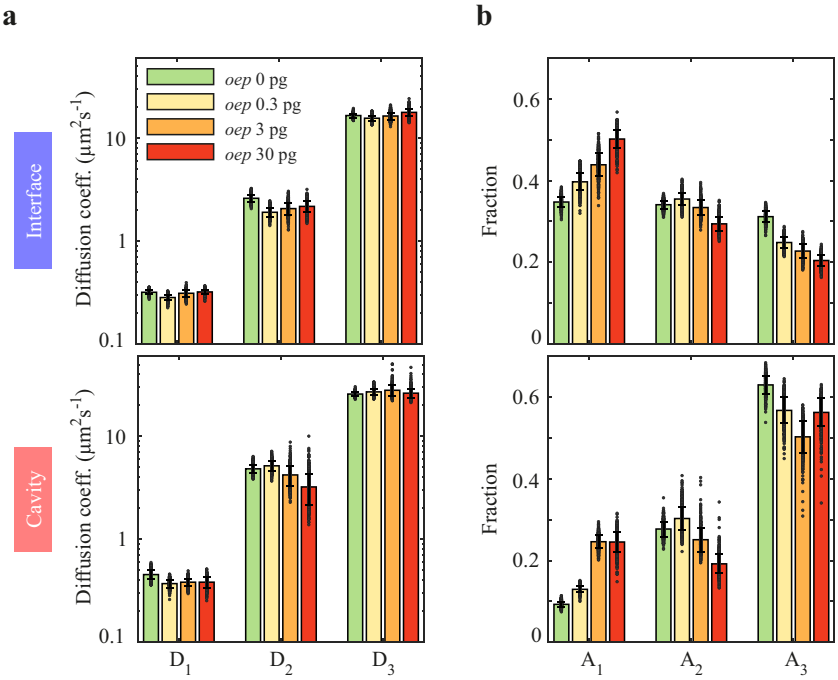

Fig. 5 | Mobility of Squint decreases with overexpression of oep. a Diffusion coefficients and (**b**) fractions of the three-component diffusion model in interfaces and cavities for Squint at different amounts of mRNA encoding Oep. Data are represented as mean values ± s.d. from 500 resamplings with randomly selected 50% of the data. For full experimental statistics see Supplementary Table 5. Source data are provided as a Source Data file.

compared to cavities despite similar receptor spacing in both compartments (Fig. 3d, Supplementary Fig. 9d, e).

Our simulations showed that the surprising enrichment of extracellular molecules in cavities can be explained purely by geometric constraints, and predicted that the diffusing molecules could be pushed out of this compartment into interfaces by increasing receptor density homogeneously in the tissue (Fig. 6c). To test this prediction, we measured the distribution of extracellular GFP in zebrafish embryos with different levels of membrane-tethered GFP-binding nanobodies[69]. Similar to our TALM findings (Figs. 1d, 2), secreted GFP was mainly distributed in cavities ($\rho_c/\rho_i > 2$) in case of no or low amount (25 pg) of injected nanobody mRNA. With high nanobody expression (100 pg), the GFP signal became more enriched in cell-cell interfaces ($\rho_c/\rho_i < 1$) (Fig. 6d and Supplementary Fig. 9g), in accordance with our simulations. Our results suggest that geometric constraints, such as the width of interfaces, bias morphogens to preferably localize in extracellular cavities. Strong binding to receptors can overcome this bias to increase morphogen localization in cell-cell interfaces.

Together, our single-molecule measurements and simulations provide strong support for the hindered diffusion model, in which differences in effective diffusivities between Nodals and Leftys are an emergent property arising from differential binding of morphogens in a compartmentalized extracellular environment.

Discussion

Multiple mechanisms have been proposed to underlie the dispersal of morphogens for developmental patterning, from simple extracellular diffusion to repeated secretion and cellular uptake, filopodia-based distribution, and signal relay[2,9,13,14,30,70–77]. In particular, the hindered diffusion model postulating free diffusion intermitted by transient binding on cell surfaces has gained popularity[7]. Dispersal models have been inferred from observations of large averaged morphogen ensembles and bulk mobility measurements using techniques such as FCS or FRAP. However, the resulting data has to be carefully interpreted because bulk measurements may only provide indirect evidence for transport mechanisms[38,78–80]. To directly determine the mechanisms of transport, single-molecule experiments are necessary, but these measurements have so far not been performed for any morphogen in a living embryo.

We performed single-molecule measurements of individual Nodal and Lefty morphogens in developing zebrafish embryos. Our results suggest that morphogens undergo fast diffusive motion in extracellular cavities, whereas diffusion is more constrained and slower in cell-cell interfaces. The coefficients of fast diffusion were similar for Nodals and Leftys. In contrast, Nodals, and in particular the ultra-short-range morphogen Cyclops, exhibited a larger fraction of molecules bound to the cell membrane than Leftys. Our direct single-molecule observations are consistent with previous inference from indirect bulk measurement techniques such as FCS and FRAP[2,14,25,38], and here we show both diffusion and reversible morphogen binding with single-molecule resolution in strong support of the influential hindered diffusion model.

Surprisingly, we observed an unexpected accumulation of morphogens in extracellular cavities, although binding interactions were more pronounced in cell-cell interfaces than in cavities. Using agent-based simulations of morphogen transport, we found that the architecture of the extracellular space with large cavities and narrow cell-cell interfaces favors heterogeneous distribution of morphogens and their accumulation in cavities. Our simulations predicted that binding to receptors would counteract this effect, and we validated this idea by measuring the distribution of extracellular GFP in zebrafish embryos with different levels of membrane-tethered artificial GFP-binding receptors[69]. In addition, stronger or more frequent binding, implemented by longer residence times or higher receptor densities, respectively, retained morphogens in cell-cell interfaces. Furthermore, the narrow width of interfaces contributed to enhanced binding by concentrating morphogens to cell surfaces.

The influence of tissue architecture on effective diffusion coefficients has been discussed in previous studies[2,14,38]: Numerical simulations and experiments using FCS and FRAP with secreted GFP inferred a reduction of effective diffusion compared to free diffusion by a factor of approximately two-fold[25,38], rationalizing the idea that

https://doi.org/10.1038/s41467-022-33704-z

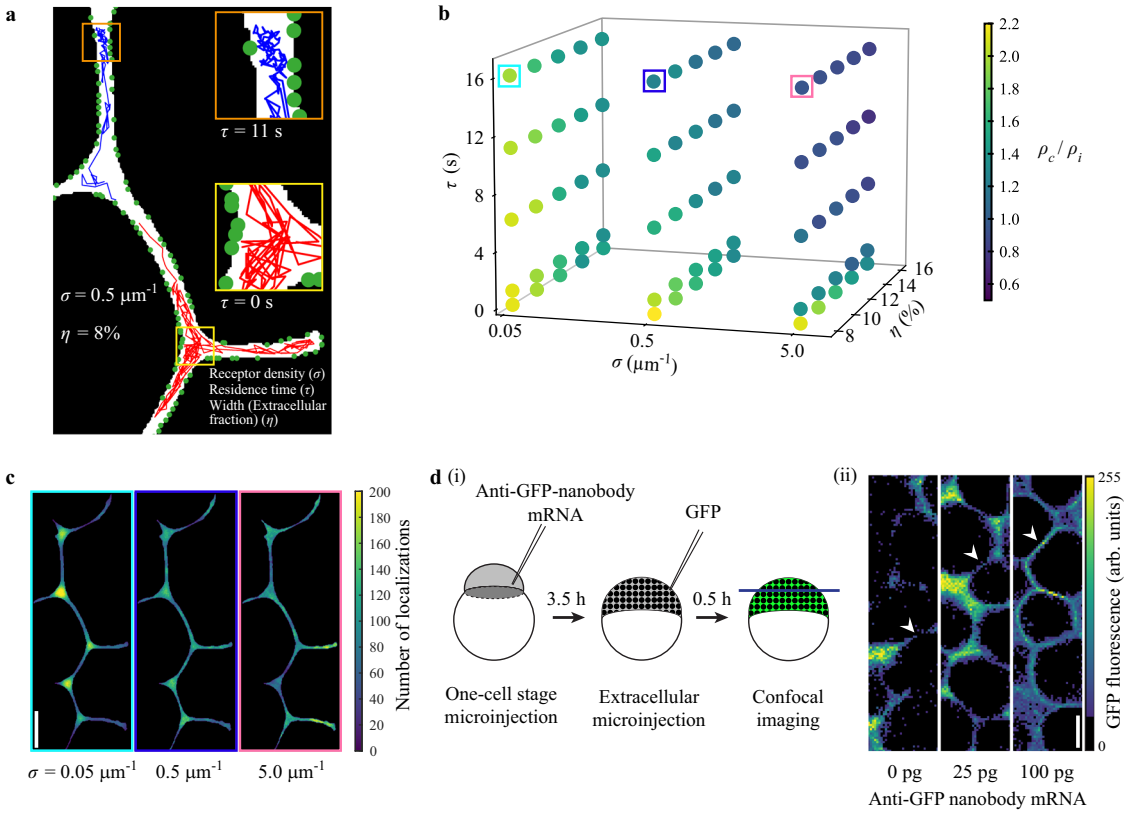

Fig. 6 | An agent-based model reveals key parameters affecting morphogen behavior in the extracellular space. a Illustration of the model with a section of the two-dimensional simulation geometry showing simulated tracks (200 steps or 2 s) for two morphogens with residence times τ of 11 s (blue track) and 0 s (red track), respectively. Green circles indicate receptors. The receptor density σ is given as the number of receptors per μm of membrane length. The width of the extracellular region in terms of extracellular fraction is given by the parameter η. Morphogens are allowed to move in the extracellular space (white). A morphogen becomes 'immobile' or bound upon detecting a receptor in proximity and performs smaller jumps corresponding to the bound diffusion coefficient. **b** Three-dimensional scatter plot of simulated parameter combinations showing corresponding localization density ratios (ρ_c/ρ_i). Five residence times τ (0 s, 1 s, 6 s, 11 s, and 16 s), three receptor densities σ (0.05 μm^{-1}, 0.5 μm^{-1}, and 5.0 μm^{-1}) and five extracellular fractions η (8%, 10%, 12%, 14%, and 16%) were simulated. **c** Localization density plots of simulated morphogens with increasing receptor densities σ (0.05 μm^{-1}, 0.5 μm^{-1}, and 5.0 μm^{-1}; τ = 16 s, η = 8%). Frame colors correspond to colored boxes in **b**). **d** (i) Schematic depicting the experimental procedure to acquire confocal images of GFP localization in zebrafish embryos. (ii) Representative images of regions of interest used for GFP signal measurements. Cell-cell interface regions are indicated by arrowheads. Scale bars in c and **d** (ii) are 10 μm. n = 5 different regions of interest were measured per embryo and treatment; see Supplementary Fig. 9g for detailed statistical analysis. Source data are provided as a Source Data file for Fig. 6**b**.

secreted molecules have to bypass other cells compared to diffusion in free space. Our direct single-molecule measurements and simulations suggest a molecular mechanism of long-range morphogen spreading in a tortuous environment, where diffusion predominantly occurs in a network of extracellular cavities. This mechanism differs from the morphogen dispersal mode recently described in a two-dimensional human embryonic stem cell culture system, in which – unlike in the three-dimensional embryo context – Nodal molecules presumably cannot be retained in the extracellular space and are instead lost into the culturing medium[75]. Cavity accumulation in the loosely packed zebrafish blastoderm may allow for the rapid morphogen transport required to accomplish tissue patterning within the short, hour-long timescales during early embryogenesis. Dynamic changes in tissue geometry and cell numbers during development will likely influence morphogen diffusion. For instance, cell-rounding and loss of cell-cell adhesion during zebrafish morphogenesis could increase the extracellular cavity fraction to allow for faster diffusion[49,81]. Conversely, during later zebrafish somitogenesis, fluid-to-solid jamming transitions in the tissue architecture might severely inhibit fast extracellular diffusion[82]. Depending on the spatiotemporal scale of patterning, different tissues require different gradient ranges, and strongly hindered diffusion in densely packed epithelia without large extracellular cavities may allow for the slow day-long patterning timescales observed in tissues such as the *Drosophila* wing disc[2]. Additionally, changes in binding partner numbers could alter the bound morphogen fraction to further influence morphogen diffusion.

We observed that binding differed between the Nodals Cyclops and Squint. First, the bound fractions were higher for Cyclops than for Squint, and binding times of Cyclops were on average 5 s longer. This contrasts with measurements showing that Squint binds to the Type II receptor Acvr2b-a with higher affinity than Cyclops[14]. Second, we observed that bound Squint molecules frequently exhibited slow diffusion along the membrane, while bound Cyclops molecules were mostly localized within a small area and effectively immobilized. Our single-molecule measurements are oblivious to the molecular identity of the morphogen binding partners and therefore represent a neutral description of overall cell surface binding. The differing mobilities of bound Cyclops and Squint might reflect differences in how both members of Nodal bind to components of the extracellular matrix. There are numerous potential extracellular binding partners, for example the EGF-CFC co-receptor Oep or other immobilized diffusion regulators such as heparan sulfate proteoglycans[7,8,17–21,69,83]. The different degrees of hindered diffusion that we observed – shorter residence times and lower fraction of bound Squint compared to Cyclops – are likely to underlie the different ranges of Nodal gradients (short-to-mid range for Squint and ultra-short range for Cyclops)[25,84–87].

Interestingly, while we also observed labeled Nodals and Leftys in the cytoplasm (excluded in the present analysis) in addition to their extracellular localization, we only rarely (in approximately 3 out of 100 movies) observed events where single molecules clearly passed the membrane and entered the cytoplasm. This indicates that internalization of Nodals/Leftys is a rare event, as opposed to the prolonged binding of Nodals on the cell surface, which provides a possible explanation for the hour-long half-lives of Nodals/Leftys in living zebrafish embryos[25,41,88]. Rare internalization also contrasts with the transcytosis mechanism described for the TGF-β superfamily ligand Dpp in *Drosophila*, in which repeated rounds of exocytosis and endocytosis lead to morphogen dispersal[72]. The differences in the dispersal mechanisms might be explained by the different time scales required for patterning of the zebrafish embryo (hours) and the *Drosophila* wing disc (days)[2].

In summary, we propose that Nodal and Lefty spreading follows a compartmentalized hindered diffusion model, in which cell-cell interfaces provide a confined, obstructive environment with restricted diffusion in particular for Nodal, whereas long-distance spreading of morphogens occurs within cavities between cells.

Methods

Zebrafish husbandry

The research was performed in accordance with all relevant ethical regulations. Wild Indian Karyotype (WIK) and TE zebrafish were maintained according to the guidelines of the EU directive 2010/63/EU, the German Animal Welfare Act and the State of Baden-Württemberg (Germany) and approved by the Regierungspräsidium Tübingen and the Regierungspräsidium Freiburg. Zebrafish were maintained exclusively for breeding and experiments were performed exclusively on zebrafish embryos.

Generation of constructs

The designs for the HaloTag-tagged zebrafish Nodals Squint and Cyclops, Lefty1 and Lefty2 as well as secreted HaloTag were based on previously published GFP fusion constructs[25].

To generate pCS2-2xHA-HALO-3xGS, HaloTag was isolated using primers containing a tandem HA-Tag and primers containing a triple GS-linker, which was then cloned into the BamHI and XbaI sites of the pCS2 backbone[42].

HaloTag was then amplified from pCS2-2xHA-HALO-3xGS, and fusion constructs for Nodals and Leftys were generated using splicing-by-overlap-extension PCR[89–91] using the pCS2 backbone. The following primers were used:

For pCS2-2xHA-HALO-3xGs: GATCGGATCCATGTACCCATACGATGTTCCAGATTACGCTGGATATCCATATGATGTTCCAGATTATGCTCGAGGAGCAGAAATCGGTACTGGCTT, GATCATCTAGAGATCGAGGCGCGCCGATCGATTAATTAAGCTTCCGGAGCCAGAACCTGAGCCGGAAATCTCGAGCG

For pCS2-Squint-HaloTag: GCAGGATCCCATCGATGCCACCATGTTTTCCTGCGGGCTCC, GGCTCGAGAGGCCTTGAATTCTCAGTGGCAGCCGCATTCTGC, CTCGAGATTTCCGGCGGATCCGCAGCAGCAG, CTGCTGCTGCGGATCCGCCGGAAATCTCGAG, GATCCACCGGTACCACCGGAGCAGAAATCGGTAC, GTACCGATTTCTGCTCCGGTGGTACCGGTGGATC

For pCS2-Cyclops-HaloTag: GCAGGATCCCATCGATGCCACCATGCACGCGCTCGGAGTCGC, GGCTCGAGAGGCCTTGAATTCTCACAGGCATCCGCACTCCTC, GCCGCCGGGGGCCAGGAGCAGAAATCGGTAC, GTACCGATTTCTGCTCCTGGCCCCCGGCGGC, CTCGAGATTTCCGGCCCTGTCAGGAGCCCAG, CTGGGCTCCTGACAGGGCCGGAAATCTCGAG

For pCS2-Lefty1-HaloTag: GCAGGATCCCATCGATGCCACCATGACTTCAGTCCGCGCCG, CTATAGTTCTAGAGGCTCGAGTCAGCCGGAAATCTCGAG, GATCCACCGGTCGCCACCGGAGCAGAAATCGGTAC, GTACCGATTTCTGCTCCGGTGGCGACCGGTGGATC

For pCS2-Lefty2-HaloTag: GCAGGATCCCATCGATGCCACCATGGCTCTGTTCATCCAGC, CTATAGTTCTAGAGGCTCGAGTCAGCCGGAAATCTCGAG, CCCTCCAGTCCTGGGCGGAGCAGAAATCGGTAC, GTACCGATTTCTGCTCCGCCCAGGACTGGAGGG

To generate pCS2-secreted-HaloTag, HaloTag was amplified with the primers GATCCACCGGTACCACCGGAGCAGAAATCGGTAC and CTATAGTTCTAGAGGCTCGAGTCAGCCGGAAATCTCGAG and cloned by restriction digest using AgeI and XbaI.

pCS2-secreted-HaloTag-GFP was generated based on pCS2-secreted-HaloTag. GFP was fused to the C-terminus of the HaloTag (separated by a GS linker) via splicing-by-overlap-extension PCR with the following primers: CCACCGGTACCACCGGAGC, GCCTTGAATTCTCACTTGTACAGCTCGTCC, CTCGCCCTTGCTCACGGATCCGCCGGAAATC, GATTTCCGGCGGATCCGTGAGCAAGGGCGAG. The fused construct was cloned by restriction digest using AgeI and XbaI afterwards.

mRNA synthesis

For capped mRNA synthesis, pCS2-Cyclops-HaloTag, pCS2-Squint-HaloTag, pCS2-Lefty1-HaloTag, pCS2-Lefty2-HaloTag, pCS2-secreted-HaloTag, pCS2-Squint-GFP[25] and pCS2-mem-GFP[44] were linearized with NotI, and a mMESSAGE mMACHINE SP6 Kit (Invitrogen) was used for in vitro transcription according to the manufacturer's recommendations. To generate mRNA encoding Oep, pCDNA3-oep-FLAG was linearized with NotI and transcribed using an mMESSAGE mMACHINE T7 Kit (Invitrogen) according to the manufacturer's recommendations.

Quantitative reverse transcription PCR (qRT-PCR)

To validate the biological activity of the Halo-tagged Nodals and Leftys, we performed qRT-PCR assays for the Nodal target gene *goosecoid* (*gsc*). The previously characterized GFP fusion constructs[25] were used as positive controls, and the mRNAs for each morphogen and their corresponding fusions were synthesized in parallel. The qRT-PCR was performed as described in[25] with the following changes: The total RNA was extracted using NucleoZOL (Macherey-Nagel). Up to 1 µg of purified total RNA was used to synthesize cDNA using the SuperScript III First-Strand Synthesis SuperMix (Thermo Fisher). The Platinum SYBR Green qPCR SuperMix-UDG (Thermo Fisher) was used in a LightCycler® 96 Instrument (Roche) for 45 cycles using 2-step amplification. Quantification cycle (Cq) values were obtained using the LightCycler® 96 software.

Confocal fluorescence microscopy

TE embryos were injected at the one-cell stage with 50 pg of mRNA encoding secreted-HaloTag, Squint-HaloTag or Cyclops-HaloTag or 60 pg of mRNA encoding Lefty1-HaloTag or Lefty2-HaloTag. Embryos were proteolytically dechorionated using 10 mg Pronase (Sigma Aldrich) in 10 ml Danieau's medium and washed with Danieau's medium to remove the Pronase. The embryos were then incubated in a 1:5000 dilution of TMR HaloTag Ligand (5 mM; Promega) in Danieau's medium. After 30–60 min at 28 °C, they were rinsed with embryo medium twice and mounted in a glass bottom dish using 1.5% low-melting agarose. Imaging was performed with an LSM 780 NLO (ZEISS) system using an LD LCI Plan-Apochromat 25×/0.8 Imm Korr DIC objective to acquire animal views at a depth of approximately 35 µm into the tissue.

Sample preparation for single-molecule imaging

Embryos were dechorionated directly after fertilization using 10 mg Pronase (Sigma Aldrich) in 10 ml Danieau's medium and washed with Danieau's medium to remove the Pronase. To express morphogen constructs, embryos were injected at the 1-cell stage with 1 pg of mRNA encoding Squint-HaloTag, Lefty1-HaloTag, Lefty2-HaloTag, secreted HaloTag, or 2 pg of mRNA encoding Cyclops-HaloTag together with

10 pg of mRNA encoding memGFP into the animal pole. The diameter of the injection mix droplet was measured with a stereo microscope (Olympus SZX2-ZB10) equipped with a camera (CAM-SC50) and the CellSens Entry 2.3 (Build 18987) imaging software (Olympus), and set to 124 μm, corresponding to a droplet volume of 1 nl, by adjusting the injection duration. For Oep experiments, 1 pg of mRNA encoding HaloTag-Squint was injected together with 0.3 pg, 3 pg, or 30 pg of mRNA encoding Oep and 10 pg of mRNA encoding memGFP.

To label the HaloTag, embryos at the 2-cell stage were placed into two separate glass tubes, and most of the embryo buffer was removed such that embryos were just covered sufficiently. 1 ml of 5 nM HaloTag-JF549[45] dye solution was then added into one of the tubes and 10 nM HaloTag-JF549 dye solution into the other tube and incubated for 30 min. After staining, zebrafish were washed with Danieau's buffer, followed by two additional washing steps each after 15 min.

Embryos were incubated at room temperature (22 °C). We monitored the transition from the 64-cell to the 128-cell stage and visually identified synchronously developing embryos. 6–8 embryos at the 128-cell stage stained with 10 nM dye solution were then mounted onto the microscope by placing them into a glass bottom dish with a thickness of 0.17 mm (Delta T, Bioptechs, Butler, PA). If the density of visible fluorescent molecules was too high, the mounted embryos were exchanged with embryos stained with 5 nM dye solution. On the microscope, embryos grew further at room temperature. Transitions between embryo stages were counted by identifying cytoplasmic divisions (cytokinesis events), when the GFP-stained cell membrane grows inward until cell division. Fluorescence imaging was stopped when embryos reached the sphere stage.

Reflected light-sheet microscopy (RLSM)

Single-molecule imaging of live zebrafish embryos was carried out using a custom-built reflected light-sheet microscope[63] with modifications to image live zebrafish embryos[42]. The microscope was built around a commercial Nikon TI microscope body equipped with a water-immersion objective (60× 1.20 NA Plan Apo VC W, NIKON), a dichroic mirror (F73–866/F58–533, AHF), an emission filter (F72–866/F57–532, AHF), a notch filter (F40–072/F40–513, AHF) and an EM-CCD Camera (iXon Ultra DU 897U, Andor). Fluorescence light was post-magnified by a factor of 1.5× before reaching the camera chip, which resulted in a pixel size of 166 nm. The microscope was controlled using the NIS Elements software Version 4.40.00 64 bit (Nikon) and a NIDAQ data acquisition card (National Instruments).

Reflected light-sheet illumination was achieved using a custom-built tower mounted above the sample dish. AOTF (AOTFnC-400.650-TN, AA Optoelectronics) controlled laser light of 488 nm (IBEAM-SMART-488-S-HP, 200 mW, Toptica) and 561 nm (Jive 300 mW, Cobolt) was coupled into the tower via a single-mode fiber, where it was focused by a cylindrical lens into the back-focal plane of a water-dipping objective (40 × 0.8 NA HCX Apo L W, Leica) and subsequently reflected by the chip of an AFM cantilever (custom-coated cantilever based on model: HYDRA2R-100N-TL-20 but with both sides coated in 40 nm Al). The resulting light-sheet had a thickness of approximately 3 μm. The laser power of the light-sheet was 40 mW for the 561 nm laser and 4 mW for the 488 nm laser.

Compared to previous measurements with the mEos2 label[42], HaloTag together with JF549 allowed for faster frame cycle times and longer tracks. Movies of morphogens were recorded with 10 ms exposure time and a total frame cycle time of 11.7 ms. The illumination time was set to match the exposure time.

For continuous movies, a sequence starting with 10 frames with 488 nm laser illumination showing the membrane-GFP signal was recorded, followed by 1000 frames of 561 nm laser illumination to image single morphogen molecules and finalized by another 10 frames of 488 nm illumination.

For time-lapse microscopy movies of Squint-HaloTag and Cyclops-HaloTag, frames were illuminated for one frame with the 561 nm laser followed by one frame with 488 nm laser illumination. Dark times of different lengths were introduced between illuminated frames, resulting in frame acquisitions every 58 ms, 199 ms or 1006 ms (time-lapses) for which a total number of 200, 59 and 24 illuminated frames were recorded, respectively.

Splitting movies into reference channel and single-molecule channel

Movies containing frames with memGFP signal as well as frames with signal of Halo-tagged morphogens were separated using TrackIts movie splitter. Two separate movies were obtained, one containing only the memGFP signal and one containing only single-molecule signal. Movies were discarded if considerable drift due to embryo movement was evident in order to guarantee a correct classification of tracks to their region classes (cavity, interface).

Segmentation of extracellular regions using a CNN

A U-Net[92] CNN was trained to segment extracellular regions of developing zebrafish embryos based on the memGFP intensity using ZeroCostDL4Mic[48], a state-of-the-art image segmentation platform. Target images for training were created by first using TrackIt's sub-region drawing tool to manually draw outlines around the extracellular space of 452 images. The "Average frames" function was used to average all frames of a memGFP movie, and the "Gaussian filter" function with a kernel size of 1 px was applied to smoothen the averaged image. A custom Matlab script was then used to create a U-Net compatible 8-bit.tif file containing the training masks.

Training was performed in the cloud using the Google Colaboratory platform provided by DL4Mic. The model was trained over 200 epochs on 90% of the training images while 10% of images were used for validation. This resulted in a final training loss of 0.163. The trained model was downloaded and integrated into a custom Python program to create regions of interest compatible with our single-molecule tracking software TrackIt[47]. All frames of the memGFP movies in a folder were averaged and padded with zeros to match the U-Net network requirements. The images were then segmented with the trained model, and binary masks were created by applying a user-defined intensity threshold between 0-255, which was set to 240. Polygonal regions of interest with a minimum size of 150 px were then saved in a TrackIt compatible .roi file.

Once loaded into TrackIt, the segmentation results were visually quality-controlled for each movie. Parts where the memGFP signal was blurry (e.g. when lying far away from the edge of the zebrafish), or parts where the laser light was blocked or absorbed, were either adjusted or cut-off manually.

A second region containing extracellular cavities was added by manually selecting parts of the regions that had been segmented by the CNN (see for example Fig. 1d). Cavities were defined as areas, where the cell membranes of more than two cells meet and the memGFP signal of all cells are distinguishable. Interfaces were defined as areas, where two cells are aligned in a way that the memGFP signal of the cell membranes of both cells overlap and are not distinguishable.

Tracking of single-molecule microscopy data for mobility analysis of morphogens

Single-molecule microscopy data of Halo-tagged Cyclops, Squint, Lefty1 & Lefty2 and secreted-HaloTag were analyzed with TrackIt[47]. A threshold factor of 1.5 was used to detect single-molecule events. The nearest neighbor algorithm was used with a tracking radius of 10 px (= 1.66 μm) to link single-molecule detections into tracks, and 1 gap frame was allowed to bridge detection gaps if a molecule was already detected for at least 2 consecutive frames. TrackIt's "Delete tracks touching borders" option was used, which means that tracks were

assigned to regions if they lied completely inside the region of interest while tracks crossing region borders were discarded and treated as non-linked detections.

Distribution of jump distances and diffusion analysis

For diffusion analysis, TrackIt's data analysis tool was used to fit the cumulative distribution of jump distances with a three-component Brownian diffusion model. The total number of bins of the cumulative jump distance histogram was set to 1660 corresponding to a bin size of 1 nm. Generally, two-dimensional tracks acquired in single-molecule tracking are a projection of three-dimensional motion, which underestimates diffusion coefficients. Biases also arise from molecules moving out of the depth of focus of the objective (approx. 0.7 μm), which overestimates the fraction of bound molecules[93,94]. We did not correct for these effects in our analysis. However, since all morphogens/conditions will experience similar bias, the comparisons between species we discuss will not be affected. To prevent an overrepresentation of bound molecules, a maximum of 10 jumps was considered per track. Jumps over gap frames were not considered. The errors of diffusion coefficients $D_{1,2,3}$ and fractions $A_{1,2,3}$ were estimated by repeating the analysis 500 times using random samples of 50% of the jump distances, and the standard deviation of the resulting diffusion coefficients and fractions were calculated. To assess whether a two- or three-component model best describes our data, we compared the reduced chi-squared of the 2-rate and 3-rate model fits and furthermore used the Akaike Information Criterion (AIC)[58]. For model comparison, we calculated the difference in AIC values using the residual sum of squares (RSS) obtained from the least squares fit[95]:

$$\Delta \mathrm{AIC_i} = \left(2k_{2rate} + n\ln\left(RSS_{2rate}\right)\right) - \left(2k_{3rate} + n\ln\left(RSS_{3rate}\right)\right) \quad (1)$$

where k is the number of parameters used in each model and n is the number of data points.

To visualize the diffusion analysis results, the probability distribution $p(r)$, as obtained from the fit results, was plotted together with the histogram of jump distances using

$$p(r) = \frac{1}{2\tau} r \cdot \Delta r \left(\frac{A_1}{D_1} \exp\left(\frac{-r^2}{4\tau D_1}\right) + \frac{A_2}{D_2} \exp\left(\frac{-r^2}{4\tau D_2}\right) + \frac{\frac{A_3}{D_3} \exp\left(\frac{-r^2}{4\tau D_3}\right)}{1 - \exp\left(\frac{-r_{tr}^2}{4\tau D_3}\right)} \right) \quad (2)$$

where r is the jump distance, Δr is the bin width of the jump-distance histogram (here 20 nm), τ is the frame cycle time and D_i and A_i are the diffusion coefficients and fractions resulting from the cumulative jump distance distribution fit. The last term is normalized by $\left(1 - \exp\left(\frac{-r_{tr}^2}{4\tau D_3}\right)\right)$, with r_{tr} representing the tracking radius, to account for the cut-off due to the lower and upper limit of jump distances.

Jump angle analysis

Jump angles θ were calculated from two consecutive jumps (three consecutive localizations)[47]. The angle θ indicates the change in direction of a molecule after it has moved in one direction (see inset in Fig. 3e). While an angle of 0° indicates no change, i.e., a direct forward movement of the molecule, an angle of 180° indicates that a molecule moved backward in the opposite direction. Angles <180° or >180° indicate a movement to the right or left, respectively. The degree of reverse motion was quantified by calculating the 'fold anisotropy' metric, $f_{180/0}$[60], which measures how many-fold more likely a backward jump is, compared to a jump forward, using:

$$f\left(180/0\right) = \frac{\mathrm{BWD}}{\mathrm{FWD}} = P\left(\frac{180^\circ \pm 30^\circ}{O^\circ \pm 30^\circ}\right) \quad (3)$$

where BWD is the probability for a backward jump with an angle θ of 150°–210° and FWD is the probability for a forward jump with an angle θ of 330°–30°.

To calculate the angle between a jump and the region border, we first identified the point of the polygonal ROI that was closest to both detections of a jump. We then calculated the average of the orientation of the two neighboring polygonal border segments. Subsequently we determined the acute angle between the track segment and the ROI border segment.

Mean squared displacement (MSD) analysis

For MSD analysis, tracks with a minimum duration of 20 frames were considered. The first 10 points of the MSD curves were fitted with the linear function $\mathrm{MSD} = 4 \cdot D \cdot \tau + c$, where D is the diffusion coefficient and c is a constant to account for the localization error.

Spot density ratio

The density of single-molecule detections was calculated for each movie and region class separately by dividing the number of detections in each of the regions by its number of pixels. The ratio between the spot density in the cavity region and the spot density in the interface region was then calculated for each movie. Movies containing no detections in one of the regions or movies with only one region class were discarded. p-values were calculated using the non-parametric Kruskal-Wallis-Test using GraphPad Prism 9.0.1.

Analysis of time-lapse microscopy data

Tracking settings were optimized for the nearest-neighbor algorithm to track only bound molecules based on the time spend within a certain area by using small tracking radii in combination with larger minimum track lengths. TrackIt's automatic tracking radii prediction tool was used to ensure equal tracking-loss probabilities due to tracking errors and photobleaching across all time-lapse conditions. The resulting tracking radii for a loss probability of 0.005 were: 1.55 pixels or 257 nm (continuous), 2.05 pixels or 340 nm (58 ms time-lapse), 2.92 pixels or 485 nm (200 ms time-lapse) and 3.62 pixels or 601 nm (1 s time-lapse). To ensure that no freely diffusing molecules were tracked and to minimize false connections, a minimum track length of 5 frames was used for continuous and 3 frames for time-lapse movies. Other tracking settings were as described above.

Fluorescence survival time distributions of Squint and Cyclops were extracted from the single-molecule tracks, and GRID[61] was used to determine the dissociation rate spectrum. In brief, GRID uses a superposition of 40 exponential functions with fixed decay rate constants between $10^{-2}\,\mathrm{s}^{-1}$ and $10^{2}\,\mathrm{s}^{-1}$ and an appropriate set of regularizations to ensure robust convergence of the fit to the survival time distributions. As a result, GRID yields the amplitudes corresponding to each of the fixed decay rates. Binding times were calculated as the inverse of the dissociation rate. The tails of the survival time distributions were cut off below a probability of 0.01 due to a low number of events.

The rate spectrum is a measure for how often dissociation events of a certain dissociation rate population occur within a specific time (Supplementary Fig. 6b). This can be converted into a "state" spectrum by dividing the fractions of the event spectrum with the respective dissociation rates. This results in the distribution of binding states at any given point in time. To estimate errors of the dissociation rate spectra, a 500× resampling was performed with randomly selected 80% of the data. Boundaries for dissociation rate clusters were then manually assigned to calculate the standard deviation of the results.

Agent-based modelling

Agent-based models were implemented in Python3[96]. Morphogens were modeled as agents performing a random walk on a

two-dimensional simulation geometry. The geometry was generated in Fiji[97] by scaling the binary masks of extracellular space such that each pixel in the image was 10 nm × 10 nm. Reflective boundary conditions were used. All intracellular pixels were set to 0 and extracellular to 1. The extracellular space was populated with 100 morphogens at random starting positions with a fraction of morphogens in bound state. The initial bound fraction (BF_I) was estimated using an empirical function of the receptor density (σ), residence time (τ), and binding strength (S) to ensure that the equilibrium bound fractions were achieved quickly during the simulation.

$$BF_I = \frac{\tau \cdot S}{50 \cdot \log_{10}\left(\frac{10}{\sigma}\right)} \quad (4)$$

Morphogens were allowed to occupy only the extracellular positions. The receptors were placed at the boundary of the extracellular region with uniform spacing based on the required receptor density. The morphogen position and state (bound or unbound) was updated at each simulation step (10,000 steps of 10 ms each). To simulate random walks of morphogens, their jump distances (r) were drawn from a range of jumps with probabilities given by the probability density function:

$$p(r) = \frac{f(r)}{\sum_x f(x)} \quad (5)$$

given that

$$f(r) = \frac{r}{2 \cdot D \cdot \tau} \cdot e^{\left(\frac{-r^2}{4 \cdot D \cdot \tau}\right)} \quad (6)$$

where D is the diffusion coefficient (either D_{free} or D_{bound}), τ is the timestep (10 ms) and $r,x \in [0,2]$.

The free and bound diffusion coefficients were set to 30 μm²/s (D_{free}) and 0.5 μm²/s (D_{bound}) as estimated from the experimental observations. A new position in the extracellular space was picked randomly from the available positions at distance r from the current position. The morphogen state was changed from unbound to bound if the distance to a receptor was ≤ 20 nm. The morphogen stayed bound for the time $t_b = \tau \cdot \log_{10}\left(\frac{1}{v}\right)$, where v is a random number between 0 and 1, and τ is the residence time. The jump and angular histograms and localization plots were generated in a similar manner as the experimental dataset to validate the model.

For the parameter screen, the two-dimensional simulation geometry was modified to narrow or widen the extracellular space. This was achieved by iteratively changing the pixel values at the extracellular boundary. For each iteration, the width of the extracellular space was changed by 20 nm, thereby changing the extracellular fraction ($\eta = \frac{\text{Extracellular Area} \times 100}{\text{Total Area}}$). Five η values ranging from 8% to 16%, three receptor densities σ (0.05, 0.5, 5.0 μm^{-1}) and 5 residence times τ (0, 1, 6, 11, 16 s) were tested.

Morphotrap experiments and image analysis

Images of zebrafish embryos injected with different amounts of membrane-tethered GFP-binding nanobody were acquired as described previously[69]. Image analysis was performed manually in Fiji 2.9.0[97]. The GFP channel of the confocal images was converted into a.tif file. Five regions of interest (ROIs, 64 × 171 pixel) were manually selected from the image. For each ROI, 15 cavity and interface regions were selected, and the mean gray value was measured to quantify the GFP localization in each region. The ratio of the mean gray value of the cavity to that of the interface was used as ρ_c/ρ_i.

Reporting summary

Further information on research design is available in the Nature Research Reporting Summary linked to this article.

Data availability

All single-particle tracking data and simulated tracks are freely available at Dryad [https://doi.org/10.5061/dryad.9kd51c5kg]. Source data for figures are provided with this paper in 'Source Data.xlsx'. Data supporting the findings of this manuscript will be available from the corresponding authors after publication upon reasonable request.

Code availability

The TrackIt software is freely available. TrackIt was written in Matlab and is available on GitLab [https://gitlab.com/GebhardtLab/TrackIt] and Zenodo [https://doi.org/10.5281/zenodo.7092296]. The code for the agent-based model is available on GitHub [https://github.com/mueller-lab/morphogenDiffusion-ABM] and Zenodo [https://doi.org/10.5281/zenodo.7104354].

References

1. Čapek, D. & Müller, P. Positional information and tissue scaling during development and regeneration. *Development* **146**, dev177709 (2019).
2. Müller, P., Rogers, K. W., Yu, S. R., Brand, M. & Schier, A. F. Morphogen transport. *Development* **140**, 1621–1638 (2013).
3. Brunt, L. et al. Vangl2 promotes the formation of long cytonemes to enable distant Wnt/β-catenin signaling. *Nat. Commun.* **12**, 2058 (2021).
4. Hatori, R., Wood, B. M., Oliveira Barbosa, G. & Kornberg, T. B. Regulated delivery controls Drosophila Hedgehog, Wingless, and Decapentaplegic signaling. *Elife* **10**, 1–23 (2021).
5. Simon, E. et al. Glypicans define unique roles for the Hedgehog co-receptors boi and ihog in cytoneme-mediated gradient formation. *Elife* **10**, 1–29 (2021).
6. Patel, A. et al. Cytonemes coordinate asymmetric signaling and organization in the Drosophila muscle progenitor niche. *Nat. Commun.* **13**, 1185 (2022).
7. Stapornwongkul, K. S. & Vincent, J.-P. Generation of extracellular morphogen gradients: The case for diffusion. *Nat. Rev. Genet.* **22**, 393–411 (2021).
8. Rogers, K. W. & Schier, A. F. Morphogen gradients: From generation to interpretation. *Annu. Rev. Cell Dev. Biol.* **27**, 377–407 (2011).
9. Rogers, K. W. & Müller, P. Nodal and BMP dispersal during early zebrafish development. *Dev. Biol.* **447**, 14–23 (2019).
10. Gregor, T., Wieschaus, E. F., McGregor, A. P., Bialek, W. & Tank, D. W. Stability and nuclear dynamics of the Bicoid morphogen gradient. *Cell* **130**, 141–152 (2007).
11. Drocco, J. A., Wieschaus, E. F. & Tank, D. W. The synthesis–diffusion–degradation model explains Bicoid gradient formation in unfertilized eggs. *Phys. Biol.* **9**, 055004 (2012).
12. Grimm, O., Coppey, M. & Wieschaus, E. Modelling the Bicoid gradient. *Development* **137**, 2253–2264 (2010).
13. Yu, S. R. et al. Fgf8 morphogen gradient forms by a source-sink mechanism with freely diffusing molecules. *Nature* **461**, 533–536 (2009).
14. Wang, Y., Wang, X., Wohland, T. & Sampath, K. Extracellular interactions and ligand degradation shape the Nodal morphogen gradient. *Elife* **5**, e13879 (2016).
15. Ries, J., Yu, S. R., Burkhardt, M., Brand, M. & Schwille, P. Modular scanning FCS quantifies receptor-ligand interactions in living multicellular organisms. *Nat. Methods* **6**, 643–645 (2009).
16. Wang, X., Harris, R. E., Bayston, L. J. & Ashe, H. L. Type IV collagens regulate BMP signalling in Drosophila. *Nature* **455**, 72–77 (2008).

17. Yan, D. & Lin, X. Shaping morphogen gradients by proteoglycans. *Cold Spring Harb. Perspect. Biol.* **1**, a002493–a002493 (2009).
18. Baeg, G.-H. & Perrimon, N. Functional binding of secreted molecules to heparan sulfate proteoglycans in Drosophila. *Curr. Opin. Cell Biol.* **12**, 575–580 (2000).
19. Han, C. et al. Distinct and collaborative roles of Drosophila EXT family proteins in morphogen signalling and gradient formation. *Development* **131**, 1563–1575 (2004).
20. Baeg, G.-H., Selva, E. M., Goodman, R. M., Dasgupta, R. & Perrimon, N. The wingless morphogen gradient is established by the cooperative action of Frizzled and Heparan Sulfate Proteoglycan receptors. *Dev. Biol.* **276**, 89–100 (2004).
21. Belenkaya, T. Y. et al. Drosophila Dpp morphogen movement is independent of dynamin-mediated endocytosis but regulated by the Glypican members of Heparan Sulfate Proteoglycans. *Cell* **119**, 231–244 (2004).
22. Ohkawara, B., Iemura, S., ten Dijke, P. & Ueno, N. Action range of BMP is defined by its N-terminal basic amino acid core. *Curr. Biol.* **12**, 205–209 (2002).
23. Duchesne, L. et al. Transport of fibroblast growth factor 2 in the pericellular matrix is controlled by the spatial distribution of its binding sites in heparan sulfate. *PLoS Biol.* **10**, e1001361 (2012).
24. Sakuma, R. et al. Inhibition of Nodal signalling by Lefty mediated through interaction with common receptors and efficient diffusion. *Genes Cells* **7**, 401–412 (2002).
25. Müller, P. et al. Differential diffusivity of Nodal and Lefty underlies a reaction-diffusion patterning system. *Science* **336**, 721–724 (2012).
26. Feldman, B. et al. Zebrafish organizer development and germ-layer formation require Nodal-related signals. *Nature* **395**, 181–185 (1998).
27. Dougan, S. T., Warga, R. M., Kane, D. A., Schier, A. F. & Talbot, W. S. The role of the zebrafish nodal-related genes squint and cyclops in patterning of mesendoderm. *Development* **130**, 1837–1851 (2003).
28. Rebagliati, M. R., Toyama, R., Fricke, C., Haffter, P. & Dawid, I. B. Zebrafish nodal-related genes are implicated in axial patterning and establishing left–right asymmetry. *Dev. Biol.* **199**, 261–272 (1998).
29. Fan, X. et al. Nodal signals mediate interactions between the extra-embryonic and embryonic tissues in zebrafish. *Dev. Biol.* **310**, 363–378 (2007).
30. van Boxtel, A. L. et al. A temporal window for signal activation dictates the dimensions of a Nodal signaling domain. *Dev. Cell* **35**, 175–185 (2015).
31. Meno, C. et al. Mouse Lefty2 and zebrafish Antivin are feedback inhibitors of nodal signaling during vertebrate gastrulation. *Mol. Cell* **4**, 287–298 (1999).
32. Feldman, B. et al. Lefty antagonism of Squint is essential for normal gastrulation. *Curr. Biol.* **12**, 2129–2135 (2002).
33. Rogers, K. W. et al. Nodal patterning without Lefty inhibitory feedback is functional but fragile. *Elife* **6**, e28785 (2017).
34. Bennett, J. T. et al. Nodal signaling activates differentiation genes during zebrafish gastrulation. *Dev. Biol.* **304**, 525–540 (2007).
35. Chen, C. & Shen, M. M. Two modes by which Lefty proteins inhibit Nodal signaling. *Curr. Biol.* **14**, 618–624 (2004).
36. Cheng, S. K., Olale, F., Brivanlou, A. H. & Schier, A. F. Lefty blocks a subset of TGFβ signals by antagonizing EGF-CFC coreceptors. *PLoS Biol.* **2**, e30 (2004).
37. Soh, G. H., Pomreinke, A. P. & Müller, P. Integration of Nodal and BMP signaling by mutual signaling effector antagonism. *Cell Rep.* **31**, 107487 (2020).
38. Bläßle, A. et al. Quantitative diffusion measurements using the open-source software PyFRAP. *Nat. Commun.* **9**, 1582 (2018).
39. Almuedo-Castillo, M. et al. Scale-invariant patterning by size-dependent inhibition of Nodal signalling. *Nat. Cell Biol.* **20**, 1032–1042 (2018).
40. Lord, N. D., Carte, A. N., Abitua, P. B. & Schier, A. F. The pattern of Nodal morphogen signaling is shaped by co-receptor expression. *Elife* **10**, e54894 (2021).
41. Preiß, H. et al. Regulation of Nodal signaling propagation by receptor interactions and positive feedback. *Elife* **11**, e66397 (2022).
42. Reisser, M. et al. Single-molecule imaging correlates decreasing nuclear volume with increasing TF-chromatin associations during zebrafish development. *Nat. Commun.* **9**, 5218 (2018).
43. Greiss, F., Deligiannaki, M., Jung, C., Gaul, U. & Braun, D. Single-molecule imaging in living Drosophila embryos with reflected light-sheet microscopy. *Biophys. J.* **110**, 939–946 (2016).
44. Morita, H. et al. The physical basis of coordinated tissue spreading in zebrafish gastrulation. *Dev. Cell* **40**, 354–366.e4 (2017).
45. Grimm, J. B. et al. A general method to improve fluorophores for live-cell and single-molecule microscopy. *Nat. Methods* **12**, 244–250 (2015).
46. Kimmel, C. B., Ballard, W. W., Kimmel, S. R., Ullmann, B. & Schilling, T. F. Stages of embryonic development of the zebrafish. *Dev. Dyn.* **203**, 253–310 (1995).
47. Kuhn, T., Hettich, J., Davtyan, R. & Gebhardt, J. C. M. Single molecule tracking and analysis framework including theory-predicted parameter settings. *Sci. Rep.* **11**, 9465 (2021).
48. von Chamier, L. et al. Democratising deep learning for microscopy with ZeroCostDL4Mic. *Nat. Commun.* **12**, 2276 (2021).
49. Petridou, N. I., Grigolon, S., Salbreux, G., Hannezo, E. & Heisenberg, C.-P. Fluidization-mediated tissue spreading by mitotic cell rounding and non-canonical Wnt signalling. *Nat. Cell Biol.* **21**, 169–178 (2019).
50. Mazza, D., Abernathy, A., Golob, N., Morisaki, T. & McNally, J. G. A benchmark for chromatin binding measurements in live cells. *Nucleic Acids Res* **40**, e119–e119 (2012).
51. Grünwald, D. et al. Probing intranuclear environments at the single-molecule level. *Biophys. J.* **94**, 2847–2858 (2008).
52. Shaban, H. A., Barth, R., Recoules, L., & Bystricky, K. Hi-D: Nanoscale mapping of nuclear dynamics in single living cells. *Genome Biol.* **21**, 1–21 (2020).
53. Schmidt, J. C., Zaug, A. J. & Cech, T. R. Live cell imaging reveals the dynamics of telomerase recruitment to telomeres. *Cell* **166**, 1188–1197.e9 (2016).
54. Saxton, M. J. & Jacobson, K. Single-particle tracking: Applications to membrane dynamics. *Annu. Rev. Biophys. Biomol. Struct.* **26**, 373–399 (1997).
55. Manzo, C. & Garcia-Parajo, M. F. A review of progress in single particle tracking: from methods to biophysical insights. *Rep. Prog. Phys.* **78**, 124601 (2015).
56. Veith, R. et al. Balbiani ring mRNPs diffuse through and bind to clusters of large intranuclear molecular structures. *Biophys. J.* **99**, 2676–2685 (2010).
57. Höfling, F. & Franosch, T. Anomalous transport in the crowded world of biological cells. *Reports Prog. Phys.* **76**, 046602 (2013).
58. Matsuoka, S., Shibata, T. & Ueda, M. Statistical analysis of lateral diffusion and multistate kinetics in single-molecule imaging. *Biophys. J.* **97**, 1115–1124 (2009).
59. Izeddin, I. et al. Single-molecule tracking in live cells reveals distinct target-search strategies of transcription factors in the nucleus. *Elife* **3**, e02230 (2014).
60. Hansen, A. S., Amitai, A., Cattoglio, C., Tjian, R. & Darzacq, X. Guided nuclear exploration increases CTCF target search efficiency. *Nat. Chem. Biol.* **16**, 257–266 (2020).
61. Reisser, M. et al. Inferring quantity and qualities of superimposed reaction rates from single molecule survival time distributions. *Sci. Rep.* **10**, 1758 (2020).

62. Popp, A. P., Hettich, J. & Gebhardt, J. C. M. Altering transcription factor binding reveals comprehensive transcriptional kinetics of a basic gene. *Nucleic Acids Res* **49**, 6249–6266 (2021).
63. Gebhardt, J. C. M. et al. Single-molecule imaging of transcription factor binding to DNA in live mammalian cells. *Nat. Methods* **10**, 421–426 (2013).
64. Fujiwara, T. K. et al. Confined diffusion of transmembrane proteins and lipids induced by the same actin meshwork lining the plasma membrane. *Mol. Biol. Cell* **27**, 1101–1119 (2016).
65. Chojnacki, J. et al. Envelope glycoprotein mobility on HIV-1 particles depends on the virus maturation state. *Nat. Commun.* **8**, 545 (2017).
66. Yan, Y.-T. et al. Dual roles of Cripto as a ligand and coreceptor in the Nodal signaling pathway. *Mol. Cell. Biol.* **22**, 4439–4449 (2002).
67. Gritsman, K. et al. The EGF-CFC protein One-Eyed Pinhead is essential for Nodal signaling. *Cell* **97**, 121–132 (1999).
68. Marcon, L., Diego, X., Sharpe, J. & Müller, P. High-throughput mathematical analysis identifies Turing networks for patterning with equally diffusing signals. *Elife* **5**, e14022 (2016).
69. Mörsdorf, D. & Müller, P. Tuning protein diffusivity with membrane tethers. *Biochemistry* **58**, 177–181 (2019).
70. Wolpert, L. Positional information and pattern formation. in *Current Topics in Developmental Biology* **117**, 597–608 (Elsevier Inc., 2016).
71. Kornberg, T. B. Scripting a place in time. *Dev. Biol.* **447**, 24–27 (2019).
72. Romanova-Michaelides, M. et al. Morphogen gradient scaling by recycling of intracellular Dpp. *Nature* **602**, 287–293 (2022).
73. Crick, F. Diffusion in embryogenesis. *Nature* **225**, 420–422 (1970).
74. Kicheva, A. et al. Kinetics of morphogen gradient formation. *Science* **315**, 521–525 (2007).
75. Liu, L. et al. Nodal is a short-range morphogen with activity that spreads through a relay mechanism in human gastruloids. *Nat. Commun.* **13**, 497 (2022).
76. Reilly, K. M. & Melton, D. A. Short-range signaling by candidate morphogens of the TGFβ family and evidence for a relay mechanism of induction. *Cell* **86**, 743–754 (1996).
77. Wilcockson, S. G., Sutcliffe, C. & Ashe, H. L. Control of signaling molecule range during developmental patterning. *Cell. Mol. Life Sci.* **74**, 1937–1956 (2017).
78. Sprague, B. L. & McNally, J. G. FRAP analysis of binding: proper and fitting. *Trends Cell Biol.* **15**, 84–91 (2005).
79. Zhou, S. et al. Free extracellular diffusion creates the Dpp morphogen gradient of the Drosophila wing disc. *Curr. Biol.* **22**, 668–675 (2012).
80. Sigaut, L., Pearson, J. E., Colman-Lerner, A. & Ponce Dawson, S. Messages do diffuse faster than messengers: Reconciling disparate estimates of the morphogen Bicoid diffusion coefficient. *PLoS Comput. Biol.* **10**, e1003629 (2014).
81. Petridou, N. I., Corominas-Murtra, B., Heisenberg, C.-P. & Hannezo, E. Rigidity percolation uncovers a structural basis for embryonic tissue phase transitions. *Cell* **184**, 1914–1928.e19 (2021).
82. Mongera, A. et al. A fluid-to-solid jamming transition underlies vertebrate body axis elongation. *Nature* **561**, 401–405 (2018).
83. Wartlick, O., Kicheva, A. & Gonzalez-Gaitan, M. Morphogen gradient formation. *Cold Spring Harb. Perspect. Biol.* **1**, a001255–a001255 (2009).
84. Chen, Y. & Schier, A. F. The zebrafish Nodal signal Squint functions as a morphogen. *Nature* **411**, 607–610 (2001).
85. Chen, Y. & Schier, A. F. Lefty proteins are long-range inhibitors of Squint-mediated Nodal signaling. *Curr. Biol.* **12**, 2124–2128 (2002).
86. Jing, X., Zhou, S., Wang, W. & Chen, Y. Mechanisms underlying long- and short-range Nodal signaling in zebrafish. *Mech. Dev.* **123**, 388–394 (2006).
87. Tian, J., Andrée, B., Jones, C. M. & Sampath, K. The pro-domain of the zebrafish Nodal-related protein Cyclops regulates its signaling activities. *Development* **135**, 2649–2658 (2008).
88. Rogers, K. W., Bläßle, A., Schier, A. F. & Müller, P. Measuring protein stability in living zebrafish embryos using Fluorescence Decay After Photoconversion (FDAP). *J. Vis. Exp.* **95**, e52266 (2015).
89. Higuchi, R., Krummel, B. & Saiki, R. A general method of in vitro preparation and specific mutagenesis of DNA fragments: study of protein and DNA interactions. *Nucleic Acids Res.* **16**, 7351–7367 (1988).
90. Ho, S. N., Hunt, H. D., Horton, R. M., Pullen, J. K. & Pease, L. R. Site-directed mutagenesis by overlap extension using the polymerase chain reaction. *Gene* **77**, 51–59 (1989).
91. Heckman, K. L. & Pease, L. R. Gene splicing and mutagenesis by PCR-driven overlap extension. *Nat. Protoc.* **2**, 924–932 (2007).
92. Ronneberger, O., Fischer, P. & Brox, T. U-Net: Convolutional Networks for Biomedical Image Segmentation. in *Medical Image Computing and Computer-Assisted Intervention* -- MICCAI *2015* (eds. Navab, N., Hornegger, J., Wells, W. M. & Frangi, A. F.) 234–241 (Springer International Publishing, 2015) https://doi.org/10.1007/978-3-319-24574-4_28.
93. Goulian, M. & Simon, S. M. Tracking single proteins within cells. *Biophys. J.* **79**, 2188–2198 (2000).
94. Hansen, A. S. et al. Robust model-based analysis of single-particle tracking experiments with Spot-On. *Elife* **7**, e33125 (2018).
95. Burnham, K. P. & Anderson, D. R. Multimodel Inference. *Sociol. Methods Res.* **33**, 261–304 (2004).
96. Van Rossum, G. & Drake, F. L. *Python 3 Reference Manual*. (CreateSpace, 2009).
97. Schindelin, J. et al. Fiji: an open-source platform for biological-image analysis. *Nat. Methods* **9**, 676–682 (2012).

Acknowledgements

We thank Gilbert Weidinger (Ulm University) for his constant support by providing access to his zebrafish facility, members of the Gebhardt and Michaelis labs for helpful discussions, Karlotta Bosch and Maximilian Haas for help cloning the HaloTag constructs, Astrid Bellan-Koch for help cloning the secHalo-GFP, and Catrin Weiler and Marianne Wiechers for generating mRNAs. The work was funded by the European Research Council (ERC) under the European Union's Horizon 2020 Research and Innovation Program (No. 637987 ChromArch to J.C.M.G., No. 637840 QUANTPATTERN to P.M., No. 863952 ACE-OF-SPACE to P.M.) and the German Research Foundation (No. 422780363 SPP 2202 GE 2631/2–1 and No. 427512076 GE 2631/3–1 to J.C.M.G.). Support by the Collaborative Research Centre 1279, the Center for Translational Imaging MoMAN of Ulm University, the DFG Centre for the Advanced Study of Collective Behaviour (EXC 2117) and the International Max Planck Research School "From Molecules to Organisms" is acknowledged.

Author contributions

P.M. and J.C.M.G. conceived the project; T.K., D.M., P.M., and J.C.M.G. designed the project; D.M. cloned morphogen fusion proteins and performed confocal microscopy; D.C. and A.N.L. validated the activity of the fusion proteins with injections and qRT-PCR; T.K. performed the single-molecule measurements; J.C. contributed to the single-molecule measurements; T.K. programmed TrackIt; J.G. and T.K. created the CNN segmentation tool; T.K. analyzed data with contributions from J.C. and J.C.M.G.; A.N.L. performed simulations; T.K., A.N.L., P.M., and J.C.M.G wrote the manuscript with comments from all authors.

Funding

Open Access funding enabled and organized by Projekt DEAL.

Competing interests

The authors declare no competing interests.

Additional information

Supplementary information The online version contains supplementary material available at https://doi.org/10.1038/s41467-022-33704-z.

Correspondence and requests for materials should be addressed to Patrick Müller or J. Christof M. Gebhardt.

Peer review information *Nature Communications* thanks the anonymous reviewers for their contribution to the peer review of this work. Peer reviewer reports are available.

Supplementary Information

Single-molecule tracking of Nodal and Lefty in live zebrafish embryos supports hindered diffusion model

Timo Kuhn[1], Amit N. Landge[2,*], David Mörsdorf[3,4,*], Jonas Coßmann[1], Johanna Gerstenecker[1], Daniel Čapek[2], Patrick Müller[#,2,3] and J. Christof M. Gebhardt[#,1]

[1]Institute of Biophysics, Ulm University, Albert-Einstein-Allee 11, 89081 Ulm, Germany

[2]University of Konstanz, Universitätsstraße 10, 78464 Konstanz, Germany

[3]Friedrich Miescher Laboratory of the Max Planck Society, Max-Planck-Ring 9, 72076 Tübingen, Germany

[4]University of Vienna, Department of Neurosciences and Developmental Biology, Djerassiplatz 1, 1030 Vienna, Austria

[*]These authors contributed equally

[#]To whom correspondence should be addressed:
patrick.mueller@uni-konstanz.de
christof.gebhardt@uni-ulm.de

Contents

Supplementary Figures

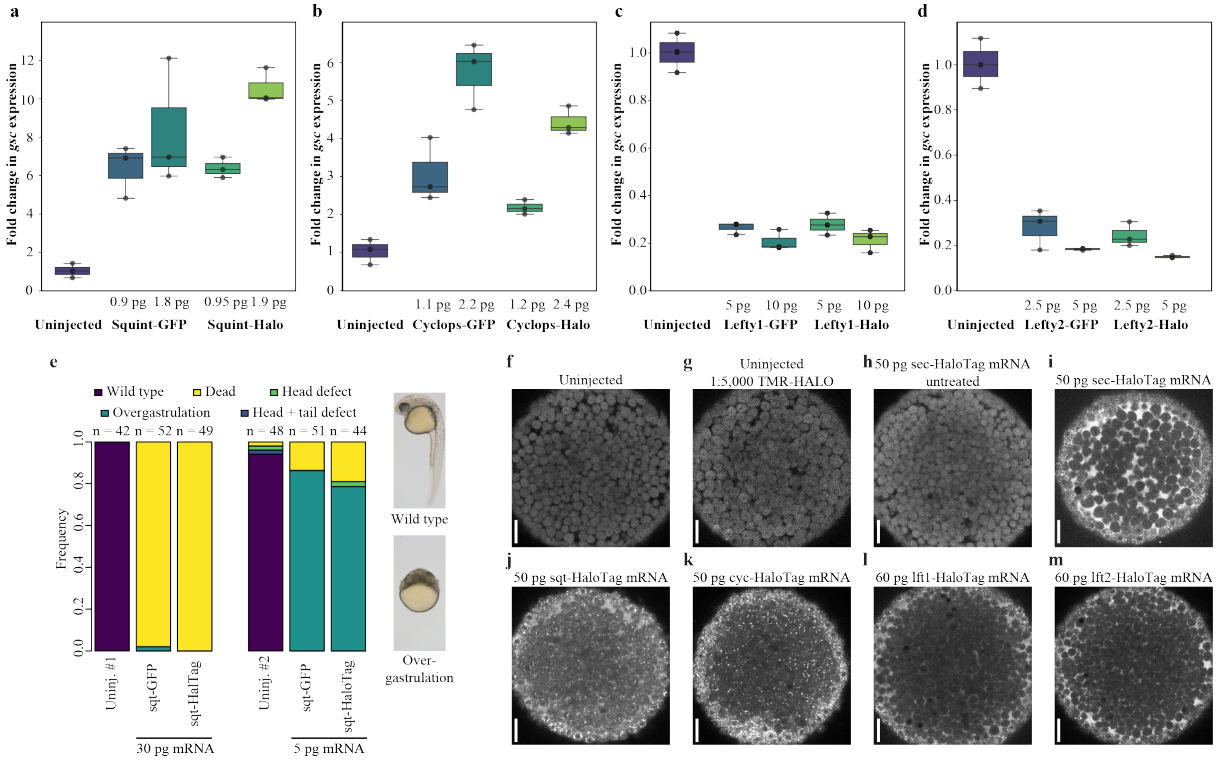

Supplementary Figure 1. Activity and localization of HaloTag fusions. a-d) One-cell stage zebrafish embryos were injected with the indicated equimolar amounts of mRNAs encoding the fusion constructs and collected when their uninjected siblings reached 50% epiboly. Fold change in expression of the Nodal target gene goosecoid (*gsc*) compared to the uninjected embryos is shown for embryos injected with fusion constructs of Nodals (a,b) and Leftys (c,d). The previously characterized GFP-fusion constructs[25,37,39] were used as positive controls. The zebrafish elongation factor *eF1α* was used as a normalization control. Each biological replicate is plotted as a black dot. The center line of the boxplot marks the median, the bounds of the box show interquartile ranges, and the whiskers extend to the minimum and the maximum of the data. n = 3 biological replicates per treatment with ten embryos per biological replicate. **e)** The phenotypes upon injection of squint-GFP or squint-HaloTag mRNA are comparable. High (30 pg mRNA, left) and low (5 pg mRNA, right) expression levels were assessed. **f-m)** Representative optical slices (animal views) of embryos that were uninjected (f, 14 embryos from 3 independent experiments), uninjected but treated with TMR-HALO ligand (g, 3 embryos), injected with secreted-HaloTag-encoding mRNA but not treated with TMR-HALO ligand (h, 2 embryos), and embryos expressing Secreted-HaloTag (i, 4 embryos), Squint-HaloTag (j, 6 embryos), Cyclops-HaloTag (k, 7 embryos), Lefty1-HaloTag (l, 5 embryos), or Lefty2-HaloTag (m, 6 embryos) which were labeled with TMR-HALO ligand. Background fluorescence is similar in unlabeled Secreted-HaloTag-expressing embryos and TMR-HaloTag-treated uninjected embryos, but note that the fluorescence intensities between panels are not comparable due to different detector gain settings. Scale bar = 50 µm. Source data are provided as a Source Data file for Fig. S1a-d.

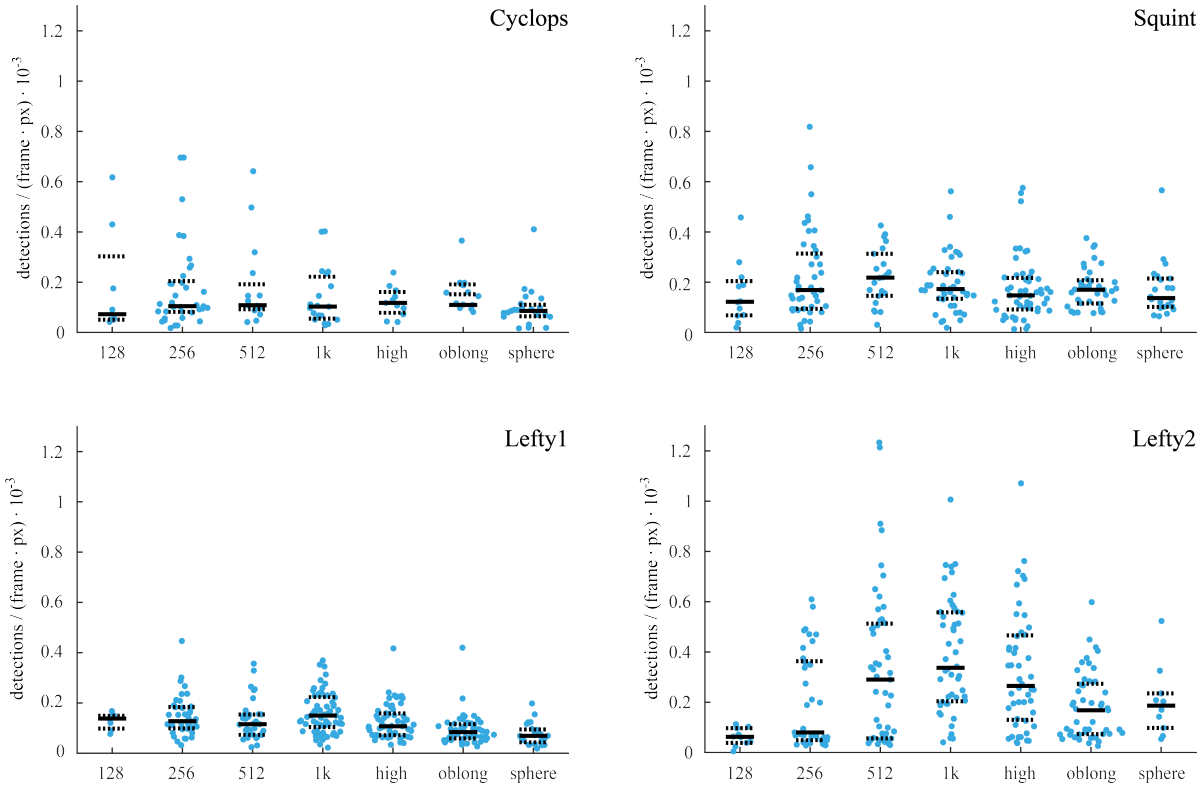

Supplementary Figure 2. Average number of extracellular single molecule detections per frame in each movie. Solid black lines indicate the median values, dashed black lines the 0.25 and 0.75 quantiles. For full experimental statistics see Supplementary Table 7. Source data are provided as a Source Data file.

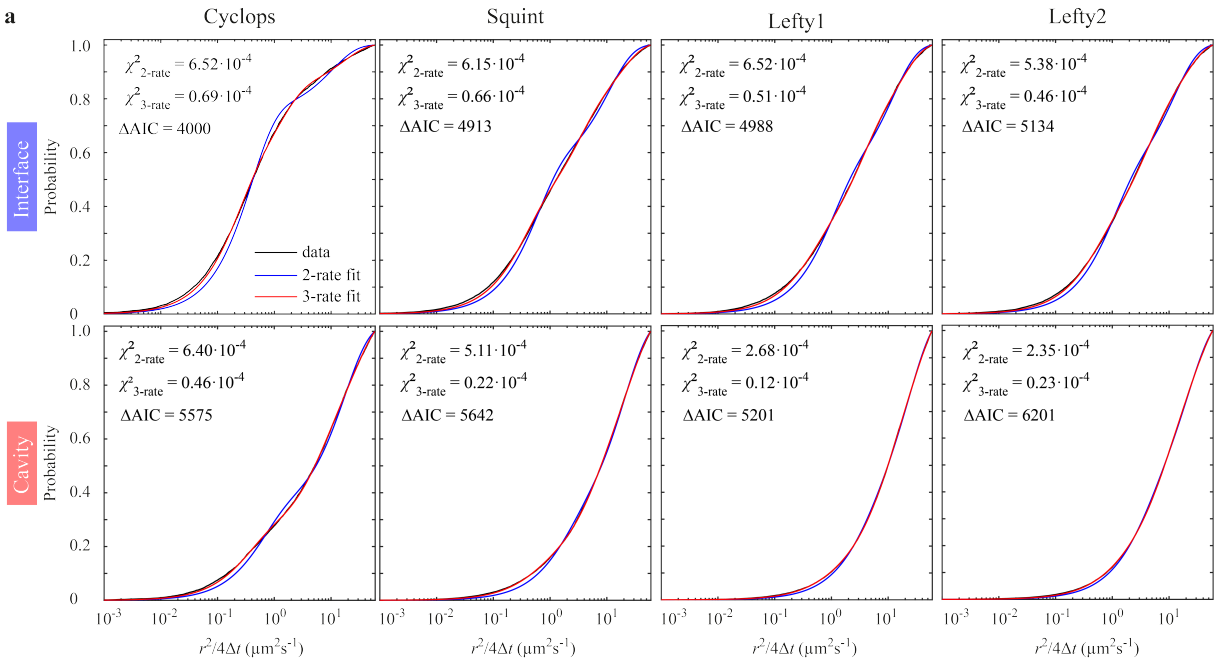

Supplementary Figure 3. **Fitting of jump distance distributions with a 2-rate and 3-rate diffusion model in interface (top) and cavity (bottom) regions for Cyclops, Squint, Lefty1 and Lefty2.** Based on the reduced χ^2 and the Akaike Information Criterion (AIC), a three-component diffusion model best described the data.

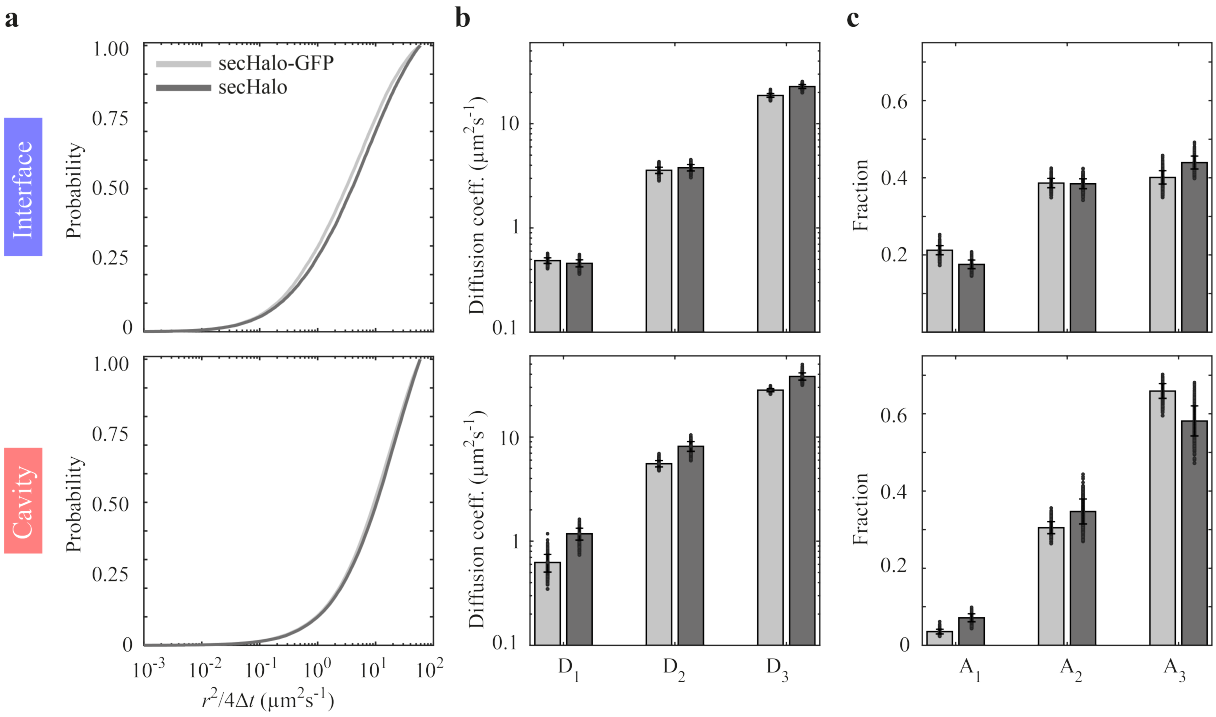

Supplementary Figure 4. Mobility of sec-Halo-GFP and sec-Halo in cell-cell interfaces and extracellular cavities. a) Cumulative distributions of jump distances in interfaces and cavities for sec-Halo-GFP and sec-Halo. **b)** Diffusion coefficients and **c)** fractions of the three-component diffusion model (Supplementary Table 1 and 2). Data are presented as mean values ± s.d. of 500 resamplings with randomly selected 50% of the data. For full experimental statistics see Supplementary Table 5. Source data are provided as a Source Data file.

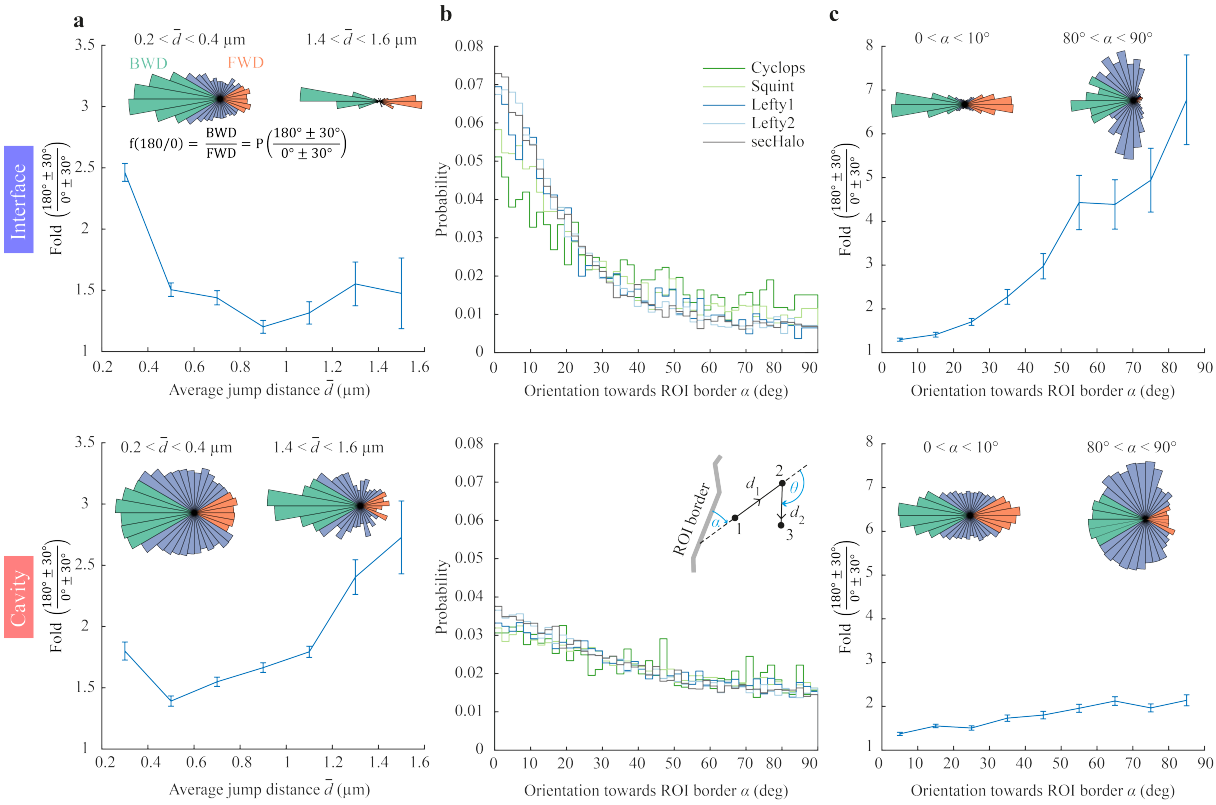

Supplementary Figure 5. Track orientation and jump angles reveal restricted diffusion in interfaces and cavities. a) Fold anisotropy $f_{180/0}$ as a function of the mean jump distance $\overline{d} = \frac{d_1+d_2}{2}$ of the two involved track segments. In interfaces, the anisotropy was higher for small mean jump distances, possibly indicating partial trapping or immobilization. In contrast, the anisotropy increased with larger average jump distances in cavities, reflecting a forced change in direction for higher average jump distances in these regions. Insets: distribution of jump angles for the lowest and highest analyzed mean jump distances. Probabilities for backward and forward motion shown in green and red, respectively. Data of all morphogens and sec-Halo pooled. **b)** Distribution of the orientation of jumps with respect to the nearest ROI border in interfaces and cavities for the indicated morphogen and sec-Halo. Inset: illustration showing the definition of the angle α between track segments and the ROI border, and the jump angle θ towards the subsequent track segment. **c)** Fold anisotropy $f_{180/0}$ as a function of the orientation towards the region border. In interfaces, the anisotropy increases strongly for larger angles due to the reduced dimensionality. For jumps parallel to interface regions, the subsequent jumps were directed comparably in forward or backward direction, whereas jumps at an angle to the ROI border were predominantly followed by a jump in backward direction. This effect is much less pronounced in cavities. Insets: distribution of jump angles of tracks oriented parallel and perpendicular to ROI border. Probabilities for backward and forward motion shown in green and red, respectively. Data of all morphogens and sec-Halo pooled. Center values in a,c) are calculated from the formula using all data, error bars show standard deviation of 50 resamplings with 50% of the data. Lines are given as guide to the eye. For full experimental statistics see Supplementary Table 5. Source data are provided as a Source Data file.

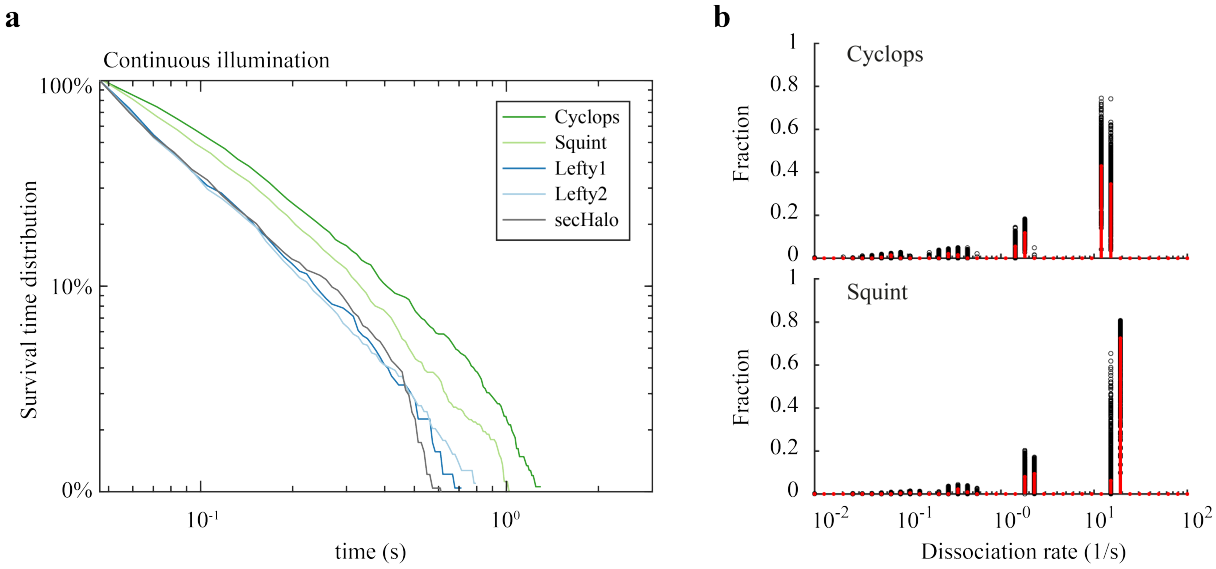

Supplementary Figure 6. Residence times in the extracellular space. a) Survival-time distributions of bound molecules obtained from continuous movies. **b)** Rate spectra of dissociation rates of Cyclops and Squint obtained by GRID using all data (red bars) and 500 resampling runs with randomly selected 80% of data (black data points) as an error estimation of the spectra. For full experimental statistics see Supplementary Table 6. Source data are provided as a Source Data file.

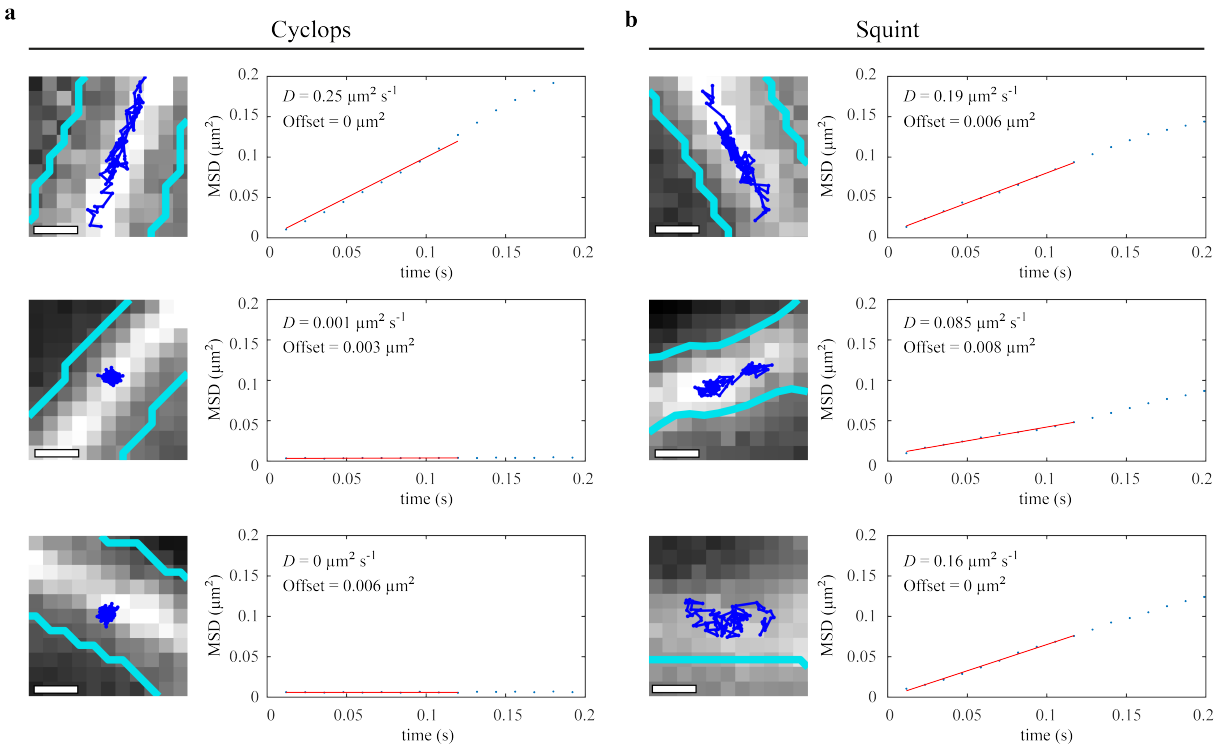

Supplementary Figure 7. Mean-squared displacement (MSD) analysis of an example set of extracellular binding events of Cyclops and Squint (Supplementary Movie 6 and 7). a,b) Left: memGFP signal averaged over 10 frames with overlaid track of a binding event (blue) with a minimum duration of 20 frames (234 ms) in the extracellular region (cyan). Right: MSD as a function of time (blue dots) with overlaid linear fit (red) for the determination of the diffusion coefficient of the tracks depicted on the left. Scale bars: 0.5 µm.

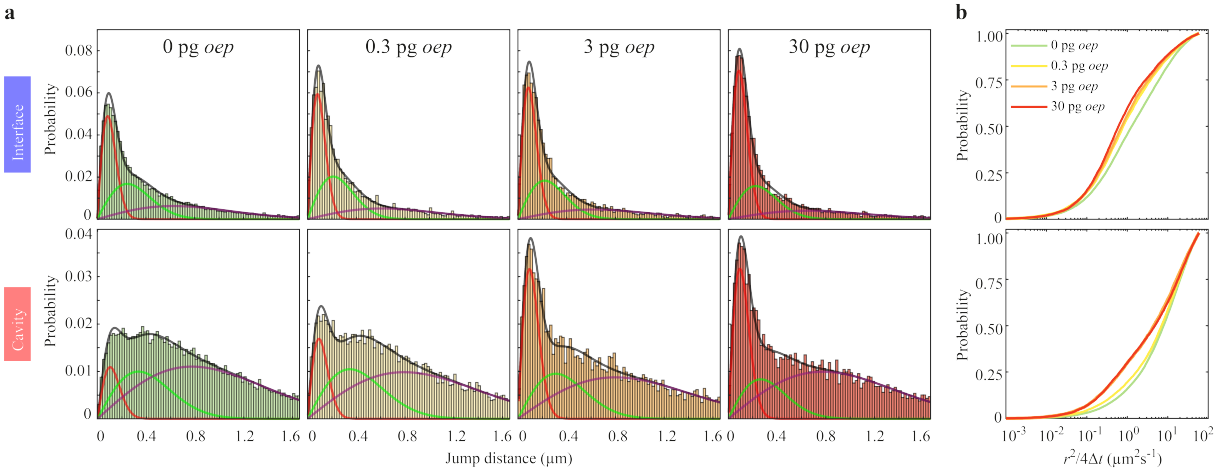

Supplementary Figure 8. Mobility of Squint decreases with overexpression of *oep*. a) Distribution of jump distances within single-molecule tracks in interfaces and cavities of Squint with the indicated amount of co-injected *oep*. Lines represent a three-component diffusion model (black) and the individual components (red, green, purple). **b)** Cumulative distributions of jump distances. For full experimental statistics see Supplementary Table 5. Source data are provided as a Source Data.

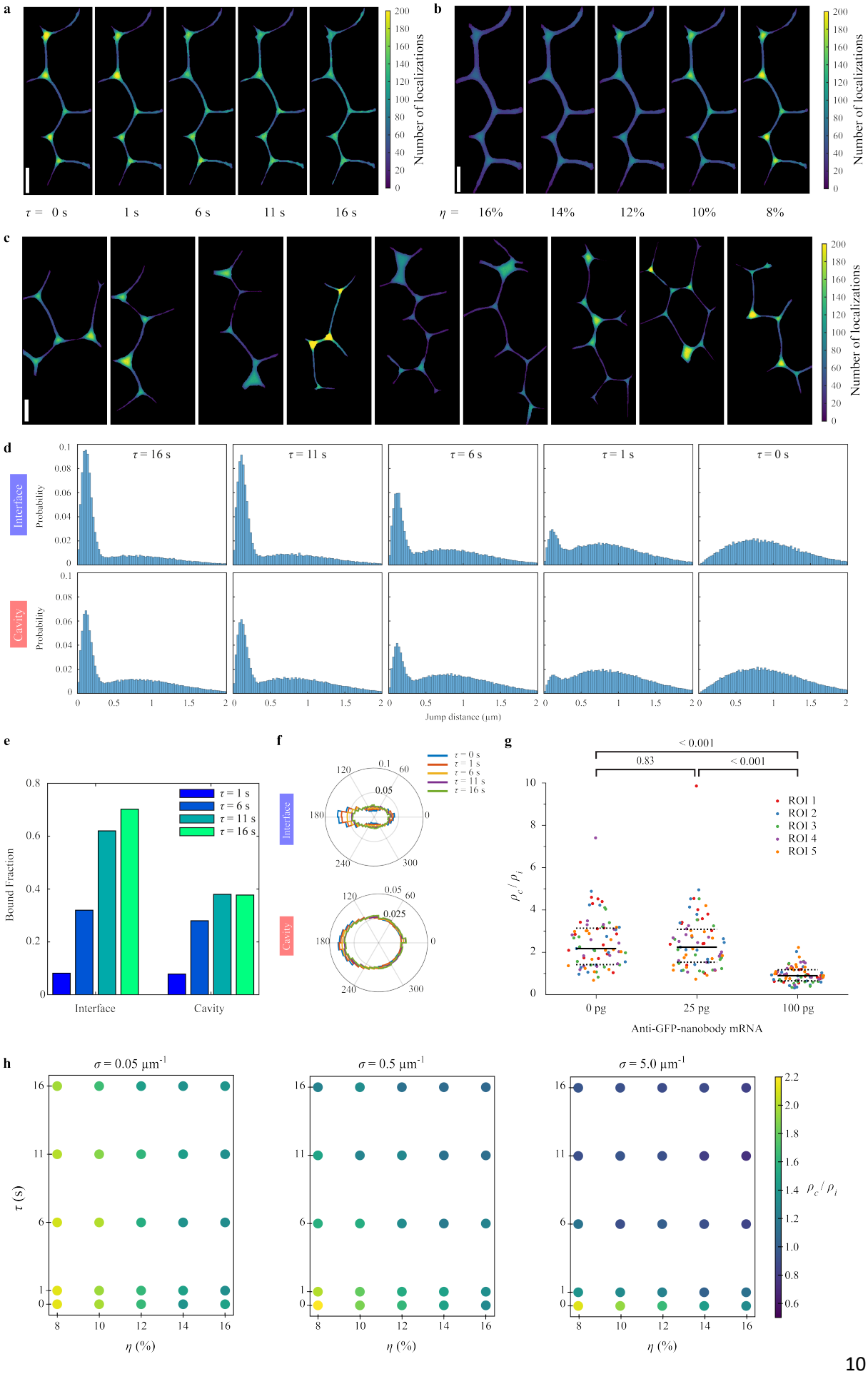
a
b
c
d
e
f
g
h
Number of localizations
τ = 0 s
1 s
6 s
11 s
16 s
η = 16%
14%
12%
10%
8%
Interface
Cavity
Probability
Jump distance (μm)
Bound Fraction
τ = 1 s
τ = 6 s
τ = 11 s
τ = 16 s
< 0.001
0.83
ROI 1
ROI 2
ROI 3
ROI 4
ROI 5
0 pg
25 pg
100 pg
Anti-GFP-nanobody mRNA
σ = 0.05 μm-1
σ = 0.5 μm-1
σ = 5.0 μm-1
τ (s)
η (%)

Supplementary Figure 9. An agent-based model reveals key parameters affecting morphogen behavior in the extracellular space. a) Localization density plots of simulated morphogens with increasing residence times (τ) at σ =0.5 μm^{-1} and η = 8%. **b)** Localization density plots of simulated morphogens with decreasing extracellular fraction (η) at τ = 0 s, and σ = 0.5 μm^{-1}. **c)** Localization density plots of morphogens simulated on different geometries of the extracellular space; η = 8%, τ = 0 s, and σ = 0.5 μm^{-1}. **d)** Distribution of jump distances of simulated morphogens in interfaces and cavities for different residence times. **e)** Fraction of bound molecules in interfaces and cavities for different residence times. **f)** Distributions of angles between consecutive track segments of simulated morphogens in interfaces and cavities for different residence times. **g)** Ratio of mean GFP intensities in cavity and interface (ρ_c/ρ_i) for zebrafish embryos injected with different amounts of mRNA encoding membrane-tethered GFP-binding nanobody. Solid black lines indicate the median values, dashed black lines the 0.25 and 0.75 quantiles. The scattered dots show individual data points and are color-coded based on the regions of interest (ROIs) used for measurements. For each condition, fifteen cavity and interface regions each were measured from five ROIs. p-values (0 pg - 25 pg: 0.83; 0 pg - 100 pg: < 0.001; 25 pg - 100 pg: < 0.001) were calculated using the Kruskal-Wallis-Test. **h)** Two-dimensional representations of the three-dimensional scatter plot displayed in Figure 6b, showing the localization density ratios (ρ_c/ρ_i) for each of the simulated receptor densities σ (0.05 μm^{-1}, 0.5 μm^{-1}, and 5.0 μm^{-1}). Five residence times τ (0 s, 1 s, 6 s, 11 s, and 16 s) and five extracellular fractions η (8%, 10%, 12%, 14%, and 16%) were simulated for each receptor density condition. Scale bars in a, b and c are 10 μm. Source data are provided as a Source Data file for Fig. S9d,e,f,g.

Supplementary Tables

Interface	Cyclops	Squint	Lefty1	Lefty2	sec-Halo	sec-Halo-GFP
D_1 ($\mu m^2 s^{-1}$)	0.2 ± 0.02	0.32 ± 0.01	0.35 ± 0.04	0.43 ± 0.03	0.46 ± 0.04	0.49 ± 0.03
D_2 ($\mu m^2 s^{-1}$)	1.2 ± 0.1	2.6 ± 0.2	2.6 ± 0.3	3 ± 0.2	3.8 ± 0.3	3.6 ± 0.2
D_3 ($\mu m^2 s^{-1}$)	17 ± 1	17 ± 1	16 ± 1	17 ± 1	23 ± 1	19 ± 1
A_1, immobile	0.44 ± 0.03	0.35 ± 0.01	0.21 ± 0.02	0.24 ± 0.01	0.18 ± 0.01	0.21 ± 0.01
A_2, intermediate	0.39 ± 0.03	0.34 ± 0.01	0.39 ± 0.01	0.38 ± 0.01	0.38 ± 0.01	0.38 ± 0.01
A_3, fast	0.17 ± 0.01	0.31 ± 0.01	0.4 ± 0.02	0.37 ± 0.02	0.44 ± 0.02	0.4 ± 0.02

Supplementary Table 1. Diffusion parameters in interface regions obtained from fitting the cumulative distribution of jump distances of Cyclops, Squint, Lefty1 and Lefty2 shown in Figure 3.

Cavity	Cyclops	Squint	Lefty1	Lefty2	sec-Halo	sec-Halo-GFP
D_1 ($\mu m^2 s^{-1}$)	0.31 ± 0.02	0.45 ± 0.04	0.63 ± 0.11	0.73 ± 0.09	1.19 ± 0.15	0.6 ± 0.12
D_2 ($\mu m^2 s^{-1}$)	5.2 ± 0.7	4.8 ± 0.4	6.7 ± 0.7	5.5 ± 0.4	8.1 ± 0.9	5.5 ± 0.4
D_3 ($\mu m^2 s^{-1}$)	28 ± 3	26 ± 1	30 ± 2	27 ± 1	38 ± 3	28 ± 1
A_1, immobile	0.22 ± 0.01	0.09 ± 0.01	0.05 ± 0.01	0.06 ± 0.01	0.07 ± 0.01	0.03 ± 0.01
A_2, intermediate	0.3 ± 0.04	0.28 ± 0.02	0.31 ± 0.03	0.33 ± 0.02	0.34 ± 0.03	0.3 ± 0.02
A_3, fast	0.48 ± 0.04	0.63 ± 0.02	0.64 ± 0.04	0.61 ± 0.02	0.58 ± 0.04	0.66 ± 0.02

Supplementary Table 2. Diffusion parameters in cavity regions obtained from fitting the cumulative distribution of jump distances of Cyclops, Squint, Lefty1 and Lefty2 shown in Figure 3.

Interface	*oep* 0.3 pg	*oep* 3 pg	*oep* 30 pg
D_1 ($\mu m^2 s^{-1}$)	0.28 ± 0.02	0.31 ± 0.02	0.32 ± 0.02
D_2 ($\mu m^2 s^{-1}$)	1.9 ± 0.2	2 ± 0.3	2.2 ± 0.3
D_3 ($\mu m^2 s^{-1}$)	16 ± 1	16 ± 1	18 ± 1
A_1, immobile	0.4 ± 0.02	0.44 ± 0.03	0.5 ± 0.02
A_2, intermediate	0.35 ± 0.02	0.33 ± 0.02	0.29 ± 0.02
A_3, fast	0.25 ± 0.01	0.23 ± 0.02	0.21 ± 0.01

Supplementary Table 3. Diffusion parameters in interface regions obtained from fitting the cumulative distribution of jump distances of Squint upon overexpression of *oep* with 0.3 pg, 3 pg and 30 pg mRNA shown in Figure 5.

Cavity	*oep* 0.3 pg	*oep* 3 pg	*oep* 30 pg
D_1 ($\mu m^2 s^{-1}$)	0.37 ± 0.03	0.38 ± 0.03	0.38 ± 0.04
D_2 ($\mu m^2 s^{-1}$)	5.1 ± 0.6	4.1 ± 0.9	3 ± 1.1
D_3 ($\mu m^2 s^{-1}$)	27 ± 2	27 ± 4	26 ± 3
A_1, immobile	0.13 ± 0.01	0.25 ± 0.02	0.25 ± 0.03
A_2, intermediate	0.3 ± 0.03	0.24 ± 0.03	0.18 ± 0.02
A_3, fast	0.57 ± 0.03	0.51 ± 0.04	0.57 ± 0.03

Supplementary Table 4. Diffusion parameters in cavity regions obtained from fitting the cumulative distribution of jump distances of Squint with overexpression of *oep* with 0.3 pg, 3 pg and 30 pg mRNA shown in Figure 5

	Days	Embryos	Movies	Tracks			Jumps			
				Interface	Cavity	Combined	Interface	Cavity	Combined	Jumps/movie
Cyclops	7	32	128	2837	4063	6900	8569	8685	17254	135.5
Squint (S)	7	33	231	6903	15842	22745	31615	17983	49598	214.7
Lefty1	4	23	289	5012	18474	23486	32295	11050	43345	150.1
Lefty2	4	19	253	9365	28642	38007	62118	21539	83657	330.6
S + 0.3 pg *oep*	2	14	200	2987	6425	9412	12495	7070	19565	103.6
S + 3 pg *oep*	3	20	288	2875	3589	6464	6917	7721	14638	50.8
S + 30 pg *oep*	3	23	255	2729	3067	5796	5533	8224	13757	49.4
sec-Halo	3	20	281	9969	28655	38624	20585	52351	72936	259.6
sec-Halo-GFP	2	14	184	11385	29961	41346	25945	64001	89946	488.8

Supplementary Table 5. Statistics for continuous movie analysis.

	Movies	Tracks	Tracks per movie
Cyclops 12 ms	128	1418	11.1
Squint 12 ms	252	1782	7.1
Cyclops 58 ms	78	883	11.3
Squint 58ms	131	886	6.8
Cyclops 200 ms	91	986	10.8
Squint 200 ms	135	770	5.7
Cyclops 1000 ms	93	550	5.9
Squint 1000 ms	119	508	4.2

Supplementary Table 6. Statistics of single-molecule tracks.
n = 32 embryos in 7 days (Cyclops) and n = 42 embryos in 9 days (Squint) were measured.

	Number of movies in developmental stage						
	128-cell	256-cell	512-cell	1k	high	oblong	sphere
Cyclops	8	37	16	19	11	14	23
Squint	12	44	22	44	51	36	22
Lefty1	7	41	35	69	60	53	24
Lefty2	10	37	51	48	48	49	10

Supplementary Table 7. Statistics of movie numbers for different developmental stages.

4. Paper 3 – Self-organized traveling waves in a synthetic multicellular reaction-diffusion system

4.1. Synopsis

If we understand the principles of biological patterning, can we go one step further and build synthetic multicellular systems capable of pattern formation? Can abstract multicomponent reaction-diffusion networks derived from mathematical analyses be implemented in bacterial cells to enable cell-cell communication and emergence of coordinated multicellular behaviors? To address these questions, we constructed a novel synthetic multicellular system based on a mathematically predicted pattern-forming reaction-diffusion network with positive and negative feedback interactions and diffusible signaling molecules. We investigated the emergence of oscillatory dynamics and spatially periodic patterns of gene expression in the synthetic multicellular system. We observed traveling wave patterns of gene expression which showed an intriguing ability of geometry sensing. This work has implications in understanding design principles of multicellular pattern formation in the context of artificial and embryonic patterning systems (e.g. traveling waves in vertebrate segmentation).

4.2. Author contributions

Here, I highlight my contributions to the project: I contributed to conceptualization of the project and development of the experimental and theoretical methods. I performed the experiments and data analysis. I generated mathematical models, wrote the code, and performed numerical simulations and analysis. I wrote the initial draft of the manuscript. The details on contributions of all co-authors are provided in the manuscript.

Self-organized traveling waves in a synthetic multicellular reaction-diffusion system

Amit Landge[1,2,3], Luciano Marcon[2], Gary Soh[2], Erik Kehr[4], Lennart Lohrmann[4], Stefan Volkwein[4], Patrick Müller[1,2,3,#]

[1]Systems Biology of Development, University of Konstanz, Konstanz (Germany)
[2]Friedrich Miescher Laboratory of the Max Planck Society, Tübingen (Germany)
[3]Centre for the Advanced Study of Collective Behaviour, Konstanz (Germany)
[4]Department of Mathematics, University of Konstanz, Konstanz (Germany)
[#]Correspondence: patrick.mueller@uni-konstanz.de

Abstract

Diffusible signaling molecules are essential for cellular communication, guiding patterning and collective behavior in multicellular systems. Cell signaling combined with positive and negative genetic feedbacks can foster emergent phenomena such as traveling waves of gene activity, which are pivotal in directing morphogenesis and cell migration directionality. Addressing the potential to engineer such phenomena synthetically, we developed a novel bacterial multicellular system with orthogonal and modular synthetic genetic circuits based on diffusible quorum-sensing signals. Through time-lapse imaging in a quasi-2D configuration, we observed the generation of traveling waves. Mathematical models mirrored this behavior, highlighting negative feedback and boundary conditions as key drivers. Additionally, by varying boundary conditions, we demonstrate the system's capability to predictably sense and react to domain boundaries. Our findings not only offer a versatile synthetic platform for probing multicellular collective behaviors but also broaden the understanding of domain sensing and pattern formation mechanisms in multicellular arrangements.

Introduction

Multicellular systems have a remarkable ability to generate complex, self-organized collective behaviors and spatial order by coupling genetic feedback mechanisms with cell-cell signaling mediated by diffusible molecules[1-4]. Cell-cell signaling coupled with genetic feedbacks is important for embryonic patterning[5-7] and forms the basis of many synthetic multicellular systems capable of pattern formation[8-15]. The types of patterning outcomes – such as synchronized oscillations, traveling waves, spatially periodic patterns – are largely determined by the nature of feedback interactions, parameters governing feedback strength, delays, and the range of diffusible signals[16-19]. Particularly, the framework of activator-inhibitor interactions has been widely recognized as the core network for generating temporal oscillations as well as spatially periodic patterns (Fig. 1a)[2-4,14-16,18-22]. In addition, geometric constraints and boundary conditions can further shape key characteristics of the patterns such as size, shape and directionality[10,11,13,23-25].

Many natural as well as synthetic multicellular systems have been shown to exhibit oscillations and traveling waves of gene expression[2]. A prominent example of a natural multicellular oscillator is the vertebrate pre-somitic mesoderm. During somitogenesis, traveling waves of gene-expression in the pre-somitic mesoderm lead to periodic specification of the somites[7]. Negative feedbacks with delay (Fig. 1a) are crucial to generate the oscillatory gene-expression patterns in the pre-somitic mesoderm cells, while the phase of the oscillation depends on the position of the cell along the anterior-posterior axis. The repressilator is a prominent example of a synthetic multicellular system capable of generating oscillatory gene expression patterns, also based on the delayed negative feedback[26]. Artificial multicellular patterning systems have also been developed with embryonic stem cells[10,11]. Human embryonic stem-cells have been shown to generate spatial differentiation patterns reminiscent of embryonic development when they are confined to a micropatterned circular chip. In this system, the radial symmetry

of the micropatterned chip and the loss of diffusible signaling molecules from the colony edge resulted in the emergence of distinct cell-fates at fixed radial positions in the micropatterned stem-cell colonies.

We asked how the interplay of genetic feedbacks, diffusible signals, and system geometry regulates self-organized pattern formation in multicellular systems. To address this question in a tractable modular system, we developed a synthetic feedback network involving diffusible signals. We implemented orthogonal genetic circuits encoding positive and negative feedback networks and cell-cell communication via diffusible quorum sensing molecules in *E. coli* to reveal geometric constraints and boundary conditions that result in different self-organized patterning outcomes. We first characterized the positive and negative feedback modules separately and then combined them to generate the complete genetic circuit. We found that the bacteria engineered with the complete genetic circuit produced traveling waves of fluorescent reporter expression in our quasi-2D multicellular setup. We performed perturbation analyses to show different patterning outcomes and reveal the role of system geometry and boundary conditions in pattern formation.

Results

Design and biological implementation of a synthetic system for pattern formation

We designed a novel genetic network that implements positive and negative feedbacks as well as cell-cell signaling via diffusible molecules. Positive feedbacks are necessary for signal amplification when starting from initial low signal level, and negative feedbacks are important to generate oscillatory dynamics (Fig. 1a). Cell-cell signaling via diffusible signals was incorporated in the system design to enable spatial coupling between cells in a multicellular setup. The synthetic system was implemented in *E. coli* using quorum sensing components (Acyl-Homoserine Lactones, AHLs) which have been widely used and characterized[27].

The system design allows for modular implementation and characterization of positive and negative feedback modules (Fig. 1b,c, Supplementary Fig. 1). The positive feedback module uses N-3-(oxohexanoyl)-L-homoserine lactone (AHL_6) as the diffusible signal from the LuxI-LuxR quorum sensing system of *Vibrio fischeri*[28]. AHL_6 ligands bind to the receptor LuxR to form an AHL_6-LuxR complex, which activates the *pLux* promoter[28]. The *pLux* promoter drives expression of *luxI* encoding the AHL_6-synthase enzyme responsible for the synthesis of AHL_6[29], thus completing the positive feedback loop. A destabilized *superfolder GFP* (*sfGFP-ssrA*)[30,31] reporter was placed under the *pLux* promoter to provide a dynamic readout of the positive feedback module output. To tune the output of the circuit, an arabinose-inducible system was implemented. The *aiiA* gene from *Bacillus thuringiensis*, encoding Lactonase, was placed under the arabinose-inducible *pBAD* promoter. Lactonase can catalyze the cleavage of the lactone ring in the AHL_6 molecules, thus causing AHL_6 degradation[32].

The negative feedback module contains another diffusible signal – N-(3-Oxododecanoyl)-L-homoserine lactone (AHL_{12}) from the LasI-LasR quorum sensing system of *Pseudomonas aeruginosa*[33]. The negative feedback is implemented by inhibition of the *pLas* promoter activity by binding of anti-quorum sensing protein 1 (Aqs1) to LasR[34]. In short, the *pLas* promoter drives expression of AHL_6-synthase (LuxI) leading to the production of AHL_6 and the activation of *pLux* promoter. Aqs1 is expressed under the *pLux* promoter and binds to LasR, thus inhibiting *pLas* promoter activity. Additionally, non-specific binding of AHL_{12} to LuxR can also activate Aqs1 expression under the *pLux* promoter. A destabilized mCherry-ssrA reporter is used in the negative feedback module as the *pLas* activity readout. In both feedback modules, the activator proteins – LuxR and LasR – are produced under constitutive promoters.

We first constructed the positive and negative feedback modules separately and characterized them to ensure proper functioning of the modules. We measured activity of the individual modules in liquid cultures of engineered *E. coli* to obtain temporal dynamics and dose-response characteristics. In parallel,

we developed data-driven mathematical models that could recapitulate key features of the experimental system. Further, we quantified AHL diffusion rates using lawns of AHL sensor strains grown on LB-agar. Then, we combined the modules and tested the emergence of multicellular patterns in quasi-2D lawns of engineered *E. coli*.

Characterization of the feedback modules in engineered E. coli

To quantify the dynamics of the positive feedback module (Fig. 2a) in engineered *E. coli*, we measured sfGFP intensity in homogeneous liquid culture. To screen for optimal circuit output and dynamic range, we generated four distinct plasmids – pAL101, pAL102, pAL103, and pAL104 (Supplementary Fig. 1). The plasmids pAL101 and pAL103 contain different *pLux* promoter sequences, with pAL103 having a more stringent version[35]. The plasmids pAL102 and pAL104 were generated by deletion of the *luxR* cassette from the pAL101 and pAL103 plasmids, respectively. We tested these plasmids in the *E. coli* Marionette strain, which contains a chromosomal copy of *luxR* under a constitutive promoter[35].

We observed that the strains carrying pAL101 and pAL103 maintained high levels of sfGFP output for up to 12 h in liquid culture at 37°C (Fig. 2b, Supplementary Fig. 2, Supplementary Fig. 4), while strains carrying the plasmids pAL102 and pAL104 showed transiently high levels of sfGFP intensity (Supplementary Fig. 3, Supplementary Fig. 5). The pAL102 and pAL104 strains have a single chromosomal copy of *luxR*, unlike the pAL101 and pAL103 strains that additionally express *luxR* from the plasmids. Consequently, we observed high *luxR* mRNA levels for the pAL101 strain compared to the pAL102 strain (Supplementary Fig. 3i). This could explain the overall high sfGFP levels in the pAL101 and pAL103 strains (Supplementary Fig. 2a, Supplementary Fig. 3a, Supplementary Fig. 4a, Supplementary Fig. 5a).

Next, we asked if arabinose-inducible expression of Lactonase (aiiA) (Fig. 2a) could control the output of the circuit by tunable degradation of AHL_6. Upon arabinose treatments, the mRNA levels of *aiiA* were increased as expected (Supplementary Fig. 2g, Supplementary Fig. 3g). The dose-response analysis (Supplementary Fig. 4d) showed arabinose dose-dependent decrease in sfGFP intensities. Particularly, arabinose doses of 1000 nM and higher could strongly decrease sfGFP output. The inhibitory threshold concentration of arabinose was estimated to be in the range 480 nM to 1402 nM (Supplementary Fig. 2d, Supplementary Fig. 3d, Supplementary Fig. 4d, Supplementary Fig. 5d; Supplementary Table 3). The pAL103 circuit, which had the highest dynamic range (Supplementary Table 3), was selected for further analysis. Based on these experimental data, we devised a mathematical model to recapitulate the positive feedback circuit dynamics and dose-response behavior *in silico* (Supplementary Fig. 4e, Supplementary Note 1).

To simplify the implementation and characterization of the negative feedback module, we further divided it into submodules – AHL_{12} sensor, AHL_{12} production, and LasR inhibition (Fig. 2e-f, Supplementary Fig. 1, Supplementary Fig. 6a). The AHL_{12} sensor plasmid consists of destabilized mCherry (mCherry-ssrA) expressed under the AHL_{12}-inducible *pLas* promoter. The activator protein LasR – needed to form the AHL_{12}-LasR complex – is expressed under a constitutive promoter (Supplementary Fig. 1a). We characterized the dose-response behavior of the circuit output (mCherry fluorescence) under different levels of AHL_{12}, to find a robust induction with high dynamic range and low leakiness with an activation threshold concentration of 76 ± 4 nM (Fig. 2g, Supplementary Fig. 6b-e). Moreover, qRT-PCR analysis showed that the mCherry expression was AHL_{12}-specific (Supplementary Fig. 6f), and mCherry mRNA levels increased with increasing dosage of AHL_{12} (Supplementary Fig. 6g) while LasR mRNA levels were not strongly affected (Supplementary Fig. 6h-i). Based on these experimental results, we developed a mathematical model for AHL_{12} sensor module (Supplementary Note 1) to recapitulate the observed mCherry output dynamics and dose-response profile (Supplementary Fig. 6e).

The negative feedback on the mCherry output is implemented by inhibition of the activator protein LasR. We utilized Aqs1 from phage DMS3 to inhibit LasR[34]. To this end, we generated the LasR inhibition plasmid by placing *Aqs1* under the *pLux* promoter and co-transformed it along with the AHL_{12} sensor plasmid into the Marinette strain. We first tested whether the LasR inhibition strain – carrying both the AHL_{12} sensor and LasR inhibition plasmids – can give tunable mCherry fluorescence output upon treatment with different AHL_{12} concentrations (Fig 2i). The activation threshold concentration of AHL_{12} was 93 ± 2 nM (Supplementary Fig. 6j). Note, that this activation threshold is higher than that for the AHL_{12} sensor strain (Supplementary Fig. 6d), because in the LasR inhibition strain AHL_{12} can also partially activate the *Aqs1* expression via cross-reactivity with the *pLux* promoter (Supplementary Fig. 6l). Moreover, addition of 1 μM AHL_6 increased the activation threshold to 160 ± 22 nM (Supplementary Fig. 6j). Thus, Aqs1 can inhibit LasR to tune the output of the negative feedback module. A mathematical model of the negative feedback module implementing increased AHL_{12} threshold via Aqs1-mediated LasR-inhibition successfully captured the observed dose-response behavior in numerical simulations (Supplementary Fig. 6k).

In the synthetic network (Fig. 1c), the input of AHL_{12} needs to be dynamically controlled. To this end, we cloned the AHL_{12} synthase gene *LasI* under anhydrotetracycline (ATc)-inducible *pTet* promoter[36] to generate the AHL_{12} production plasmid (Supplementary Fig. 1c). This plasmid was designed such that it can be maintained along with the AHL_{12} sensor plasmid in the Marionette strain. A dose-response assay was performed for the co-transformed strain (termed the 'AHL_{12} production strain') to quantify mCherry fluorescence output under different ATc treatments (Fig. 2h). The highest fluorescence normalized to cell density (OD_{600}) was achieved at 10 nM ATc treatment (Fig. 2i, Supplementary Fig. 6n). Considerable basal mCherry intensity was observed, possibly due to leaky expression of *LasI*. As expected, qRT-PCR analysis showed that *LasI* mRNA levels increased in a dose-dependent manner upon ATc treatment (Supplementary Fig. 6o), but very high LasI mRNA levels (for ATc ≥ 100 nM) did not result in a corresponding increase in mCherry fluorescence output (Fig. 2h). On the contrary, we observed a decrease in mCherry mRNA levels as well as fluorescence readout (Supplementary Fig. 6p, Fig. 2h). These data suggest that the AHL_{12} production strain can give basal *pLas* promoter activation through leaky production of AHL_{12} synthase enzyme (LasI) and even higher *pLas* activity is achieved by increasing AHL_{12} production at 10 nM ATc induction.

As we wanted to study the role of feedback networks as well as diffusible signals in multicellular pattern formation, we next characterized the diffusion rates of AHLs using lawns of AHL sensor strains on agar.

Estimation of AHL diffusion rates using sensor strains

To estimate the diffusion coefficients of AHL molecules in our experimental setup, we used AHL sensor strains that show dose-dependent fluorescent reporter expression upon AHL treatment (Supplementary Fig. 9a, Supplementary Fig. 6d, Supplementary Fig. 8d). We added a known amount of AHL at the center of the lawn of the sensor cells growing on nutrient agar. The gradient of AHL concentration created by diffusion led to a fluorescent reporter signal gradient (Supplementary Fig. 9a). This fluorescence gradient was quantified at multiple time points to generate dynamic radial profiles that expanded radially outward as the AHL molecules diffused in the sensor cell lawn. Mathematical models of the sensor strain dynamics (Supplementary Note 1) were used to obtain simulated radial profiles. We estimated AHL diffusion coefficients by fitting these simulated profiles to experimental profiles (Supplementary Fig. 9b-e). To validate our method, we performed measurements and fits with gradients generated by fluorescein-labeled dextran molecules under the same experimental conditions and using the same fitting methods (Supplementary Fig. 9f).

We found that the diffusion coefficient estimates for dextrans were 120 ± 5 and 67 ± 12 $\mu m^2/s$ for 3 kDa and 10 kDa dextrans, respectively (Supplementary Fig. 9f, Supplementary Table 4), similar to previously reported values[37]. Our method slightly underestimates the diffusion rates because we approximate the geometry of the system as 1D in our numerical simulations, whereas in the experimental setup the molecules diffuse in the 3D agar slab (diameter ~35 mm, thickness ~1 mm). For AHL_6 and AHL_{12}, we estimated diffusion coefficients of 313 ± 69 and 320 ± 59 $\mu m^2/s$, respectively. Here, we didn't compare the estimates for AHL_6 and AHL_{12}, because the fluorescent reporters used in AHL_6 sensor and AHL_{12} sensor strains have different maturation kinetics. Overall, we generated useful estimates of AHL diffusion coefficients in our experimental setup. These estimates were used to further develop mathematical models of spatial pattern formation in the synthetic multicellular system.

Next, all the characterized parts were combined to generate two compatible plasmids (Supplementary Fig. 1d) carrying the complete synthetic genetic network. We introduced them into the Marionette strain to generate the complete circuit strain for analysis of multicellular pattern formation.

The synthetic multicellular system generates spontaneous traveling waves

We developed a time-lapse imaging method to test for emergence of spatiotemporal patterns in quasi-2D lawns of the engineered *E. coli* strains (Fig. 3a). A multicellular lawn of engineered *E. coli* was created by carefully pipetting cells mixed with low-melting-temperature agarose gel onto a plate containing LB-agar medium and incubated for 2 h at 37°C. Then, fluorescence and bright-field images were obtained at 15 min intervals using an automated microscope.

We expected that the engineered cells may show dynamic oscillations of fluorescence output because of the implemented genetic feedback loops. Interestingly, we observed spontaneous traveling waves of mCherry fluorescence (Fig. 3b-d, Supplementary Movie 1). The dynamics of the traveling waves can be elucidated using space-time plots of the measured fluorescence intensities. First, the mCherry fluorescence increased uniformly for 6 h, except for the lower intensity at the lawn periphery. The lower signal at the lawn periphery is likely due to lower cell-density at the periphery as observed in the bright-field channel (Supplementary Movie 1). The first traveling wave was observed as the signal decayed radially outward, followed by the initiation of the second traveling wave at the lawn center at ~10 h. The second wave reached the edge of the lawn at ~16 h. Quantification of the mean fluorescence intensity of the lawn over time showed a single peak for sfGFP, whereas oscillatory dynamics were observed for mCherry (Fig. 3e). For mCherry, the fluorescence signal increased for the first 6 h. But, as the first wave propagated outward the signal decreased (mostly at the center), reaching a minimum at ~11 h. After the initiation of the second wave, at ~12 h, the signal increased until 18 h, followed by a slight decrease afterwards. Some of the movies were continued until 26 h, but initiation of a third wave was not observed. To validate that the traveling wave patterns are specific to the synthetic circuit, we imaged the original Marionette strain (no-plasmid control) and constitutive mCherry expression strain (control for plasmid-specific effects) using the same experimental setup (Supplementary Fig. 10, Supplementary Movie 2). The no-plasmid control showed basal auto-fluorescence signal for both sfGFP and mCherry, whereas the constitutive mCherry expression strain showed slowly increasing levels of mCherry signal, which were above the auto-fluorescence background, but much lower than the synthetic circuit mCherry levels. The space-time analysis of mCherry fluorescence signal clearly showed the traveling waves for the complete circuit strain, which were absent in the control strains (Supplementary Fig. 10, Supplementary Movie 2). These data suggest that the traveling wave patterns are specific to our synthetic circuit strain.

We developed a mathematical model of the complete synthetic circuit, based on previous experimental characterization data and the models of the feedback modules (Supplementary Note 1). Numerical simulations of the mathematical model in 1D and 2D geometry recapitulated the experimental observation

of traveling wave patterns (Fig. 3f-h, Supplementary Movie 6). The simulations further suggested that the initial gradient in the cell-density profile was important for emergence of the traveling waves (Supplementary Fig. 11, Supplementary Movie 6). Because, in the uniform cell density condition, oscillations in the mCherry levels could be seen, but no traveling waves were observed.

Perturbation analysis reveals the role of geometry for pattern formation

In multicellular patterning networks, system geometry may serve as an important determinant of pattern initiation, directionality and dynamics. Hence, we assessed the role of geometry on traveling wave dynamics and wave direction by varying lawn size and lawn position (Fig. 4a). In the standard experimental setup, we loaded 20 µl of the cell suspension onto the LB agar, creating a lawn of ~10 mm diameter. We generated a small lawn of ~8 mm diameter by loading 10 µl of cell-mix and a large lawn covering the entire well (~16 mm diameter) by loading 40 µl of the cell suspension. We hypothesized that the diffusion of AHL molecules into the agar not covered by the cell lawn may regulate the traveling wave dynamics. Particularly, smaller lawns have larger free agar area around them, acting as a sink. AHLs can diffuse into this area from the lawn boundary and hence smaller lawns may show slower traveling wave dynamics, whereas larger lawns retain almost all of the produced AHLs inside and hence may display faster dynamics. Indeed, we observed that the big lawn showed faster appearance and decay of sfGFP signal and fast traveling waves of mCherry signal, albeit with a much lower amplitude (Fig. 4b, Supplementary Movie 2). The small lawn, conversely, showed slower or delayed traveling wave dynamics. The sfGFP signal decayed much slower, and the second wave of mCherry signal was delayed by ~4 h. Quantification of mean fluorescence intensities over the lawn area further supported delayed wave dynamics in the smaller lawns (Fig. 4c,d). Our mathematical simulations in 1D and 2D qualitatively recapitulated the experimental findings (Fig. 4e,f, Supplementary Movie 7). In the mathematical model, we assumed that nutrient depletion due to cell division and growth may lead to reduced rates of AHL production (Supplementary Note 1). This accounted for the faster sfGFP dynamics in bigger lawns (Fig. 4c,e), but the 1D simulations only partially recapitulated the mCherry dynamics (Fig. 4d,f).

We observed radially isotropic wave propagation in the standard size experimental setup. We asked if the wave propagation can become anisotropic in response to varying the position of the lawn with respect to the domain boundary (Fig. 4a). We tested off-center and at-edge lawn positions – generated by loading 20 µl of the cell suspension at a slightly off-center position in the well and closer to the edge of the well, respectively. For the off-center lawn position, initially the sfGFP and mCherry signals appeared starting from the lawn center, however the subsequent wave propagation was no longer radially isotropic (Fig. 4g-j, Supplementary Movie 4). We observed that the wave initial center no longer coincided with the lawn center, but it was shifted closer to the well boundary (left side in Fig. 4g). We performed a space-time analysis by dividing the lawn region into left (closer to well boundary) and right subregions. The space-time plots prominently showed traveling waves in the right subregion but not in the left one (Fig. 4h,i, Supplementary Movie 4). Numerical simulations also showed the anisotropy in the wave propagation (Fig. 4j, Supplementary Movie 8). Further, the wave propagation anisotropy was even more pronounced when the lawn was positioned at the edge of the well (Fig. 4k-m, Supplementary Movie 4). These results indicate that the directional loss of diffusible signals (AHLs) from the cell-lawn into the cell-free agar as well as reflective boundary conditions determine the direction of the traveling waves.

Our characterization experiments showed that arabinose-inducible expression of lactonase can inhibit the positive feedback circuit output via tunable AHL degradation (Fig. 2c). Hence, we reasoned that perturbation by addition of arabinose would reduce overall AHL levels thereby abolishing the traveling waves. To test our reasoning, we perturbed the system with three different arabinose treatments - 1 nM, 1 µM and 1 mM (Supplementary Fig. 12a). Since the threshold concentration of arabinose is in the

micromolar range (Supplementary Fig. 4d, Supplementary Table 3), 1 nM treatment did not show a strong effect on the traveling waves as compared to controls (Supplementary Fig. 12b-e, Supplementary Movie 5). Treatment with 1 μM arabinose reduced the sfGFP signal peak, but the mCherry traveling waves were still observed (Supplementary Movie 5). Strikingly, 1 mM arabinose treatment reduced sfGFP signal almost completely, and a single peak of mCherry signal was observed (Supplementary Fig. 12d-e). The mCherry peak signal was increased ~5-fold compared to the control condition. Presumably, the complete reduction of *pLux* activity, due to AHL_6 degradation, reduced the Aqs1 levels so low that LasR inhibition was negligible, leading to the observed high mCherry levels. However, it is surprising that mCherry levels increase rather than reducing upon 1 mM arabinose treatment, because lactonase is also able to degrade AHL_{12}[38]. These results can be explained if the rate of AHL_{12} degradation by lactonase is much lower than the rate of AHL_6 degradation. Previous studies have reported that lactonase shows slower hydrolysis rates for AHL substrates with longer acyl chains[38]. In our mathematical model, we implemented a 10-fold lower rate of AHL_{12} degradation compared to the rate of AHL_6 degradation. In the simulations, we could recapitulate the decrease in sfGFP levels and a single mCherry peak upon 1 mM arabinose treatment (Supplementary Fig. 12f-h). Overall, we conclude that the perturbations using 1 mM arabinose abolished the second traveling wave via AHL degradation.

Discussion

Engineering self-organizing multicellular patterning systems with controllable behavior has been a long-standing challenge in synthetic biology[27,39,40]. Here, we advanced the capabilities and framework for synthetic multicellular pattern formation by implementing a novel multicomponent genetic circuit with feedback networks and diffusible signaling molecules. We used a modular circuit design framework for the positive and negative feedback modules. The modular design allowed us to characterize the system parts separately before building the complete synthetic circuit. Using the experimental data on system kinetics and dose-response profiles, we devised data-driven mathematical models that could recapitulate key dynamical aspects of the experimental system. Finally, we combined the modules into a complete synthetic circuit that could generate traveling waves of gene expression in a multicellular lawn of the engineered *E. coli*. These traveling waves are reminiscent of traveling waves in somitogenesis[2,7]. Using mathematical modeling and perturbation analyses, we showed that the traveling waves arise due to the interplay of feedback circuits, initial conditions, and boundary conditions. Particularly, initial radial gradient of cell-density generated in our experimental setup was necessary to introduce the phase shifts that led to the traveling wave phenomenon. Further, we found that in our system, geometric parameters (lawn size, lawn position) play a crucial role in determining wave propagation dynamics and isotropy.

The role of negative feedbacks with delay has been previously explored in biological oscillators[7,26]. Similarly, in our system the delayed negative feedback is provided by inhibition of LasR by Aqs1. As multiple intermediate steps of transcription and translation are required to implement the delayed negative feedback, the period of oscillation in our system is in the range of 8-10 h leading to two oscillations during the 24-hour experimental time. We also emphasize the role of boundary conditions in generating radially symmetric patterns. Previous studies have shown that loss of signaling molecules from the lawn edge can give rise to radially symmetric patterns of gene expression[10,11]. In our system, the diffusible signaling molecules diffuse into the cell-free area of the agar from the edge of the bacterial lawn. When the lawn center was positioned at the center of the LB-agar in the well, we observed radially isotropic traveling wave patterns. These traveling waves became anisotropic when the center of the lawn was shifted closer to the well boundary. Thus, the boundary conditions of the patterning system provide an additional mechanism to control the directionality of the traveling waves.

Implementation of synthetic multicomponent gene networks in bacteria poses some practical limitations. Our orthogonal synthetic circuit uses the cellular resources, for example – biosynthesis of the AHL molecules requires S-adenosyl-methionine, which is also important for cell division[41]. A future challenge will be to generate more sustainable synthetic circuits that consume minimal cellular resources or that integrate into the cellular metabolic pathways to reduce the burden of implementing the artificial network. We used destabilized fluorescent reporters to obtain a dynamic readout of the synthetic circuit performance, and it will be useful to encode morphogenetic changes as the circuit output[8,9]. We avoided effects of cell movement by embedding the bacterial cells in a gel of low-melting-temperature agarose. However, in the context of collective multicellular behaviors, the role of cell motility on dynamic traveling waves of gene expression may provide new insights into emergent properties of cell collectives. Overall, our synthetic multicellular system offers a simple, tunable test-bed for the investigation of multicellular pattern formation and collective multicellular behaviors.

Acknowledgments

This project has received funding from the European Research Council (ERC) under the European Union's Horizon 2020 research and innovation program (grant agreement No 863952 (ACE-OF-SPACE)). This work was also funded by the Max Planck Society, the EMBO Young Investigator Program and the Deutsche Forschungsgemeinschaft (DFG, German Research Foundation) under Germany's Excellence Strategy – EXC 2117 – 422037984. We are grateful to support from the Blue Sky research program of the University of Konstanz (Project EvoDevoGPT).

Author contributions

Conceptualization: AL, LM, PM; Methodology: AL, GS, EK, LL, SV, PM; Investigation: AL, EK, LL; Visualization: AL, PM; Funding acquisition: PM; Project administration: PM; Writing: AL, PM. The authors declare that they have no competing interests.

Materials and Methods

Plasmid design and cloning

In general, all plasmid sequences were designed using SnapGene or SeqBuilder. The sequences of the genetic parts were obtained from iGEM parts repository (http://parts.igem.org/Catalog) and previous studies[12,42,43]. All plasmids were designed rationally based on the synthetic genetic circuit design. The circuit was implemented in parts on different plasmids to enable characterization of the output of each part. The AHL_6 sensor plasmid pBC-A1-001 was a gift from Brian Chow[42] (Addgene plasmid # 78688, http://n2t.net/addgene:78688, RRID: Addgene_78688). All the other plasmids were designed in the lab and either ordered as synthetic DNA fragments (Synbio Technologies) or cloned using standard molecular cloning techniques. The details are given below.

The pAL101 plasmid was generated as follows. pTD103luxI_sfGFP[43] (from Jeff Hasty (Addgene plasmid # 48885, http://n2t.net/addgene:48885, RRID: Addgene_48885)) was digested with EcoRI; the backbone containing *LuxI* and *LuxR* coding sequences was self-ligated and introduced into One Shot™ TOP10 chemically competent *E. coli* (Catalog number: C404010) by heat-shock transformation method, and transformants were selected using kanamycin. The resulting plasmid was then modified by addition of a C-terminal 6xHIS tag to *LuxI* using site-directed mutagenesis (Q5® Site-Directed Mutagenesis Kit - E0554S; primers- 2985, 2986). Correct clones were identified by sanger sequencing (primers – 2973, 2974, 2975, 2976). Another site-directed mutagenesis was performed to insert a constitutive promoter (BBa_J23100, http://parts.igem.org/Part:BBa_J23100) upstream *LuxR* (primers 2987, 2988). The correct clones were identified by sanger sequencing (primers - 2973, 2974, 2975, 2976). The plasmid was digested with ClaI and EcoRI and then assembled with DNA fragments containing aiiA (under pBAD promoter) and sfGFP (under *pLux* promoter) using Gibson assembly method (Gibson Assembly® Cloning Kit - E5510S). The aiiA and sfGFP fragments were generated by PCR (aiiA fragment: [template: pTurL1, synthetic DNA (BioCat GmbH)] [primers: 3086,3087], sfGFP fragment: [template: pTD103luxI_sfGFP –R, Addgene plasmid # 48887] [primers: 3088,3089]). The final resultant plasmid has sfGFP and LuxI under *pLux* promoters, LuxR under the constitutive promoter, and aiiA under the pBAD promoter. The plasmid sequence was confirmed using sanger sequencing (primers – 2973, 2976, 2977, 2978, 2496, 2497).

The pAL102 plasmid was generated from the pAL101 plasmid by deletion of the *LuxR* cassette using the site-direction mutagenesis method (Q5® Site-Directed Mutagenesis Kit, primers – 4093, 4094).

The pAL103 plasmid was generated from the positive-feedback circuit (1) plasmid by restriction digestion (XmaI and EcoRI) and ligation with insert containing a modified *pLux* promoter (primers – 4466, 4467). This resulted in a plasmid with a single stringent *pLux* promoter driving both *sfGFP* and *LuxI* bicistronically.

The pAL104 plasmid was generated from the pAL103 plasmid by deletion of the *LuxR* cassette using the site-direction mutagenesis method (Q5® Site-Directed Mutagenesis Kit, primers – 4093, 4094).

The entire sequence for the negative feedback circuit plasmids was ordered as two synthetic DNA fragments (from BioCat and Synbio Technologies) with compatible restriction sites (XhoI and AsiSI). The synthetic fragments were restriction digested and ligated to generate a plasmid called pAL201. pAL201.1 was created from pAL201 by restriction digestion with PacI and self-ligation. pAL201.2 was created from pAL201.1 by modifying the ribosome-binding-site (RBS) upstream *LasI* using site-directed-mutagenesis (primers - 4201, 4202). Spacer sequences flanking *LasR* cassette were added by PCR (primers- 4254, 4255) and the amplicon was cloned into pAL201 backbone using FseI and XmaI sites to generate the plasmid pAL201.4.

The AHL_{12}-sensor plasmid (pAL201.5) was created from pAL201.4. The coding sequence of *LuxR* was PCR amplified (primers – 4275, 4276) from pAL201.4 with flanking spacer[44] sequences and restriction sites (AscI, XmaI); the pAL201.4 vector and the PCR amplified insert were restriction digested with AscI and XmaI and ligated followed by transformation and selection of correct clones.

The AHL_{12} production plasmid (pAL209) was generated by performing multiple cloning steps as follows. The plasmid pAL205 was obtained by digesting pTD103aiiA(Cm)-R (a gift from Jeff Hasty (Addgene plasmid # 48888, http://n2t.net/addgene:48888, RRID:Addgene_48888) with XhoI and AvrII and ligated with *LasI-Myc* which was PCR amplified from plasmid pAL203 (primers – 4352, 4353) and digested with the same restriction enzymes. The plasmid pAL203 was generated by addition of mfLon (Lon protease from *Mesoplasma florum*) and *LasI-Myc* cassettes to pAL201.5 by Gibson cloning method. The chloramphenicol resistance gene of pAL205 was replaced with ampicillin resistance gene by restriction digestion and ligation to yield pAL206. The Myc-tag was deleted from LasI in pAL206 by site-directed mutagenesis (primers - 4416, 4417) to yield pAL209.

The LasR inhibition (1) plasmid (pAL210) and LasR inhibition (2) plasmid (pAL211) were generated as follows. A synthetic DNA fragment containing coding sequence of anti-quorum-sensing protein 1 (Aqs1[34]) with flanking *pLux* promoter, RBS and terminator sequences was cloned into pAL206 backbone using restriction digestion with XhoI and AvrII and ligation to get resulting pAL210 plasmid. The pAL210 plasmid was modified with site-directed mutagenesis method (primers – 4456, 4457) to replace the *pLux* promoter and RBS, respectively with a more stringent *pLux* and a weaker RBS, resulting in pAL211.

The LasR inhibition (3) plasmid (pAL207) and LasR inhibition (4) plasmid (pAL212) were generated as follows- The *mfLon* coding sequence along-with upstream *pLux* promoter, RBS and downstream terminator sequences was PCR amplified (primers – 4397, 4398) using pAL203 as template and cloned into the pAL206 backbone using AvrII and XhoI restriction sites to create plasmid pAL207. The pAL207 plasmid was modified with site-directed mutagenesis method (primers – 4458, 4459) to replace the *pLux* promoter and RBS, respectively with a more stringent *pLux* and a weaker RBS, resulting in pAL212.

AHL_{12} production + LasR inhibition (pAL214) plasmid was generated by combining the pAL209 (AHL_{12} production, pTet:LasI) and pAL211 (LasR inhibition, *pLux*:Aqs1) plasmids. To this end, pTet:LasI cassette was PCR amplified (primers 4561, 4562) from pAL209 and cloned into pAL211 using the XhoI restriction site.

AHL_{12} sensor + AHL_6 synthase (pAL215) plasmid was generated by inserting AHL_6 synthase gene under *pLas* promoter (*pLas*:LuxI-FLAG from pAL201) to the pAL201.5 (AHL_{12} sensor) plasmid. To this end, *pLas*:LuxI-FLAG cassette was PCR amplified (primers 4554, 4555) from pAL201 and cloned into pAL201.5 using the PacI restriction site. This plasmid contains kanamycin resistance gene (*nptII*).

The plasmid pAL214_103 was generated by combining the all the positive feedback circuit parts form pAL103 with the pAL214 plasmid. To this end, the positive loop circuit sequences were PCR amplified from pAL103 (primers 4586, 4587) and cloned into pAL214 using the AatII restriction site. This resulted in the plasmid pAL214_103 with ampicillin resistance marker gene and the circuit parts for positive feedback + AHL_{12} production + LasR inhibition.

The plasmid pAL214_104 was generated similarly to the pAL214_103 plasmid. Here, pAL104 was used to PCR amplify the positive loop parts. Note that, pAL104 lacks the *LuxR* sequence.

Generation of E. coli strains for characterization of the synthetic genetic circuits

E. coli (strain: Marionette- sAJM.1504 from Christopher Voigt (Addgene # 108251)[35]) were transformed with the plasmid to be characterized using the electroporation method (voltage = 1.8 kV, 1 mm cuvette, BIO-RAD MicroPulser). The transformants were selected using an appropriate antibiotic. Glycerol stocks were prepared from overnight grown cultures (200 rpm, 37°C, ~12 h) by mixing 0.5 ml of culture with 0.5 ml of 50% glycerol (v/v, aq.) and stored at -80°C.

Implementation of synthetic circuits was achieved by transformation of *E. coli* with the plasmids listed in the table below:

#	***Synthetic circuit strain***	***Plasmid(s)***	***Ori***	***Antibiotic***
1	AHL_6 sensor (in DH5α strain)	pBC-A1-001[42]	pMB1	Chloramphenicol
2	AHL_{12} sensor	pAL201.5	pMB1	Kanamycin
3	Positive feedback circuit (1)	pAL101	pMB1	Kanamycin
4	Positive feedback circuit (2)	pAL102	pMB1	Kanamycin
5	Positive feedback circuit (3)	pAL103	pMB1	Kanamycin
6	Positive feedback circuit (4)	pAL104	pMB1	Kanamycin
7	AHL_{12} production circuit	pAL209	p15A	Ampicillin
8	LasR inhibition circuit (1) – Aqs1 based	pAL211	p15A	Ampicillin
9	LasR inhibition circuit (2) – mfLon based	pAL212	p15A	Ampicillin
10	AHL_{12} production and LasR inhibition (1) (Aqs1 based) circuits	pAL214	p15A	Ampicillin
11	AHL_{12} sensor and AHL_6 production (via *pLas*:LuxI-FLAG) circuits	pAL215	pMB1	Kanamycin
12	AHL_{12} production, LasR inhibition (1) (Aqs1 based), and positive feedback (3) circuits	pAL214_103	p15A	Ampicillin
13	AHL_{12} production, LasR inhibition (1) (Aqs1 based), and positive feedback (4) circuits	pAL214_104	p15A	Ampicillin
14	AHL_{12} sensor and AHL_{12} production circuits	pAL201.5, pAL209	pMB1, p15A	Kanamycin, Ampicillin
15	AHL_{12} sensor and LasR inhibition (1) (Aqs1 based) circuits	pAL201.5, pAL211	pMB1, p15A	Kanamycin, Ampicillin

16	AHL_{12} sensor and LasR inhibition (2) (mfLon based) circuits	pAL201.5, pAL212	pMB1, p15A	Kanamycin, Ampicillin
17	Negative loop [AHL_{12} sensor, AHL_{12} production and LasR inhibition (1)] circuit	pAL201.5, pAL214	pMB1, p15A	Kanamycin, Ampicillin
18	Negative loop [AHL_{12} sensor, AHL_{12} production and LasR inhibition (1)] circuit + AHL_6 production (*pLas*:LuxI-FLAG)	pAL215, pAL214	pMB1, p15A	Kanamycin, Ampicillin
19	Complete synthetic circuit (1)	pAL214_103, pAL215	p15A, pMB1	Ampicillin, Kanamycin
20	Complete synthetic circuit (2)	pAL214_104, pAL215	p15A, pMB1	Ampicillin, Kanamycin
21	Constitutive mCherry circuit	pAL000	pMB1	Kanamycin

Fluorescence quantification in liquid culture

For analysis of dose-response behavior of engineered *E. coli* strains to treatment with different inducer doses, fluorescence measurements were performed for liquid cultures in a 96-well plate. To this end, bacterial primary cultures were grown overnight (~12 h) in LB medium at 37°C and 200 rpm, (Sartorius Certomat® IS UHK-25), starting from single colonies or glycerol stocks. The next day, a secondary culture was inoculated and allowed to grow until early log phase of growth (optical density at 600 nm (OD_{600}) of 0.4). The cells were harvested by centrifugation (2000 rcf, Eppendorf centrifuge 5424) and re-suspended in fresh LB medium. The treatments were performed in 1.5 ml sterile tubes by adding calculated amounts of inducer to 1 ml of the bacterial culture. The culture was transferred to 96-well plates (Corning® 3904). The fluorescence intensities and OD_{600} values were measured using a plate-reader instrument (TECAN infinite M200 PRO).

Diffusion coefficient estimation using sensor strains

Diffusion coefficients of the AHLs were estimated in LB-agar at 37°C by adding a known amount of the AHL to the center of the lawn of corresponding AHL sensor strain and analyzing the fluorescence gradient produced by the sensor strain. In detail, overnight primary culture and following secondary culture of AHL sensor strain was grown as described above. Then, cells were harvested by centrifugation and re-suspended in LB medium to an effective OD_{600} of 1.0. This resuspension was used to coat a plate with ~ 1 mm layer of LB-agar and grown at 37°C for 4 h to generate a near-uniform bacterial lawn. A known amount of corresponding AHL (1 µl of 1 µM) was added to the center of the lawn to induce expression of a fluorescent reporter (sfGFP for AHL_6 and mCherry for AHL_{12}). Images were acquired every hour (0 h to 4h) using Axio Zoom V16 (ZEISS). Control measurements with fluorescent dextrans (3 kDa and 10 kDa) were performed using the same setup to validate the method and compare the results in other methods.

Radial profiles of fluorescent intensity were measured using FiJi (Radial Profile plugin) and saved as .csv files. A custom python script was developed (https://github.com/mueller-lab/SyntheticPatterns/) to generate simulated datasets and estimate the diffusion coefficients by fitting the simulated profiles to

the experimental data. The noisy ends of the gradients were omitted while generating the fits. The mathematical models were based on the experimental data of the reaction kinetics in liquid cultures obtained using plate reader assays. FiPy[45] was used to solve PDEs describing the mathematical models. The SciPy[46] library of Python (scipy.optimize.minimize) was used for solving the optimization problem to get the fit.

Fluorescence imaging of bacterial lawn

A quasi-2D time-lapse imaging method was developed for the analysis of spatiotemporal patterning in a multicellular lawn of the synthetic bacterial strains. First, the bacteria were grown overnight in LB medium containing the proper antibiotic at 200 rpm and 37°C. The next day, a secondary culture was started by inoculating the overnight culture in plain LB medium (1/100 dilution). After the OD_{600} of 0.4 was reached, the cells were harvested by centrifugation and re-suspended in a gel of 0.5% low-melting-temperature agarose (NuSieve™ GTG™ Agarose, Catalog #: 50080) to make a cell-agarose mixture with 5-fold higher cell density than that of the 0.4 OD_{600} culture. This cell-mixture was then loaded carefully on LB-agar in a 24-well plate to get a lawn of bacteria. We note that the slight curvature of the agar surface causes a slightly higher initial cell-density at the middle of the well. The cells were allowed to grow for two hours before making treatments and starting the time-lapse imaging.

Time-lapse imaging was performed using an automated high-throughput fluorescence microscope (Keyence BZ-X810). Images were acquired using a 2x apochromat objective (PlanApo 2x 0.10/8.50mm) with 3.7 W LED transmitted light source, and an 80 W metal halide lamp or 40 W LED as fluorescent light source. Images were saved as 8 bit, 480 × 360-pixel or 1920 × 1440 pixel TIFF files.

Image analysis

Image analysis was performed using FiJi (ImageJ 2.9.0/1.53t). For Image stitching and quantifications were performed using a custom ImageJ macro (https://github.com/mueller-lab/SyntheticPatterns/). The quantifications of mean-intensity and radial fluorescence profile were saved as .csv files and plotted using custom Python code (https://github.com/mueller-lab/SyntheticPatterns/). The BaSiC ImageJ plugin was used for shading correction[47].

Quantitative reverse transcription PCR (qRT-PCR)

Bacterial cells were harvested as described in the *Fluorescence quantification in liquid culture* section. The treatments were performed in 1.5 ml sterile tubes by adding calculated amounts of inducer to 1 ml of the bacterial culture and it was incubated for 4 h at 37°C and 200 rpm. The cells were pelleted at 2000 rcf with a standard tabletop centrifuge (Eppendorf 5424). Total RNA was extracted using NucleoZOL (# 740404.200) method. Synthesis of cDNA was performed using up to 1 µg of total RNA and the SuperScript™ III First-Strand Synthesis SuperMix (# 11752050) kit. No-reverse transcription control reactions were performed in parallel. The cDNA was 5-fold diluted with nuclease-free water and used to set up the qPCR reaction with appropriate primers and the Platinum™ SYBR™ Green qPCR SuperMix-UDG kit (# 11733038). The qPCR reaction and quantification were performed using the CFX Connect Real-Time PCR Detection System. Data analysis and plotting was performed using Python (https://github.com/mueller-lab/SyntheticPatterns/).

Mathematical modeling

Mathematical models were developed to numerically simulate system dynamics using known interactions and reaction kinetics and also to predict system behavior upon perturbations. All equations are described in Supplementary Note 1, and parameter values are provided in Supplementary Table 1. All numerical simulations were performed by implementing the FiPy (a finite volume PDE solver)[45] in a custom python code (available at https://github.com/mueller-lab/SyntheticPatterns/). The simulations

were performed on a discrete 1D or 2D grid with zero-flux boundary conditions. The simulation results for Fig. 3, Fig. 4, Supplementary Fig. 11-12 were generated by performing 1D simulations and setting the simulation conditions (initial and boundary conditions) as closely matching the experimental conditions as possible. We further confirmed these findings in more relevant 2D simulations (Supplementary Movies 6-8).

Data and code availability

The open-source code along with example data is available from https://github.com/mueller-lab/SyntheticPatterns/.

Figure Legends

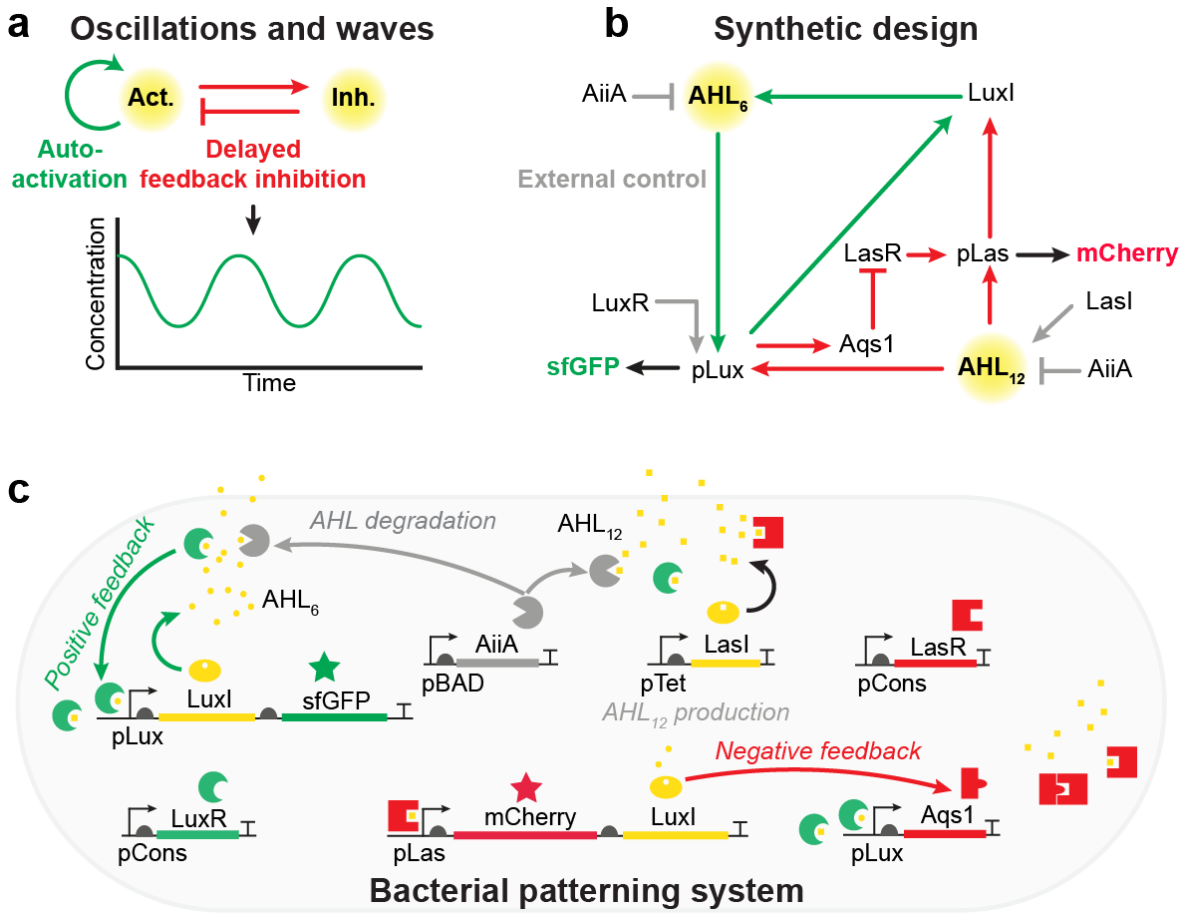

Figure 1 | Design of a synthetic multicellular system with genetic feedbacks and diffusible signals. **(a)** A conceptual framework for different biological oscillators. **(b)** Detailed network diagram showing the complete genetic interaction network with positive feedback module (green) and negative feedback module (red). Diffusible components are indicated by a yellow halo. AHL_6: N-(3-Oxohexanoyl)-L-homoserine lactone, AHL_{12}: N-(3-Oxododecanoyl)-L-homoserine lactone, AiiA: Lactonase, LuxI: AHL_6 synthase, LasI: AHL_{12} synthase, LuxR and LasR: activator proteins specific to respective *pLux* and *pLas* promoters, Aqs1: anti quorum sensing protein 1, sfGFP and mCherry: destabilized fluorescent reporters to monitor dynamic circuit output, ssrA: protein-degradation tag, pBAD: arabinose inducible promoter, *pLux*: AHL_6–inducible promoter (*pLux* is also activated non-specifically by AHL_{12}), *pLas*: AHL_{12}-inducible promoter. **(c)** A schematic of a bacterial cell engineered to execute the synthetic network with genetic feedbacks. AHL_6 signal provides positive feedback to drive more AHL_6 synthesis. The *pLas* system promotes expression of Aqs1 which provides negative feedback for *pLas* activity. The AHLs are degraded by Lactonase (*AiiA*) driven under an arabinose-inducible pBAD promoter. AHL_{12} production by LasI is placed under the anhydrotetracycline-inducible pTet system.

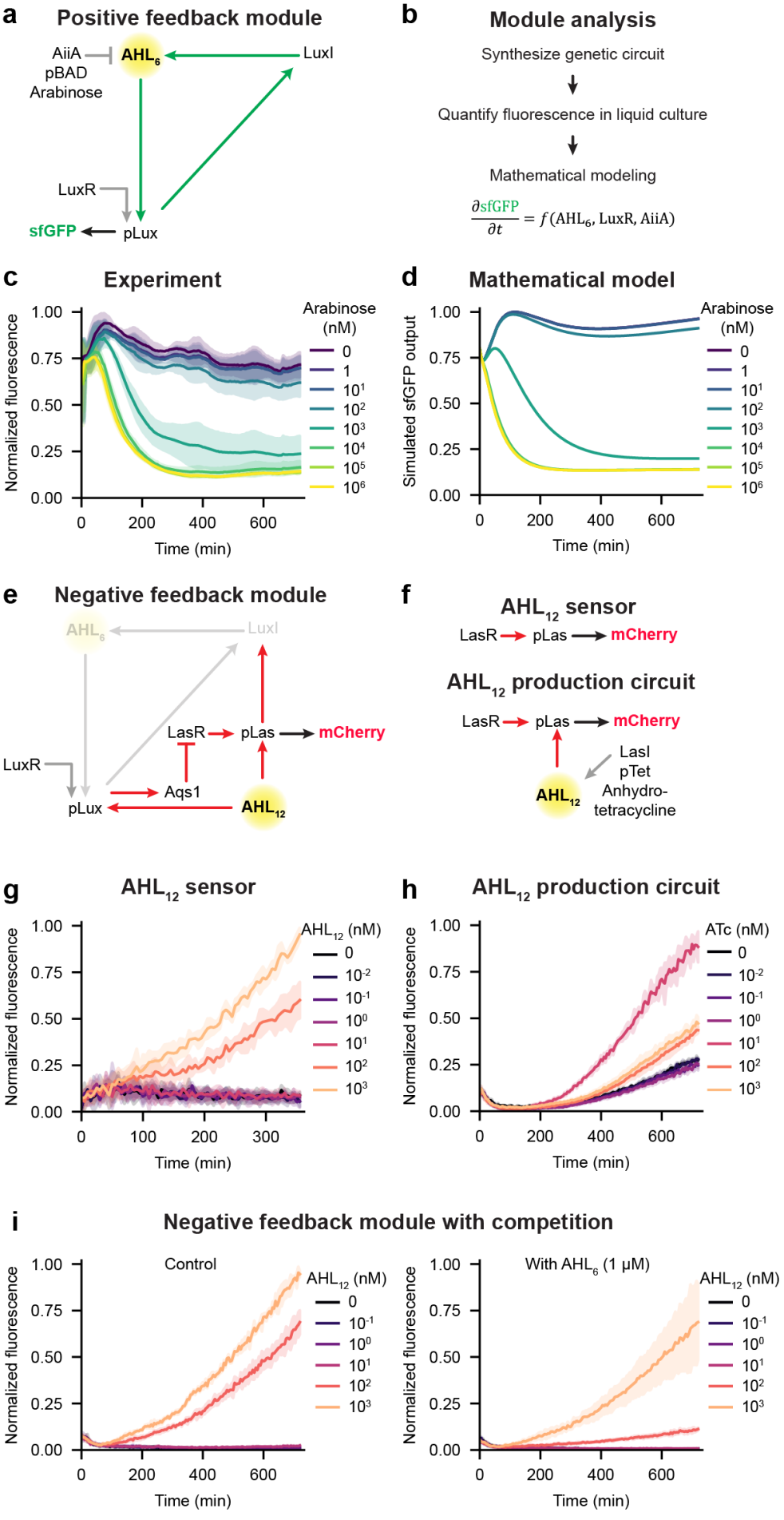
a
Positive feedback module
AiiA
pBAD
Arabinose
AHL6
LuxI
LuxR
sfGFP
pLux
b
Module analysis
Synthesize genetic circuit
Quantify fluorescence in liquid culture
Mathematical modeling
∂sfGFP/∂t = f(AHL6, LuxR, AiiA)
c
Experiment
Normalized fluorescence
Time (min)
Arabinose (nM)
0
1
10^1
10^2
10^3
10^4
10^5
10^6
d
Mathematical model
Simulated sfGFP output
Time (min)
Arabinose (nM)
e
Negative feedback module
AHL6
LuxI
LasR
pLas
mCherry
LuxR
Aqs1
pLux
AHL12
f
AHL12 sensor
LasR
pLas
mCherry
AHL12 production circuit
LasR
pLas
mCherry
LasI
pTet
Anhydro-tetracycline
AHL12
g
AHL12 sensor
Normalized fluorescence
Time (min)
AHL12 (nM)
0
10^-2
10^-1
10^0
10^1
10^2
10^3
h
AHL12 production circuit
Normalized fluorescence
Time (min)
ATc (nM)
i
Negative feedback module with competition
Control
With AHL6 (1 μM)
Normalized fluorescence
Time (min)
AHL12 (nM)

Figure 2 | Characterization of *E. coli* strains engineered with the positive-feedback and negative-feedback modules. (a) Schematic of the positive-feedback module. The AHL_6 signal induces expression of LuxI (AHL_6 synthase) under the *pLux* promoter. The activator protein – LuxR – is expressed under a constitutive promoter. AHL degradation can be carried out by arabinose-inducible expression of AiiA (Lactonase). **(b)** Module analysis strategy. **(c-d)** Time-series plots showing sfGFP fluorescence (normalized by OD_{600}) for positive feedback strain carrying plasmid pAL103 for different arabinose treatments. (c) shows experimental data (n = 3 biological replicates with 2 technical replicates each), (d) shows simulation results of a mathematical model of the positive-feedback module. **(e)** Schematic showing the negative-feedback module **(f)** The module is divided into – AHL_{12} sensor, LasR inhibition, and AHL_{12} production submodules. AHL_{12} sensor, and AHL_{12} production submodules are shown. LasR inhibition submodule inhibition of LasR by *pLux* via Aqs1. **(g)** For the AHL_{12} sensor submodule, time-series of mCherry fluorescence intensity (normalized by OD_{600}) for different AHL_{12} doses is shown (n = 2 biological replicates with 2 technical replicates each). **(h)** For the AHL_{12} production submodule, time-series of mCherry fluorescence intensity (normalized by OD_{600}) for different ATc doses (n = 1 biological replicate with 3 technical replicates) is shown. **(i)** For the LasR inhibition module, time-series plots of mCherry fluorescence intensity (normalized by OD_{600}) for different AHL_{12} doses, without AHL_6 (left) and with 1 μM AHL_6 (right), is shown. (n = 1 biological replicate with 3 technical replicates).

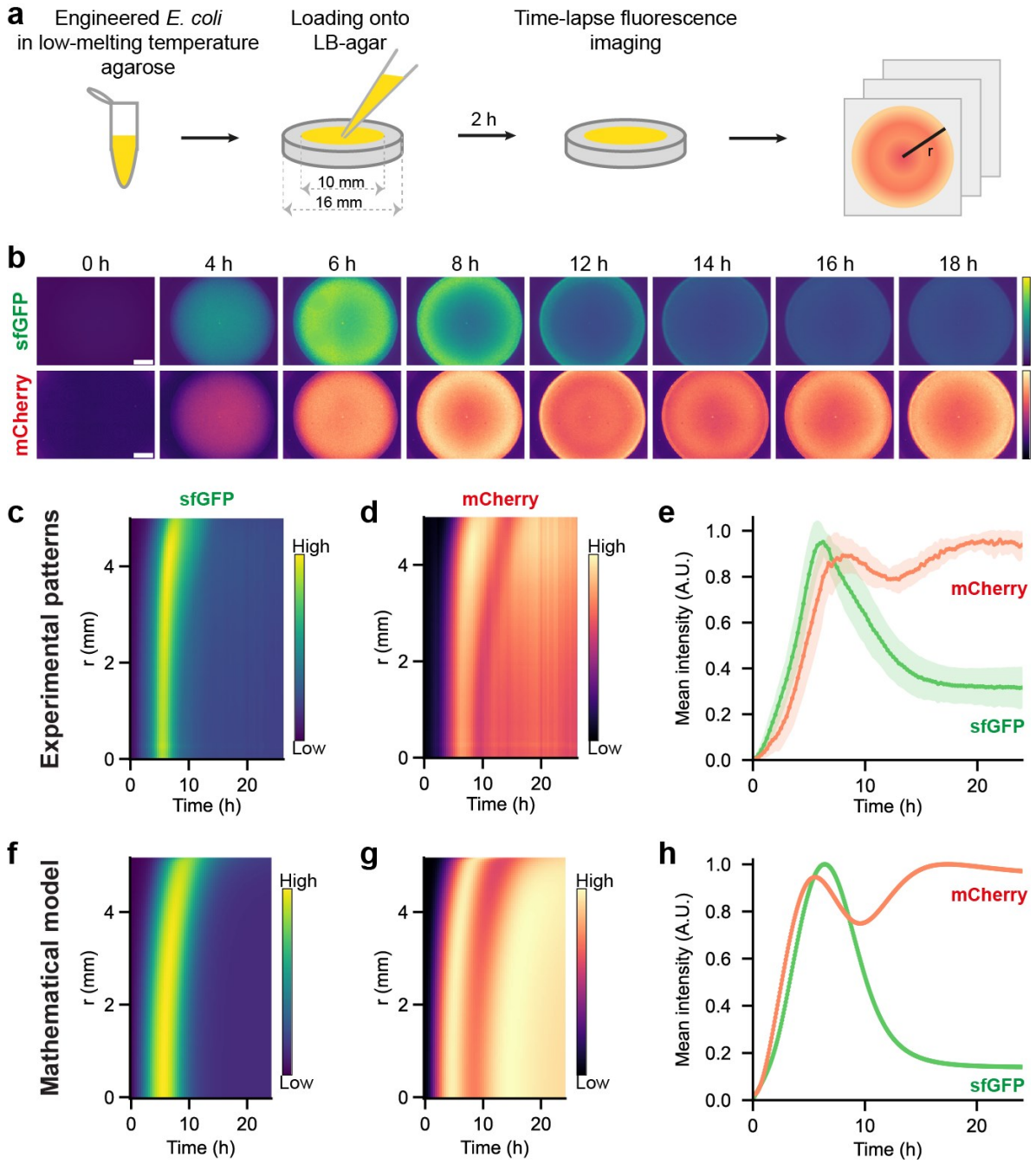

Figure 3 | Spontaneous traveling-wave patterns emerge in a lawn of the engineered *E. coli*. (a) Schematic depicting the method to test for emergence of spatiotemporal patterns in a quasi-2D lawn of the engineered *E. coli*. **(b)** Fluorescence images showing sfGFP and mCherry signal in the lawn of *E. coli* engineered with the complete synthetic circuit. The gray value range (16-bit images) is adjusted for better visualization (sfGFP: 10-255, mCherry: 20-60). Viridis and magma lookup tables are applied to sfGFP and mCherry images, respectively. Scale-bar: 2 mm. **(c, d)** Space-time plots showing radially averaged (c) sfGFP and (d) mCherry intensities at 15 min intervals for 24 h. **(e)** Quantification of sfGFP and mCherry mean intensities in the lawn area. n = 9 biological replicates. **(f-h)** Numerical simulation results showing space-time plots of (f) sfGFP and (g) mCherry and (h) mean sfGFP and mCherry outputs over time.

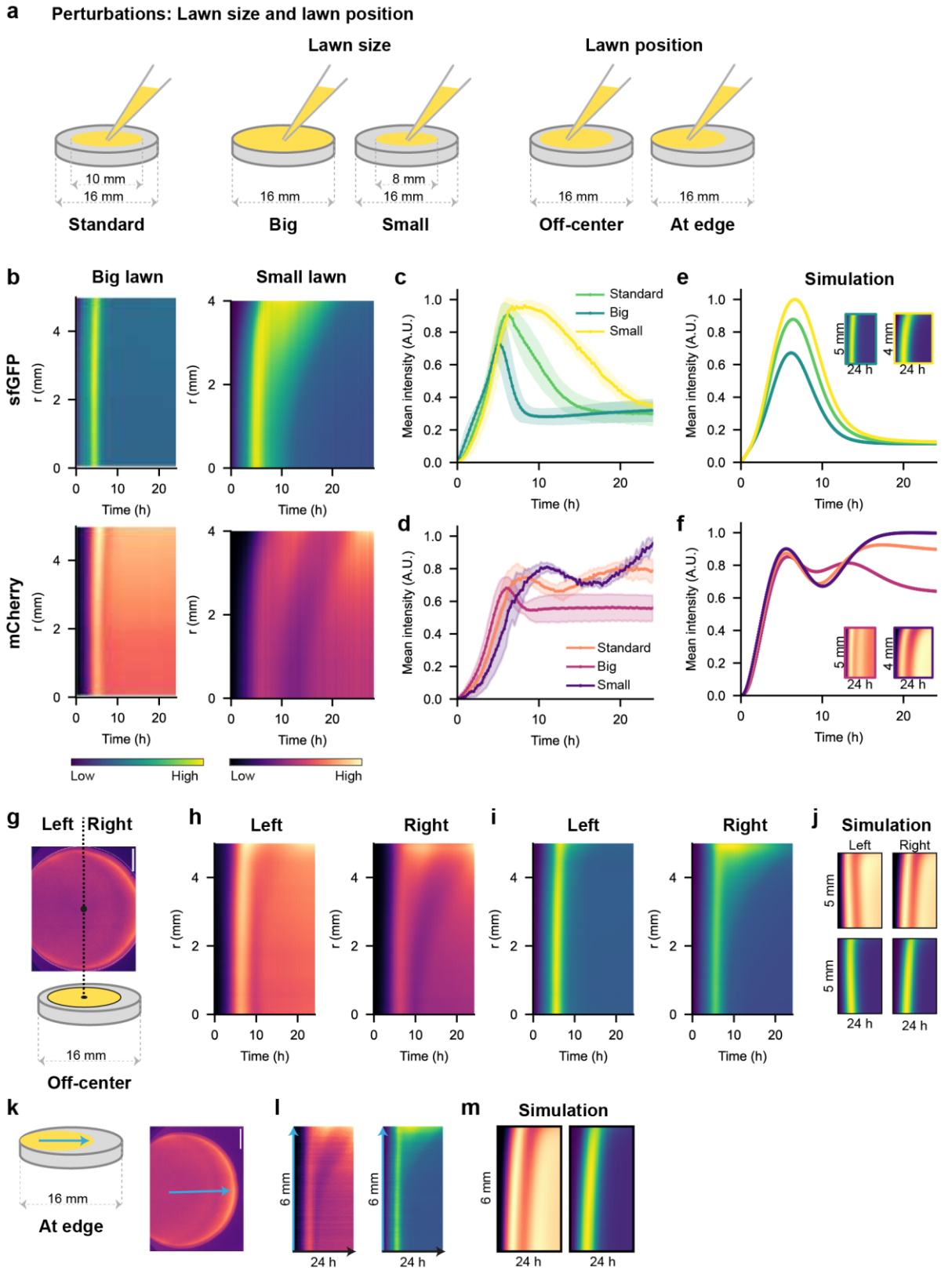

Figure 4 | Perturbation analysis to reveal boundary effects on the traveling-wave patterns. (a) Schematic showing different perturbations to assess boundary effects on pattern formation. **(b)** Representative space-time plots of sfGFP and mCherry fluorescence for big and small lawn sizes (n = 6 biological replicates). **(c, d)** Mean intensities of (c) sfGFP and (d) mCherry in the lawn area for the different lawn sizes. (n = 6 biological replicates for big and small lawns). The data for standard lawn size is the same as in Fig. 4e. **(e, f)** Simulated (e) sfGFP and (f) mCherry mean intensities for the three

lawn sizes. Insets show simulated space time plots of (e) sfGFP and (f) mCherry for the big and small lawn sizes (the plot borders are color coded). **(g)** Illustration of quantification method used to analyze effect of lawn position (off-center) on the direction of wave propagation (propagation anisotropy). A representative image of mCherry fluorescence is shown (scale bar: 2 mm). The lawn is assigned left and right sides based on the shift of the lawn center. Radial profiles of fluorescence intensity are quantified in the semicircular region on each side. **(h, i)** Representative space-time plots of (h) mCherry and (i) sfGFP intensities on the left and right sides of the off-center lawn (n = 6 biological replicates). **(j)** Simulated space-time plots of mCherry and sfGFP for the off-center lawn condition. **(k, l)** Illustration showing the method used to measure space-time profile for the at-edge lawn position. A representative mCherry fluorescence image for this condition, indicating with a blue arrow the region used for generating space-time plots in (l). Here, radial profiles of fluorescence were not generated, instead the region-of-interest (blue arrow) was manually selected in the direction of wave-propagation. (l) Space-time plots of mCherry and sfGFP fluorescence for the at-edge lawn position (n = 6 biological replicates). **(m)** Simulated space-time profiles of mCherry and sfGFP fluorescence generated by implementing the at-edge lawn position in the custom python code.

References

1 Landge, A. N., Jordan, B. M., Diego, X. & Müller, P. Pattern formation mechanisms of self-organizing reaction-diffusion systems. *Developmental Biology* **460**, 2-11 (2020). https://doi.org:10.1016/j.ydbio.2019.10.031

2 Deneke, V. E. & Di Talia, S. Chemical waves in cell and developmental biology. *J Cell Biol* **217**, 1193-1204 (2018). https://doi.org:10.1083/jcb.201701158

3 Kondo, S. & Miura, T. Reaction-diffusion model as a framework for understanding biological pattern formation. *Science* **329**, 1616-1620 (2010). https://doi.org:10.1126/science.1179047

4 Gierer, A. & Meinhardt, H. A theory of biological pattern formation. *Kybernetik* **12**, 30-39 (1972). https://doi.org:10.1007/BF00289234

5 Raspopovic, J., Marcon, L., Russo, L. & Sharpe, J. Digit patterning is controlled by a Bmp-Sox9-Wnt Turing network modulated by morphogen gradients. *Science* **345**, 566-570 (2014). https://doi.org:10.1126/science.1252960

6 Müller, P. *et al.* Differential diffusivity of nodal and lefty underlies a reaction-diffusion patterning system. *Science* **336**, 721-724 (2012). https://doi.org:10.1126/science.1221920

7 Dequéant, M.-L. & Pourquié, O. Segmental patterning of the vertebrate embryonic axis. *Nature Reviews Genetics* **9**, 370-382 (2008). https://doi.org:10.1038/nrg2320

8 Gu, F. *et al.* A synthetic population-level oscillator in non-microfluidic environments. *Communications Biology* **6**, 515 (2023). https://doi.org:10.1038/s42003-023-04904-0

9 Duran-Nebreda, S. *et al.* Synthetic Lateral Inhibition in Periodic Pattern Forming Microbial Colonies. *ACS Synthetic Biology* **10**, 277-285 (2021). https://doi.org:10.1021/acssynbio.0c00318

10 Tewary, M. *et al.* A stepwise model of reaction-diffusion and positional information governs self-organized human peri-gastrulation-like patterning. *Development* **144**, 4298-4312 (2017). https://doi.org:10.1242/dev.149658

11 Warmflash, A., Sorre, B., Etoc, F., Siggia, E. D. & Brivanlou, A. H. A method to recapitulate early embryonic spatial patterning in human embryonic stem cells. *Nature Methods* **11**, 847-854 (2014). https://doi.org:10.1038/nmeth.3016

12 Danino, T., Mondragón-Palomino, O., Tsimring, L. & Hasty, J. A synchronized quorum of genetic clocks. *Nature* **463**, 326-330 (2010). https://doi.org:10.1038/nature08753

13 Cao, Y. *et al.* Collective Space-Sensing Coordinates Pattern Scaling in Engineered Bacteria. *Cell* **165**, 620-630 (2016). https://doi.org:https://doi.org/10.1016/j.cell.2016.03.006

14 Sekine, R., Shibata, T. & Ebisuya, M. Synthetic mammalian pattern formation driven by differential diffusivity of Nodal and Lefty. *Nat Commun* **9**, 372490-372490 (2018). https://doi.org:10.1101/372490

15 Karig, D. *et al.* Stochastic Turing patterns in a synthetic bacterial population. *Proceedings of the National Academy of Sciences of the United States of America* **115**, 6572-6577 (2018). https://doi.org:10.1073/pnas.1720770115

16 Scholes, N. S., Schnoerr, D., Isalan, M. & Stumpf, M. P. H. A Comprehensive Network Atlas Reveals That Turing Patterns Are Common but Not Robust. *Cell Systems* **9**, 243-257.e244 (2019). https://doi.org:10.1016/j.cels.2019.07.007

17 Diego, X., Marcon, L., Muller, P. & Sharpe, J. Key Features of Turing Systems are Determined Purely by Network Topology. *Physical Review X* **8**, 021071-021071 (2018). https://doi.org:10.1103/PhysRevX.8.021071

18 Zheng, M. M., Shao, B. & Ouyang, Q. Identifying network topologies that can generate turing pattern. *Journal of Theoretical Biology* **408**, 88-96 (2016). https://doi.org:10.1016/j.jtbi.2016.08.005

19 Marcon, L., Diego, X., Sharpe, J. & Muller, P. High-throughput mathematical analysis identifies Turing networks for patterning with equally diffusing signals. *Elife* **5** (2016). https://doi.org:10.7554/eLife.14022

20 Marcon, L. & Sharpe, J. Turing patterns in development: What about the horse part? *Curr Opin Genet Dev* **22**, 578-584 (2012). https://doi.org:10.1016/j.gde.2012.11.013

21 Maini, P. K., Woolley, T. E., Baker, R. E., Gaffney, E. A. & Seirin Lee, S. Turing's model for biological pattern formation and the robustness problem. *Interface Focus* **2**, 487-496 (2012). https://doi.org:10.1098/rsfs.2011.0113

22 Andresén, P., Bache, M., Mosekilde, E., Dewel, G. & Borckmanns, P. Stationary space-periodic structures with equal diffusion coefficients. *Physical Review E - Statistical Physics, Plasmas, Fluids, and Related Interdisciplinary Topics* **60**, 297-301 (1999). https://doi.org:10.1103/PhysRevE.60.297

23 Almuedo-Castillo, M. *et al.* Scale-invariant patterning by size-dependent inhibition of Nodal signalling. *Nature Cell Biology* **20**, 1032-1042 (2018). https://doi.org:10.1038/s41556-018-0155-7

24 Othmer, H. G. & Pate, E. Scale-invariance in reaction-diffusion models of spatial pattern formation. *Proceedings of the National Academy of Sciences of the United States of America* **77**, 4180-4184 (1980). https://doi.org:10.1073/pnas.77.7.4180

25 Umulis, D. M. & Othmer, H. G. The importance of geometry in mathematical models of developing systems. *Curr Opin Genet Dev* **22**, 547-552 (2012). https://doi.org:10.1016/j.gde.2012.09.007

26 Elowitz, M. B. & Leibler, S. A synthetic oscillatory network of transcriptional regulators. *Nature* **403**, 335-338 (2000). https://doi.org:10.1038/35002125

27 Oliver Huidobro, M., Tica, J., Wachter, G. K. A. & Isalan, M. Synthetic spatial patterning in bacteria: advances based on novel diffusible signals. *Microb Biotechnol* **15**, 1685-1694 (2022). https://doi.org:10.1111/1751-7915.13979

28 Fuqua, C., Winans, S. C. & Greenberg, E. P. CENSUS AND CONSENSUS IN BACTERIAL ECOSYSTEMS: The LuxR-LuxI Family of Quorum-Sensing Transcriptional Regulators. *Annual Review of Microbiology* **50**, 727-751 (1996). https://doi.org:10.1146/annurev.micro.50.1.727

29 Parsek, M. R., Val, D. L., Hanzelka, B. L., Cronan, J. E. & Greenberg, E. P. Acyl homoserine-lactone quorum-sensing signal generation. *Proceedings of the National Academy of Sciences* **96**, 4360-4365 (1999). https://doi.org:doi:10.1073/pnas.96.8.4360

30 Flynn, J. M. *et al.* Overlapping recognition determinants within the ssrA degradation tag allow modulation of proteolysis. *Proceedings of the National Academy of Sciences* **98**, 10584-10589 (2001). https://doi.org:10.1073/pnas.191375298

31 Karzai, A. W., Roche, E. D. & Sauer, R. T. The SsrA–SmpB system for protein tagging, directed degradation and ribosome rescue. *Nature Structural Biology* **7**, 449-455 (2000). https://doi.org:10.1038/75843

32 Billot, R. *et al.* Engineering acyl-homoserine lactone-interfering enzymes toward bacterial control. *J Biol Chem* **295**, 12993-13007 (2020). https://doi.org:10.1074/jbc.REV120.013531

33 Pearson, J. P., Pesci, E. C. & Iglewski, B. H. Roles of Pseudomonas aeruginosa las and rhl quorum-sensing systems in control of elastase and rhamnolipid biosynthesis genes. *Journal of Bacteriology* **179**, 5756-5767 (1997). https://doi.org:10.1128/jb.179.18.5756-5767.1997

34 Shah, M. *et al.* A phage-encoded anti-activator inhibits quorum sensing in Pseudomonas aeruginosa. *Molecular Cell* **81**, 571-583.e576 (2021). https://doi.org:https://doi.org/10.1016/j.molcel.2020.12.011

35 Meyer, A. J., Segall-Shapiro, T. H., Glassey, E., Zhang, J. & Voigt, C. A. Escherichia coli "Marionette" strains with 12 highly optimized small-molecule sensors. *Nature Chemical Biology* **15**, 196-204 (2019). https://doi.org:10.1038/s41589-018-0168-3

36 Gossen, M. & Bujard, H. Tight control of gene expression in mammalian cells by tetracycline-responsive promoters. *Proceedings of the National Academy of Sciences* **89**, 5547-5551 (1992). https://doi.org:doi:10.1073/pnas.89.12.5547

37 Bläßle, A. *et al.* Quantitative diffusion measurements using the open-source software PyFRAP. *Nature Communications* **9**, 1582 (2018). https://doi.org:10.1038/s41467-018-03975-6

38 Wang, L.-H., Weng, L.-X., Dong, Y.-H. & Zhang, L.-H. Specificity and Enzyme Kinetics of the Quorum-quenching N-Acyl Homoserine Lactone Lactonase (AHL-lactonase)*. *Journal of Biological Chemistry* **279**, 13645-13651 (2004). https://doi.org:https://doi.org/10.1074/jbc.M311194200

39 Toda, S., Brunger, J. M. & Lim, W. A. Synthetic development: learning to program multicellular self-organization. *Current Opinion in Systems Biology* **14**, 41-49 (2019). https://doi.org:10.1016/j.coisb.2019.02.008

40 Santos-Moreno, J. & Schaerli, Y. Using Synthetic Biology to Engineer Spatial Patterns. *Advanced Biosystems* **3**, 1800280-1800280 (2019). https://doi.org:10.1002/adbi.201800280

41 Newman, E. B. *et al.* Lack of S-adenosylmethionine results in a cell division defect in Escherichia coli. *J Bacteriol* **180**, 3614-3619 (1998). https://doi.org:10.1128/jb.180.14.3614-3619.1998

42 Magaraci, M. S. *et al.* Toolbox for Exploring Modular Gene Regulation in Synthetic Biology Training. *ACS Synth Biol* **5**, 781-785 (2016). https://doi.org:10.1021/acssynbio.6b00057

43 Prindle, A. *et al.* A sensing array of radically coupled genetic 'biopixels'. *Nature* **481**, 39-44 (2012). https://doi.org:10.1038/nature10722

44 Carr, S. B., Beal, J. & Densmore, D. M. Reducing DNA context dependence in bacterial promoters. *PLoS One* **12**, e0176013 (2017). https://doi.org:10.1371/journal.pone.0176013

45 Guyer, J. E., Wheeler, D. & Warren, J. A. FiPy: Partial Differential Equations with Python. *Computing in Science & Engineering* **11**, 6-15 (2009). https://doi.org:10.1109/MCSE.2009.52

46 Virtanen, P. *et al.* SciPy 1.0: fundamental algorithms for scientific computing in Python. *Nature Methods* **17**, 261-272 (2020). https://doi.org:10.1038/s41592-019-0686-2

47 Peng, T. *et al.* A BaSiC tool for background and shading correction of optical microscopy images. *Nature Communications* **8**, 14836 (2017). https://doi.org:10.1038/ncomms14836

Supplementary Information

Self-organized traveling waves in a synthetic multicellular reaction-diffusion system

Amit Landge[1,2,3], Luciano Marcon[2], Gary Soh[2], Erik Kehr[4], Lennart Lohrmann[4], Stefan Volkwein[4], Patrick Müller[1,2,3,#]

[1]Systems Biology of Development, University of Konstanz, Konstanz (Germany)

[2]Friedrich Miescher Laboratory of the Max Planck Society, Tübingen (Germany)

[3]Centre for the Advanced Study of Collective Behaviour, Konstanz (Germany)

[4]Department of Mathematics, University of Konstanz, Konstanz (Germany)

[#]Correspondence: patrick.mueller@uni-konstanz.de

Contents

Supplementary Note 1

Mathematical modeling

We built the step-by-step mathematical models in line with our experimental approach to design and implement the modular circuits. First, we consider the AHL sensor module.

Model 1: AHL_6 sensor

The following system of PDEs describes the AHL_6 sensor model. The sensor works by activation of pLux promoter by cooperative binding of AHL_6 and LuxR. The cooperativity is implemented by using a Hill-type function for LuxR-AHL_6 complex formation - $H(X, Y, K_T, nH, k_{leak})$.

$$H(X, Y, K_T, nH, k_{leak}) = X\left(k_{leak} + \frac{Y^{nH}}{K_T^{nH} + Y^{nH}}\right); 1 \leq n \leq 3;$$

$$\frac{\partial}{\partial t} LuxR = k_{prot} - k_{d_{prot}} LuxR$$

$$\frac{\partial}{\partial t} AHL_6 = -k_{d_{ahl}} AHL_6 + D_6 \nabla^2 AHL_6$$

$$\frac{\partial}{\partial t} GFP = k_{gfp} LuxR_{AHL6} - k_{d_{ssrA}} GFP$$

with $LuxR_{AHL6} = H(LuxR, AHL_6, K_{T6}, nH_6, k_{leak})$. AHL_6 was varied in the range [0,1000] nM.

We estimated the parameter values for this model from our experimental data (Supplementary Fig. 8b-e). For some parameters, reported estimates from literature were used [1] (Supplementary Table 1). The model was simulated using the FiPy solver[2] and the results are shown in Supplementary Fig. 8f,g.

Model 2: AHL_{12} sensor

This model describes dose-response behavior of the AHL_{12} sensor, similar to Model 1.

$$\frac{\partial}{\partial t} LasR = k_{prot} - k_{d_{prot}} LasR$$

$$\frac{\partial}{\partial t} AHL_{12} = -k_{d_{ahl}} AHL_{12} + D_{12} \nabla^2 AHL_{12}$$

$$\frac{\partial}{\partial t} mCherry = k_{mChr} LasR_{AHL12} - k_{d_{ssrA}} mCherry$$

with $LasR_{AHL12} = H(LasR, AHL_{12}, K_{T12}, nH_{12}, k_{leak})$. AHL_{12} was varied in the range [0.01,1000] nM.

The results of numerical simulations are shown in Fig. 2h,j.

Model 3: Positive feedback module

Here, we consider the mathematical model for the positive feedback loop implemented by expressing the gene responsible for AHL_6 production, i.e. *LuxI*, under AHL_6-inducible pLux promoter. This model is generated by extending the Model 1 to include pLux-driven AHL_6 production and arabinose-driven AHL_6 degradation.

$$\frac{\partial}{\partial t}LuxR = k_{prot} - k_{d_{prot}}LuxR$$

$$\frac{\partial}{\partial t}AHL_6 = k_{ahl}LuxI - AHL_6\left(k_{d_{ahl}} + k_{d1_{ahl}}AiiA\right) + D_6\nabla^2 AHL_6$$

$$\frac{\partial}{\partial t}sfGFP = k_{sfGFP}LuxR_{AHL6} - k_{d_{ssrA}}sfGFP$$

$$\frac{\partial}{\partial t}AiiA = k_{prot}ara_{indc} - k_{d_{ssrA}}AiiA$$

$$\frac{\partial}{\partial t}LuxI = k_{prot}LuxR_{AHL6} - k_{d_{ssrA}}LuxI$$

with $LuxR_{AHL6} = H(LuxR, AHL_6,\ K_{T6}, nH_6,\ k_{leak})$. This Hill-type term controls production of LuxI and sfGFP in AHL_6 concentration-dependent manner.

$ara_{indc} = H(10, ara,\ K_{Tara}, nH_{ara},\ k_{leak})$. *ara* was varied in the range [0, 10^6].

The simulation results are shown in Fig. 2c,e. The parameter values are provided in Supplementary Table 1.

Model 4: Negative feedback module (AHL_{12} sensor + LasR inhibition)

The negative feedback in implemented by expression of an inhibitor of LasR - Aqs1 - under the pLux promoter. This model simulates the behavior of AHL_{12} sensor + LasR inhibition circuit.

$$\frac{\partial}{\partial t}LasR = k_{prot} - k_{d_{prot}}LasR$$

$$\frac{\partial}{\partial t}mCherry = k_{mCherry}LasR_{AHL12} - k_{d_{ssrA}}mCherry$$

$$\frac{\partial}{\partial t}Aqs1 = k_{prot}(LuxR_{AHL6} + LuxR_{AHL12}) - k_{d_{prot}}Aqs1$$

with $LasR_{AHL12} = H(LasR, AHL_{12}, K^*_{T12}, nH_{12}, k_{leak})$, where K^*_{T12} is given by

$$K^*_{T12} = \frac{K_{T12}}{H\left(1.0, K_{Taqs}, Aqs1, nH_{aqs}, k_{leak}\right)}$$

implementing the Aqs1-mediated inhibition of LasR-AHL_{12}. AHL_{12} levels were varied in the range [0.1,1000] similar to the dose-response assay.

$LuxR_{AHL6} = H(LuxR, AHL_6,\ K_{T6}, nH_6,\ k_{leak})$; AHL_6 is 0 nM or 1000 nM.

$LuxR = 10$; is assumed to be at the steady-state level. LuxR is expressed from the Marionette strain chromosome under a constitutive promoter.

$LuxR_{AHL12} = H(LuxR, AHL_{12}, K_{T12xR}, nH_{12}, k_{leak})$ gives the non-specific activation of the *pLux* promoter by binding of LuxR and AHL_{12}. The simulation results are shown in Fig. 2n. The parameter

values are provided in Supplementary Table 1. Next, we consider spatiotemporal dynamics of the complete synthetic multicellular system combining the positive and negative feedback modules.

Model 5: Complete synthetic circuit

To explain the emergence of traveling wave patterns in the experimental system and make predictions about how the patterns can be modified with different perturbations, we developed a mathematical model of the complete synthetic circuit. The PDE-based mathematical model considers key variables and parameters of the system to capture important system properties. Model 3 and Model 4 were used as a basis for modeling the feedback interactions. The diffusion coefficients for AHLs were set to experimentally estimated values. Some variables (*LuxR*, *LasR*, *LasI*) were set to constant values to reduce model complexity without losing important dynamical aspects. The role of cell growth and nutrient depletion was considered using the variable $cell_D$.

$$\frac{\partial}{\partial t} LuxI = cell_D\left(k_{prot}(pLux + pLas) - k_{d_{ssrA}} LuxI\right)$$

$$\frac{\partial}{\partial t} AHL_{12} = cell_D\left(k_{ahl} AHL_{12cap} LasI - k_{d_{ahl12}} AHL_{12} AiiA\right) - k_{d_{AHL}} AHL_{12} + D_{12}\nabla^2 AHL_{12}$$

$$\frac{\partial}{\partial t} AHL_6 = cell_D\left(k_{ahl} AHL_{6cap} LuxI - k_{d_{ahl6}} AHL_6 AiiA\right) - k_{d_{AHL}} AHL_6 + D_6\nabla^2 AHL_6$$

$$\frac{\partial}{\partial t} mCherry = cell_D\left(k_{mChr} pLas - k_{d_{ssrA}} mCherry\right)$$

$$\frac{\partial}{\partial t} sfGFP = cell_D\left(k_{gfp} pLux - k_{d_{ssrA}} sfGFP\right)$$

$$\frac{\partial}{\partial t} AiiA = cell_D\left(k_{prot} ara_{indc} - k_{d_{ssrA}} AiiA\right)$$

$$\frac{\partial}{\partial t} Aqs1 = cell_D\left(k_{prot} pLux - k_{d_{prot}} Aqs1\right)$$

$$\frac{\partial}{\partial t} cell_D = cell_D\left(\frac{k_{cell}}{K_{cell}}\right)(K_{cell} - cell_D) + D_c\nabla^2 cell_D$$

with $LasR_{AHL12} = H(LasR, AHL_{12}, K^*_{T12}, nH_{12}, k_{leak})$, where K^*_{T12} is given by

$K^*_{T12} = \frac{K_{T12}}{H(1.0, K_{Taqs}, Aqs1, nH_{aqs}, k_{leak})}$, same as in Model 4.

$LuxR_{AHL6} = H(LuxR, AHL_6, K_{T6}, k_{leak})$, same as in Model 3.

$LuxR_{AHL12} = H(LuxR, AHL_{12}, K_{T12xR}, k_{leak})$

$LuxR = 40, LasR = 40, LasI = 2000$

$pLux = LuxR_{AHL6} + LuxR_{AHL12}$

$pLas = LasR_{AHL12}$

$ara_{indc} = H(10, ara, K_{Tara}, nH_{ara}, k_{leak})$; same as in Model 3.

$ara \in (0, 1, 10^3, 10^6)$

To implement limits on AHL production due to nutrient depletion after cell growth, the following terms were applied:

$AHL_{6cap} = \frac{(K_{cell} - cell_D)}{lawnFrac * K_{cell}}$;

$AHL_{12cap} = \frac{(1.1 * K_{cell} - cell_D)}{1.1 * lawnFrac * K_{cell}}$; the factor 1.1 is used to allow some AHL_{12} production at higher cell density.

The parameter $lawnFrac$ (between 0 to 1) controls the fraction of the domain occupied by cells. In 1D simulations it equals the length fraction of domain occupied by cells and in 2D simulations it equals the area fraction of the domain occupied by cells.

Note that not all parameters could be precisely measured and hence they were set to biologically reasonable values capable of recapitulating experimental observations. Implementation of complex synthetic multicomponent orthogonal gene networks in bacteria poses some practical limitations. Our orthogonal synthetic circuit uses the cellular resources, for example – biosynthesis of the AHL molecules requires S-adenosyl-methionine, which is also important for cell division[3]. A future challenge will be to generate more sustainable synthetic circuits that consume minimal cellular resources or that integrate into the cellular metabolic pathways to reduce the burden of implementing the artificial network. We used destabilized fluorescent reporter to obtain a dynamic readout of the synthetic circuit performance, and it will be useful to encode morphogenetic changes as the circuit output[4,5].

Supplementary Table 1. Parameters used in the simulations.

Parameter	Symbol	Value	Reference
Protein synthesis rate	k_{prot}	0.2 min^{-1}	
sfGFP synthesis plus maturation rate	k_{sfGFP}	0.1 min^{-1}	
mCherry synthesis plus maturation rate	$k_{mCherry}$	0.02 min^{-1}	
Protein degradation rate	k_{dprot}	0.0028 min^{-1}	
LVA-tagged protein degradation rate	k_{dssrA}	0.018 min^{-1}	[6]
AHL synthesis rate (via LuxI)	k_{ahl}	0.002 min^{-1}	

AHL decay rate (hydrolysis)	k_{dahl}	0.0011 min^{-1} (Half-life ~ 10 h)	[1,7]
AHL_6 degradation rate (by Lactonase)	k_{dahl6}	0.01 min^{-1}	[8]
AHL_{12} degradation rate (by Lactonase)	k_{dahl12}	0.001 min^{-1}	[8]
AHL_6 activation threshold	K_{T6}	10 nM	This study
Hill coefficient for AHL_6	nH_6	1.5	This study
AHL_6 diffusion coefficient	D_6	350 $\mu m^2/s$	This study
AHL_{12} activation threshold	K_{T12}	[50, 80] nM	This study
AHL_{12} threshold concentration for LuxR binding	K_{T12xR}	[200, 2000] nM	
Hill coefficient for AHL_{12}	nH_{12}	2	This study
AHL_{12} diffusion coefficient	D_{12}	350 $\mu m^2/s$	This study
Arabinose threshold concentration	K_{Tara}	6000 nM	This study
Hill coefficient for arabinose	nH_{ara}	1.5	This study
Aqs1 threshold concentration	K_{Taqs}	[200, 300] nM	
Hill coefficient for Aqs1	nH_{aqs}	2	
Promoter leakiness	k_{leak}	[0.05, 0.08]	
Cell density increase rate	k_{cell}	0.007	
Cell density capacity	K_{cell}	1.6	
Cell movement (diffusion) constant	D_c	0.1 $\mu m^2/s$	
Lawn fraction, i.e., fraction of domain covered with cells	lawnFrac	0.5, 0.65, 1 (for 1D)	

Supplementary Table 2. Primer list.

Name	Sequence
2985_His_SDM_F	atcaccatgccgcagcagcgaacgacgaaaat
2986_His_SDM_R	ggtgatggtgtgaatttaagactgctttttttaaactgttc
2973_LuxR_qPCR_F	catacggctaacaatggcttcg
2974_LuxR_qPCR_R	gcatgcccacgctaaacatt
2975_LuxI-ssrA_qPCR_F	ggtcaacagagtgctcccaa
2976_LuxI-ssrA_qPCR_R	tcgctctattgctgttgatgttac
2987_pJ23_SDM_F	agctagccgtcaaatcgataattgtcccgggaattgtgatatcacctattgtttgtcgcaag
2988_pJ23_SDM_R	cagtcctaggtacagtgctagcggatccaaagaggagaaacatatgaaaaacataaatgccgac
3086_Gibson_aiiA_F	gactgagctagccgtcaaatcgataggttctgttaagtaactgaacccaatgtcgttag-tgacgcttacctcttaagaggtcactgacctaacaacattgattatttgcacggc
3087_Gibson_aiiA_R	tataacaaaccattttcttgcgtaaacctgtacgatcctacaggtacaattcccggggagagcgttcaccgac
3088_Gibson_sfGFP_F	caagaaaatggtttgttatagtcgaataaagcgatcgcattaaagaggagaaaggtaccatgag
3089_Gibson_sfGFP_R	tttctcctctttaatgaattctttattcgactataacaaaccattttcttgcgtaaacctg-tacgatcctacaggtgatatcatttgtcctactcaggagagc
2977_sfGFP_qPCR_F	tacaagacgcgtgctgaagt
2978_sfGFP_qPCR_R	ccatcttcaacgttgtggcg
2979_aiiA-LAA_qPCR_F	agcgaacggaatatgaggca
2980_aiiA-LAA_qPCR_R	cgactgatggcctggagaat
2496_aiiA_F	aaagagtgcatcctgccgaa
2497_aiiA_R	ggggtatgtccaggcgtatg
4093_SDM_Mar_F	atcgataggttctgttaagtaac

4094_SDM_Mar_R	gtgaagacgaaagggc
4466_pAL103Lux_F	cgctctccccgggaattgtacctgtaggatcgtacaggtttacgcaagaaaatggttt-gttacagtcgaataaagcgatcgc
4467_pAL103Lux_R	ctctttaatgaattcttacgctgcaagggcg
4201_SDM_201_pTet_F	ggggaaatactagatgattgttcagattggc
4202_SDM_201_pTet_R	tctttctctagtattaaacaaaattatttgtagaggc
4254_pAL201_4_F	atgatcggccggccgacattgggttcagttacttaacagaacctttgacggctagctcag-tcctaggtacagtgctagcggatccaaagaggagaaacatatggccttggttgacgg
4255_pAL201_4_R	atgatccccgggaggttctgttaagtaactgaacccaatgtcgttagtgacgcttac-ctcttaagaggtcactgacctaacagagagcgttcaccgacaaac
4275_pAL201_5_F	atgatcggcgcgcccctgcagtattcattttcagcttacggaaggtagatttgacggctagctcagtc
4276_pAL201_5_R	atgatccccgggcgctgcgtctgcctcctgaccacttgag-taactgctgcgaaaaaaccccgccgaagcggggttttttgcgtcaacgcgtcgcaaac
4352_LasI_pAL205_F	agatgatcctcgagagatgctgtagtgggatg
4353_LasI_pAL205_R	agatgatccctaggttaaacaaaattatttgtagaggactg
4416_LasI_SDM_F	taacgccgaaaaccccgc
4417_LasI_SDM_R	ggaaacggccaggcgttg
4456_pAL211_SDM_F	aaagacatgagttactagatgaccaacaccgatctg
4457_pAL211_SDM_R	ctctagatttattcgactgtaacaaaccattttcttgcg
4397_mfLon_207_F	agatgatcctcgagacctgtaggatcgtacag
4398_mfLon_207_R	agatgatccctaggaaaaaattagcgcaagaagac
4458_pAL212_SDM_F	aaagacatgagttactagatgagtaaaaaaatcaaactgc
4459_pAL212_SDM_R	ctctagatttattcgactgtaacaaaccattttcttgc

4561_pAL214_x_lasI_F	agatgatcctcgagagatgctgtagtg
4562_pAL214_x_lasI_R	agatgatcctcgagttaaacaaaattatttgtagaggactg
4554_pAL215_luxI_F	agatgatcttaattaagagaaagaggagaaatactagatgacg
4555_pAL215_luxI_R	agatgatcttaattaattacttgtcgtcatcgtctttg
4586_posLoop_F	agatgatcgacgtcaaataggcgtatcacgagg
4587_posLoop_R	agatgatcgacgtcaccgtattaccgcctttg

Supplementary Table 3. Arabinose threshold concentration for positive feedback module.

Strain	Arabinose threshold (nM)	Treatment time (min)	Dynamic range
pAL101	967 ± 40	360	4.2
pAL102	1402 ± 41	120	2.4
pAL103	480 ± 18	360	6.5
pAL104	880 ± 37	120	3.9

Supplementary Table 4. Diffusion coefficient estimates.

Molecule	D [mean ± stdev] ($\mu m^2/s$)	Samples (n)	Previous estimates ($\mu m^2/s$)	Reference
Dextran (3kDa)	120 ± 5	7	170 ± 22	[9]
Dextran (10kDa)	67 ± 12	7	83 ± 8	[9]
AHL_6	313 ± 69	12	17	[10]
AHL_{12}	320 ± 59	11	83	[11]

Note: Previous estimates listed here are from different experimental setups and conditions.

Supplementary Figure Legends

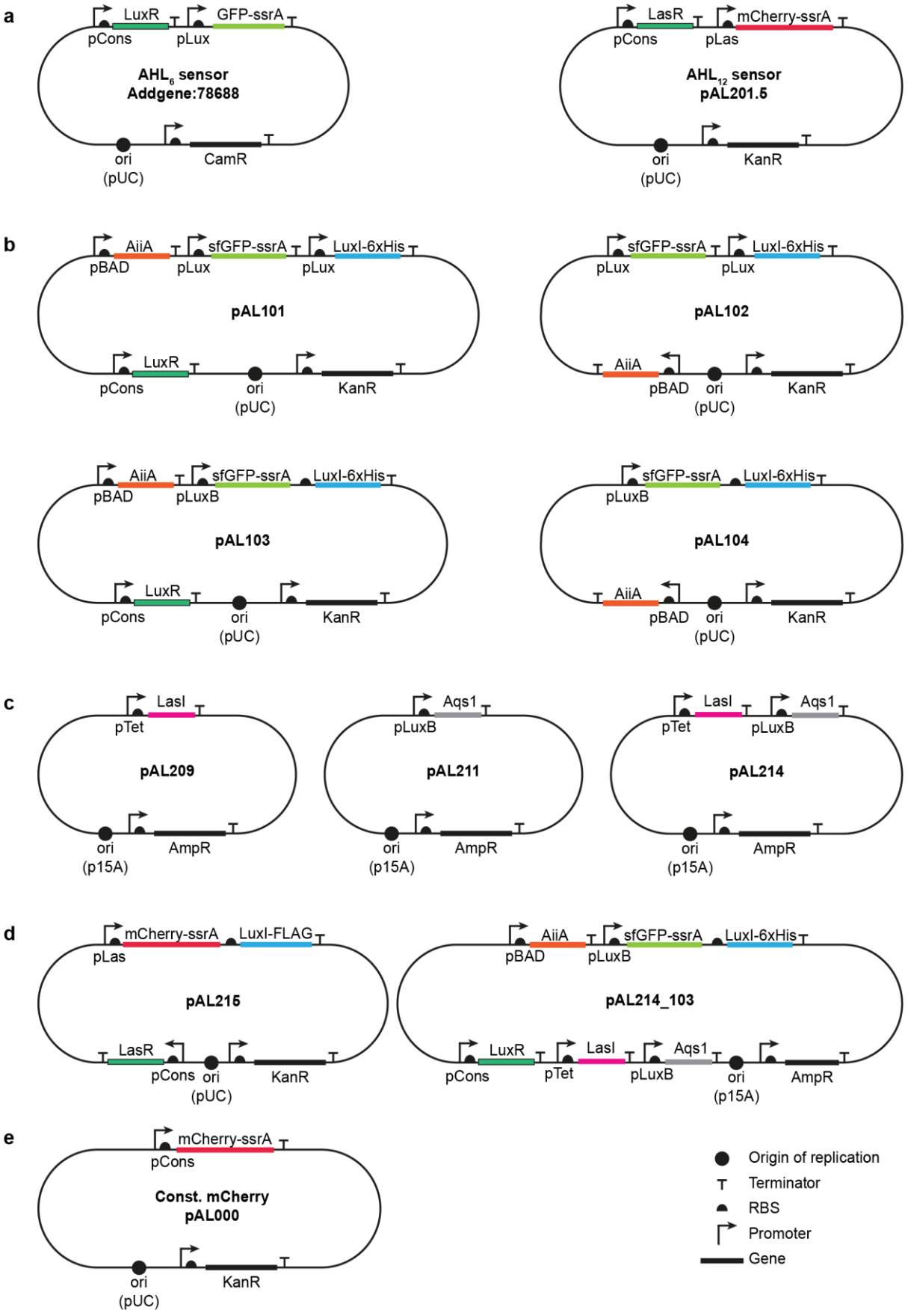

Supplementary Figure 1 | Plasmid schematics. (a) AHL sensor plasmids; **(b)** Positive feedback module plasmids; **(c)** Negative feedback modules plasmids: pAL209 – AHL_{12} production, pAL211 – LasR inhibition, pAL214 - AHL_{12} production and LasR inhibition; **(d)** Complete synthetic circuit plasmids: pAL215 – AHL_{12} sensor and AHL_6 production, pAL214_103: pAL103 cloned into pAL214; **(e)** Constitutive mCherry expression plasmid.

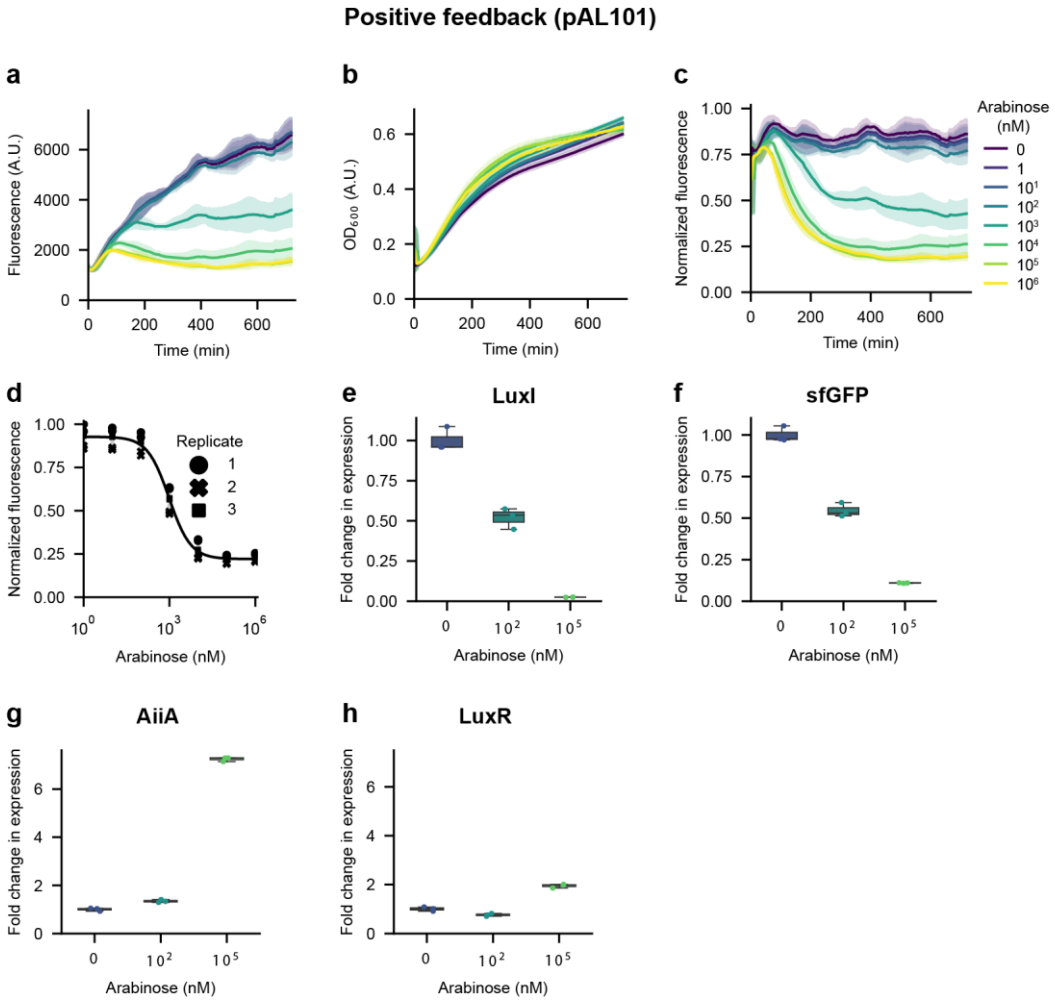

Supplementary Figure 2 | Characterization of the positive-feedback module (pAL101). (a-c) Time-series plots showing (a) sfGFP fluorescence, (b) OD_{600}, (c) Normalized fluorescence/OD_{600} for positive feedback strain carrying pAL101 plasmid under different arabinose treatments (n = 3 biological replicates with 2 technical replicates each). **(d)** Dose-response curve at 6 h after treatment with arabinose for the data shown in (a-c). **(e-h)** Boxplots showing fold-change in mRNA levels of *LuxI*, *sfGFP*, *AiiA*, *LuxR* quantified by qRT-PCR after 4 h arabinose treatments. (n = 1 biological replicate with 3 technical replicates). Reference gene- ihfβ for all the RT-qPCR analyses.

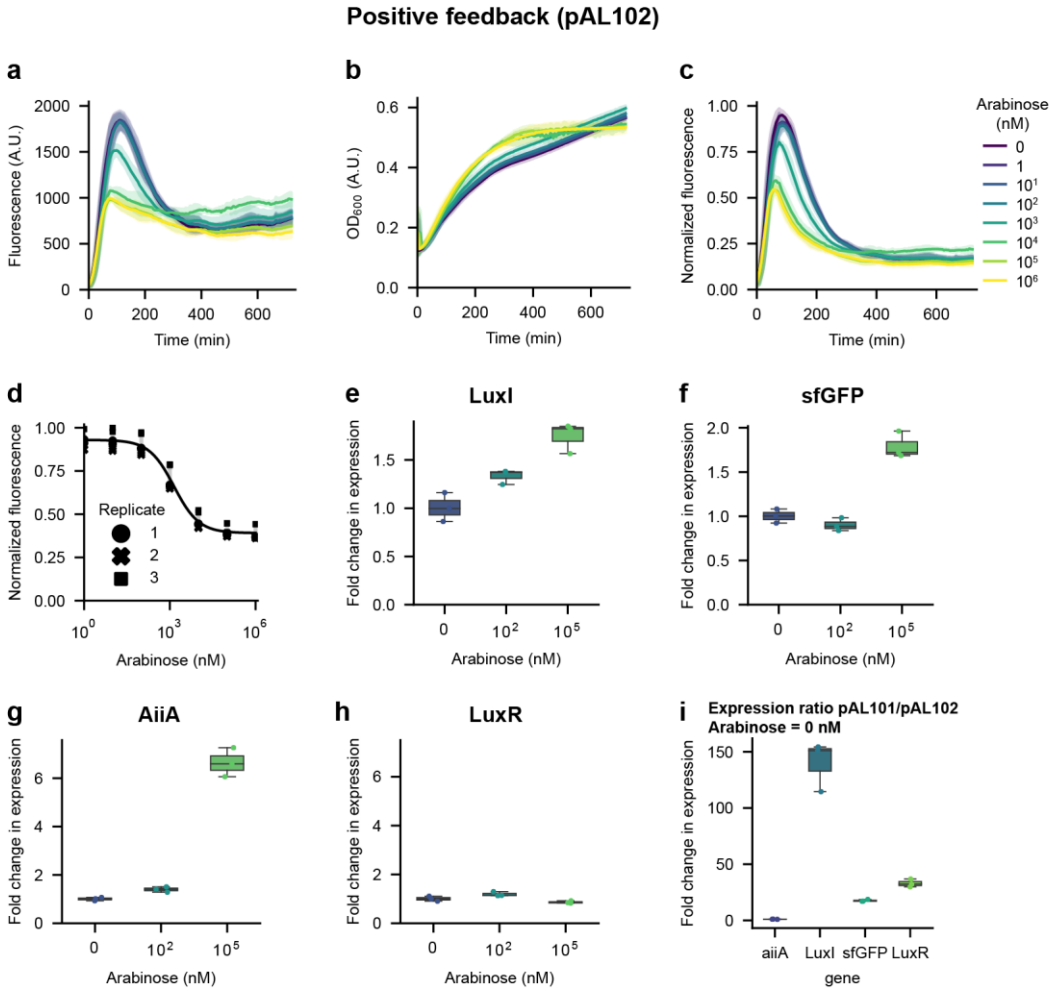

Supplementary Figure 3 | Characterization of the positive-feedback module (pAL102). (a-c) Time-series plots showing (a) sfGFP fluorescence, (b) OD_{600}, (c) Normalized fluorescence/OD_{600} for positive feedback strain carrying pAL102 plasmid under different arabinose treatments (n = 3 biological replicates with 2 technical replicates each). **(d)** Dose-response curve at 3 h after treatment with arabinose for the data shown in (a-c). **(e-h)** Boxplots showing fold-change in mRNA levels of *LuxI*, *sfGFP*, *AiiA*, *LuxR* quantified by qRT-PCR after 4 h arabinose treatments. (n = 1 biological replicate with 3 technical replicates). **(i)** Relative expression of *AiiA*, *LuxI*, *sfGFP* and *LuxR* in pAL101 and pAL102 strains without arabinose treatments. The strain carrying pAL102 only has a single chromosomal copy of *LuxR*, while pAL101 strain also expresses *LuxR* from the plasmid. Reference gene- ihfβ for all the RT-qPCR analyses.

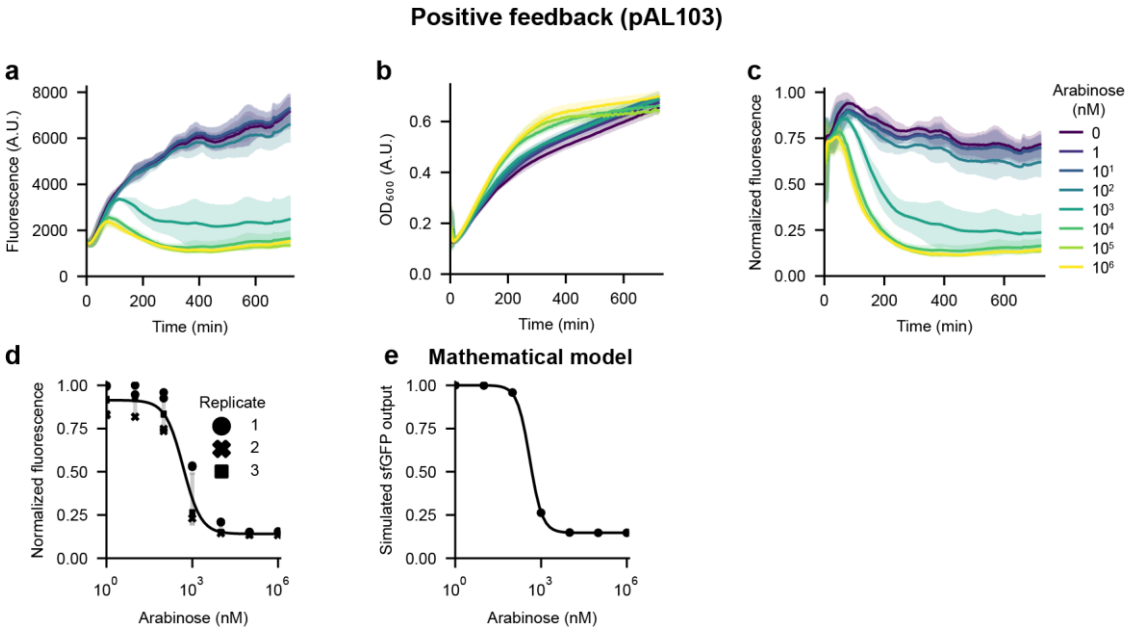

Supplementary Figure 4 | Characterization of the positive-feedback module (pAL103). (a-c) Time-series plots showing (a) sfGFP fluorescence, (b) OD_{600}, (c) Normalized fluorescence/OD_{600} for positive feedback strain carrying pAL103 plasmid under different arabinose treatments (n = 3 biological replicates with 2 technical replicates each). **(d)** Dose-response curve at 6 h after treatment with arabinose for the data shown in (a-c). A reverse-sigmoid function was fitted to the data to estimate the arabinose threshold concentration (480 ± 18 nM). **(e)** A simulated dose-response curve using the mathematical model for the positive-feedback module. Data in (c) and (d) are the same as in Fig. 2c, d.

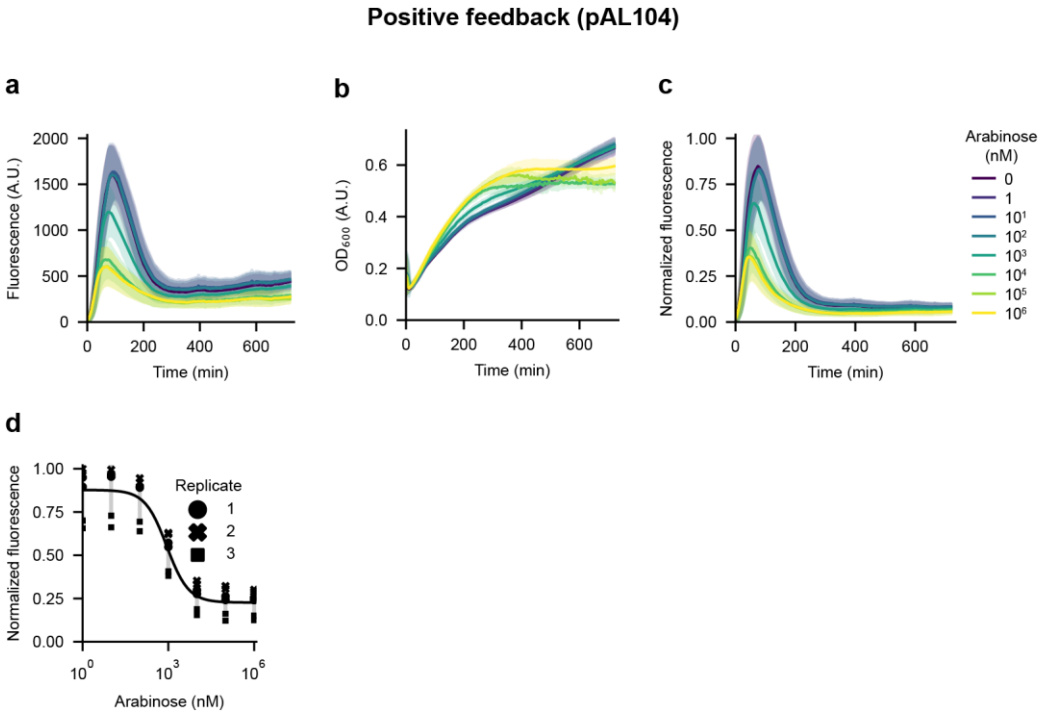

Supplementary Figure 5 | Characterization of the positive-feedback module (pAL104). (a-c) Time-series plots showing (a) sfGFP fluorescence, (b) OD_{600}, (c) Normalized fluorescence/OD_{600} for positive feedback strain carrying pAL104 plasmid under different arabinose treatments (n = 3 biological replicates with 2 technical replicates each). **(d)** Dose-response curve at 3 h after treatment with arabinose for the data shown in (a-c).

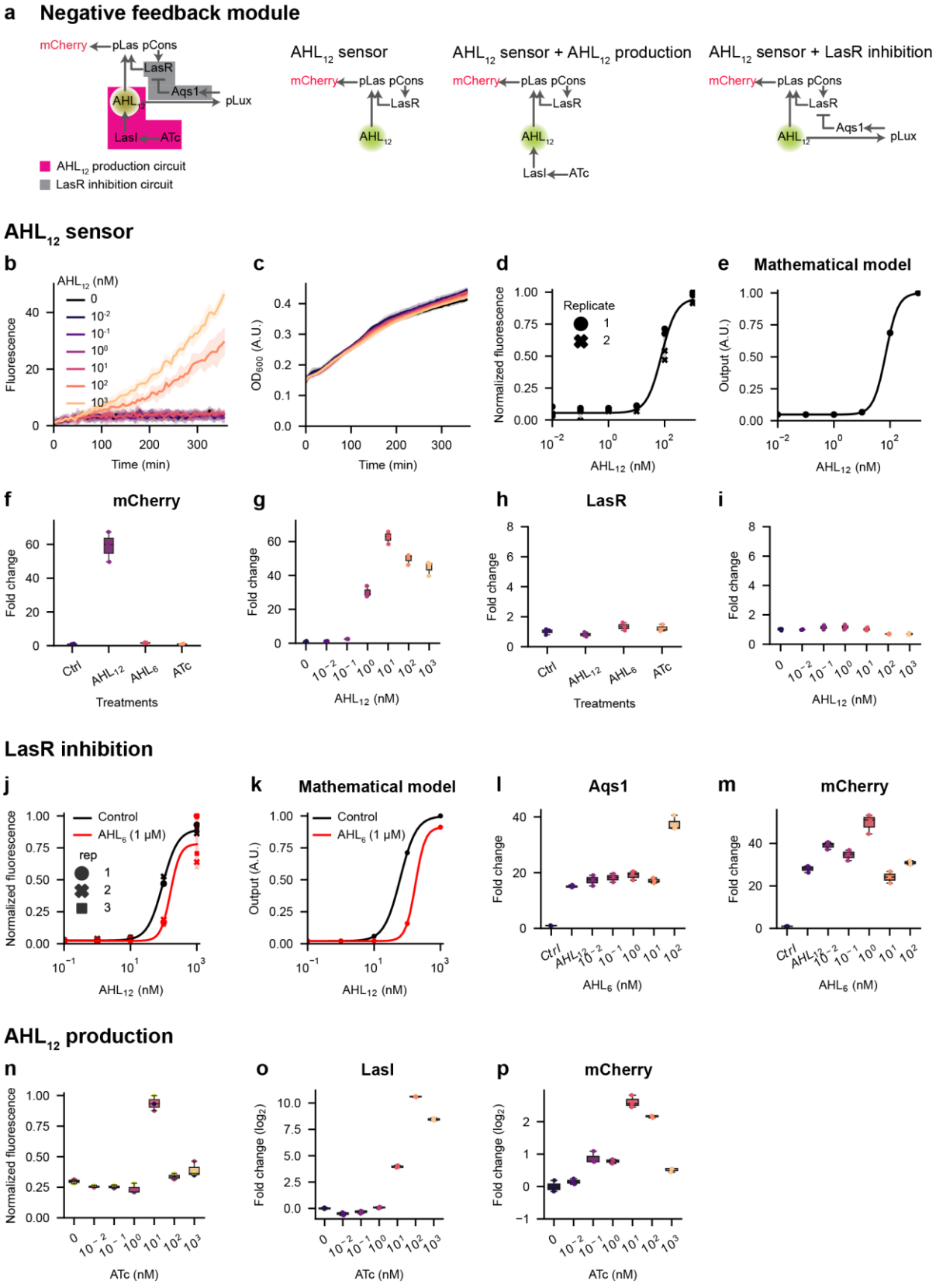

Supplementary Figure 6 | Characterization of the negative feedback submodules. (a) Schematics of the negative feedback module and submodules - AHL_{12} sensor, AHL_{12} sensor + LasI production, and AHL_{12} sensor + LasR inhibition. **(b, c)** For the AHL_{12} sensor strain, time-series plots showing (b) mCherry fluorescence, and (c) OD_{600} upon different AHL_{12} treatments (n = 2 biological replicates with

2 technical replicates each, from the same experiment as in Fig. 2g). **(d, e)** For the AHL_{12} sensor strain, dose-response curves showing normalized mCherry fluorescence upon treatment with indicated AHL_{12} doses for 6 h. (d) shows experimental data (n = 2 biological replicates with 2 technical replicates each, from the same experiment as in Fig. 2g). (e) shows model simulation results. **(f-i)** For the AHL_{12} sensor strain, RT-qPCR analysis showing change in mRNA levels of *mCherry* and *LasR* after treatments with (f, h) AHL_{12} (1000 nM), AHL_6 (1000 nM), and ATc (1000 nM) and (g, i) indicated amounts of AHL_{12} for 4 h (n = 1 biological replicate with 3 technical replicates). **(j, k)** For the LasR inhibition strain, (j) shows the dose-response curves at 6 h time-points for the data in Fig. 2i. The AHL_{12} threshold concentration increases from 93 ± 2 nM to 160 ± 22 nM. (k) Our mathematical model recapitulates these experimental findings. **(l, m)** For the LasR inhibition strain, RT-qPCR analysis showing change in mRNA levels of (l) *Aqs1* and (m) *mCherry* upon treatment with different AHL_6 concentrations for 4 h. Note, all samples except the control, were also treated with 1 µM AHL_{12} (n = 1 biological replicate with 3 technical replicates). **(n-p)** For the AHL_{12} production strain, (n) normalized mCherry output upon treatment with indicated ATc doses for 6 h. (o, p) RT-qPCR analysis showing change in mRNA levels of *LasI* and *mCherry* upon treatment with indicated ATc concentrations for 4 h (n = 1 biological replicate with 3 technical replicates). (LasI – AHL_{12} synthase, ATc – Anhydrotetracycline). Reference gene- ihfβ for all the RT-qPCR analyses.

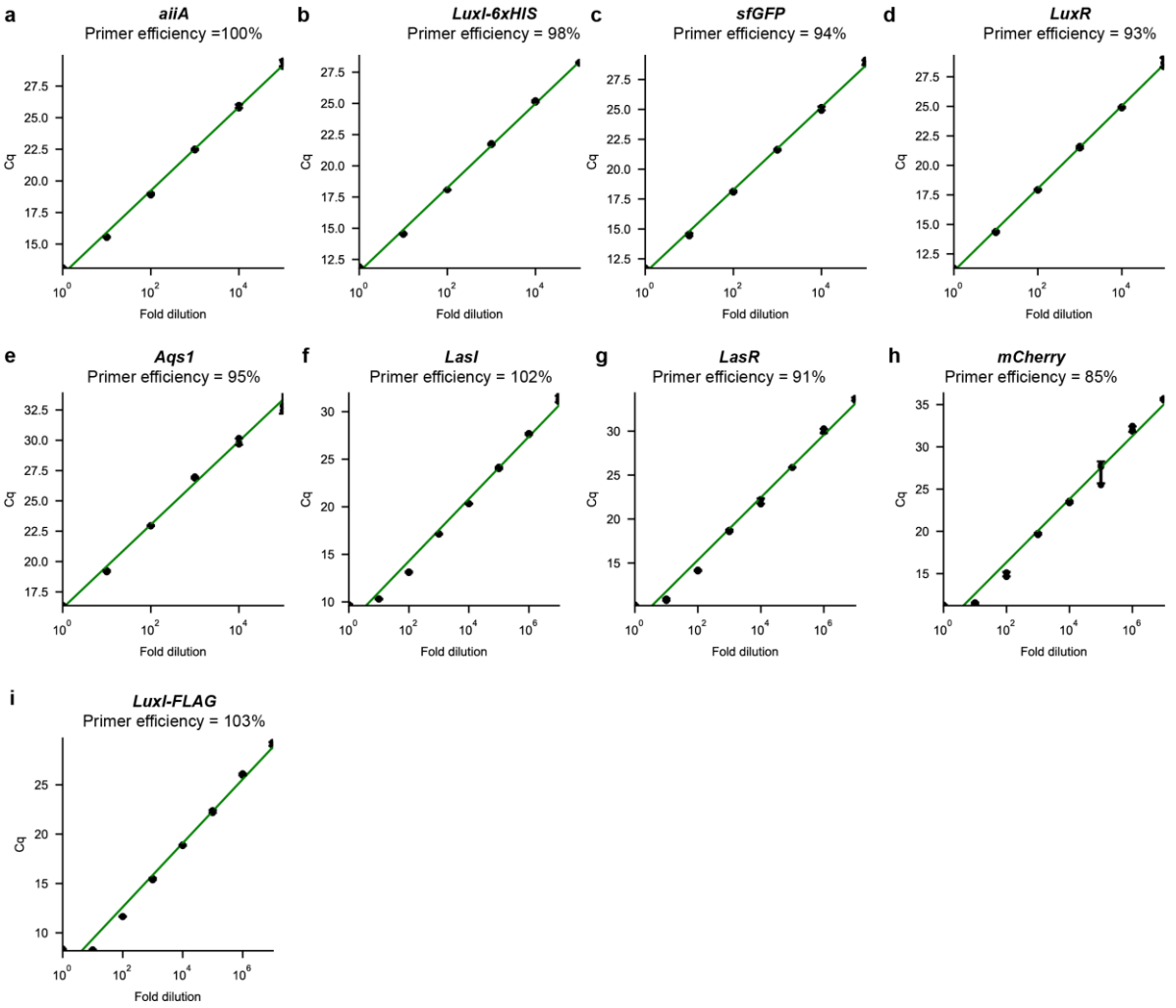

Supplementary Figure 7 | RT-qPCR primer efficiency and standard curves. (a-i) Standard curves showing quantitative cycle (Cq) value for qPCR using the designated primer and serial dilutions of an appropriate template DNA. Estimated primer efficiency values are shown. n = 1 biological replicate with 3 technical replicates.

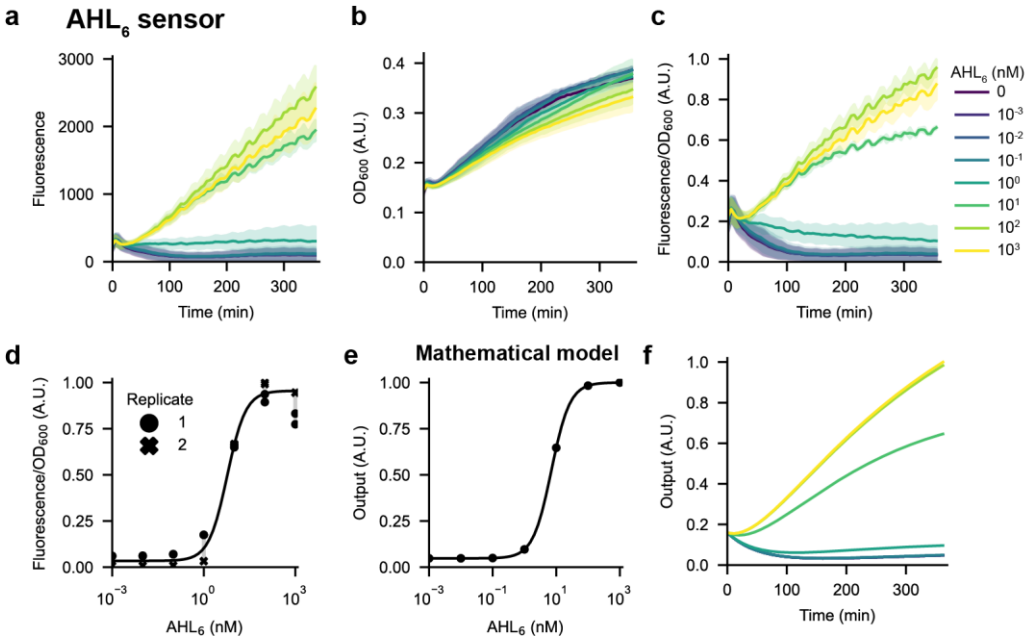

Supplementary Figure 8 | AHL_6 sensor strain characterization and mathematical modeling. (a) Schematic showing the AHL_6 sensor strain. **(b-d)** Time-series plots showing (b) GFP fluorescence, (c) OD_{600}, (d) Fluorescence/OD_{600} (scaled to 1 by dividing by the maximum) for the AHL_6 sensor strain upon different AHL_6 treatments (n = 2 biological replicates with 2 technical replicates each). **(e)** Dose-response curve after 6 h AHL_6 treatment for the data shown in (b-d). A sigmoid function was fitted to the data to estimate the activation threshold (6 ± 1 nM). **(f, g)** Mathematical model of the AHL_6 sensor recapitulates the dose-response profile (f) as well as dynamics of fluorescence output (g).

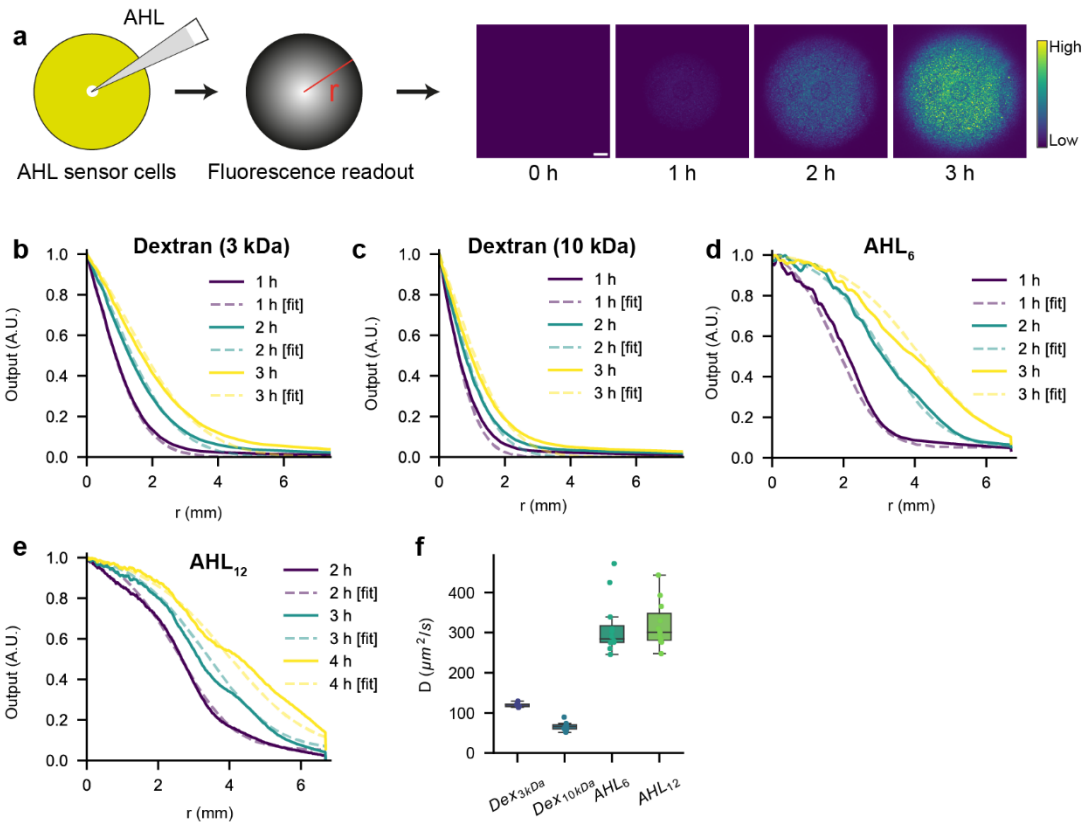

Supplementary Figure 9 | Estimation of AHL diffusion coefficients using AHL sensor strains. **(a)** Schematic showing a method to generate fluorescence gradients in a lawn of an AHL sensor strain by adding the inducer (AHL) at the lawn center. These gradients are quantified and fitted to simulated gradients using a mathematical model of the AHL sensor to estimate the AHL diffusion coefficient. **(b-e)** Representative fits of experimental gradients and simulated gradients for dextran (3 kDa), dextran (10 kDa), AHL_6, and AHL_{12}. The Fluorescein-labeled dextrans were used to validate the method. **(f)** Boxplot showing estimated diffusion coefficients; n = 7, 7, 12, 11 respectively for dextran (3 kDa), dextran (10 kDa), AHL_6, AHL_{12}.

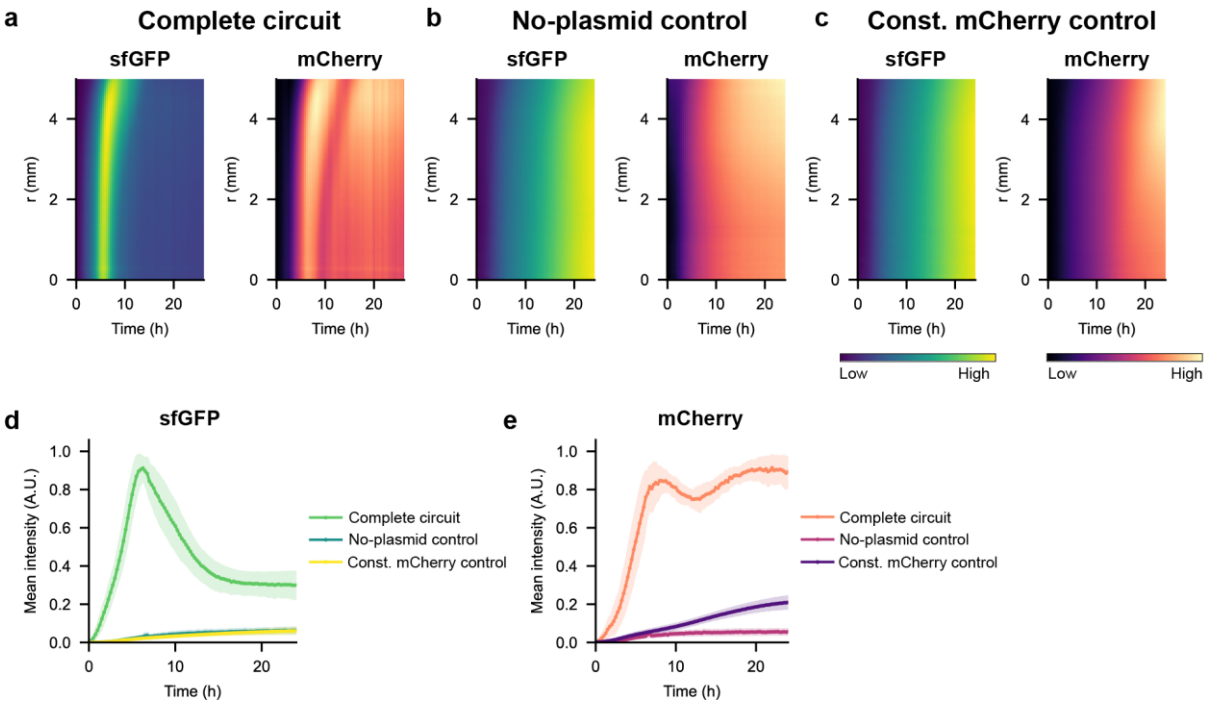

Supplementary Figure 10 | Traveling waves are observed specifically for the complete circuit strain. (a-c) Representative space-time plots of radial profiles of sfGFP and mCherry fluorescence for (a) complete circuit strain, (b) no-plasmid control strain, and (c) constitutive mCherry expression strain. Data in (a) are same at in Fig 4c,d. For (b) and (c), n = 3 biological replicates. **(d, e)** Mean intensities of (d) sfGFP and (e) mCherry for the indicated strains. The values are normalized to scale the maximum to 1. Data for the complete circuit strain are the same as in Fig. 4.

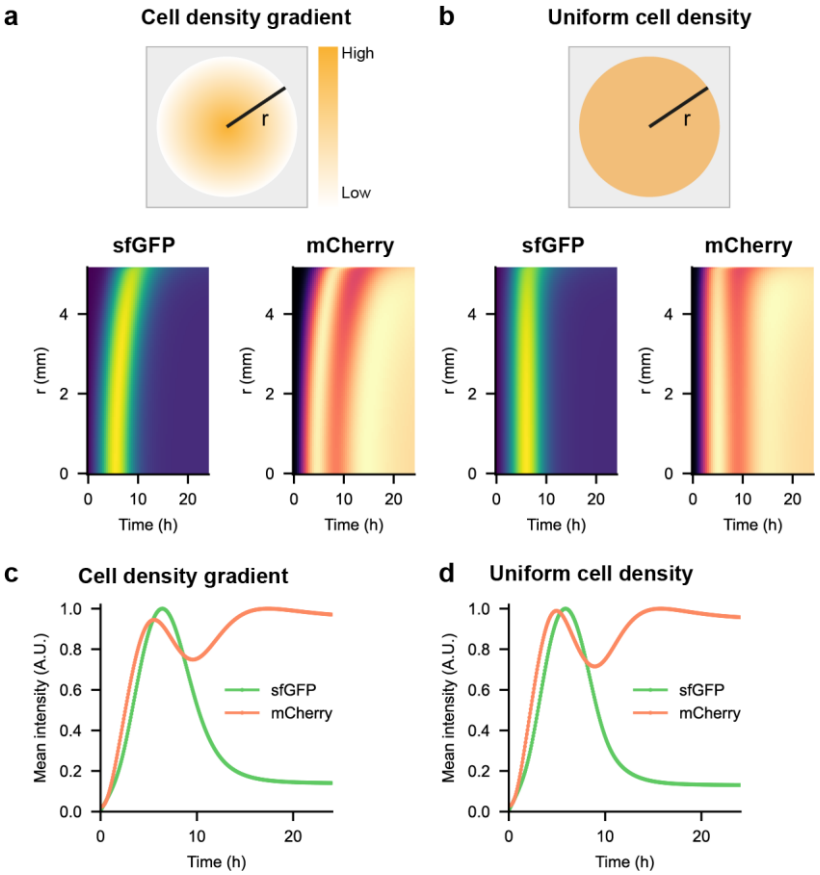

Supplementary Figure 11 | Mathematical simulations reveal role of cell-density gradient for the traveling waves. **(a, b)** Schematic showing the simulation setup along with space-time plots of simulated sfGFP and mCherry levels for (a) graded cell-density and (b) uniform cell-density conditions. (c, d) Mean sfGFP and mCherry intensities in the simulated cell-lawn for the indicated cell-density conditions.

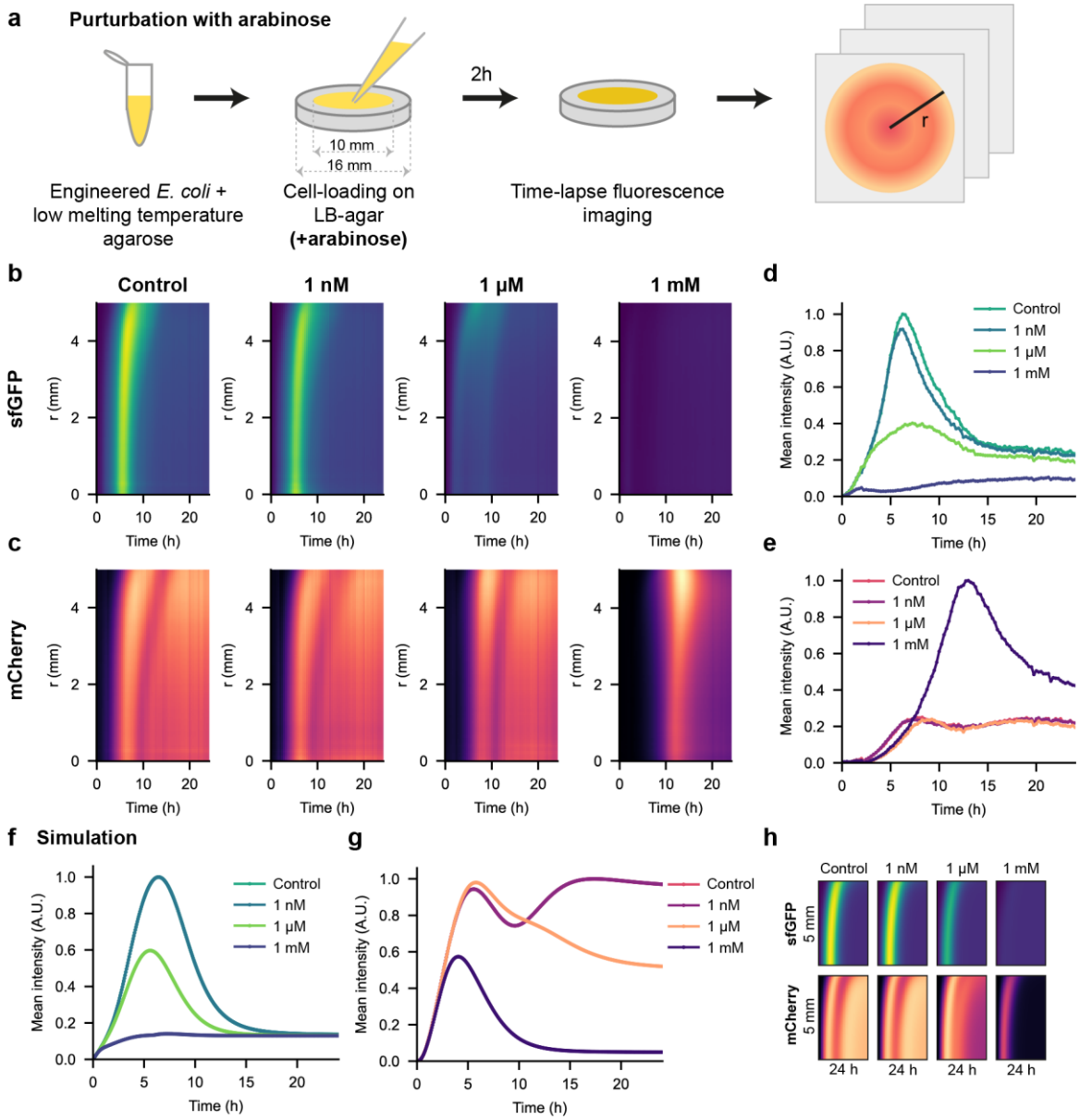

Supplementary Figure 12 | Perturbation analysis with arabinose-induced AHL degradation. (a) Schematic showing the experimental setup. The cells mixed with low-melting temperature agarose are loaded on LB-agar that contains a known concentration of arabinose. **(b, c)** Space-time plots of (b) sfGFP and (c) mCherry fluorescence for indicated arabinose treatment conditions. The movies were recorded for 24 hours with 15-minute intervals (n = 1 biological replicate). **(d, e)** Mean intensities over time of (d) sfGFP and (e) mCherry for the indicated arabinose treatment conditions. The raw values are normalized by dividing by the maximum value of the dataset. **(f, g)** Simulated (f) sfGFP and (g) mCherry profiles for the indicated arabinose treatments. **(h)** Simulated space-time plots of sfGFP and mCherry for the indicated arabinose treatments. The simulations were performed by solving a PDE-based model (Model 5 in Supplementary Note 1) on a 1D grid using custom python code.

Supplementary Movie Legends

For Supplementary Movies 1-5, viridis and magma lookup tables were used for sfGFP and mCherry, respectively. The pixel gray value range was adjusted to better visualize the data. All images within the same time-lapse have the same gray value range. Supplementary Movies 6-8 show results of 2D simulations.

Supplementary Movie 1 | Complete circuit strain showing traveling waves. The movie was recorded for 24 hours at 15-minute intervals. Traveling waves of mCherry fluorescence signal can be observed. Scale bar = 2 mm. n = 9 biological replicates.

Supplementary Movie 2 | Control strains do not show traveling waves. The movie was recorded for 24 hours at 15-minute intervals. The no-plasmid strain shows low levels of autofluorescence in GFP and mCherry channels. The constitutive mCherry expression strain show autofluorescence in GFP channel and elevated levels of mCherry fluorescence signal in the mCherry channel. Scale bar = 2 mm. n = 6 biological replicates.

Supplementary Movie 3 | Effect of lawn size on the traveling wave patterns. The movie was recorded for 24 hours at 15-minute intervals. Three lawn sizes are shown. Scale bar = 2 mm. n = 4 biological replicates.

Supplementary Movie 4 | Effect of lawn position on the traveling wave patterns. The movie was recorded for 24 hours at 15-minute intervals. Three lawn positions are shown. Scale bar = 2 mm. n = 6 biological replicates.

Supplementary Movie 5 | Effect of arabinose-induced AHL degradation on the traveling waves. The movie was recorded for 24 hours at 15-minute intervals. Four arabinose treatments are shown. Scale bar = 2 mm. n = 1 biological replicate.

Supplementary Movie 6 | Simulation of the traveling waves with graded and uniform cell density. This movie shows results of a 2D simulation with different initial cell density conditions. Top: Graded cell-density, bottom: uniform cell-density, left: sfGFP, right: mCherry.

Supplementary Movie 7 | Simulation of the traveling waves with different lawn sizes. This movie shows results of a 2D simulation with different lawn sizes. Left: sfGFP, right: mCherry.

Supplementary Movie 8 | Simulation of the traveling waves with different lawn positions. This movie shows results of a 2D simulation with different lawn positions. Left: sfGFP, right: mCherry.

Supplementary References

1 Delalande, L. *et al.* N-hexanoyl-l-homoserine lactone, a mediator of bacterial quorum-sensing regulation, exhibits plant-dependent stability and may be inactivated by germinating Lotus corniculatus seedlings. *FEMS Microbiology Ecology* **52**, 13-20 (2005). https://doi.org:10.1016/j.femsec.2004.10.005

2 Guyer, J. E., Wheeler, D. & Warren, J. A. FiPy: Partial Differential Equations with Python. *Computing in Science & Engineering* **11**, 6-15 (2009). https://doi.org:10.1109/MCSE.2009.52

3 Newman, E. B. *et al.* Lack of S-adenosylmethionine results in a cell division defect in Escherichia coli. *J Bacteriol* **180**, 3614-3619 (1998). https://doi.org:10.1128/jb.180.14.3614-3619.1998

4 Gu, F. *et al.* A synthetic population-level oscillator in non-microfluidic environments. *Communications Biology* **6**, 515 (2023). https://doi.org:10.1038/s42003-023-04904-0

5 Duran-Nebreda, S. *et al.* Synthetic Lateral Inhibition in Periodic Pattern Forming Microbial Colonies. *ACS Synthetic Biology* **10**, 277-285 (2021). https://doi.org:10.1021/acssynbio.0c00318

6 Andersen, J. B. *et al.* New unstable variants of green fluorescent protein for studies of transient gene expression in bacteria. *Appl Environ Microbiol* **64**, 2240-2246 (1998). https://doi.org:10.1128/aem.64.6.2240-2246.1998

7 Chen, C.-C., Riadi, L., Suh, S.-J., Ohman, D. E. & Ju, L.-K. Degradation and synthesis kinetics of quorum-sensing autoinducer in Pseudomonas aeruginosa cultivation. *Journal of Biotechnology* **117**, 1-10 (2005). https://doi.org:https://doi.org/10.1016/j.jbiotec.2005.01.003

8 Wang, L.-H., Weng, L.-X., Dong, Y.-H. & Zhang, L.-H. Specificity and Enzyme Kinetics of the Quorum-quenching N-Acyl Homoserine Lactone Lactonase (AHL-lactonase). *Journal of Biological Chemistry* **279**, 13645-13651 (2004). https://doi.org:https://doi.org/10.1074/jbc.M311194200

9 Bläßle, A. *et al.* Quantitative diffusion measurements using the open-source software PyFRAP. *Nature Communications* **9**, 1582 (2018). https://doi.org:10.1038/s41467-018-03975-6

10 Basu, S., Gerchman, Y., Collins, C. H., Arnold, F. H. & Weiss, R. A synthetic multicellular system for programmed pattern formation. *Nature* **434**, 1130-1134 (2005). https://doi.org:10.1038/nature03461

11 Karig, D. *et al.* Stochastic Turing patterns in a synthetic bacterial population. *Proceedings of the National Academy of Sciences of the United States of America* **115**, 6572-6577 (2018). https://doi.org:10.1073/pnas.1720770115

5. Discussion

5.1. Biological pattern formation by reaction-diffusion

Biological pattern formation is a fascinating and complex area of research that has implications not only for understanding how order emerges from interactions of parts in complex systems, but also for designing and building synthetic biological systems capable of pattern formation. The reaction-diffusion mechanism offers a general framework to explain emergence of self-organized spatial patterns in a vast array of biological systems ranging from subcellular protein patterns (Glock et al., 2019; Halatek et al., 2018; Halatek & Frey, 2018) to embryonic patterning (Müller et al., 2012; Raspopovic et al., 2014; Sheth et al., 2012; Tewary et al., 2017; Turing, 1952) and beyond (Murray, 1993a, 1993b).

Two-component reaction-diffusion systems have been the focus of mathematical and experimental investigations for self-organized pattern formation. In the seminal 1952 paper on the chemical basis of morphogenesis, Alan Turing mainly focused on two-component reaction-diffusion systems (Turing, 1952). He discussed six possible patterning outcomes- stationary and oscillatory patterns, each with extreme short, extreme long, and finite wavelengths. The case of stationary patterns with finite wavelength is widely known as ‘Turing patterns.’ However, he also considered three-component reaction-diffusion systems to describe the emergence of traveling wave patterns (oscillatory patterns with finite wavelength). Later on, Gierer and Meinhardt proposed the theory of biological pattern formation based on analyses of two-component reaction-diffusion systems (Gierer & Meinhardt, 1972). They considered activator-inhibitor and substrate-depletion models, and computed many different patterns by varying the reaction-diffusion parameters as well as initial and boundary conditions. In brief, they proposed that two interacting morphogens (activator and inhibitor) in an embryo can generate a ‘primary pattern’ of concentrations that can assign positional information and determine cell fates. Their theory connected the important concepts of morphogen gradient, positional information, cell fates, source density, morphogen diffusion and decay, gradient scaling (or ‘the French flag problem’) irrespective of the exact molecular mechanisms (Crick, 1970; Gierer & Meinhardt, 1972; Wolpert, 1969). Three key assumption of the theory were – 1. The activator has a short range and the inhibitor has a long range, 2. The reactions are non-linear, and 3. The densities of the

morphogen sources relate to the density of cell types that can produce the morphogens. The source densities change much slower that the changes in morphogen concentrations. These abstract theoretical concepts inspired many experimental investigations to discover biological signaling molecules that fit the profile of morphogens (Affolter & Basler, 2007; Chen & Schier, 2001; Driever & Nüsslein-Volhard, 1988; Ferguson & Anderson, 1992; Harish et al., 2023; Heemskerk & DiNardo, 1994; Kiecker & Niehrs, 2001; Rogers & Schier, 2011; Struhl et al., 1989). Despite considerable progress in biochemical and biophysical characterization of these morphogens, only a few examples of the activator-inhibitor pairs of morphogens have been found (Kondo & Miura, 2010; Müller et al., 2012; Sick et al., 2006). This raises questions regarding the generality of the two-component activator-inhibitor patterning systems and motivates analysis of multicomponent reaction-diffusion frameworks (Marcon et al., 2016; Raspopovic et al., 2014).

The old paradigms of ‘differential-diffusivity’ and ‘local activation and long-range inhibition’ have been updated in light of the recent analyses of multicomponent reaction-diffusion systems, wherein differential diffusivity constraints are no longer required for Turing pattern formation (Diego et al., 2018; Landge et al., 2020; Marcon et al., 2016; White & Gilligan, 1998; Zheng et al., 2016). Discovery of multicomponent reaction-diffusion networks capable pattern formation at a wide range of reaction-diffusion conditions will pave the way not only for a better understanding of the embryonic patterning networks, but also for designing synthetic biological pattern-forming systems. Multicomponent networks that consist of diffusible and non-diffusible components have the advantage that they can account for non-diffusible components such as receptors, signal transducers, transcription factors, and genetic regulatory elements, involved in signal interpretation and gene expression.

Another limitation of the activator-inhibitor framework is that it makes simplifying assumptions about the molecular mechanism of morphogen dispersal. The morphogens are assumed to spread by free diffusion and the effects of the complex extracellular environment and geometry of a multicellular embryo on morphogen diffusion are not considered. Hence, the framework needs to be updated with in-depth experimental

investigations. With advanced imaging technologies and computational tools, we investigated the molecular mechanisms of morphogen dispersal for the Nodal-Lefty activator-inhibitor pair.

5.2. Mechanisms of morphogen dispersal for pattern formation

Which mechanism is involved in dispersal of Nodals and Leftys in the zebrafish embryo? Previous studies have provided support for the hindered diffusion model (Müller et al., 2012; Müller et al., 2013). In our recent work, we performed single-molecule imaging and tracking of these morphogens in live zebrafish embryos, which provided further support for the hindered-diffusion model. Our analyses revealed how Nodals and Leftys can show order of magnitude differences in their effective diffusivities despite their similar molecular sizes. Nodals showed higher fraction of immobile molecules than Leftys, which contributed to their overall low effective diffusivity. Interestingly, both the morphogens showed lower localization densities and higher immobile fractions in the cell-cell interfaces than in the extracellular cavities. This observation was counterintuitive, because immobilization of morphogens in the cell-cell interfaces did not lead to their accumulation in the interfaces. To clarify this puzzling observation, I developed an agent-based model of morphogen dispersal.

The agent-based modeling framework involves three main considerations – 1. Agents, 2. System geometry, and 3. Space and time discretization (Figure 5). The morphogens and the extracellular receptors that bind them are the agents in the model (Figure 5A). Each agent has a set of attributes that makes it unique, such as an agent ID, type (morphogen or receptor), position (x, y), state (bound or unbound), etc. The agents are created and assigned a position on a discretized grid consisting of intracellular and extracellular regions. The receptors are always placed on the boundary of the intracellular and extracellular regions. The morphogens move in the extracellular area by performing a random walk. The grid was defined in such a way that the fraction of the extracellular space can be increased or decreased to test the effects of system geometry on morphogen diffusion (Figure 5B). The space discretization was achieved by considering each position (x,y) as a square of length dx (Figure 5C). The simulations were performed using a custom Python code implementing an iterative process with a fixed timestep (dt) to achieve time-discretization.

Using this framework, I performed systematic model simulations by varying three important model parameters – 1. Receptor density, 2. Residence times for morphogen-receptor binding, and 3. Extracellular area fraction (Kuhn et al., 2022). The simulations clarified that the narrow cell-cell interfaces concentrated the morphogens to cell surfaces, thereby increasing morphogen-receptor interactions and binding. Hence, the interfaces had a higher fraction of immobile morphogens than the cavities. By uniformly increasing receptor densities, we could show that the higher immobile fractions could indeed lead to high localization densities in the interfaces. These results indicated that the differences in the geometry of the interfaces and the cavities bias the morphogens to localize preferentially in the cavities, but this bias can be overcome by increasing receptor densities. Increasing the morphogen residence time and extracellular area fraction simulation parameters had similar effects on localization densities as increasing the receptor density. At the highest tested values of residence time, receptor density, and extracellular area fraction, higher morphogen localization densities in the interfaces compared to those in the cavities could be achieved (Kuhn et al., 2022) (Section 3).

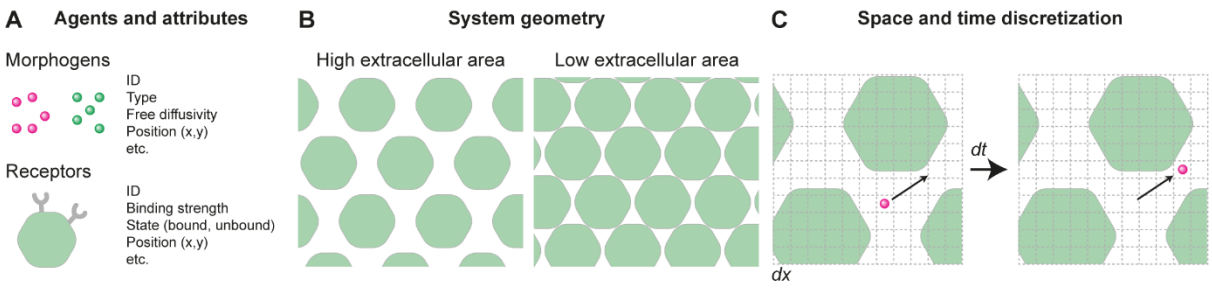

Figure 5: Agent-based modeling of morphogen dispersal
A) The agents in this model are the morphogens and the receptors that immobilize them. **B)** The effect of tissue-geometry is considered by modifying the extracellular area fraction. **C)** To simulate the model, a proper space and time discretization method is needed. Here, we consider a uniform square grid with each element of size *dx* for space discretization and each simulation step uses timestep *dt*.

Other studies have also provided support for the hindered-diffusion model (Harish et al., 2023; Lord et al., 2021; Preiß et al., 2022; Stapornwongkul & Briscoe, 2022). By performing careful transplantation experiments, it was shown that the absence of the Nodal-signaling co-receptor, One-eyed pinhead (Oep), leads to expansion in Nodal-signaling range (Lord et al., 2021). These results suggested that binding to Oep can hinder Nodal diffusion, thereby limiting Nodal signaling range in wild-type embryos. In

our single-molecule analyses, Oep overexpression could increase the fraction of immobile Nodals, further supporting that binding to extracellular receptors regulates morphogen mobility and diffusion range. Similar to the co-receptor Oep, the Nodal receptors Acvr1b-a and Acvr1b-b were shown to regulate Nodal dispersal and signaling range (Preiß et al., 2022). In the single-molecule tracking experiments, the exact molecular identity of the receptor was not known, but a combined effect of binding to the available receptors was observed (Kuhn et al., 2022). Future experiments can be focused on decoupling the contributions of different extracellular receptors and addressing if cooperativity in binding regulates the strength of binding-mediated hindrance. For the fibroblast growth factor 8a (FGF8a) morphogens in developing zebrafish neural plate, tagging of endogenous FGF8a proteins with EGFP (enhanced green fluorescent protein) enabled visualization of the morphogen gradient in real-time (Harish et al., 2023). Further, fluorescence correlation microscopy analysis showed that most of the FGF8a protein molecules (92%) move by free-diffusion in the extracellular space with a diffusion coefficient of 56 $\mu m^2 s^{-1}$, while a small fraction (8%) shows a low diffusion coefficient of 8 $\mu m^2 s^{-1}$. The slow-moving fraction was reduced by cleavage of heparan sulphate proteoglycans (HSPGs) in the extracellular matrix, suggesting that HSPGs play a role in the hindered diffusion of FGF8a (Harish et al., 2023). Other studies have shown that a combination of different mechanisms (hindered diffusion, recycling, transcytosis) can regulate the Dpp morphogen dispersal in the *Drosophila* wing imaginal discs (Romanova-Michaelides et al., 2022). In the growing imaginal discs, the contributions of different Dpp transport mechanisms change in order to scale the Dpp gradient to the tissue length. In large imaginal discs, increased recycling of the internalized Dpp molecules mobilizes them to the diffusing extracellular pool. Additionally, cytonemes have been shown to play a role in Dpp transport in the *Drosophila* wing discs (Hsiung et al., 2005; Roy et al., 2014). It will be interesting to see how the relative contributions of different transport mechanisms change depending on the organism, tissue context, and extracellular geometry.

5.3. Synthetic multicellular pattern formation

Can we translate our current understanding of multicellular pattern formation and reaction-diffusion systems into synthetic multicellular patterning systems? Mathematical analyses of reaction-diffusion systems revealed multicomponent networks, consisting of diffusible and non-diffusible components, that could produce self-organized Turing

patterns under a wide range of reaction and diffusion rates (Marcon et al., 2016; Scholes et al., 2019; Zheng et al., 2016). Figure 6A shows, one such four-component reaction-diffusion network with two diffusible components (V, Z) and two non-diffusible components (U, W).

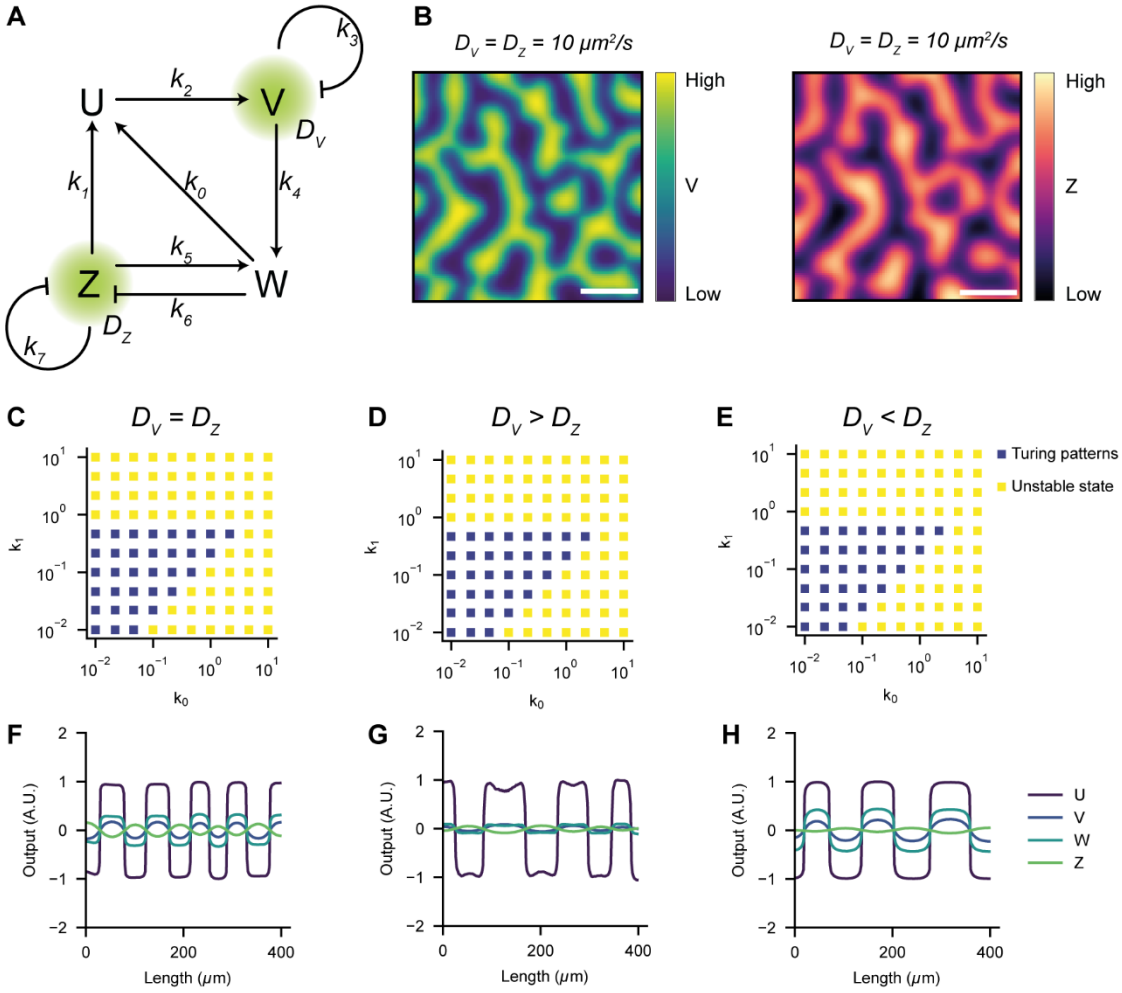

Figure 6: Mathematical analysis of the four-component network
A) A four-component reaction-diffusion network is shown. The diffusible components V and Z (marked with green halo) have diffusion coefficients D_V and D_Z, respectively. The interactions are depicted using directed arrows (for example, U activates V is shown by a pointed arrow, and W inhibits Z is shown with a blunt arrow). The linear reaction rates $(k_i, i = 0, 1, \dots, 7)$ are shown next to the interaction arrows. The type of the interaction (activation or inhibition) is given by the sign of k_i (activation: +ve or k_i > 0; inhibition: -ve or k_i < 0) and the strength of the interaction is given by the magnitude of k_i (high k_i means a stronger interaction). **B)** Results of 2-dimensional simulations of the four-component network with $D_V = D_Z = 10\ \mu m^2 s^{-1}$, $k_0 = 0.5$, $k_1 = 0.1$, $k_2 = 1.0\ min^{-1}$, $k_3 = -4.0\ min^{-1}$, $k_4 = 0.1\ min^{-1}$, $k_5 = 0.1\ min^{-1}$, $k_6 = -1.0\ min^{-1}$, $k_7 = -0.2\ min^{-1}$. **C-E)** Linear stability analyses for the four-component network showing different patterning regimes over the parameter space of k_0 and k_1 and indicated conditions for D_V and D_Z. In C) $D_V = D_Z = 10\ \mu m^2 s^{-1}$, in D) $D_V =$

$100\ \mu m^2 s^{-1}$, $D_Z = 10\ \mu m^2 s^{-1}$, and in E) $D_V = 10\ \mu m^2 s^{-1}, D_Z = 100\ \mu m^2 s^{-1}$. The analysis shows that this four-component network does not require differential diffusivities for the emergence of Turing patterns. **F-H)** Simulation results (1-dimensional) showing emergence of Turing patterns for the four-component network with the diffusion coefficients, in F) $D_V = D_Z = 10\ \mu m^2 s^{-1}$, in G) $D_V = 100\ \mu m^2 s^{-1}$, $D_Z = 10\ \mu m^2 s^{-1}$, and in H) $D_V = 10\ \mu m^2 s^{-1}, D_Z = 100\ \mu m^2 s^{-1}$. Other parameter values are the same as in (B). The wavelength of the patterns varies depending on the values of D_V and D_Z. Note that, appropriate saturation terms (cubic saturation) were used to avoid infinities in the numerical solutions, similar to (Marcon et al., 2016).

The partial-differential equations describing this network are:

$$\frac{\partial}{\partial t} U = k_0 * W + k_1 * Z$$

$$\frac{\partial}{\partial t} V = k_2 * U + k_3 * V + D_v * \nabla^2 V$$

$$\frac{\partial}{\partial t} W = k_4 * V + k_5 * Z$$

$$\frac{\partial}{\partial t} Z = k_6 * W + k_7 * Z + D_z * \nabla^2 Z$$

This network was identified using the RDNets software (Marcon et al., 2016) and it can generate Turing patterns without the 'diffusivity constraints' (Figure 6B), as opposed to the two-component activator-inhibitor network. The relaxation of the diffusivity constraint permits emergence of Turing patterns at a vast range of reaction and diffusion rates, as suggested from the linear stability analyses and numerical simulations (Figure 6C-H) (Marcon et al., 2016). It should be noted, however, that the linear stability analysis is limited to dynamics of the system close to the steady state where linear approximations of the system kinetics are reasonable (Cross & Hohenberg, 1993). Synthetic biological networks are complex and highly nonlinear; hence, analysis of linear systems can only serve as a good starting point from which one should perform more detailed analysis considering nonlinear kinetics (Section 4). Nonlinear analysis can reveal additional features and dynamical properties of the system which are not obvious from the linear approximations and analyses.

The candidate reaction-diffusion networks generated from the high-throughput mathematical analyses can be used to create synthetic multicellular pattern-forming systems. However, major challenges to implementation of such synthetic networks include scarcity of standard biological parts, context-dependence of genetic regulatory

elements and biological circuits, high levels of leakiness in dose-response functions, limited tunability of circuit output, difficulties in coupling many circuits to produce large networks, nonlinear reaction-kinetics, limited availability of accurate biochemical rate parameters, unpredictable circuit behaviors and genetic interactions, cross-reactivity of circuit parts, and cellular metabolic stress caused by the synthetic circuits (Chakraborty et al., 2022; Santos-Moreno & Schaerli, 2019). Despite the challenges, considerable advances have been made in synthetic biological circuit design and implementation (Basu et al., 2005; Carr et al., 2017; Danino et al., 2010; Duran-Nebreda et al., 2021; Elowitz & Leibler, 2000; Karig et al., 2018; Magaraci et al., 2016; Morsut et al., 2016; Sekine et al., 2018).

Based on the four-component reaction-diffusion network, I designed and implemented genetic circuits to investigate synthetic multicellular pattern formation in bacteria (Section 4). Our findings highlighted the key role of genetic feedback networks, diffusible signals, and system geometry for emergence of spontaneous traveling wave patterns in the synthetic multicellular system. We limited the role of cell movements on the traveling wave patterns by immobilizing the bacteria in low-melting-temperature agarose. Interesting collective cell behaviors and gene expression patterns may be observed in this multicellular system by allowing cell movements and changing the viscosity of the medium. Further work is needed to expand the biological parameter space for this system and investigate the emergence of self-organized Turing patterns. This could be achieved by using optimized genetic parts and diffusible signaling molecules that can operate at the reaction-diffusion rates required for emergence of Turing patterns. In the future, it will be interesting to see if advances in nonlinear theories of reaction-diffusion and availability of standard synthetic biology parts could enable robust synthetic multicellular pattern formation for practical applications such as synthetic tissues capable of self-organization and regeneration.

6. Conclusions

I conclude that the framework of reaction-diffusion systems has enabled quantitative understanding of biological pattern formation. Future analyses should focus on multicomponent reaction-diffusion networks that show emergence of self-organized patterns without strict constraints on the reaction-diffusion rates.

The morphogens Nodal and Lefty form a reaction-diffusion system where Nodal acts as a short-range activator and Lefty acts as a long-range inhibitor. Single-molecule tracking of these morphogens in live zebrafish embryos shows that they diffuse in the extracellular space and their diffusion is hindered by binding to receptors. Nodal diffusion is hindered more strongly compared to Lefty, resulting in a short-range Nodal gradient and a long-range Lefty gradient. In the extracellular space, the narrow cell-cell interfaces have high fraction of immobile morphogens, whereas the wide cavity regions have high fraction of freely diffusing morphogens. Hence, control of extracellular geometry offers a mechanism to regulate morphogen dispersal.

Synthetic multicellular systems based on multicomponent reaction-diffusion networks can exhibit spontaneous traveling waves of gene expression. Such synthetic systems are important to not only reveal the role of feedback networks and boundary conditions in pattern formation, but also to enable future applications in the field of synthetic tissue engineering.

7. References

Affolter, M., & Basler, K. (2007). The Decapentaplegic morphogen gradient: from pattern formation to growth regulation. *Nature Reviews Genetics*, *8*(9), 663-674. https://doi.org/10.1038/nrg2166

Akiyama, T., & Gibson, M. C. (2015). Morphogen transport: theoretical and experimental controversies. *WIREs Developmental Biology*, *4*(2), 99-112. https://doi.org/https://doi.org/10.1002/wdev.167

Basu, S., Gerchman, Y., Collins, C. H., Arnold, F. H., & Weiss, R. (2005). A synthetic multicellular system for programmed pattern formation. *Nature*, *434*(7037), 1130-1134. https://doi.org/10.1038/nature03461

Carr, S. B., Beal, J., & Densmore, D. M. (2017). Reducing DNA context dependence in bacterial promoters. *PLoS ONE*, *12*(4), e0176013. https://doi.org/10.1371/journal.pone.0176013

Casas-Tintó, S., & Portela, M. (2019). Cytonemes, Their Formation, Regulation, and Roles in Signaling and Communication in Tumorigenesis. *Int J Mol Sci*, *20*(22). https://doi.org/10.3390/ijms20225641

Chakraborty, D., Rengaswamy, R., & Raman, K. (2022). Designing Biological Circuits: From Principles to Applications. *ACS Synthetic Biology*, *11*(4), 1377-1388. https://doi.org/10.1021/acssynbio.1c00557

Chen, Y., & Schier, A. F. (2001). The zebrafish Nodal signal Squint functions as a morphogen. *Nature*, *411*(6837), 607-610. https://doi.org/10.1038/35079121

Clark, E., & Akam, M. (2016). Odd-paired controls frequency doubling in Drosophila segmentation by altering the pair-rule gene regulatory network. *eLife*, *5*, e18215. https://doi.org/10.7554/eLife.18215

Crick, F. (1970). Diffusion in Embryogenesis. *Nature*, *225*(5231), 420-422. https://doi.org/10.1038/225420a0

Cross, M. C., & Hohenberg, P. C. (1993). Pattern formation outside of equilibrium. *Reviews of Modern Physics*, *65*(3), 851-1112. https://doi.org/10.1103/RevModPhys.65.851

Danino, T., Mondragón-Palomino, O., Tsimring, L., & Hasty, J. (2010). A synchronized quorum of genetic clocks. *Nature*, *463*(7279), 326-330. https://doi.org/10.1038/nature08753

Dequéant, M.-L., & Pourquié, O. (2008). Segmental patterning of the vertebrate embryonic axis. *Nature Reviews Genetics*, *9*(5), 370-382. https://doi.org/10.1038/nrg2320

Diego, X., Marcon, L., Muller, P., & Sharpe, J. (2018). Key Features of Turing Systems are Determined Purely by Network Topology. *Physical Review X*, *8*(2), 021071-021071. https://doi.org/10.1103/PhysRevX.8.021071

Driever, W., & Nüsslein-Volhard, C. (1988). A gradient of bicoid protein in Drosophila embryos. *Cell*, *54*(1), 83-93. https://doi.org/https://doi.org/10.1016/0092-8674(88)90182-1

Duran-Nebreda, S., Pla, J., Vidiella, B., Piñero, J., Conde-Pueyo, N., & Solé, R. (2021). Synthetic Lateral Inhibition in Periodic Pattern Forming Microbial Colonies. *ACS Synthetic Biology*, *10*(2), 277-285. https://doi.org/10.1021/acssynbio.0c00318

Elowitz, M. B., & Leibler, S. (2000). A synthetic oscillatory network of transcriptional regulators. *Nature*, *403*(6767), 335-338. https://doi.org/10.1038/35002125

Ferguson, E. L., & Anderson, K. V. (1992). decapentaplegic acts as a morphogen to organize dorsal-ventral pattern in the Drosophila embryo. *Cell*, *71*(3), 451-461. https://doi.org/https://doi.org/10.1016/0092-8674(92)90514-D

Gierer, A., & Meinhardt, H. (1972). A theory of biological pattern formation. *Kybernetik*, *12*(1), 30-39. https://doi.org/10.1007/BF00289234

Glock, P., Ramm, B., Heermann, T., Kretschmer, S., Schweizer, J., Mucksch, J., Alagoz, G., & Schwille, P. (2019). Stationary Patterns in a Two-Protein Reaction-Diffusion System. *ACS Synth Biol*, *8*(1), 148-157. https://doi.org/10.1021/acssynbio.8b00415

Halatek, J., Brauns, F., & Frey, E. (2018). Self-organization principles of intracellular pattern formation. *Philosophical Transactions of the Royal Society B: Biological Sciences*, *373*(1747), 20170107. https://doi.org/10.1098/rstb.2017.0107

Halatek, J., & Frey, E. (2018). Rethinking pattern formation in reaction–diffusion systems. *Nature Physics*, *14*(5), 507-514. https://doi.org/10.1038/s41567-017-0040-5

Harish, R. K., Gupta, M., Zöller, D., Hartmann, H., Gheisari, A., Machate, A., Hans, S., & Brand, M. (2023). Real-time monitoring of endogenous Fgf8a gradient attests to its role as a morphogen during zebrafish gastrulation. *Development*, dev.201559. https://doi.org/10.1242/dev.201559

Heemskerk, J., & DiNardo, S. (1994). Drosophila hedgehog acts as a morphogen in cellular patterning. *Cell*, *76*(3), 449-460. https://doi.org/https://doi.org/10.1016/0092-8674(94)90110-4

Hsiung, F., Ramirez-Weber, F.-A., David Iwaki, D., & Kornberg, T. B. (2005). Dependence of Drosophila wing imaginal disc cytonemes on Decapentaplegic. *Nature*, *437*(7058), 560-563. https://doi.org/10.1038/nature03951

Huang, H., & Kornberg, T. B. (2015). Myoblast cytonemes mediate Wg signaling from the wing imaginal disc and Delta-Notch signaling to the air sac primordium. *eLife*, *4*, e06114. https://doi.org/10.7554/eLife.06114

Karig, D., Michael Martini, K., Lu, T., DeLateur, N. A., Goldenfeld, N., & Weiss, R. (2018). Stochastic Turing patterns in a synthetic bacterial population. *Proceedings of the National Academy of Sciences of the United States of America*, *115*(26), 6572-6577. https://doi.org/10.1073/pnas.1720770115

Kiecker, C., & Niehrs, C. (2001). A morphogen gradient of Wnt/β-catenin signalling regulates anteroposterior neural patterning in Xenopus. *Development*, *128*(21), 4189-4201. https://doi.org/10.1242/dev.128.21.4189

Klika, V., Baker, R. E., Headon, D., & Gaffney, E. A. (2012). The Influence of Receptor-Mediated Interactions on Reaction-Diffusion Mechanisms of Cellular Self-organisation. *Bulletin of Mathematical Biology*, *74*(4), 935-957. https://doi.org/10.1007/s11538-011-9699-4

Kondo, S., & Miura, T. (2010). Reaction-diffusion model as a framework for understanding biological pattern formation. *Science*, *329*(5999), 1616-1620. https://doi.org/10.1126/science.1179047

Kuhn, T., Landge, A. N., Mörsdorf, D., Coßmann, J., Gerstenecker, J., Čapek, D., Müller, P., & Gebhardt, J. C. M. (2022). Single-molecule tracking of Nodal and Lefty in live zebrafish embryos supports hindered diffusion model. *Nature Communications*, *13*(1), 6101. https://doi.org/10.1038/s41467-022-33704-z

Landge, A. N., Jordan, B. M., Diego, X., & Müller, P. (2020). Pattern formation mechanisms of self-organizing reaction-diffusion systems. *Developmental Biology*, *460*(1), 2-11. https://doi.org/10.1016/j.ydbio.2019.10.031

Levine, M. (2008). A systems view of Drosophila segmentation. *Genome Biol*, *9*(2), 207. https://doi.org/10.1186/gb-2008-9-2-207

Liao, B.-K., Jörg, D. J., & Oates, A. C. (2016). Faster embryonic segmentation through elevated Delta-Notch signalling. *Nature Communications*, *7*(1), 11861. https://doi.org/10.1038/ncomms11861

Loose, M., Fischer-Friedrich, E., Ries, J., Kruse, K., & Schwille, P. (2008). Spatial Regulators for Bacterial Cell Division Self-Organize into Surface Waves in Vitro. *Science*, *320*(5877), 789-792. https://doi.org/10.1126/science.1154413

Lord, N. D., Carte, A. N., Abitua, P. B., & Schier, A. F. (2021). The pattern of nodal morphogen signaling is shaped by co-receptor expression. *eLife*, *10*, e54894. https://doi.org/10.7554/eLife.54894

Lutkenhaus, J. (2007). Assembly Dynamics of the Bacterial MinCDE System and Spatial Regulation of the Z Ring. *Annual Review of Biochemistry*, *76*(1), 539-562. https://doi.org/10.1146/annurev.biochem.75.103004.142652

Magaraci, M. S., Bermudez, J. G., Yogish, D., Pak, D. H., Mollov, V., Tycko, J., Issadore, D., Mannickarottu, S. G., & Chow, B. Y. (2016). Toolbox for Exploring Modular Gene Regulation in Synthetic Biology Training. *ACS Synth Biol*, *5*(7), 781-785. https://doi.org/10.1021/acssynbio.6b00057

Maini, P. K., Woolley, T. E., Baker, R. E., Gaffney, E. A., & Seirin Lee, S. (2012). Turing's model for biological pattern formation and the robustness problem. *Interface Focus*, *2*(4), 487-496. https://doi.org/10.1098/rsfs.2011.0113

Marcon, L., Diego, X., Sharpe, J., & Müller, P. (2016). High-throughput mathematical analysis identifies Turing networks for patterning with equally diffusing signals. *eLife*, *5*, e14022. https://doi.org/10.7554/eLife.14022

Meyer, A. J., Segall-Shapiro, T. H., Glassey, E., Zhang, J., & Voigt, C. A. (2019). Escherichia coli “Marionette” strains with 12 highly optimized small-molecule sensors. *Nature Chemical Biology*, *15*(2), 196-204. https://doi.org/10.1038/s41589-018-0168-3

Morsut, L., Roybal, Kole T., Xiong, X., Gordley, Russell M., Coyle, Scott M., Thomson, M., & Lim, Wendell A. (2016). Engineering Customized Cell Sensing and Response Behaviors Using Synthetic Notch Receptors. *Cell*, *164*(4), 780-791. https://doi.org/https://doi.org/10.1016/j.cell.2016.01.012

Müller, P., Rogers, K. W., Jordan, B. M., Lee, J. S., Robson, D., Ramanathan, S., & Schier, A. F. (2012). Differential diffusivity of nodal and lefty underlies a reaction-diffusion patterning system. *Science*, *336*(6082), 721-724. https://doi.org/10.1126/science.1221920

Müller, P., Rogers, K. W., Yu, S. R., Brand, M., & Schier, A. F. (2013). Morphogen transport. *Development*, *140*(8), 1621-1638. https://doi.org/10.1242/dev.083519

Müller, P., & Schier, A. F. (2011). Extracellular movement of signaling molecules. *Dev Cell*, *21*(1), 145-158. https://doi.org/10.1016/j.devcel.2011.06.001

Murray, J. D. (1993a). Animal Coat Patterns and Other Practical Applications of Reaction Diffusion Mechanisms. In J. D. Murray (Ed.), *Mathematical Biology* (pp. 435-480). Springer Berlin Heidelberg. https://doi.org/10.1007/978-3-662-08542-4_15

Murray, J. D. (1993b). Spatial Pattern Formation with Reaction/Population Interaction Diffusion Mechanisms. In J. D. Murray (Ed.), *Mathematical Biology* (pp. 372-434). Springer Berlin Heidelberg. https://doi.org/10.1007/978-3-662-08542-4_14

Newell, P. C. (1983). Attraction and adhesion in the slime mold Dictyostelium. *Fungal differentiation: a contemporary synthesis*, 43-71.

Nüsslein-Volhard, C., & Wieschaus, E. (1980). Mutations affecting segment number and polarity in Drosophila. *Nature*, *287*(5785), 795-801. https://doi.org/10.1038/287795a0

Potvin-Trottier, L., Lord, N. D., Vinnicombe, G., & Paulsson, J. (2016). Synchronous long-term oscillations in a synthetic gene circuit. *Nature*, *538*(7626), 514-517. https://doi.org/10.1038/nature19841

Preiß, H., Kögler, A. C., Mörsdorf, D., Čapek, D., Soh, G. H., Rogers, K. W., Morales-Navarrete, H., Almuedo-Castillo, M., & Müller, P. (2022). Regulation of Nodal signaling propagation by receptor interactions and positive feedback. *eLife*, *11*, e66397. https://doi.org/10.7554/eLife.66397

Ramírez-Weber, F.-A., & Kornberg, T. B. (1999). Cytonemes: Cellular Processes that Project to the Principal Signaling Center in Drosophila Imaginal Discs. *Cell*, *97*(5), 599-607. https://doi.org/10.1016/S0092-8674(00)80771-0

Ramm, B., Goychuk, A., Khmelinskaia, A., Blumhardt, P., Eto, H., Ganzinger, K. A., Frey, E., & Schwille, P. (2021). A diffusiophoretic mechanism for ATP-driven transport without motor proteins. *Nature Physics*, *17*(7), 850-858. https://doi.org/10.1038/s41567-021-01213-3

Raskin, D. M., & de Boer, P. A. J. (1999). Rapid pole-to-pole oscillation of a protein required for directing division to the middle of Escherichia coli. *Proceedings of the National Academy of Sciences*, *96*(9), 4971-4976. https://doi.org/10.1073/pnas.96.9.4971

Raspopovic, J., Marcon, L., Russo, L., & Sharpe, J. (2014). Digit patterning is controlled by a Bmp-Sox9-Wnt Turing network modulated by morphogen gradients. *Science*, *345*(6196), 566-570. https://doi.org/10.1126/science.1252960

Rogers, K. W., & Müller, P. (2019). Nodal and BMP dispersal during early zebrafish development. *Dev Biol*, *447*(1), 14-23. https://doi.org/10.1016/j.ydbio.2018.04.002

Rogers, K. W., & Schier, A. F. (2011). Morphogen Gradients: From Generation to Interpretation. *Annual Review of Cell and Developmental Biology*, *27*(1), 377-407. https://doi.org/10.1146/annurev-cellbio-092910-154148

Rohith, R., Chih-Chia, C., Elliott, W. Z. W., Thomas, M. G., & Scott, M. C. (2022). A programmable reaction-diffusion system for spatiotemporal cell signaling circuit design. *bioRxiv*, 2022.2011.2015.516470. https://doi.org/10.1101/2022.11.15.516470

Romanova-Michaelides, M., Hadjivasiliou, Z., Aguilar-Hidalgo, D., Basagiannis, D., Seum, C., Dubois, M., Jülicher, F., & Gonzalez-Gaitan, M. (2022). Morphogen gradient scaling by recycling of intracellular Dpp. *Nature*, *602*(7896), 287-293. https://doi.org/10.1038/s41586-021-04346-w

Roy, S., Huang, H., Liu, S., & Kornberg, T. B. (2014). Cytoneme-Mediated Contact-Dependent Transport of the Drosophila Decapentaplegic Signaling Protein. *Science*, *343*(6173), 1244624. https://doi.org/10.1126/science.1244624

Santos-Moreno, J., & Schaerli, Y. (2019). Using Synthetic Biology to Engineer Spatial Patterns. *Advanced Biosystems*, *3*(4), 1800280. https://doi.org/https://doi.org/10.1002/adbi.201800280

Scholes, N. S., Schnoerr, D., Isalan, M., & Stumpf, M. P. H. (2019). A Comprehensive Network Atlas Reveals That Turing Patterns Are Common but Not Robust. *Cell Systems*, *9*(3), 243-257.e244. https://doi.org/10.1016/j.cels.2019.07.007

Schweizer, J., Loose, M., Bonny, M., Kruse, K., Mönch, I., & Schwille, P. (2012). Geometry sensing by self-organized protein patterns. *Proceedings of the National Academy of Sciences*, *109*(38), 15283-15288. https://doi.org/10.1073/pnas.1206953109

Sekine, R., Shibata, T., & Ebisuya, M. (2018). Synthetic mammalian pattern formation driven by differential diffusivity of Nodal and Lefty. *Nat Commun*, *9*(1), 372490-372490. https://doi.org/10.1101/372490

Sheth, R., Marcon, L., Bastida, M. F., Junco, M., Quintana, L., Dahn, R., Kmita, M., Sharpe, J., & Ros, M. A. (2012). Hox Genes Regulate Digit Patterning by Controlling the Wavelength of a Turing-Type Mechanism. *Science*, *338*(6113), 1476-1480. https://doi.org/10.1126/science.1226804

Sick, S., Reinker, S., Timmer, J., & Schlake, T. (2006). WNT and DKK Determine Hair Follicle Spacing Through a Reaction-Diffusion Mechanism. *Science*, *314*(5804), 1447-1450. https://doi.org/10.1126/science.1130088

Smith, S., & Dalchau, N. (2018). Beyond activator-inhibitor networks: The generalised Turing mechanism. *arXiv*. http://arxiv.org/abs/1803.07886

Stanganello, E., Hagemann, A. I. H., Mattes, B., Sinner, C., Meyen, D., Weber, S., Schug, A., Raz, E., & Scholpp, S. (2015). Filopodia-based Wnt transport during vertebrate tissue patterning. *Nature Communications*, *6*(1), 5846. https://doi.org/10.1038/ncomms6846

Stanganello, E., & Scholpp, S. (2016). Role of cytonemes in Wnt transport. *J Cell Sci*, *129*(4), 665-672. https://doi.org/10.1242/jcs.182469

Stapornwongkul, K. S., & Briscoe, J. (2022). In preprints: morphogens in motion. *Development*, *149*(14), dev201066. https://doi.org/10.1242/dev.201066

Struhl, G., Struhl, K., & Macdonald, P. M. (1989). The gradient morphogen bicoid is a concentration-dependent transcriptional activator. *Cell*, *57*(7), 1259-1273. https://doi.org/https://doi.org/10.1016/0092-8674(89)90062-7

Tewary, M., Ostblom, J., Prochazka, L., Zulueta-Coarasa, T., Shakiba, N., Fernandez-Gonzalez, R., & Zandstra, P. W. (2017). A stepwise model of reaction-diffusion and positional information governs self-organized human peri-gastrulation-like patterning. *Development*, *144*(23), 4298-4312. https://doi.org/10.1242/dev.149658

Thompson, D. A. W. (1942). *On Growth and Form* (J. T. Bonner, Ed.). Cambridge University Press. https://doi.org/DOI: 10.1017/CBO9781107325852

Toda, S., Blauch, L. R., Tang, S. K. Y., Morsut, L., & Lim, W. A. (2018). Programming self-organizing multicellular structures with synthetic cell-cell signaling. *Science*, *361*(6398), 156-162. https://doi.org/10.1126/science.aat0271

Turing, A. M. (1952). The chemical basis of morphogenesis. *Philosophical transactions of the Royal Society of London. Series B, Biological sciences*, *237*(641), 37-72. https://doi.org/10.1098/rstb.1952.0012

Tyson, J. J., & Murray, J. D. (1989). Cyclic AMP waves during aggregation of Dictyostelium amoebae. *Development*, *106*(3), 421-426. https://doi.org/10.1242/dev.106.3.421

Warmflash, A., Sorre, B., Etoc, F., Siggia, E. D., & Brivanlou, A. H. (2014). A method to recapitulate early embryonic spatial patterning in human embryonic stem cells. *Nature Methods*, *11*(8), 847-854. https://doi.org/10.1038/nmeth.3016

White, K. A. J., & Gilligan, C. A. (1998). Spatial heterogeneity in three-species, plant-parasite-hyperparasite, systems. *Philosophical Transactions of the Royal Society B: Biological Sciences*, *353*(1368), 543-557. https://doi.org/10.1098/rstb.1998.0226

Wolpert, L. (1969). Positional information and the spatial pattern of cellular differentiation. *Journal of Theoretical Biology*, *25*(1), 1-47. https://doi.org/https://doi.org/10.1016/S0022-5193(69)80016-0

Zheng, M. M., Shao, B., & Ouyang, Q. (2016). Identifying network topologies that can generate turing pattern. *Journal of Theoretical Biology*, *408*, 88-96. https://doi.org/10.1016/j.jtbi.2016.08.005